The Laser Calibration System of the JUNO Pre-Detector OSIRIS

Dissertation

der Mathematisch-Naturwissenschaftlichen Fakultät
der Eberhard Karls Universität Tübingen
zur Erlangung des Grades eines
Doktors der Naturwissenschaften
(Dr. rer. nat.)

vorgelegt von
Tobias Richard Sterr
aus Stuttgart

Tübingen
2024

Gedruckt mit Genehmigung der Mathematisch-Naturwissenschaftlichen
Fakultät der Eberhard Karls Universität Tübingen.

Tag der mündlichen Qualifikation:	21.02.2025
Dekan:	Prof. Dr. Thilo Stehle
1. Berichterstatter:	Prof. Dr. Tobias Lachenmaier
2. Berichterstatter:	Prof. Dr. Josef Jochum

Für meine Großeltern Walli, Erika, Richard, und Werner,
ohne die ich heute nicht die Person wäre, die ich bin.

Contents

Abstract

Answering the question about the ordering of the neutrino masses is one of the large unanswered questions of neutrino physics. A candidate to answer this question is the **J**iangmen **U**nderground **N**eutrino **O**bservatory (JUNO), which is a large 20 kt liquid scintillator based neutrino oscillation experiment located in southern China that will begin data collection in 2025. To achieve this goal, JUNO requires an unprecedented energy resolution of $3\,\%/\sqrt{E_{vis}[\mathrm{MeV}]}$. In such a measurement, reducing radioactive backgrounds that might mimic neutrino signals plays a crucial role. Therefore, keeping the concentration of uranium and thorium at a level of 10^{-15} g/g is crucial to the success of the experiment. To monitor this purity of the liquid scintillator during the filling phase of JUNO, the **O**nline **S**cintillator **I**nternal **R**adioactivity **I**nvestigation **S**ystem (OSIRIS) was introduced. OSIRIS is an 18 t liquid scintillator pre-detector of JUNO, featuring a 3 m x 3 m acrylic vessel housed in a 9 m x 9 m water-filled steel tank. Equipped with 76 20-inch photomultiplier tubes (twelve in the water Cherenkov muon veto and 64 in the inner detector), this system will be used to continuously monitor the produced liquid scintillator's purity.
In the scope of this work, a laser calibration system responsible for the timing and charge calibration of the photomultiplier tubes of OSIRIS was developed, built, characterized, and installed. In addition, parts of the slow control system of OSIRIS have been produced.
This thesis will present the schematic of the laser calibration system, its control software, as well as the results of the characterization measurements done with the system. Furthermore, analysis of first data taken by OSIRIS with the laser calibration system will be presented. In the last chapter, a description of the parts of the slow control of OSIRIS created in the scope of this work is given.

Zusammenfassung

Die Frage nach der Anordnung der Massen der Neutrinos ist nach wie vor eine der großen ungeklärten Fragen der Neutrinophysik. Das **J**iangmen **U**nderground **N**eutrino **O**bservatory (JUNO), welches ein Flüssigszintillator-basiertes Neutrinooszillationsexperiment in Südchina ist, soll mit dem Beginn der Datennahme Anfang 2025 dazu beitragen, diese Frage zu beantworten. Um dieses Ziel zu erreichen muss JUNO eine beispiellose Energieauflösung von $3\,\%/\sqrt{E_{vis}[\mathrm{MeV}]}$ erreichen. Bei einer solchen Messung muss speziell bei der Wahl der Bauteile und Materialien auf Eignung und mögliche Quellen für Untergrundereignisse geachtet werden um diese so weit wie möglich zu reduzieren. Für den Erfolg des Experimentes ist es daher wichtig, die Konzentration von Uran und Thorium im Flüssigszintillator auf eine Konzentration von 10^{-15}g/g zu beschränken. Zur Überwachung dieser Konzentrationsgrenze wurde daher das **O**nline **S**cintillator **I**nternal **R**adioactivity **I**nvestigation **S**ystem (OSIRIS) entwickelt.
OSIRIS ist ein 18 Tonnen fassender Flüssigszintillatordetektor in dessen Zentrum sich ein 3ṁ x 3 m großer Acryltank befindet, welcher in einem 9 m x 9 m großen wassergefüllten Stahltank untergebracht ist. Ausgestattet mit 76, 20-Zoll großen, Photoelektronenvervielfacherröhren (zwölf davon im Wasser-Cherenkov Muon veto sowie 64 weitere im inneren Detektor), wird dieses System fortlaufend die Qualität des produzierten Flüssigszintillators überprüfen.
Im Rahmen dieser Arbeit wurde ein Laserkalibrationssystem zur Zeit- und Ladungskalibration der Photoelektronenvervielfacherröhren entwickelt, gebaut, charakterisiert und vor Ort installiert. Zusätzlich wurden Teile der Steuerungssoftware von OSIRIS geschrieben.
Die vorliegende Arbeit wird den Aufbau des Laserkalibrationssystems, seine Steuerung sowie die Resultate der Charaterisierungsmessungen des Systems präsentieren. Darüber hinaus werden erste Analysen von Daten, welche mit dem Laserkalibrationsystems von OSIRIS aufgenommen wurden, gezeigt. Eine Übersicht über die im Rahmen dieser Arbeit geschriebenen Steuerungsprogramme wird dann im letzten Kapitel gegeben.

Chapter 1

Introduction

"Everything starts somewhere, although many physicists disagree."
-Death

from "Hogfather" by Terry Pratchett, 1996

In the last almost seventy years, neutrino physics has developed to one of the most active fields of (astro)particle physics. Since the first (experimental) steps in the field have been done by Cowan and Reines[1] a vast range of experiments has been carried out up to now[2–13]. All of these experiments faced the same challenge: The fact that neutrinos only interact weakly and therefore pass through matter with almost no interaction[14]. Although this behavior led to an experimental challenge in the beginning, quite some natural sources of neutrinos have been identified and used by various experiments since then. These sources include but are not limited to the sun, the atmosphere and radioactive decays. In modern times, several advancements in material sciences, chemistry, information technology and microelectronics, led to a set of experiments currently under construction[15–18], which will be able to not only set new limits to the several parameters of the neutrino sector but to answer questions such as the ordering of the neutrino masses and the existence of sterile neutrinos. Due to the size and the required precision of these new experiments, the requirements for electronics, background, data acquisition and detector control led to more complex experimental setups. Additionally, run times of a few decades also sets high standards for long-term reliability and performance.
One of the remaining open questions in neutrino physics is the ordering of the

neutrino masses. Solving this question also has a massive impact on open question in astroparticle and fundamental physics [19, 14]. Since the sign of the large squared mass difference Δm^2_{3x} still remains unknown, two different possibilities for the neutrino mass ordering remain: the normal mass ordering and the inverted mass ordering. One of the experiments trying to solve this question is the Jiangmen Underground Neutrino Observatory (JUNO). JUNO is a large scale, liquid scintillator experiment located in Jiangmen, Guangdong, P.R.China, that will be starting to take data in 2025. The primary goal of JUNO is to resolve the neutrino mass ordering with 3σ in the first 6.5 years of data taking using two nearby nuclear power plants as neutrino sources. In addition, other scientific goals have been defined, including setting new limits to the remaining neutrino oscillation parameters, geo-neutrinos, atmospheric neutrinos, supernova neutrinos and rare event searches like proton decay or dark matter interactions.
Resolving the neutrino mass ordering requires JUNO to be able to resolve the neutrino oscillation patterns on an unprecedented level, requiring an energy resolution of $3\%/\sqrt{E_{vis}[MeV]}$. Such a precision also sets limits to quality and radioactive purity of almost all parts of the detector, with a higher focus on all parts that contribute to reach the desired energy resolution of the detector. As a consequence, this automatically implies a focus on the photomultiplier tubes (PMTs) as well as the liquid scintillator itself.
To address these implications, 20'000 20-inch PMTs of JUNO have been carefully tested and characterized during a large campaign between 2017 and 2022 [20–22] resulting in qualification and characterisation values for each individual PMT in the experiments. However, since the liquid scintillator (LS) of JUNO will only be mixed prior to the filling of the detector, such a pre-testing is not possible. Additionally, given the large mass of 20 kt of required LS and the small contamination limits of $10^{-15}(10^{-16}g/g$ for inverse beta-decay (solar) neutrinos of the scintillator, the development of an appropriate testing device was a complex matter resulting in the creation of the Online Scintillator Internal Radioactivity Investigation System (OSIRIS). OSIRIS is installed as a pre-detector of JUNO located at the very end of the LS production line in the underground LS hall of the laboratory. Using the same PMTs and electronics as the main detector of JUNO, OSIRIS features a cylindrical acrylic vessel with a capacity of 18t of LS. Testing approximately 10% of the LS during the filling phase of JUNO, OSIRIS will be focusing on testing the radio-purity of the liquid scintillator, recycling all LS failing the acceptance criteria.

This work largely contributed to the setup, installation, calibration and control of the OSIRIS detector. In the first chapter (2), a short introduction into the theory of neutrino physics is given, followed by the second chapter (3) giving a more detailed picture about JUNO. Going into more detail of OSIRIS, chapter 4 delivers a description of OSIRIS and its sub-systems. This is followed by chapter 5 providing information about the laser calibration system of OSIRIS which has been developed in the scope of this work. As an initial example of data taken with OSIRIS, chapter 6 provides results from the first calibration campaigns of OSIRIS. This work concludes with chapter 7 giving information

about the parts of the slow control of OSIRIS written for this work as well as an conclusion and outlook (chapter 8) of the topics discussed.

Chapter 2

Neutrinos in the Standard Model

"Oh, before I forget...
I think you dropped this back at Black Mesa.
Good luck out there, buddy. You're gonna need it."
-Barney Calhoun

from "Half life 2", 2004

2.1 Neutrino mass

In the standard model of particle physics, neutrinos are massless elementary Dirac particles without electric charge [23] [24], only interacting weakly. Neutrinos can be observed in three different (leptonic) flavors, as both particle and anti-particle: electron neutrino (ν_e and $\bar{\nu}_e$), muon neutrino (ν_μ and $\bar{\nu}_\mu$) and tau neutrino (ν_τ and $\bar{\nu}_\tau$).
Due to the violation of the parity symmetry in the weak force, neutrinos (anti-neutrinos) occur only in left-handed (right-handed) chirality [25]. Therefore, neutrinos are introduced in the standard particle model as left-handed only doublets [24], together with the corresponding lepton (electron, muon, tauon). Their right-handed counterparts, however, are introduced as singlets. One should note that the helicity of the neutrino was measured in the Goldhaber experiment [25] and found to be identical to the helicity of a massless fermion[1]. Though neutrinos have been found to have finite mass (with the Homestake experiment [10] being the first experiment to find first hints of this neutrino property) and since

[1] Within the given uncertainty of $H = -1.0 \pm 0.3$

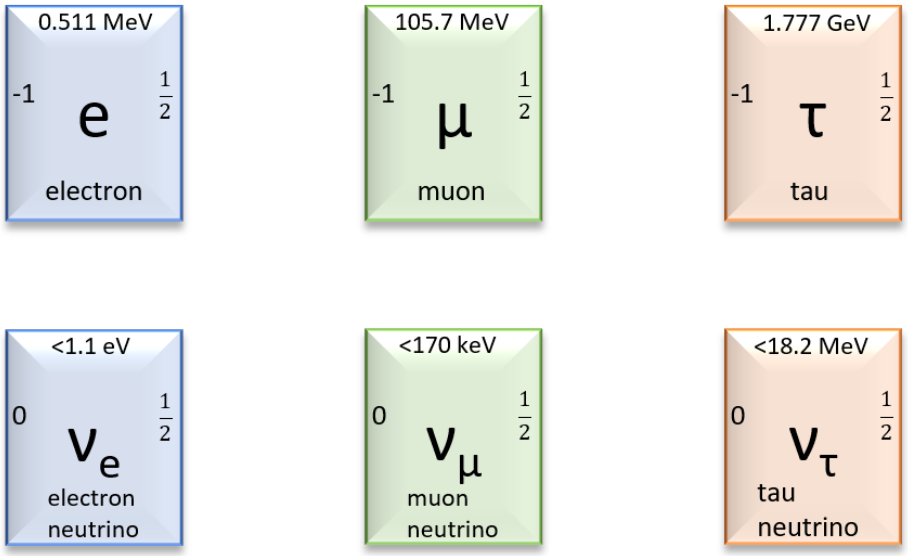

Figure 2.1: Properties of the leptons of the standard model of particle physics in units of the elementary charge. The numbers are: mass/upper limit for mass (top), electric charge (left) and spin (right). Each column corresponds to a lepton flavor. The lepton number of each flavor is conserved in the standard model of particle physics with massless neutrinos. Values are taken from [24, 30–32].

helicity is not invariant under Lorentz transformation, in this work the chiralty is named instead of the helicity.

In nature, neutrinos are created in many naturally occurring processes that include weak interactions, including supernovae, nuclear fusion and fission, interaction of cosmic radiation with Earth's atmosphere and natural radioactive beta-decay. In addition to these natural sources, some man-made sources are also known that include particle accelerators and nuclear power plants (NPP). Experiments have shown the significantly smaller mass of neutrinos in comparison to the other massive fermions of the standard model (SM) [24]. A question, that arises from this observation is whether the mechanism of mass generation is the same for neutrinos as for the other leptons. To address this question, several new models—such as the 'seesaw' mechanism—were introduced [26]. These theories amend the known properties of the neutrino of the standard model of particle physics in order to better explain the measured properties of neutrinos (for further information, see [27–29] and figure 2.1). Most recent results from direct neutrino mass measurements of KATRIN give an upper limit of $m_\nu < 0.45\,\mathrm{eV}$ (90 % C.L.) for the electron antineutrinos [30]. Additionally, the CMB observations of Planck gave a (cosmological model depending) limit for the sum of all neutrinos of $\sum_\nu m_\nu < 120$ meV (95% C.L.) [33].

Due to the properties of neutrinos and the limitations of current measurement setups and experiments, several open question remain in the neutrino sector:

- *Are neutrinos Dirac or Majorana particles?*
  It is possible that neutrinos are their own anti-particle, which means that neutrino and anti-neutrino are identical particles differing only by their helicity. In this case neutrinos are considered to be Majorana particles, in contrast to the remaining fermions of the standard model that are considered to be Dirac particles. Another implication of the possible Majorana nature of neutrinos would be the possibility of lepton number violation. Searches for Majorana neutrinos are currently conducted by experiments like LEGEND200 [34] or nEXO [35].

- *What is the ordering of the neutrino masses?*
  The ordering of the neutrinos masses is not yet determined. Two different orderings are possible (see section 2.3). Since neutrinos are part of many processes found in nature (see above), different probes are possible for this property. Many experiments are trying to solve this question, including JUNO [19], DUNE [17], IceCube [8] and HyperK [16]. For further information on JUNO, see chapter 3.

- *Are there more than three neutrino flavors?*
  The existence of additional 'sterile' neutrino flavors has not been ruled out. A "sterile" neutrino is a neutrino that does not interact via weakly interaction, which means they can only be detected through disappearance experiments. Experiments searching for sterile neutrinos are, for example, MiniBooNE [36] and STEREO [37].

- *Do neutrinos violate the CP symmetry?*
  Due to the existing δ-phase in the mixing matrix (see section 2.2) it is possible, that the neutrino sector does violate the CP symmetry. Several experiments (e.g., T2K [3] and NOνA [5]) are currently searching for such a CP symmetry violation.

- *What is the octant of Θ_{23}?*
  In addition to the topics already mentioned, some details in the field of neutrino oscillations are still not completely known. E.g., the octant of Θ_{23} is not known, yet. Experiments investigating this question include NOνA, DUNE, and again T2K [38].

2.2 Neutrino Oscillation

The solar neutrino problem is considered to be one of the first hints to the incompleteness of the standard model: Davis and others [39] discovered a significant deficit compared to the expected neutrino flux coming from the sun [40]. Located in the Homestake mine in South Dakota, the experiment was designed to measure the solar neutrino flux for more than 20 years using a liquid neutrino target of perchlorethene. The detection channel used was the counting of decays of unstable argon atoms produced in the capturing process of neutrinos by chlorine nuclei [41]. The result of the measurement of the neutrino flux was only about a third of the electron neutrino flux predicted by the standard solar model, which could not be explained by any error of the electron neutrino flux, neither statistically nor systematically. A modification of the standard solar model (SSM) was considered, but later discarded since no modification could explain this effect in completion [42]. After other experiments like GALLEX/GNO [11] and SAGE [12] confirmed the findings of Homestake [2]. After investigations by Super-K and Kamland the apparent anomaly turned out to be the result of a spontaneous and periodic change in the flavor of neutrinos. This however, requires neutrinos to have a finite mass and mixed lepton flavors [19].
The first experiments observing neutrino oscillation were Super Kamiokande [2] and SNO [9]. Both experiments measured the neutrino flux as well as the neutrino flavor changes without the dependency of an underlying model (the neutrino source of Super-K was the atmosphere, whilst SNO used the sun). More recently, several other neutrino experiments have been conducted, including: OPERA (ν_μ,ν_τ) [4], Daya Bay ($\bar{\nu}_e$) [7], MINOS (ν_e, ν_μ) [43] and NOνA (ν_μ, ν_e) [44]. Due to the results of the mentioned experiments, a extension of the standard model of particle physics seems inevitable to explain non vanishing mass differences as well as other not excluded phenomena like the violation of the lepton number conservation.
The eigenstates of the neutrino (flavor eigenstates and mass eigenstates) form an orthogonal, complete basis of the neutrino within the (unaltered) SM. Whilst the flavor eigenstates couple to the $W^{\pm}$ vector boson in the weak interaction, the mass eigenstates diagonalize the Hamiltonian operator of the free-particle neutrino and therefore describe its time evolution [3]. Both bases can be transformed into each other via the Pontecorvo-Maki-Nakagawa-Sakata (PMNS) matrix U_{PMNS}:

$$|\nu_\alpha\rangle = \sum_k U^*_{\alpha k} |\nu_k\rangle, \tag{2.1}$$

$$|\nu_k\rangle = \sum_\alpha U_{\alpha k} |\nu_\alpha\rangle. \tag{2.2}$$

[2] GALLEX/GNO and SAGE also found additional details of the solar neutrino production mechanism like the existence of pp neutrinos.

[3] and hence also its propagation

Here, all ν_k (k=1,2,3,...) are the mass eigenstates, ν_α (α = e, μ, τ) the flavor eigenstates and $U_{\alpha k}$ the elements of the PMNS [4] matrix:

$$\begin{pmatrix} \nu_e \\ \nu_\mu \\ \nu_\tau \\ \vdots \end{pmatrix} = \begin{pmatrix} U_{e1} & U_{e2} & U_{e3} & \cdots \\ U_{\mu 1} & U_{\mu 2} & U_{\mu 3} & \cdots \\ U_{\tau 1} & U_{\tau 2} & U_{\tau 3} & \cdots \\ \vdots & \vdots & \vdots & \ddots \end{pmatrix} \begin{pmatrix} \nu_1 \\ \nu_2 \\ \nu_3 \\ \vdots \end{pmatrix} \tag{2.3}$$

In the case of the three neutrino theory, the PMNS matrix is reduced to a 3x3 unitary matrix. Should there be hints of non-unitarity of this matrix, the possibility of additional, possibly sterile flavors of neutrinos becomes more likely. The PMNS matrix being the identity matrix leads to an equality of mass and flavor eigenstates (even though experiments have shown that this is not the case). However, one should note that the unitarity of the PMNS matrix depends on the number of light neutrino flavors[5] (see [45] and [46]).
In the most common parametrization of the PMNS matrix, three parameters are the three "mixing" angles Θ_{ij} (i,j = 1,2,3, $i < j$) and an additional parameter is the complex phase δ which describes CP violation in the case of $\delta \neq 0$ and $\delta \neq \pi$:

$$\begin{aligned} U &= \begin{pmatrix} U_{e1} & U_{e2} & U_{e3} \\ U_{\mu 1} & U_{\mu 2} & U_{\mu 3} \\ U_{\tau 1} & U_{\tau 2} & U_{\tau 3} \end{pmatrix} \\ &= \begin{pmatrix} 1 & 0 & 0 \\ 0 & c_{23} & s_{23} \\ 0 & -s_{23} & c_{23} \end{pmatrix} \begin{pmatrix} c_{13} & 0 & -s_{13}e^{-i\delta} \\ 0 & 1 & 0 \\ -s_{13}e^{i\delta} & 0 & c_{13} \end{pmatrix} \begin{pmatrix} c_{12} & s_{12} & 0 \\ -s_{12} & c_{12} & 0 \\ 0 & 0 & 1 \end{pmatrix} \\ &= \begin{pmatrix} c_{12}c_{13} & s_{12}c_{13} & s_{13}e^{-i\delta} \\ -s_{12}c_{23} - c_{12}s_{23}s_{13}e^{i\delta} & c_{12}c_{23} - s_{12}s_{23}s_{13}e^{i\delta} & s_{23}c_{13} \\ s_{12}s_{23} - c_{12}c_{23}s_{13}e^{i\delta} & -c_{12}s_{23} - s_{12}c_{23}s_{13}e^{i\delta} & c_{23}c_{13} \end{pmatrix} \end{aligned} \tag{2.4}$$

with $s_{ij} = \sin\Theta_{ij}$ and $c_{ij} = \cos\Theta_{ij}$.
A free neutrino exists in a superposition of its mass eigenstates. Since each eigentstate propagates with an individual velocity, the superposition dephases during propagation. This dephasing directly leads to a change in the lepton flavor composition and therefore to an oscillation pattern in these flavor contributions over distance. This, however, is only valid in case of full quantum mechanical state coherence, which is true given the (very) small masses of neutrinos in comparison to their kinetic energy.
This time evaluation can be noted as:

[4] To be precise, the PMNS matrix always refers to the 3x3 form of this matrix.
[5] As mentioned, there are possibilities for additional, sterile neutrino flavors. The search for these sterile neutrinos is one of the topics of current and future neutrino experiments.

$$|\nu_k(t)\rangle = e^{-i(E_k \cdot t - \vec{p_k} \cdot \vec{x})} |\nu_k(0)\rangle \tag{2.5}$$

Using $\vec{p_k}$ and $\vec{x}$ as the relativistic momentum and position vectors of the particle at its source in natural units. In the case of a neutrino produced in a flavor $|\nu_\alpha\rangle$, an overlap with an eigenstate $|\nu_\beta\rangle$ exists after propagation of a distance L. With the relativistic approximation for neutrinos with a momentum much larger than their mass

$$E_k = \sqrt{|\vec{p}^2 + m_k^2|} \approx p + \frac{m_k^2}{2p} \tag{2.6}$$

and $\vec{x} = L$ as well as $t = L/c \approx L$ [6] the exponent can be written as

$$E_k L - \vec{p} L \approx \left(p + \frac{m_k^2}{2p} \right) L - pL = \frac{m_k^2 \cdot L}{2E} \tag{2.7}$$

where $p \approx E$ was used for relativistic neutrinos. This leads to a transition probability from flavor α at the source to flavor β at the detector.

$$\begin{aligned} P_{\alpha\to\beta} &= |\langle \nu_\beta | \nu_\alpha(L) \rangle|^2 \\ &= \left| \sum_k \sum_l U^*_{\alpha k} U_{\beta l} e^{-i \frac{m_k^2 L}{2E}} \langle \nu_l | \nu_k \rangle \right|^2 \\ &= \left| \sum_k U^*_{\alpha k} U_{\beta k} e^{-i \frac{m_k^2 L}{2E}} \right|^2 \\ &= \delta_{\alpha\beta} - 4 \sum_{k>j} \mathfrak{Re}(U^*_{\alpha k} U_{\beta k} U_{\alpha j} U^*_{\beta j}) \sin^2 \frac{\Delta m^2_{kj} L}{4E} \\ &\quad + 2 \sum_{k>j} \mathfrak{Im}(U^*_{\alpha k} U_{\beta k} U_{\alpha j} U^*_{\beta j}) \sin^2 \frac{\Delta m^2_{kj} L}{2E} \end{aligned} \tag{2.8}$$

with $\Delta m^2_{kj} := m_k^2 - m_j^2$. Dropping natural units, the argument of the sine can be expressed as:

$$\begin{aligned} \frac{\Delta m^2 c^3 L}{4\hbar E} &= \frac{GeV \cdot fm}{4\hbar c} \times \frac{\Delta m^2}{eV^2} \frac{L \cdot MeV}{m \cdot E} \\ &\approx 1.27 \times \frac{\Delta m^2}{eV^2} \frac{\frac{L}{E}}{\frac{m}{MeV}} \end{aligned} \tag{2.9}$$

Further information can be found in [23].
Plotting the survival probability of e.g., the electron anti-neutrino

$$\begin{aligned} P_{\bar{\nu}_e \to \bar{\nu}_e} &= 1 - \sin^2 2\Theta_{12} \cos^4 \Theta_{13} \sin^2 \Delta_{21} \\ &\quad - \sin^2 2\Theta_{13} \cdot (\sin^2 \Theta_{12} \sin^2 \Delta_{32} + \cos^2 \Theta_{12} \sin^2 \Delta_{31}) \end{aligned} \tag{2.10}$$

[6] Since natural units are still considered in this calculation.

Table 2.1: Best fit values of the variables in the three-neutrino case to global data taken in November 2023. Both mass ordering cases are shown (left: normal, right: inverted). Δm^2_{3l} defines the largest mass difference for each ordering, leading to $\Delta m^2_{3l} > 0$ in the case of normal ordering and $\Delta m^2_{3l} < 0$ for the inverted ordering. For further details about the two different possibilities, see chapter 2.3. Values gathered from [47] and the corresponding database [48].

	Normal Ordering (global best fit)		Inverted Ordering ($\Delta\chi^2 = 6.4$)	
	bfp $\pm 1\sigma$	3 σ range	bfp $\pm 1\sigma$	3 σ range
$\sin^2\Theta_{12}$	$0.303^{+0.012}_{-0.012}$	$0.270 \to 0.341$	$0.303^{+0.012}_{-0.011}$	$0.270 \to 0.341$
$\Theta_{12}[^\circ]$	$33.41^{+0.75}_{-0.72}$	$31.31 \to 35.74$	$33.41^{+0.75}_{-0.72}$	$31.31 \to 35.74$
$\sin^2\Theta_{23}$	$0.451^{+0.019}_{-0.016}$	$0.408 \to 0.603$	$0.569^{+0.016}_{-0.021}$	$0.412 \to 0.613$
$\Theta_{23}[^\circ]$	$42.2^{+1.1}_{-0.9}$	$39.7 \to 51.0$	$49.0^{+1.0}_{-1.2}$	$39.9 \to 51.5$
$\sin^2\Theta_{13}$	$0.02225^{+0.00056}_{-0.00059}$	$0.02052 \to 0.02398$	$0.02223^{+0.00058}_{-0.00058}$	$0.02048 \to 0.02416$
$\Theta_{13}[^\circ]$	$8.58^{+0.11}_{-0.11}$	$8.23 \to 8.91$	$8.57^{+0.11}_{-0.11}$	$8.23 \to 8.94$
$\delta_{CP}[^\circ]$	232^{+36}_{-26}	$144 \to 350$	276^{+22}_{-29}	$194 \to 344$
$\frac{\Delta m^2_{21}}{10^{-5}eV^2}$	$7.41^{+0.21}_{-0.20}$	$6.82 \to 8.03$	$7.41^{+0.21}_{0.20}$	$6.82 \to 8.03$
$\frac{\Delta m^2_{3l}}{10^{-3}eV^2}$	$+2.507^{+0.026}_{-0.027}$	$+2.427 \to 2.590$	$-2.486^{+0.025}_{-0.028}$	$-2.570 \to -2.406$

leads to the well known neutrino oscillation pattern (see figure 2.2. A table of all current best-fit values[7] based on the results of various experiments can be found in table 2.1. As a conclusion, one should add, that there are still some large unknowns in this data. On the one hand, there is still no determination of the sign of Δm^2_{3l}, on the other hand is the octant of Θ_{23} still unclear. As a last remark, it should be mentioned that the CP conservation is still not ruled out in current measurements ($\delta = 0$).

[7] values given in [bfp]: "best fit point"

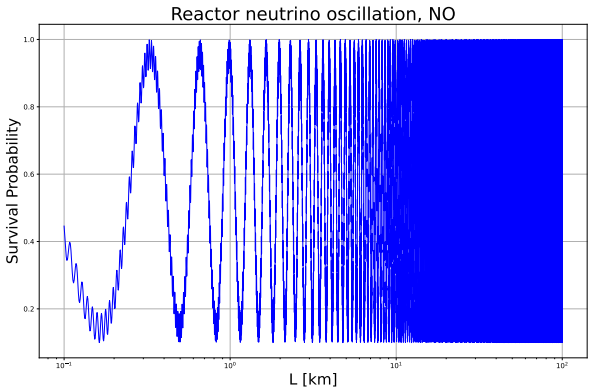

(a)

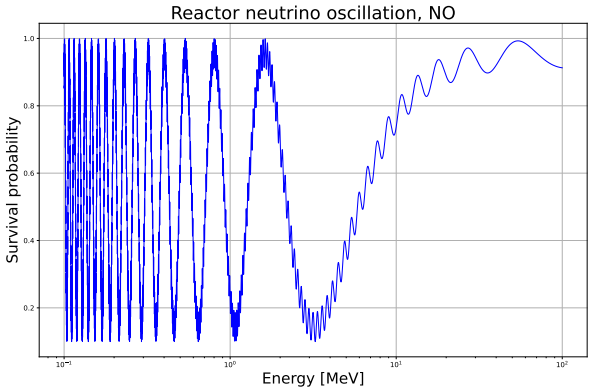

(b)

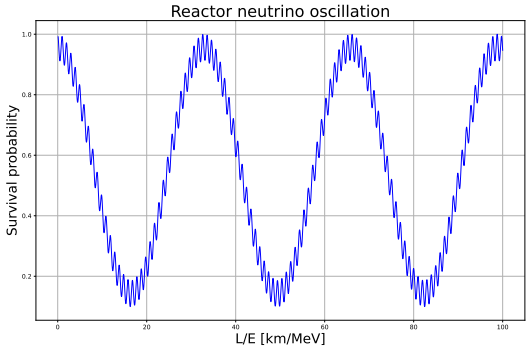

(c)

Figure 2.2: Plots of the anti-electron neutrino survival probability for the case of normal ordering. Plot a shows the dependence of the survival probability to the distance [0.1,100] km, with a fixed energy of 10 MeV, plot b the dependence to the energy [0.1,100] MeV with a fixed distance of 53 km and plot c the dependence of the combined factor L/E [0.1,100] km/MeV.

2.3 Neutrino mass ordering

One of the main goals of JUNO is to answer one of the major remaining open questions of neutrino physics: the determination of the neutrino mass ordering (also referred to as "neutrino mass hierarchy NMH"). There are two possibilities for the sorting of the neutrino masses:

- **Normal Ordering (NO)**
  In the case of NO the masses are sorted in ascending order:

  $$m_1 < m_2 < m3 \tag{2.11}$$

  following

  $$|U_{e1}|^2 > |U_{e2}|^2 > |U_{e3}|^2 \tag{2.12}$$

  which can be translated to m_1 being the eigenstate with the highest electron neutrino contribution.

- **Inverted Ordering (IO)**
  The other possible case to be considered is the IO, in which the mass ordering starts with m_3 being the lightest mass eigenstate:

  $$m_3 < m_1 < m_2 \tag{2.13}$$

  The absolute value of Δm^2_{31} only differs slightly between NO and IO. However, the uncertainty of previous experiments measuring this parameter was larger than the difference between the two orderings. As a result, there is still no final determination of the sign of the large atmospheric mass squared difference[8] This is in contrast to the measurements of Δm^2_{21} which has been proven to be larger than zero (using the MSW effect [50, 51]).

A graphical representation of the possibilities for the neutrino mass ordering can be seen in figure 2.3. Current measurements of T2K [3], NOνA [5] and Super-K [2] show a slight preference to the normal ordering (even though there are some discrepancies in the measurements of T2K and NOνA [52]), however, since there is still no determination of the phase σ_{CP}, these results depend on assumptions about this value..

There are several implications for the results of the determination of the neutrino mass hierarchy: As examples, the determination of the absolute neutrino mass and the search for $0\nu\beta\beta$ decay (see figures 2.4 and 2.5) needs to be mentioned. The figures show the allowed regions of different planes of the neutrino oscillation based on a current global analysis and the dependence of the search for neutrinoless double beta decay on the mass ordering, respectively. There are

[8] There are different definitions of the atmospheric neutrino mass squared difference. This includes for example different mass squares for the two orderings in the case of the NuFit group ($\Delta m^2_A = \Delta n^2_{23}(IO)$, $\Delta m^2_A = |\Delta m^2_{13}|(NO)$), or a mixture of both ($\Delta m^2_A) = \frac{1}{2}|\Delta m^2_{13} + \Delta m^2_{23}|(NO, IO)$ in the case of the Bari analysis group [49].

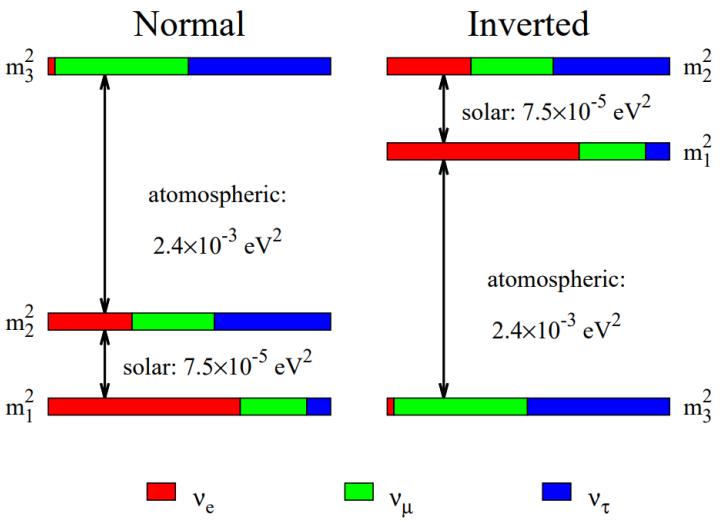

Figure 2.3: Graphical representation of the possible neutrino mass orderings [19]. Colors are indicating the flavor composition of the mass eigenstates, m_1 is considered the eigenstate with the largest ν_e contribution.

also implications to other neutrino oscillation parameters like Θ_{13}, Θ_{23} and δ_{CP} since in global fits these values are sensitive to the sign of Δm^2_{31}. Furthermore, there are implications that the neutrino mass ordering could also play a role in the origin of neutrino masses and mixing [19].

An experimental determination of the neutrino mass ordering has thus been discussed broadly in the scientific community [19, 55]. The approach is an experimental setup that is sensitive to the sign of Δm_{31}, which can be done by the precise measurement of neutrino oscillation. Such a setup requires a sufficiently high energy resolution to resolve distinct features in the neutrino oscillation spectrum which are related to the neutrino mass ordering (for both cases, IO and NO) [56, 57]. For an exemplary neutrino oscillation spectrum showing these features, see figure 2.6.

An example of an experiment capable of measuring some of the parameters mentioned above (Θ_{13} and the sign of Δm^2_{32} as the primary goal) is the JUNO detector. It will feature an energy resolution even exceeding the required limits as well as the background levels necessary to determine the neutrino mass ordering. A further discussion of JUNO can be found in chapter 3. As a conclusive remark, it must be mentioned, that there are other experimental ideas to determine the neutrino mass ordering. These include the use of matter effects in long-baseline accelerator experiments (e.g., NOνA, DUNE) [59, 60] which is the terrestrial MSW effect that influences traversing atmospheric neutrinos (e.g., HyperK[61], DUNE [62]) . Some extensive reviews can be found in [55] and [63].

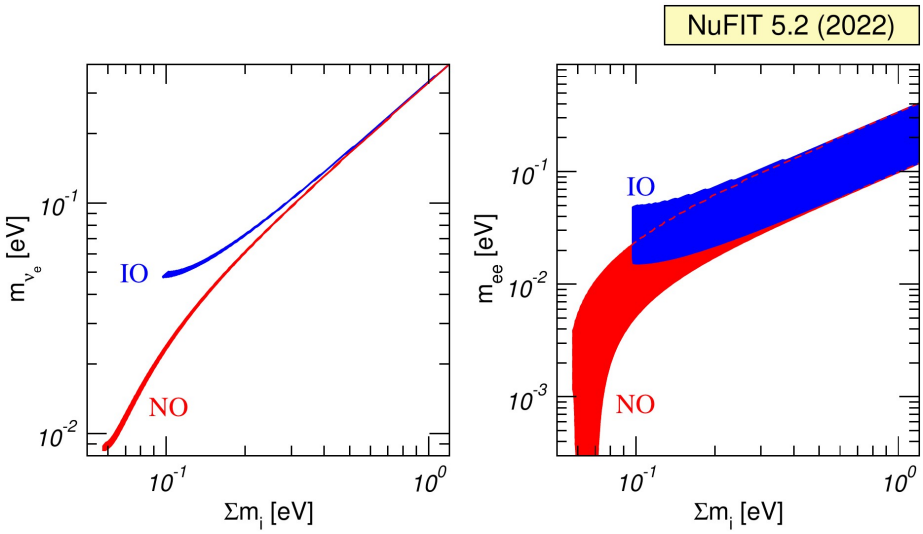

Figure 2.4: Allowed regions at 2σ (2 dof) obtained by projecting the results of the global analysis of oscillation data (w/o Super-K atm, since these results create some tension with the results of the other experiments used for this analysis) onto the planes (Σm_ν, $m_{\nu_e} = \sqrt{\Sigma m_i^2 |U_{ei}^2|}$) and ($\Sigma m_\nu$, $m_{ee} = |\Sigma m_i U_{ei}^2|$). The colored region for each ordering is defined with respect to its local minimum. [48]

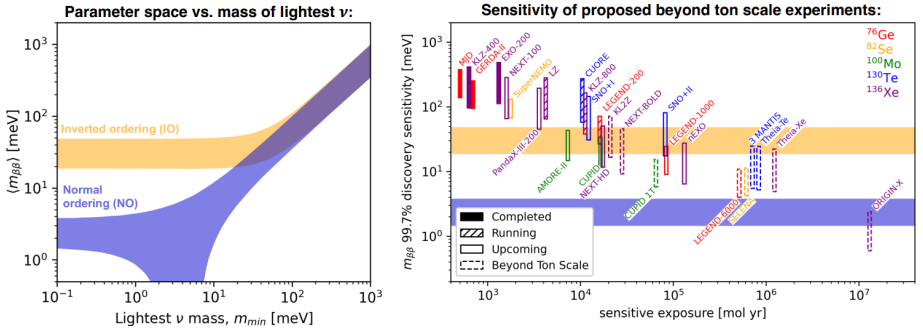

Figure 2.5: Displayed is the dependency of the search for the neutrinoless double beta decay to the neutrino mass ordering. The available parameter space and therefore the measurement possibilities of the several $0\nu\beta\beta$ experiments highly depends on the mass of the lightest neutrino. [53, 54]

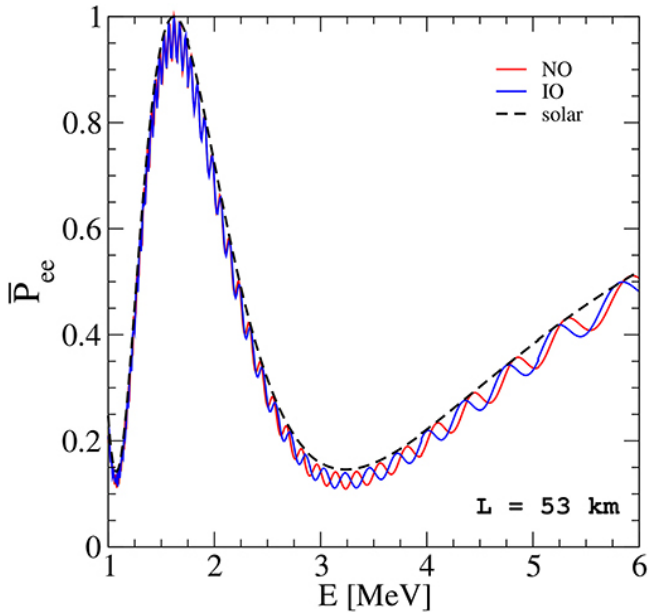

Figure 2.6: Antineutrino oscillation probability (survival probability) for both IO and NO at a distance to source of 53 km. Due to the two different mass differences of the two orderings, the probability slightly differs at a given energy and distance. A precise measurement of this probability would provide a clear hint, which mass ordering occurs in nature. The difference between the two orderings is clearest around 3 MeV, which is also the reason, why most experiments are focusing their energy resolution goals on that energy. Plot taken from [58].

Chapter 3

The Jiangmen Underground Neutrino Observatory

"American components, Russian components, all made in Taiwan"
- Lev Andropov

from "Armageddon", 1998

3.1 Introduction and Overview

The Jiangmen Underground Neutrino Observatory (JUNO) is a large-scale, multi-purpose neutrino experiment located in the Guangdong province near the town of Kaiping in the prefecture of Jiangmen City, southern China (see figure 3.1). Although originating from the Daya Bay experiment, JUNO developed its own collaboration, goals and experimental site, which were defined during its founding meeting in 2014 [64]. In contrast to Daya Bay, which utilized several detectors in a close distance to a neutrino source to measure the Θ_{13} mixing angle, JUNO will primarily focus on determining the neutrino mass ordering. To achieve this goal, a detector with a large fiducial volume and excellent energy resolution was developed. At the time of writing of this work, JUNO is near the completion of the construction.

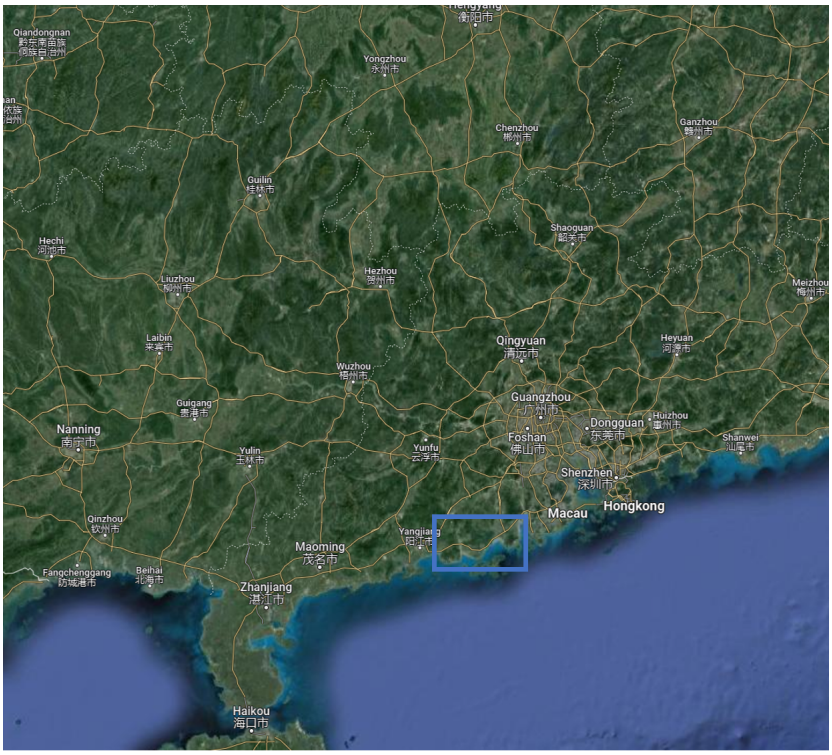

(a) The greater position of the JUNO experiment in the greater south east China.

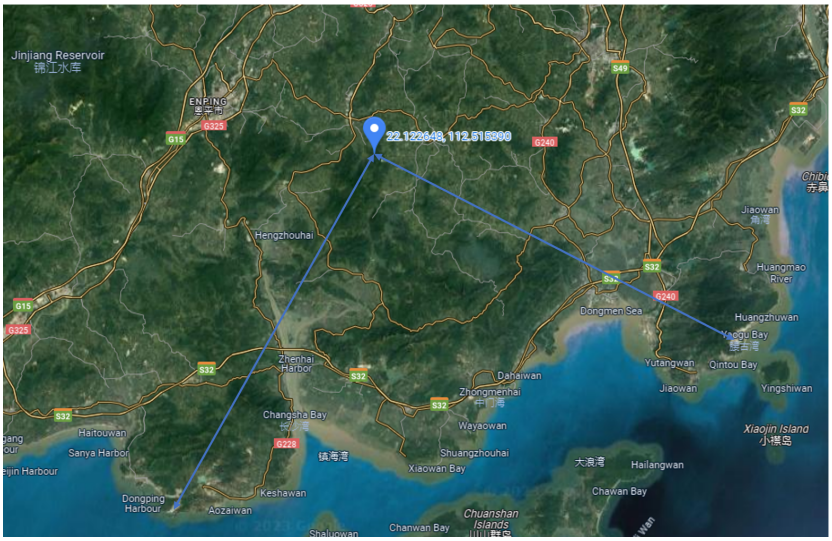

(b) The position of the JUNO experiment (22.1250°N 112.5095°E) in the vicinity of the Nuclear Power Plants (NPPs) JUNO uses as (anti)neutrino sources. Distances to the NPPs are approximately 53km.

Figure 3.1

The JUNO collaboration consists of 695 members of 69 institutions from 17 countries in Asia, Europe and the Americas[1]. JUNO is mainly funded by the Institute of High Energy Physics (IHEP), Beijing, the Chinese Academy of Science (CAS) and the national funding agencies of the participating countries. Data taking of the experiment will start in mid 2025.
JUNOs anti-neutrino sources for the determination of the neutrino mass ordering are the two nuclear power plants (NPP) in Taishan and Yangjiang, featuring a combined total thermal power of 26.6 GW (see table 3.1 for details). Both NPPs are located 53 km away from the JUNO site, which allows JUNO to measure oscillations at a distance, where it is possible to distinguish the two different orderings (see chapters 2.3, 3.2 and figure 2.6).

Table 3.1: Properties of all nearby reactor cores, including Yangjiang NPP (YJ), Taishan NPP (TS) as well as the combined thermal power of the more remote NPPs of Daya Bay (DYB) and Huizhou (HZ). In total, a sum of 26.6 GW of thermal power will be available to JUNO. [19]

Cores	YJ-C1	YJ-C2	YJ-C3	YJ-C4	YJ-C5	YJ-C6
Power [GW_{th}]	2.9	2.9	2.9	2.9	2.9	2.9
Baseline [km]	52.75	52.84	52.42	52.51	52.12	52.21
Cores/Plants	TS-C1	TS-C2	DYB	HZ		
Power [GW_{th}]	4.6	4.6	17.4	17.4		
Baseline [km]	52.76	52.63	215	265		

By the start of the data taking of JUNO in 2024, all eight reactors at the distance of 53 km will have left the testing operation and started to operate commercially.

[1]Status of the 28^{th} of September, 2024

3.2 The Physics Goals of JUNO

Since JUNO is designed to be a multi-purpose detector, a wide physics program is planned. This not only includes the neutrino mass ordering (see chapter 2.3), but also includes, but is not limited to topics like supernova neutrinos, geo-neutrinos, solar neutrinos, atmospheric neutrinos and even a search for sterile neutrinos. This chapter will briefly discuss these goals.

3.2.1 Neutrino mass ordering

As already discussed in chapter 2.3, the determination of the neutrino mass ordering is JUNO's primary physics goal; for further details, see the previous chapter. Due to its distance to the two NPP of Taishan and Yangjiang it has the unique opportunity to measure the neutrino spectrum at a position where the differences between the two orderings is most prominent. After the start of the data collection in 2025, JUNO aims for the first results with a precision of 3σ to be available after a 6.5 year measurement campaign [19].

3.2.2 Supernova burst neutrinos and DSNB

One of the most anticipated goals of low energy neutrino physics and astrophysics is the detailed measurement of the next nearby supernova (SN). Given the typical galactic distance of 10 kpc, JUNO would be able to register about 5000 neutrino events via IBD and approximately 2000 via elastic scattering at the detector target of an occurring core-collapse supernova. It is expected to detect approximately 300 events from neutrino-electron scattering [19].
JUNO will be able to generate a detailed supernova neutrino data set, which will also include flavor information. In combination with other neutrino detectors (e.g. IceCube [8], Super-Kamiokande [2]), gravitational wave detectors (e.g. Laser Interferometer Gravitational-Wave Observatory (LIGO) [65]) and electro-magnetic (EM) telescopes (e.g., Extremely Large Telescope (ELT) [66]), it will be possible to provide a detailed multi-messenger picture of the SN. These measurements as well as a further comparison with data taken of SN 1987A will greatly increase the knowledge on such events, especially given the limited statistics taken for SN 1987A [19].
Another relevant goal of JUNO is the measurement of the diffuse supernova neutrino background (DSNB), holding information like the star-formation rate, the average core-collapse neutrino spectrum, etc. JUNO will be able to either reduce the limits of these measurements already set by the Super-Kamiokande detector [67], or will even be able to find a positive signal of the DSNB. This will be possible, since JUNO features superior anti-electron neutrino tagging capabilities as well as background rejection. A measurement at the 3σ level might be achieved after ten years [19].

3.2.3 Solar and atmospheric neutrinos

The sun is a powerful neutrino source, its neutrino flux has already been measured by several experiments (e.g., Borexino [68], Sudbury Neutrino Observatory (SNO) [69]), also showing evidence of neutrino oscillation. In the two fusion cycles in the sun (pp-chain and CNO-cycle), decays and reactions are present in which neutrinos are emitted. If JUNO reaches its solar neutrino radioactivity limit[2], the experiment will focus on measurements of ^{7}Be and ^{8}B neutrinos of the pp chain, with additional interest in the CNO cycle, pep neutrinos, etc. In this way, JUNO will be able to significantly contribute to the reduction of previous limits set by other experiments [70, 71, 19].
Like solar neutrinos, the atmospheric neutrino sector has already been probed by a range of experiments [72]. However, there is still quite some effort to precise the measurement of Θ_{23}, the octant of Θ_{23} and the CP symmetry breaking phase δ_{CP} (also see chapters 2.1-2.3).
Atmospheric neutrinos have a broad range of baseline (15 km $\sim$ 13000 km) and energy (from 0.1 GeV up to 100 TeV) which makes it hard to build a device sensitive to the whole range[3]. JUNO as a Liquid Scintillator (LS) detector has a very low energy threshold of $\approx 0.1\,MeV$ and thus measures a broad range of these neutrinos with a very good energy resolution of $3\%/\sqrt{E(MeV)}$. Additionally, JUNO plans to implement techniques to reconstruct the directions of charged leptons from the timing pattern of the first-hit on the PMTs, granting additional, directional information [19].

3.2.4 Geoneutrinos

Even though the heat flux at the Earth's surface is well known (46 ± 3 TW [73]) it is not yet fully determined, what fraction of this heat originates from primordial versus radioactive sources[4]. Neutrino detectors like JUNO have the potential to answer this question, due to their sensitivity to neutrinos emitted by the radioactive decays in the mantle of the earth. Since matter is mostly transparent to neutrinos, such experiments are able to detect a few ten events per year coming from all natural occurring uranium and thorium. These measurements will ultimately be able to help answer the question of the radiogenic heating of the earth, which in turn can be used to examine mantel convection, vexing paradoxes and the source of the earth itself [19, 74].

[2]The JUNO solar limit is a background of less than $10^{-16}\,\frac{g}{g}$ uranium and thorium in the LS. Without this limit, the solar neutrino events will be covered by background events.

[3]This is true mainly for the current generation of experiments. For example, the planned IceCube upgrade will provide the opportunity to cover most of this energy range.

[4]There are some measurements by Borexino and KamLAND, even though the significance is not yet sufficient to claim any clear result.

3.2.5 Sterile neutrinos

As of now (beginning of 2024) sterile neutrinos are only hypothesized gauge singlets of the standard model which haven not been observed yet. They don't participate in the weak interaction but mix with active neutrinos through non-zero mixing between active and sterile neutrino flavors. However, the existence of sterile neutrinos would help to answer some questions in the neutrino sector. For example, heavy sterile neutrinos (masses near the Grand Unified Theory (GUT) scale could explain the smallness of the active neutrino masses via the type-I seesaw mechanism [19, 75, 76]. Additionally, this could also contribute to the leptogenesis explanation of the cosmological matter-antimatter asymmetry [77].
On the other hand, theories expecting light sterile neutrinos have been proposed, too. For example, the existence of a sterile neutrino in the keV mass range would be a candidate to prove these theories. Furthermore, there are many measurements from accelerator experiments which predict even light sterile neutrinos in the eV or sub-eV mass range [36][78][79].

3.3 Signal and Background for Reactor Neutrinos

The primary detection channel for reactor electron anti-neutrinos is the coincident decay via inverse beta decay (IBD) [19]. In this process, an incoming electron anti-neutrino interacts with a free proton in the target volume to generate an neutron and a positron:

$$\bar{\nu_e} + p \rightarrow e^+ + n \tag{3.1}$$

Looking at masses and energies in this decay, the neutron is approximately 2000 times heavier than the positron. Therefore, the positron carries most of the kinetic energy of the incoming neutrino. The exceptions are the positron rest mass, the proton-neutron mass difference and a (very) small recoil energy of the neutron. The energy threshold of this reaction is given by:

$$E_{thres,IBD} = (m_n - m_p + m_e)c^2 \approx 1.8\,MeV \tag{3.2}$$

The first signal of the actual measurable part of this process is generated by the positron. It will annihilate within a few nanoseconds, creating two 511 keV photons, which leads to a visible energy of the prompt part of the signal of:

$$E_{vis} \approx E_\nu - 0.8\,MeV \tag{3.3}$$

The delayed part of the signal of this process is dominated by the thermalization of the neutron. After its emission, the neutron thermalizes before being captured by a hydrogen of the surrounding medium (which is linear alkylbenzene (LAB) in the case of JUNO). In this capturing process, a photon with an energy of 2.2 MeV is emitted, which translates to the released binding energy of the resulting deuteron. However, due to the distinct time constants of these processes (capturing and thermalization), this signal will appear as a delayed signal ($\Delta t =\sim 230\,\mu s$). This allows for a clear distinction[5] between the two parts of the reaction and therefore to identify IBD events. A scheme of the whole process can be found in figure 3.2.

[5]In the case of several signals overlaying each other, more sophisticated methods need to be applied to identify these signals (e.g., vertex cuts, pulse shape discrimination, etc.).

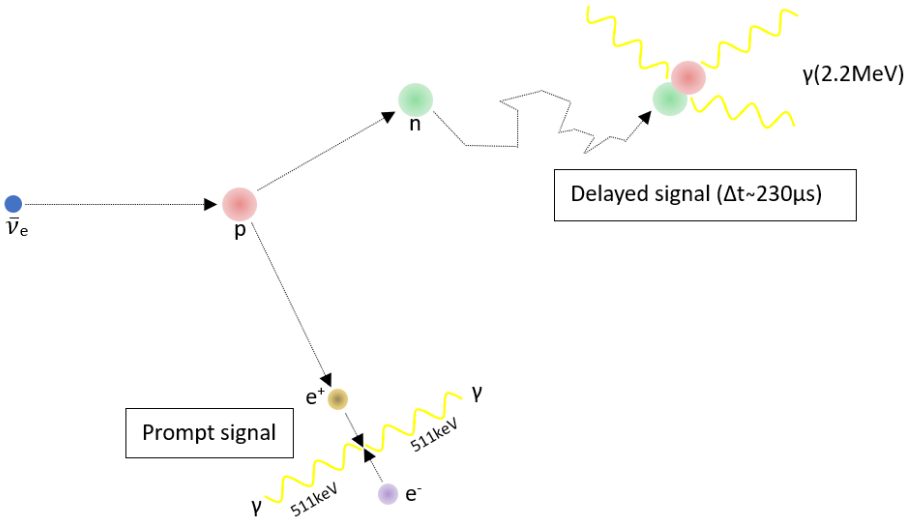

Figure 3.2: Schematic of the whole IBD process. After the capturing, a positron and a neutron are emitted. The positron almost immediately annihilates, generating two 511 keV photons. The neutron thermalizes and gets captured by a hydrogen atom, releasing the binding energy of the resulting deuteron as a photon of 2.2 MeV.

To calculate the number of the expected events, it is necessary to take three things into account[6]:

- Neutrino disappearance by oscillation:
  Since neutrinos will oscillate, some of the emitted anti-electron neutrinos will oscillate into other flavors and since IBD requires electron anti-neutrinos (see figure 3.2), some neutrinos will therefore not be visible via IBD.

- IBD cross-section:
  Given the LS of JUNO and the expected energy range of the emitted neutrinos, some neutrinos will not be detected. A more detailed view of this energy dependent cross-section can be found in figure 3.3 [80].

- Reactor anti-neutrino spectral models:
  The expected spectra of the anti-neutrinos emitted by the reactors is influenced by nuclear fuel burn-up, etc. However, this spectrum is not yet completely understood and currently under investigation (e.g., "bump" in the neutrino spectrum, fine structure, etc.) [81–85].

[6]There are other parameters that depend on the detector, like density of the LS, the mass of the target or the distance of the event vertex from the PMT. Since these parameters are mainly depending on event- and detector geometry, and to provide a more general picture, these values are neglected here. Further information can be found in [19]

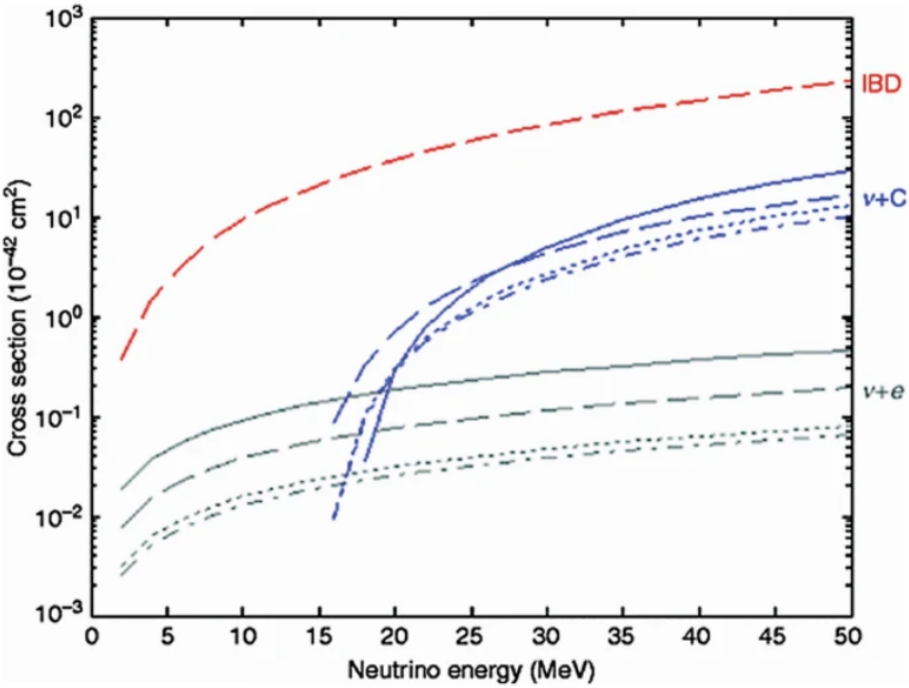

Figure 3.3: Energy dependence of the neutrino cross section for different reaction channels: Inverse beta decay (red), neutrinos and carbon (blue) as well as neutrinos and electrons. The discussed energy dependence is most relevant in the lower half of the energy scale. Plot taken from [86].

JUNO will be able to see approximately 83 IBD events per day. Given the small number of events per day, controlling the background is of utmost importance. This includes all other (naturally occurring) processes that might be able to mimic an IBD event. The main backgrounds considered for JUNO are the following:

- Accidental coincidences of unrelated processes:
  Radioactive impurities of the LS, scattering of nuclei with cosmic muons (both, elastically and in-elastically) and thermalization or decay of particles created in spallation with cosmic radiation are the main sources considered in this field. Some of these (e.g., radioactive impurities) can be controlled during the installation of the experiment, see chapter 4).

- Fast neutrons:
  Fast neutrons that are created by cosmic muons outside of the inner detector of JUNO cannot be tagged when entering the inner detector, since the producing particle (e.g., cosmic muons) does not necessarily enter the veto volume at all. The neutrons will scatter at protons of the detector volume and, if thermalized and captured, a fake signal might be produced.

- (α,n) processes:
  The α induced $^{13}C(\alpha,n)^{16}O$ process may also create such fake signals. The α particles necessary to start these processes might be obtained by the decay chains of uranium and thorium.

- Cosmogenic isotopes:
  Cosmogenic isotopes like ^{8}He and ^{9}Li produced in spallation processes at carbon atoms of the LS might also create IBD mimicking signals in the detector when decaying.

- Geo-neutrinos:
  As already mentioned in the previous chapter, geo-neutrinos might be detected by JUNO. However, since they are at first glance indistinguishable from reactor neutrinos, they also create a background to the primary electron anti-neutrino signal.

The goal of the JUNO collaboration is to gather 100k IBD events within the initial run time of 6.5 years [19]. Therefore, a sophisticated background reduction is necessary, which includes several cuts in all possible areas of the data. This involves time, volume, and coincidence cuts, along with techniques such as pulse shape discrimination and muon track reconstruction. Additionally, a precise time, charge, energy and vertex calibration of the detector is necessary. A more detailed look into these techniques can be found in [87, 88]. Table 3.2 lists all background and signal rates for reactor neutrinos as expected by the JUNO experiment.

Table 3.2: Expected background for anti-electron neutrino induced IBD events in the JUNO detector. Displayed is both, values before and after the individual cuts. All rates are given in events per day, values calculated using simulations. The final, expected signal to background ratio is ~ 15 [19].

Cut	IBD eff.	IBD	Geo-ν	Accidental	$^{8}He/^{9}Li$	Fast n	(α,n)
-	100%	83	1.5	$\sim 5.7 \cdot 10^4$	84	-	-
Fid. vol. cut	91.8%	76	1.4	410	77	0.1	0.05
Energy cut	97.8%	73%	1.3	410	71	0.1	0.05
Time cut	99.1%	73	1.3	410	71	0.1	0.05
Vertex cut	98.7%	73	1.3	1.1	71	0.1	0.05
Muon veto	83%	60	1.1	0.9	1.6	0.1	0.05
Combined	73%	60	3.8				

3.4 Energy resolution

As mentioned in the last chapters, the main goal of JUNO is closely connected to the question how well the IBD process of reactor anti-neutrinos can be measured. Given the values from table 3.2, especially given the IBD efficiency of 73%, JUNO can determine the correct neutrino mass ordering with a significance of at least 3σ within the first 6.5 years of measurement [19][89].
To achieve this goal, it is crucial to fulfill all requirements that are already necessary during the design of the detector. In the case of JUNO, it can be shown that the required energy resolution of the detector needs to be equal or smaller than the ratio between the two participating frequencies [19], which is given by equation 3.4. In fact, improving this resolution, might even increase access to other parameters like δ_{CP} in JUNO [90]:

$$\frac{\Delta m^2_{12}}{|\Delta m^2_{ee}|} \sim \frac{7.4 \cdot 10^{-5}\,\mathrm{eV}^2}{2.5 \cdot 10^{-3}\,\mathrm{eV}^2} \sim 3\,\%^{7} \tag{3.4}$$

This result directly leads to the key parameter of JUNOs detector design, which is $\sigma_E = 3\,\%/\sqrt{E[\mathrm{MeV}]}$. The energy E is the visible energy from the positron of the IBD event [15].
Achieving this resolution is crucial for JUNO, a failure to do so would smear out the oscillation fine structure in the spectrum and thus reducing the significance of the measurement. The consequences of a reduced σ_E can be seen in figure 3.4.
Several factors influence the energy resolution of a LS detector like JUNO. These include the choice of materials (both, on the detector hardware as well as on the recipe of the LS) and the precision of the understanding of the performance of the detector. Using a generic parametrization, the resolution of such a detector can be described by:

$$\frac{\sigma_E}{E} = \sqrt{\left(\frac{a}{\sqrt{E}}\right)^2 + b^2 + \left(\frac{c}{E}\right)^2}. \tag{3.5}$$

In this equation, E is the visible energy, parameter a combines all dependencies to photon statistics, b all non-stochastic elements (e.g., Cherenkov light, light quenching, etc.) and c all relevant signal noises (e.g., dark count rates of the used PMTs). Parameters a, b and c can be determined via monte-carlo simulations and calibration studies of the detector [19].

[7] Values are taken from NuFIT[48]

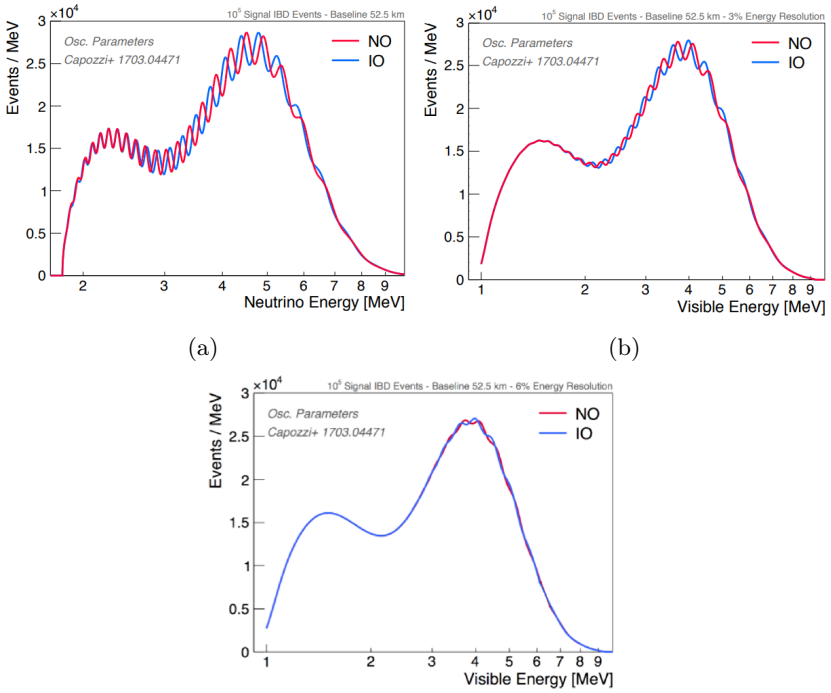

Figure 3.4: Comparison of the acquired oscillation spectrum in dependence of the energy resolution. Plot a) shows the unsmeared, ideal spectrum, plot b) the expected spectrum of JUNO with an energy resolution of 3%. Plot c) shows a spectrum with an energy resolution of 6%, the smearing of the two orderings is clearly visible. [91]

These considerations have led to the following design parameters for JUNO's main detector:[15][19][8]

- Optical coverage:
  At least 75 % of the total solid angle.
- PMTs:
  The PMTs used in the inner detector of JUNO should have a detection efficiency of approximately 30 %, a collection efficiency of at least 90 % and modest dark count rate[9].

[8] For the design parameters discussed here, a light yield of ~ 1200 p.e./MeV was considered.
[9] In JUNO, the limits for these dark count rates are ≤ 50 kHz in the case of the Hamamatsu PMTs and ≤ 100 kHz for the NNVT PMTs.

- LS:
  The LS used in JUNO should have an attenuation length of at least 20 m for 420 nm photons, a high light yield of 10^4 photons per MeV and a radio purity of 10^{-15} g/g (10^{-16} g/g) in uranium and thorium for reactor (solar) neutrino detection (see section 3.5).

- Detector size:
  To reach the required IBD events for a significance of 3σ, the size of the main detector needs to be large enough to acquire 100k events in 6.5 years of operation.

During the preparation and installation of the JUNO detector, several tests [20, 92], cleaning [93] and quality assurance steps [94] were implemented.

3.5 Liquid Scintillator

The LS of JUNO serves as the actual detection medium for the detection of anti-electron neutrinos via IBD. More information about the detection process can be found in the previous sections of this chapter.
Considering the goals of JUNO, a LS mixture was designed that consists of three parts:

- Solvent:
  As a solvent, JUNO uses linear alkylbenzene (LAB), which is a basic compound in the industrial production of soap and therefore widely available. It consists of carbon and hydrogen, which makes it an ideal solvent for a detector like JUNO. The main challenge is the required purity of the substance.

- Scintillating fluor:
  2,5-diphenyloxazole (PPO) is used as a scintillating fluor in JUNO. It is added in low concentration of only 2.5 g/l to the LAB solvent.

- Wavelength shifter:
  To shift the wavelength of the light emitted by the flour to a wavelength that can be detected by the PMTs of JUNO, 1,4-Bis(2-methylstyryl)-benzene (bis-MSB) is added in a concentration of 15 mg/l.

The wavelength shifter is crucial because of the PMTs used in JUNO[22]. In addition, this shifting to 420 nm is also the reason, why the attenuation length of the LS is specified to be measured at 420 nm.
Not only have the transparency and emitted wavelength of the LS been adjust carefully, but the light yield and radiopurity (see chapter 4.2) are also of crucial importance to the success of the detector. Given the large amount of LS used in JUNO, several studies have been performed with the JUNO LS. This includes temperature dependency [95], non linearity [96], scattering [97] and long-term stability of the mixture [98]. A closer look into the distillation and purification procedure of the LS of JUNO can be found in section 3.6.3.

3.6 Detector and Auxiliaries

In this section, a more detailed view of the detector and the auxiliaries of JUNO will be given. The principle design of JUNO follows the necessities for reaching the desired energy resolution of $3\,\%/\sqrt{E(\mathrm{MeV})}$, see section 3.4. This chapter mainly follows the JUNO conceptual design report [15].
The JUNO detector will be placed in a depth of approximately 800 m in granite rock ($\approx$ 1900 m.w.e.) to shield the experiment from secondaries from cosmic radiation. A remaining rate of $3\,\mathrm{mHz/m^2}$ for muons with an average energy of 215 GeV is expected [19, 15].
In total, the underground laboratory of JUNO features more than seven underground halls, that include space for the main detector, electronics, liquid scintillator, water purification, pre-assembling, storage and filling equipment. The installation of the detector took place between 2018 and 2024, while comissioning of the central detector will start in 2025.

3.6.1 The detector design of JUNO

The central acrylic vessel of the JUNO detector consists of an acrylic sphere with a diameter of 35.4 m and a thickness of 12 cm. This sphere will be filled with a total of 20 kt of linear alkylbenzene (LAB) based liquid scintillator (see section 3.5 for further details). A surrounding stainless steel support structure (SSS, see figure 3.6), holds the sphere in place and provides support for 17612 20-inch as well as 25600 3-inch inward pointing PMTs. The total diameter of this structure is 40.1 m. A muon Cherenkov veto is the outermost component of the detector. It has been excavated from the surrounding rock, is filled with ultra-pure water and equipped with 2400 additional 20-inch PMTs. In addition to this veto, muon veto panels inherited from the OPERA experiment have been placed above the central part of the detector (see figure 3.5) [99].
The experimental hall of the central detector is open to two electronic support rooms, housing all PMT support electronics, power supplies as well as first stage DAQ hardware. The whole hall is air conditioned, which also includes monitoring of both, particle count and radon concentration [93].

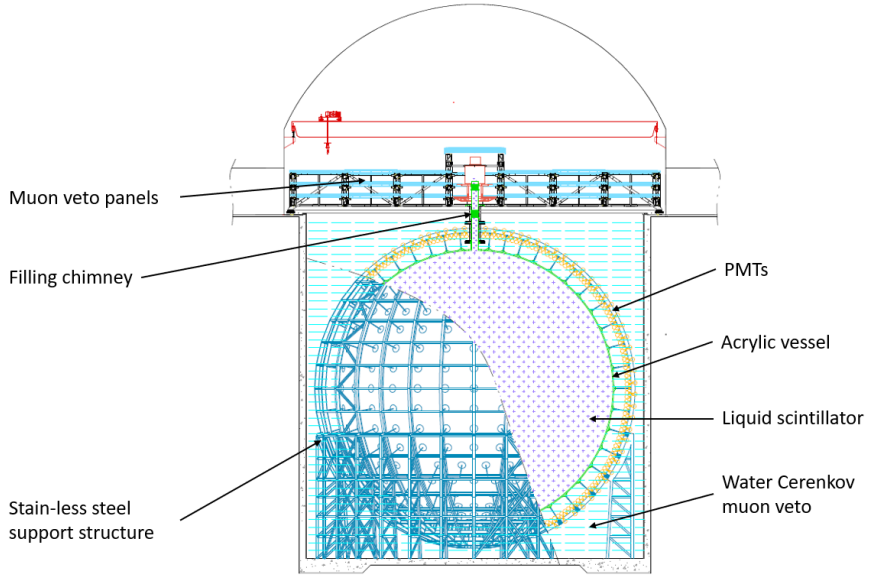

Figure 3.5: Schematic of the central detector of the JUNO experiment [100].

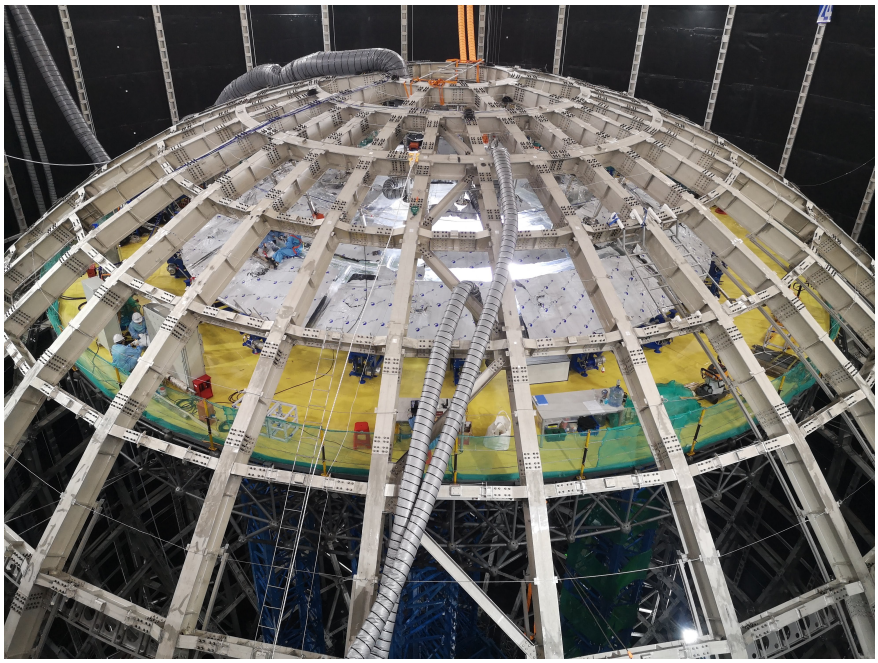

Figure 3.6: Picture of the SSS during the construction in autumn 2022. Photo by T.Sterr.

3.6.2 PMTs

JUNO utilizes three different kinds of PMTs: a 3-inch tube by Hainan Zhanchuang Photonics Technology Co., Ltd (HZC) and two 20-inch tubes by Hamamatsu Photonics K.K. and North Night Vision Technology Co., Ltd (NNVT)[101] respectively (see figure 3.7a). In total, 25600 HZC tubes, 5000 Hamamatsu tubes and 12612 NNVT tubes will be installed in the inner detector. An additional 2400 NNVT tubes will be introduced to the muon water Cerenkov veto.
Both, Hamamatsu and HZC tubes, feature a traditional dynode design whereas all NNVT tubes feature a newly developed micro channel plate (MCP) design (see figures 3.7b and 3.8). All JUNO PMTs are tested for performance and characterized to ensure the necessary high PMT quality to achieve the resolution goals.
OSIRIS initially planned to use iPMTs [102] (see section 4.4) which were based on the 20-inch Hamamatsu tubes. However, due to damages occurred during transport of the PMTs from Germany to China, a switch to LPMTs based on NNVT PMTs was necessary (see section 4.4). The performance parameters of the PMTs of JUNO can be found in table 3.3.

Table 3.3: PMT performance parameters including acceptance limits set during the characterization and performance tests [92].

Parameter	Hamamatsu Average (Limit)	NNVT Average (Limit)
Quantum Efficiency[10] (QE)	30.3 % ($\geq$ 27 %)	28.5 % ($\geq$ 26.5 %)
Collection Efficiency (CE)	95.6 %	98 % ($\geq$ 96 %)
Gain	10^7	10^7
Peak/Valley ratio	3 ($\geq$ 2.5)	3.5
Time Transit Spread (TTS)	2.7 ns ($\leq$ 3.5 ns)	12 ns ($\leq$ 15 ns)
Dark Count Rate (DCR)	10 kHz ($\leq$ 50 kHz)	$\leq$ 50 kHz (if 24 % $\leq$ PDE < 27 %) $\leq$ 60 kHz (if 27 % $\leq$ PDE < 28 %) $\leq$ 80 kHz (if 28 % $\leq$ PDE < 29 %) $\leq$ 100 kHz (if 29 % $\leq$ PDE)
Pre-pulse ratio	0.8 % ($\leq$ 1 %)	0.5 % ($\leq$ 1 %)
After-pulse ratio	10 % ($\leq$ 15 %)	10 % ($\leq$ 15 %)

[10] In the end, the value actually used is the PDE, which is the product of the quantum efficiency, collection efficiency and the effective area ratio (EAR): $PDE(\lambda) = QE(\lambda) \cdot CE \cdot EAR$. The EAR is the relative effective area ratio, where the collection efficiency is greater than 95.6 % when the diameter of a PMT is 508 mm [92]

(a) Size comparison of the two different PMT sizes of JUNO. Shown is a 20-inch NNVT MCP PMT as well as three 3-inch HZC PMTs. Picture made by the JUNO smal PMT group.

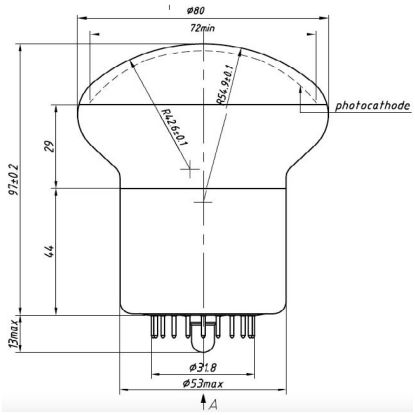

(b) Technical drawing of the 3-inch PMTs used in the JUNO main detector. Picture taken from [103]

Figure 3.7

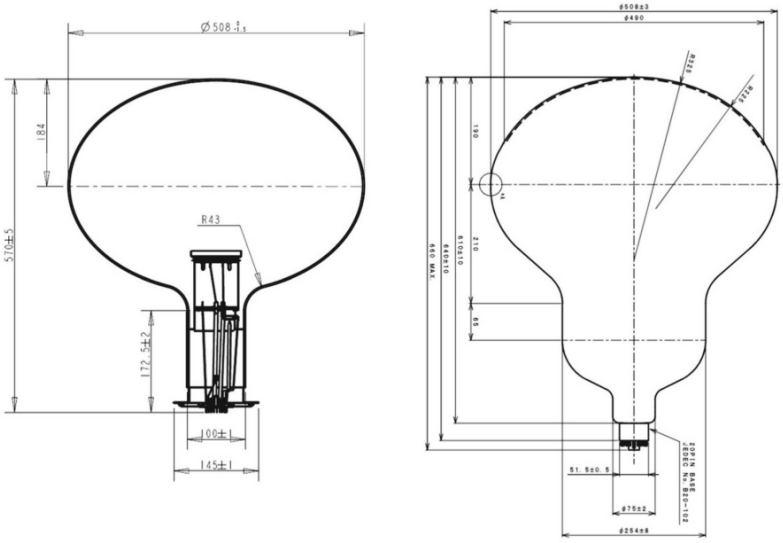

Figure 3.8: Technical drawing of the two different types of 20-inch PMTs selected for the use in JUNO. Left: NNVT MCP PMT GDB-6201, Right: Hamamatsu dynode PMT R12860. Picture taken from [92].

3.6.3 The liquid scintillator production

All LS used in JUNO is mixed, treated and purified on-site and finally tested in OSIRIS (see section 3.5 for further information as well as information about required cleanliness levels etc.). The whole LS chain can be seen in figure 3.9.

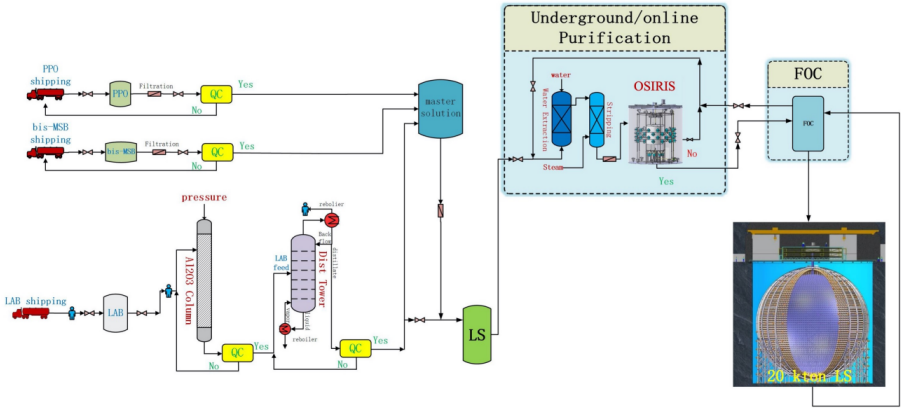

Figure 3.9: Complete LS production chain of JUNO from shipping and storing on-site to the final filling in the JUNO filling system (FOC). The procedure starts with the arrival of the raw components and the consecutive treatment of these materials (filtration and quality checking, in this plot only visible for the PPO and bis-MSB). After the pre-treatment, the LAB is filtered through an aluminum oxide filter and distilled to remove any other molecules still present, whilst PPO and bis-MSB are directly fed into the master solution tank without distillation. After entering the underground LS hall, the purification continues by water extraction and nitrogen stripping (initially, steam stripping was foreseen, however, due to technical difficulties, a switch to ultra pure nitrogen was necessary). The very last step before bringing the LS into the JUNO filling system is the quality assurance check of the LS with the OSIRIS detector. Figure taken from [102].

3.6.4 Veto Systems

The three-layer top tracker veto system was inherited from the OPERA experiment [104], adapted to the needs of JUNO and will be placed on the center top of the water tank. It will cover approximately two thirds of the opening of the JUNO water tank (see figure 3.10). As result, a tracking of cosmic muons coming from above is possible [19]. A combination of the water Cherenkov veto and the top tracker system is forseen which leads to further background reduction [105] [106].

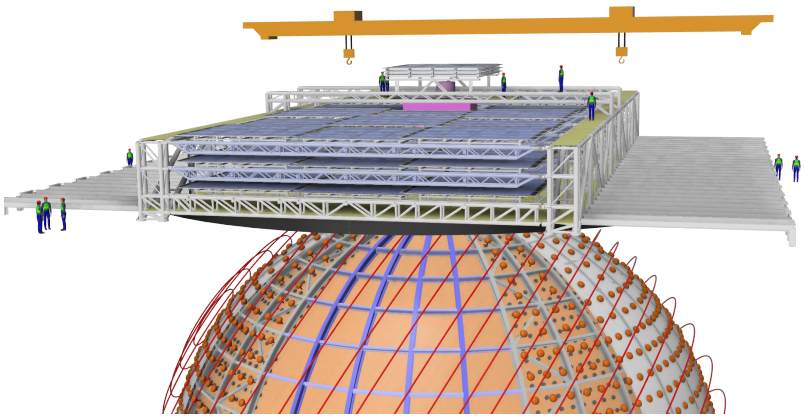

Figure 3.10: The top tracker system of JUNO that will be used as an essential part of the muon veto. The three layers as well as the central positioning of the system can be seen. Picture courtesy of the JUNO collaboration. [107]

The water tank surrounding the acrylic vessel of JUNO is equipped with 2400 20-inch MCP PMTs that provide the opportunity to use the water tank as an active water Cerenkov muon veto. A tracking efficiency in the range of 95 % for double and 98 % for single muon events is expected [108].

3.6.5 JUNO-TAO

Since there are still some features in the reactor neutrino spectrum that are not yet understood, which lead to uncertainties and systematic errors, the JUNO collaboration decided to construct an additional detector positioned in a distance of 30 m away from one of the reactor cores of the Taishan nuclear power plant (see section 3.1) [109]. This near detector, called the Taishan Antineutrino Observatory (TAO), will greatly improve the relevance of the JUNO experiment [110]. The role of the spectral distortions of the neutrino flux ("fine structures") in the determination of the neutrino mass hierarchy has been recently studied [111]. TAO will hold a total of 2.6 t of liquid scintillator (LS).

Even though both detectors, TAO and JUNO, will be filled with liquid scintillator, they differ largely in architecture. Firstly, the inner surface of TAO will covered with $10\,\mathrm{m}^2$ of silicon photo multipliers (SiPMs) with a high photosensitivity. Since almost all semi-conducting sensors tend to show high dark noises at room temperature, TAO will be operated at -50 °C. In total, these SiPMs are expected to detect about 4500 photoelectrons per MeV. Secondly, the LS of TAO will be loaded with Gadolinium to increase the cross-section of capturing neutrons and therefore the efficiency of the neutron capture detection after IBD events. In addition, Gadolinium loaded LS also features a higher de-excitation energy after a capture event. As a result of these features, TAO expects an event rate, 40 times higher than JUNO. Furthermore, an outstanding energy resolution of $1.5\,\%/\sqrt{E[\mathrm{MeV}]}$ is expected [112]. A sketch of the whole JUNO TAO setup can be found in figure 3.11.

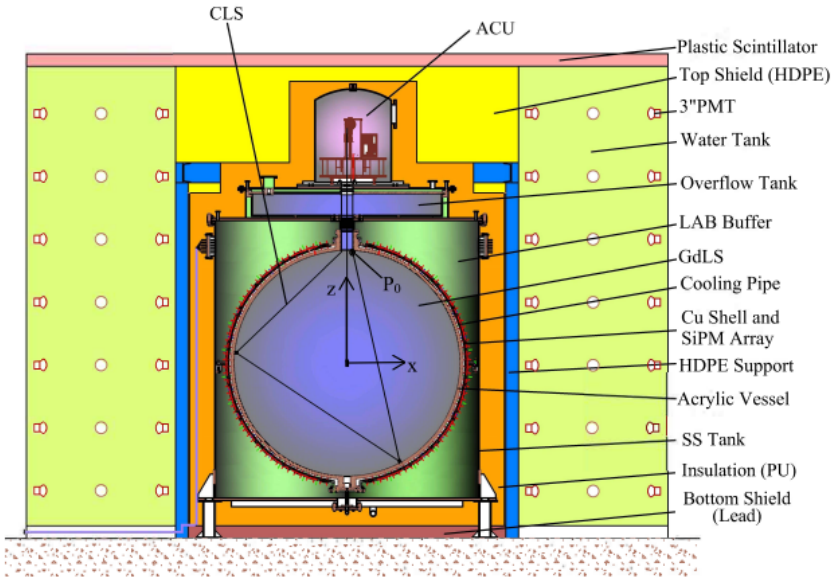

Figure 3.11: Scheme of the JUNO near detector TAO. In addition to the detector architecture, the automated calibration unit (ACU) together with its source maneuvering cable loop system (CLS) can be seen. Image taken from [113].

Chapter 4

The Online Scintillator Internal Radioactivity Investigation System - OSIRIS

"Stand back. Watch me push a button. And, ooooh, maybe I'll flip a lever." -Agent Spire

from "Guildwars 2", 2010

4.1 Introduction

The Online Scintillator Internal Radioactivity Investigation System (OSIRIS) is a subsystem of the JUNO liquid handling system (LHS) and designed for the testing of the radio purity of the liquid scintillator filled into JUNO. OSIRIS features a cylindrical central acrylic vessel with a capacity of 18 t of liquid scintillator. It is surrounded by an array of 64 photomultiplier tubes (PMTs), which are identical to the PMTs used in the main detector of JUNO. To reduce muon induced background events as well as background coming from radioactivity of the surroundings of the detector, an optically separated muon veto is placed around this inner structure. This water filled muon Cherenkov veto will be equipped with an additional twelve PMTs.
OSIRIS has two different operation modes, the "batch mode" and the "continuous mode". In batch mode, the volume of the inner vessel is exchanged

completely and then measured for up to several weeks, whereas in continuous mode the inner volume is continuously exchanged over a day whilst measuring the whole time. During commissioning and in case of extraordinary events (e.g., known pollution of a LS batch due to problems further up in the LS production chain) the batch mode will be used, however, during standard operation, OSIRIS will be operating in continuous mode.
The expected design sensitivity of the system is a level of 10^{-16} g/g of ^{238}U and ^{232}Th [102].

4.2 Sensitivity Goals

Even trace amounts of radioactive isotopes in the LS of JUNO pose a major background for the neutrino physics program. Therefore, the LS chain was designed to purify the LS to an acceptable level (see chapter 3.5). It is the main purpose of OSIRIS to detect any impurities that may have survived this purification process. Since the decay products of these impurities might mimic the IBD signal used as a detection channel in JUNO during their decay, bismuth and polonium (and, consequently, the uranium and thorium chains) are of interest for JUNO [114]. The relevant limits for the Uranium and Thorium chains as well as individual limits for ^{210}Po, ^{40}K and ^{14}C can be found in table 4.1.

Table 4.1: Radiopurity requirements for the two main physics mode of JUNO (see chapter 3) in comparison to the values achieved on the two liquid scintillator experiments KamLAND and Borexino. [102]

Chain/ Isotope	JUNO IBD $\left[\frac{g}{g}\right]$	JUNO solar $\left[\frac{g}{g}\right]$	KamLAND $\left[\frac{g}{g}\right]$	Borexino $\left[\frac{g}{g}\right]$
^{238}U	$1 \cdot 10^{-15}$	$1 \cdot 10^{-16}$	$(5.0 \pm 0.2) \cdot 10^{-18}$	$< 1 \cdot 10^{-18}$
^{232}Th	$1 \cdot 10^{-15}$	$1 \cdot 10^{-16}$	$(1.3 \pm 0.1) \cdot 10^{-17}$	$< 1 \cdot 10^{-18}$
^{210}Po	-	$5 \cdot 10^{-24}$	$2 \cdot 10^{-23}$	$< 1 \cdot 10^{-25}$
^{40}K	$1 \cdot 10^{-16}$	$1 \cdot 10^{-17}$	$(7.3 \pm 1.2) \cdot 10^{-17}$	$< 1 \cdot 10^{-19}$
^{14}C	$1 \cdot 10^{-17}$	$1 \cdot 10^{-17}$	$(3.98 \pm 0.94) \cdot 10^{-18}$	$(2.7 \pm 0.1) \cdot 10^{-18}$

OSIRIS is optimized for the detection of uranium and thorium via tagging of fast Bi-Po coincidences that can be found in the lower half of the decay chains. However, OSIRIS will also be able to give a limit to the levels of ^{14}C and ^{210}Po isotopes.
To select these Bi-Po events, four different cuts will be applied [102]:

- Fiducial volume cut (FV):
  Even though the external gammas will be reduced by the water Cherenkov veto, an enhanced event rate is to be expected at the outer volume of the AV. Additionally, a remnant contamination of the acrylics can't be rules out. This leads to a reduced volume of 2.8 m in both height and width for the prompt event search.
- Energy selection cut:
  The energy selection is defined by the fact, that the β-spectra of bismuth features a broad energy spectrum, whilst the α decays of polonium are mono-energetic. Due to quenching, this leads to a visible energy in the range of 0.5 to 1 MeV.
- Time cut:
  The basis of this cut are the very short life times of ^{212}Po (431 ns) and

^{214}Po (237 μs). Due to these short life times, a background rejection can be done by requiring a short time delay for the detection of the coincident Po-candidate, which makes it possible to perform a single-event rejection. For OSIRIS, a conservative delta of 200 ns is required to identify these coincident prompt and delayed events [87]. The upper bound will be adjusted to further optimize the sensitivity.

- Distance cut:
  Due to the low recoil energies of the relevant bismuth and polonium isotopes, and due to the short life times, both decay at almost the same position (in fact, for OSIRIS it was assumed, that the positions are identical, only smeared out by the uncertainty of the position reconstruction). In this way, a cut value for a maximum distance between Bi and Po signals can be used to efficiently reject accidental backgrounds distributed in the LS volume.

Using the cuts and by assuming the contamination limits given in table 4.1 OSIRIS will be able to identify 11 (4) coincidence events per day for ^{214}Bi-Po (^{212}Bi-Po), with a residual background of 1.14(0.04) accidental coincidences per day.

4.2.1 Sensitivity in batch-mode

As discussed before, OSIRIS will be able to operate in batch-mode, in which a sample of LS is screened over a longer time period. The analysis in this mode gives the opportunity to also investigate radon contamination, that is not in secular equilibrium with the U/Th chains [102]. Even though the relevant isotopes (^{222}Rn for ^{238}U and ^{220}Rn for ^{232}Th) are short lived and therefore don't play a role in JUNOs background budget, they are of importance for OSIRIS, since they create an additional source of Bi-Po events. This means, that an investigation of these non-equilibrium isotopes is necessary to get an reliable contamination estimation of U/Th. Since radon tends to enter the pipes at junctions and valves from ambient air, an estimation of the additional decays per day can be made. These additional 7-45 additional decays per day translate into an initial rate of $n_{Rn}(0) = 130 - 830$ counts per day for the volume of OSIRIS, which is 1-2 magnitudes more than the desired U/Th induced decay rates.
A possibility to overcome this problem is the batch-mode of OSIRIS. In this mode, a given LS sample is screened of an extended time $T \geq \tau_i$ with $\tau_i = \tau_{222} = 5.5$ days for ^{222}Rn uranium chain) and $\tau_i = \tau_{220} = 15$h for ^{212}Pb for the thorium chain. In such a measurement the radon induced Bi-Po rate will decay exponentially over time, whilst the rate from the U/Th chains will be constant. Figure 4.1 shows the resulting U/Th sensitivity of OSIRIS. For an initial decay rate of 130 decays per day, OSIRIS will take 7 (2.5) days to set an upper limit to the IBD level of U (Th) and 22 (6) days for the solar level (see table 4.1 [102].

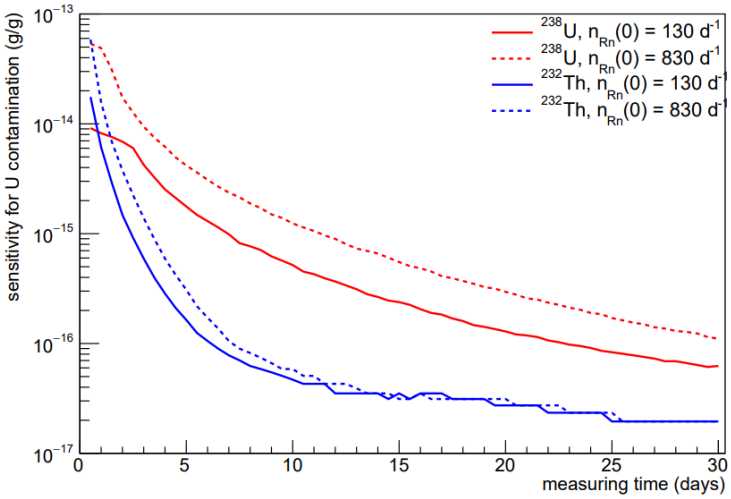

Figure 4.1: The sensitivity of OSIRIS to U/Th in the presence of an initial radon contamination Rn(0). Upper limit can be estimated using a time fit to the observed Bi-Po rate, taking also the known time profiles of ^{222}Rn and ^{220}Rn into account. Plot taken from [102].

4.2.2 Sensitivity in continuous mode

Given the large time requirements for the batch mode of OSIRIS which will only be feasible during commissioning and in case of special events, this operation mode is not suitable to be used in standard operation. Instead, the continuous mode is foreseen: A continuous filling and draining of the LS with a passing time of the LS of approximately a day. Due to this low flow rate of $1\frac{m^3}{h}$, the secondary Bi-Po rates induced by radon (see chapter 4.2.1) will be partially decay while traveling from top to bottom of the AV. A reduction by 17 % (80 %) is expected for ^{222}Rn (^{220}Rn) [102].
Because of this decay pattern, it is possible to distinguish between the height dependent, radon induced background and the constant rate from U/Th contamination. For this purpose, the reconstructed decay vertices are mapped to individual LS layers, that correspond to a given time coordinate t. The fiducial volume of OSIRIS is split into 14 of these layers, with a height of 20 cm each. By averaging and further statistical analysis (see figures 4.2 and 4.2a), an upper sensitivity limit of ^{232}Th translates to $1.4 \cdot 10^{-14}\,\frac{g}{g}$ if if $n_{Rn} = 830\,\frac{1}{d}$ or to $6 \cdot 10^{-15}\,\frac{g}{g}$ if $n_{Rn} = 130\,\frac{1}{d}$ [102].

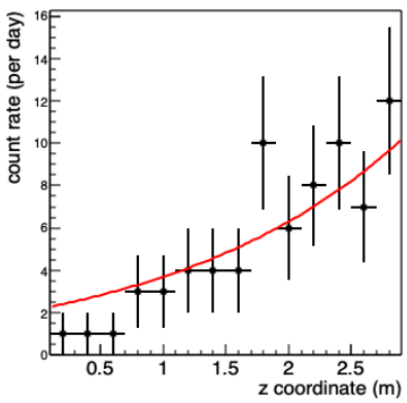

(a) Typical z Profile for Bi-Po coincidences using 14 individual LS layers in continuous mode for a initial Rn contamination of 830 cts per day. The traversing of the LS from top to bottom can be seen in the plot from left to right [102].

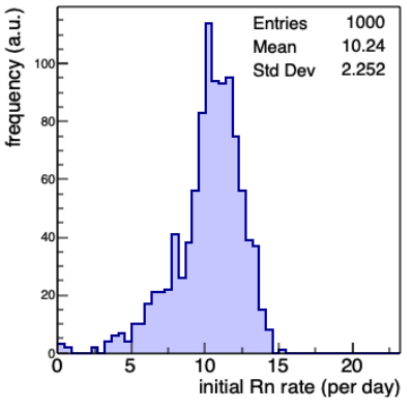

(b) Simulated fit result for the initial radon contamination for one of the LS slices used in 4.2a [102].

Figure 4.2

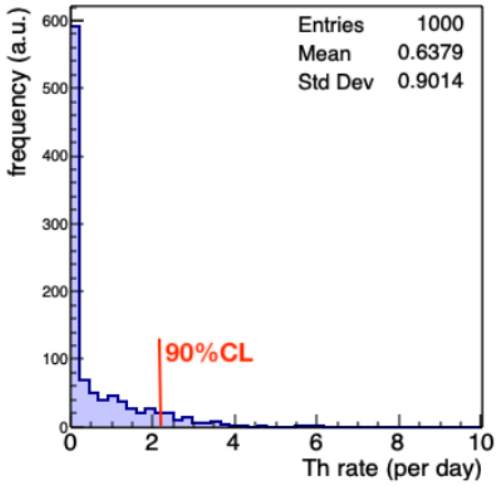

Figure 4.3: Simulated fir result for the thorium induced count rate of Bi-Po events of one of the slices of 4.2a [102].

4.2.3 Sensitivity to ^{14}C and ^{210}Po Contamination

Unlike in the case of uranium and thorium, there are no additional source for ^{14}C and ^{210}Po, which means that there aren't any beneficial secondary spectra. Any estimations need to be based on a single spectrum (see exemplary plot 4.4). Since ^{210}Po emits and α with an energy of 5.5 MeV (which is quenched to 0.5 MeV), spectral fitting can be used to identify the rate. The sensitivity of this method has been determined to be 4 % in the case of a long batch mode run (see figure 4.4) and 15 % for a day-long continuous mode run. In later mode, the minimum ^{210}Po abundance detectable is $1 \cdot 10^{-24} \frac{g}{g}$.
^{14}C will dominate the lower end of the spectrum already at a relative abundance of 10^{-18}. Since this background is overalyed by the (external) gamma background, the exact sensitivity of OSIRIS to ^{14}C will be heavily dependant on the understanding of the spectral shapes of this gamma background and ^{14}C used in the fits (see again figure 4.4.

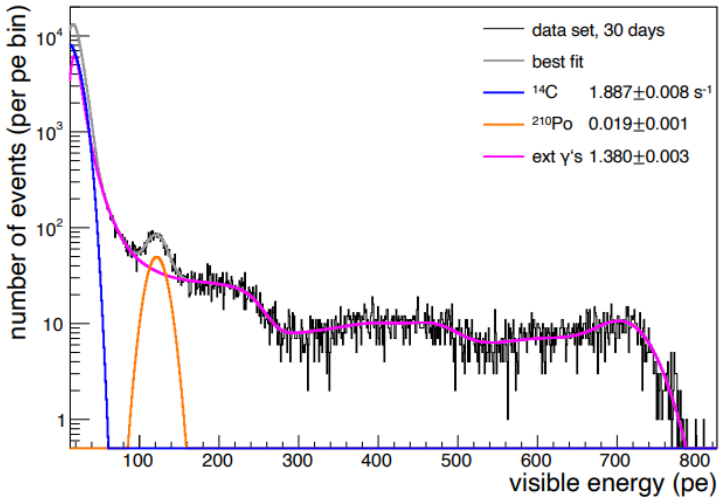

Figure 4.4: Sample photon electron spectrum as expected in OSIRIS. Here, an additional FV cut to a cylinder of 1m in diameter and height was applied. As displayed, the spectral influence of ^{14}C and ^{210}Po can be seen. Using spectral fitting methods, decay rates of ^{14}C and ^{210}Po can be interpolated. An ^{14}C abundance of 10^{-18} was assumed, whilst ^{210}Po was set to the minimum requirement defined for JUNO (80 $\frac{1}{d \cdot t}$) [102].

4.3 The OSIRIS Detector

In addition to the basic structure mentioned in the previous chapter, a gas and liquid handling systems (LHS) have been developed and constructed as well as two different calibration systems: An automated calibration unit (ACU) and a laser calibration system (LDS). In addition, two clean rooms (a temporary facility at the bottom to provide a clean access to the tank of OSIRIS and a permanent clean room on top of OSIRIS housing parts of the LDS and the ACU) as well as an electronics platform featuring all relevant DAQ and SC hardware are introduced. A picture of the inner detector can be found in figure 4.5, a complete model of the detector can be seen in figures 4.6a and 4.6b.

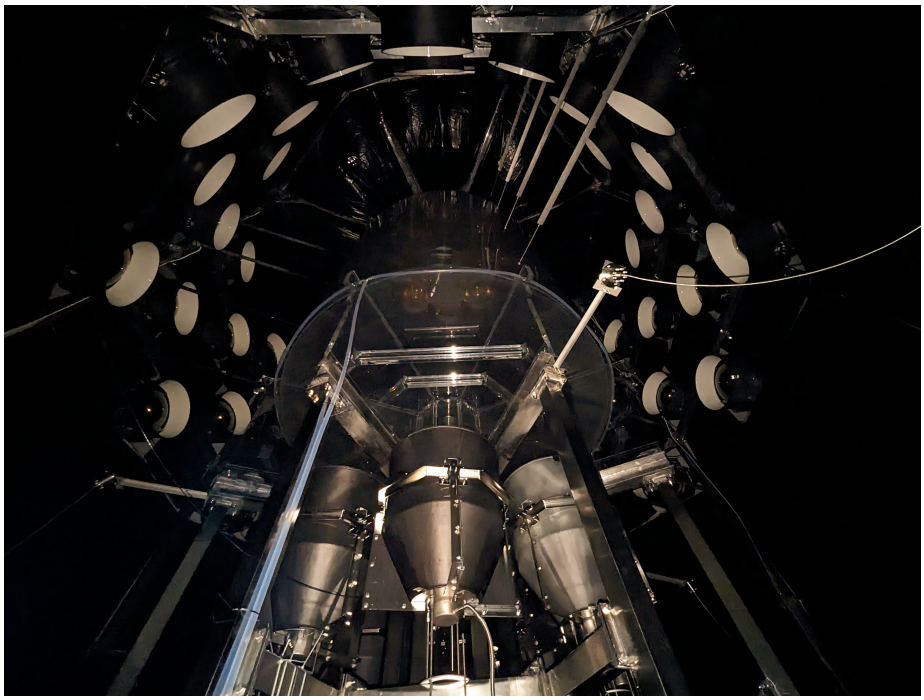

Figure 4.5: Inner view of the OSIRIS detector. On the bottom, three PMTs facing upwards can be seen, these PMTs are part of the array below the acrylic vessel (AV). This vessel, 3 m x 3 m in size, can be seen in the middle of the picture. It is positioned in the center of the 9 m x 9 m water tank of OSIRIS. Visible as white rings around the acrylic vessel are the PMTs of the PMT ring, installed with a distance of 1.5 m to the vessel. The remaining black space is the optical separation, which prevents light leakage between the inner and the outer volume. Outside of the inner detector and not visible in this picture, a muon water Cherenkov veto with a water thickness of approximately 1 m is installed. Picture taken in August 2023 by T. Sterr.

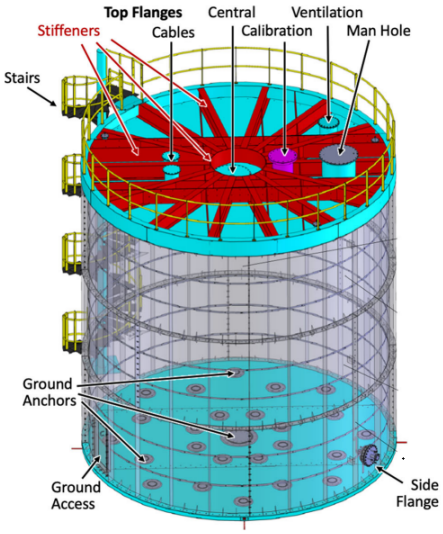

(a) Model of the water tank of OSIRIS as installed in the underground liquid scintillator hall, including all relevant access ports.

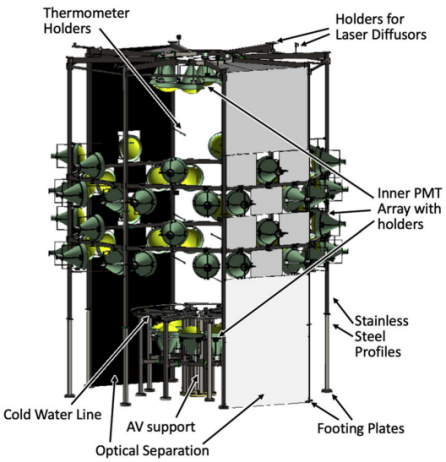

(b) Model of the inner detector of OSIRIS. All inner PMTs as well as mounting points for the diffusers and the optical separation can be seen.

Figure 4.6

- *Acrylic vessel (AV)*
  The 3 m x 3 m cylindrical acrylic vessel rests on a central stainless steel holding frame. To increase stability, the vessel features a 3 cm wall thickness as well as support fins on both, the top and the bottom of the vessel. After filling, it will contain approximately 18 t of liquid scintillator, which will be transferred into the vessel by a liquid handling system. Additional components installed in the vessel using insertion pipes include the automated calibration unit (ACU), the thermometer rod, and the level measurement pipe. A CAD drawing, as well as a picture of the actual vessel taken during installation can be seen in figures 4.7a and 4.7b.

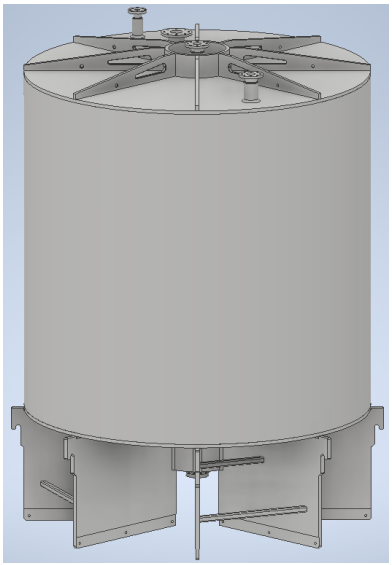

(a) CAD drawing of the central acrylic vessel of OSIRIS. Flanges on top are (from left to right): level measurement, thermometer rod, LS filling and calibration flange.

(b) Picture of central acrylic vessel of OSIRIS. In the top center of the vessel, the LAB inlet can be seen. Picture was taken prior to the installation to the optical separation, therefore, the white veto walls can be seen in the background.

Figure 4.7

- *PMT steel frame*
  The octagonal 7 m x 8 m (w x h) PMT frame consists of rectangular stainless steel profiles and holds 64 PMTs and all calibration capsules of OSIRIS (figures 4.8a and 4.8c). Additionally, most of the GCUs and temperature sensors are mounted on the frame. Since the muon veto and the inner vessel of OSIRIS need to be optically separated to function properly, the frame also supports black-and-white PET (black side facing the vessel) sheets that separate these two volumes (see figure 4.8b).

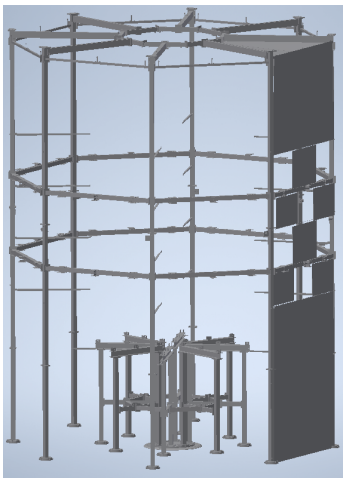

(a) CAD drawing of the PMT frame of OSIRIS. All holders and mounting points of the several auxiliaries of OSIRIS can be seen. On the right, an exemplary part of the optical separation is displayed.

(b) Three exemplary sheets of the optical separation of OSIRIS. All foils will mounted with the black face pointing inward. At the top, the stainless steel rope used for additional fixation can be seen.

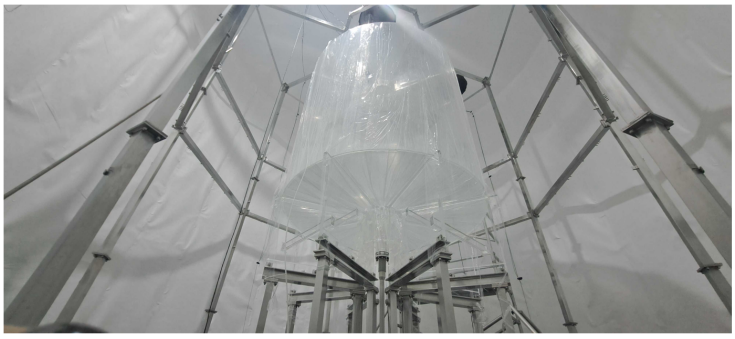

(c) The actual PMT frame together with the central acrylic vessel. Taken during the installation of OSIRIS, Oct. 2022. by T.Sterr

Figure 4.8

- *Muon Veto*
  Signals created by external sources like cosmic muons, secondary neutrons or radioactive isotopes created in spallation processes have the potential to mimic the fast coincident signals of the Bi-Po decays that are used by OSIRIS (see chapter 4.2 for details). To reduce the muonic component of this background, a veto system featuring twelve PMTs (four on top of the PMT frame and eight on the bottom around the frame, see figures 4.9a

and 4.9b) was introduced. Several studies have been conducted to get an estimate of the performance of this veto [102, 115].

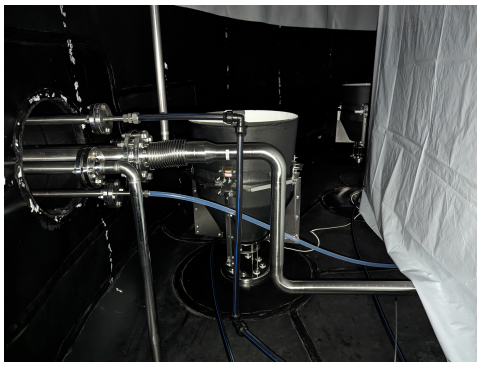

(a) Bottom veto PMT of OSIRIS in front of the connection flange of the LHS to the steel tank. Eight such PMTs are installed in the outer volume around the PMT frame. Picture taken in August 2023 by T.Sterr.

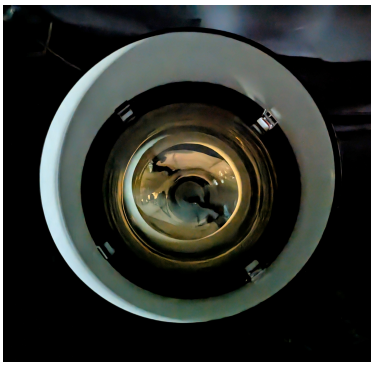

(b) One of the veto PMTs of OSIRIS mounted on the bottom of the water tank. The encasing of the PMT is a magnetic shielding, which is painted white on the inner surface to improve the detection efficiency.

Figure 4.9

- *Water tank*
  The 9 m x 9 m cylindrical water tank holds approximately 550 t of ultra high purity water and offers a 4π shielding against external gamma rays. Remaining gamma radiation has been proven to be sufficiently low for OSIRIS to achieve its goals [102]. The tank itself is not intrinsically tight since it is made from bolted carbon steel, hence the inner surface of the tank is covered by a water-tight HDPE liner. To increase the performance of the muon veto, an additional layer of white Tyvek has been installed on the inner surface. Flanges for access, ACU, LAB inlet, level measurement, sensors, cables and nitrogen exhaust are available on top of the tank. On the side of the tank the installation manhole (which will be sealed after installation work is completed) and the LAB outlet can be found (see figures 4.9a,4.10a, and 4.10b).

(a) The water tank of OSIRIS during the test assembly at the production company. The installation man hole can be seen in the center.

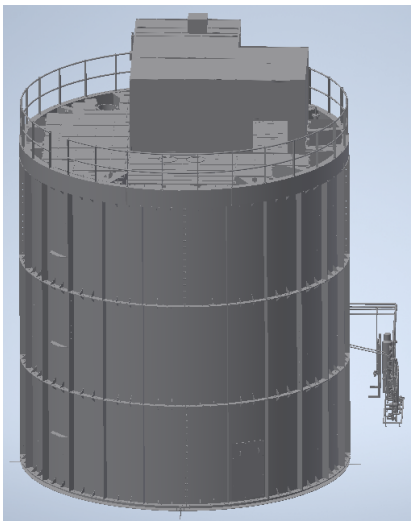

(b) CAD of the water tank of OSIRIS. On top of the tank, the ventilation flange, the two cable inlet flanges as well as the top clean room can be seen.

Figure 4.10

- *Liquid handling system (LHS)*
  Due to the complexity and the different operation modes of OSIRIS (see sections 4.2.1 and 4.2.2), a sophisticated liquid handling system (LHS) is required. For example, during the use of continuous mode to create temperature stratification levels of the LS inside the acrylic vessel, a constant flow of warm LS is inserted into the top of the AV. At the same time, a constant flow of cooler water on the outside of the AV is used to counter the warm LS. The complex pumping and control system was developed in cooperation with Fäth GmbH and Scientific Support GmbH (see figures 4.11a and 4.11b). Moreover, several tanks and buffers are included in the system, an example can be found in figures 4.12a and 4.12b. The head tank of OSIRIS is located on top of the vessel and is used to equalize the hydrostatic pressure. A buffer tank outside the water tank is used to prevent any backflow of LS in the system.

  In addition to this liquid handling system, a nitrogen handling system which provides a buffer layer of ultra-pure nitrogen to both acrylic vessel and water tank has been added. These volumes are kept at a slight overpressure to prevent contamination entering through the outlets of the two volumes.

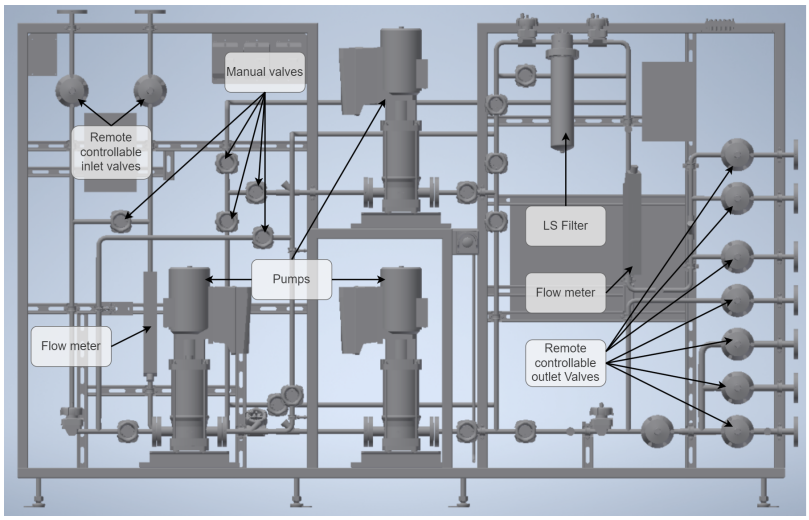

(a) CAD of the pumping station of OSIRIS. The three large, cylindrical objects are the main pumps for LS, water and backup, smaller round objects are valves (larger ones are remote controllable, smaller ones are to be controlled manually).

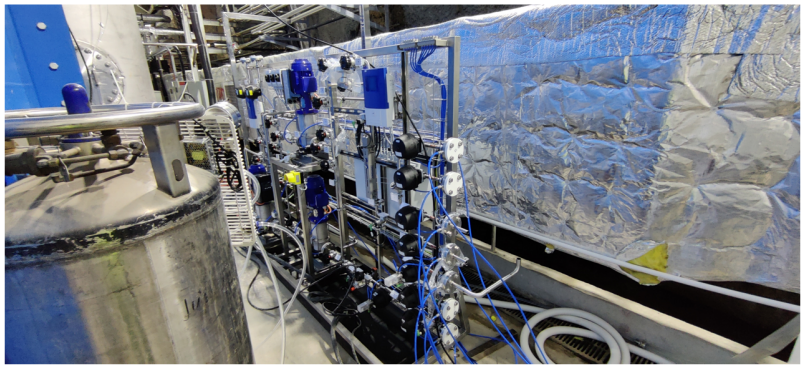

(b) Picture of the actual pumping station of OSIRIS after set up on-site. In addition to pumps and valves the blue pneumatic piping for remote control of the valves can be seen.

Figure 4.11

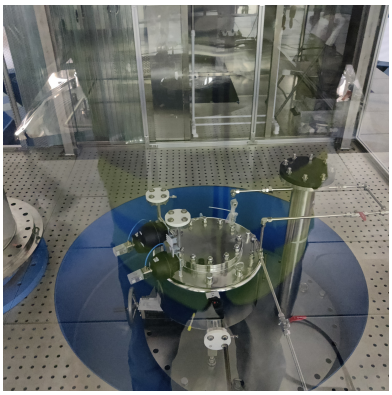

(a) Picture of the head tank of OSIRIS as installed in the top clean room.

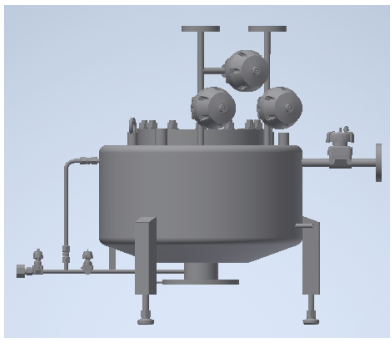

(b) CAD of the head tank of OSIRIS. In addition to the tank vessel itself, LAB connections, control valves and nitrogen connections can be seen.

Figure 4.12

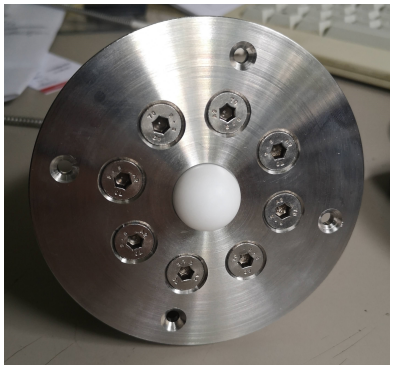

(a) Front view of a diffuser capsule. Capsule is sealed by the inner ring of screws. In the center, the PTFE diffuser bulb is visible.

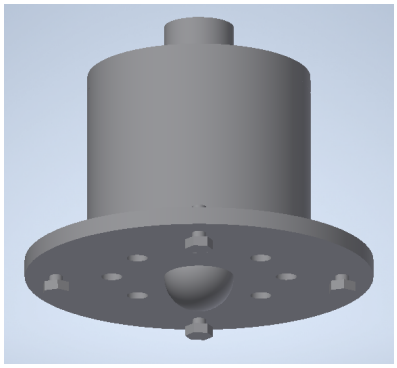

(b) CAD of the diffusers of the LCS. Capsules them selves are mounted into fixation clamps that are connected to the PMT frame.

Figure 4.13

- *Calibration systems*
  Two independent calibration systems have been introduced to OSIRIS to perform calibrations on timing and single photon charge of all PMTs as well as energy and vertex position reconstruction of the OSIRIS detector [102, 116]. On the one hand, an Automated Calibration Unit (ACU) was inherited from the Daya Bay experiment [117] and refitted for use

in OSIRIS (see figures 4.14a and 4.14b). On the other hand, a laser calibration system (LCS) was developed and built for the use in OSIRIS in the scope of this work (see chapter 5 and figures 4.13a and 4.13b).
The comprehensive calibration plan for OSIRIS includes energy and vertex calibration of the acquired events (ACU, see chapter 4.5.1) as well as charge and timing calibration of the PMTs (LCS).

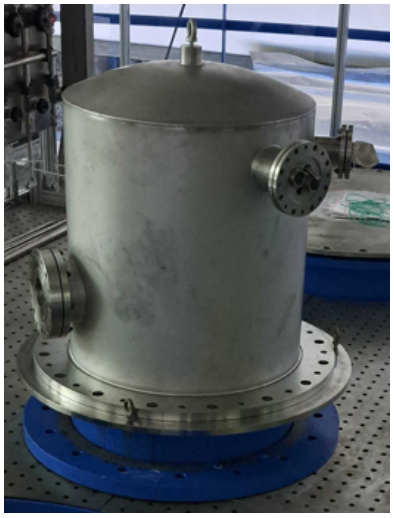

(a) Picture of the OSIRIS ACU as installed in the top clean room of OSIRIS. Visible are the flanges for visual inspection, control and nitrogen (left to right). Picture taken in fall 2022 by Cornelius Vollbrecht.

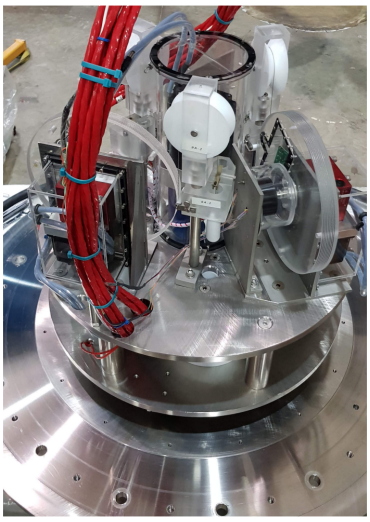

(b) The ACU with removed bell jar. Cables and deploying wheels can be seen. A detailed labeled picture of the inner parts of the ACU can be found in chapter 4.5.1. Picture taken in fall 2022 by Cornelius Vollbrecht.

Figure 4.14

- *PMTs*
  It was previously planned to use PMTs for OSIRIS that were newly developed intelligent PMTs (iPMTs). These PMTs included all relevant data and control electronics within their bases (see figure 4.15a). This included the high voltage power supply, a ZYNQ system on chip (SOC), a newly developed "VULCAN" application-specific integrated circuit (ASIC) featuring an adaptive gain and a sampling rate of 500 MS/s and all relevant slow control and data processing electronics. Connection to the detector control system of OSIRIS was for seen to be done via Ethernet cables (see figure 4.15b). In total, 75 iPMTs were produced for shipment. However, after their arrival on-site, it was found that approximately 50 % of the shipped PMT suffered damage to their high voltage power supply module

during shipment from Germany. Due to the unknown outcome of a possible repair and the tight schedule, OSIRIS switched to using the standard MCP LPMTs of JUNO [92, 21] (see figures 4.15c and 4.15d).

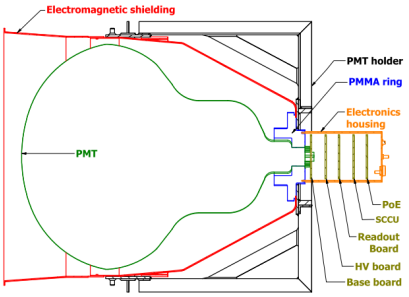

(a) Cross section of an iPMT. Not included is the PTFE bottle included into the base, which was supposed to be used as a pressure exchange volume. Picture taken from [102].

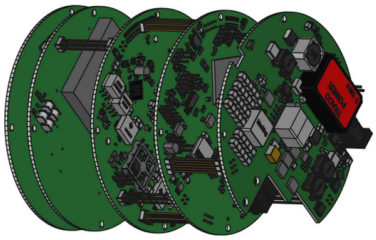

(b) Electronics stack of the iPMTs. All PMTs were newly developed for this purpose. Stack was assembled at RWTH Aachen. Boards are (from left to right): Base, HV-Board, Readout Board, SCCU (slow control) and Power over Ethernet board. Picture from [102].

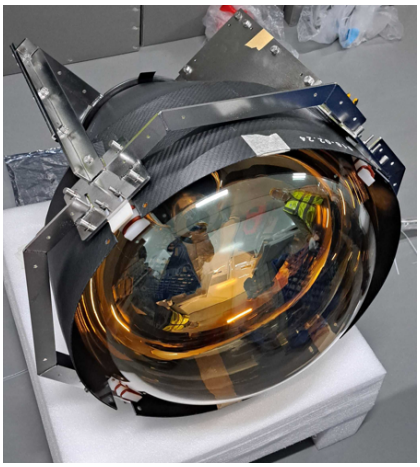

(c) Assembled OSIRIS LPMT. Elongated magnetic shielding was removed for better visibility of the PMT.

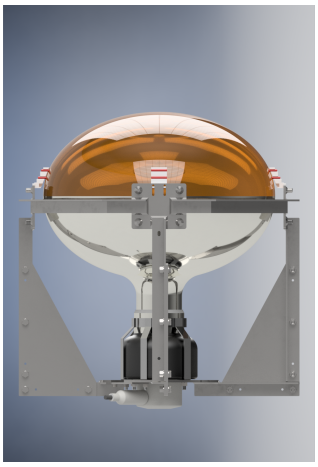

(d) Rendering of the redesigned PMT holder of OSIRIS. For better visibility, the shielding has been removed. Picture taken from [118]

Figure 4.15

The installation of the complete OSIRIS detector, including all auxiliaries, computers, DAQ hardware and remote controls took place between January 2022 and Summer 2023. Several small adjustments were necessary during this installation phase (e.g., changes of cable routing, control software). In addition to these changes, some changes regarding the new PMT type had to be made. Since the NNVT PMTs differ in shape in comparison to the previously used Hamamatsu tubes, changes in the holders of the PMTs, the mounting points of these holders, and the magnetic shielding cones were necessary.

4.4 Photo multiplier tubes (PMTs)

4.4.1 Intelligent PMTs (iPMTs)

The original design of OSIRIS included a new kind of PMT the "intelligent" iPMT [102]. This kind of PMT consists of three main parts: A 20-inch Hamamatsu R12860 tube (see table 4.2 for basic performance parameters), a surrounding mounting frame with magnetic shielding (see figure 4.15a) and an "intelligent" base, that contains all relevant hard- and software to operate the PMT, which includes high voltage power supply, digitizer, slow control and operating system. In this way, long cables between PMT and digitizing electronics can be avoided and thus the signal quality improved. The electronics stack (see figure 4.15b) is immersed in mineral oil to increase the heat transfer from the electronics to the stainless steel enclosure.

Table 4.2: Main performance parameters of the Hamamatsu R12860 20-inch tubes used in the assembly of the OSIRIS iPMTs. [102]

Parameter	Value
Transit Time Spread	2.63 ± 0.16 ns
Dark Count Rate	15.4 ± 2.6 kHz
Peak to Valley	3.21 ± 0.20

There are five different PCBs included in the intelligent base, all of them are connected via vertical interconnects [102]:

- *Base board*
  This board mainly holds the voltage divider of the PMT, the layout follows the recommendation of Hamamatsu. The tube is operated with a positive high voltage.
- *High Voltage board*
  The high voltage module of the HV board is custom made and converts 24 V to a high voltage suitable to power PMTs. In addition to the conversion module, this board houses the decoupling capacitors that extract the signal from the high voltage.
- *Read-Out board*
  As the central part of the electronics stack, this board contains a Xilinx system on chip (SOC) that combines an ARM processor together with a field-programmable gate array (FPGA), a clock data recovering logic, a newly developed "VULCAN" ASIC which contains an ADC with an adaptable gain as well as additional signal processing logic.
- *Slow Control and Configuration board*
  This board combines a micro controller and a four port Ethernet switch.

In addition, several serial control controllers are available. This board handles all internal and external communication and configuration.

- *Power Over Ethernet (PoE) board*
  Since the only connection to the iPMTs is an Ethernet cable, this board is responsible for distributing the supply power received via power-over-Ethernet (acrshortpoe). It contains several DC/DC converters as well as the PoE device controller.

4.4.2 Large PMTs (LPMTs)

All JUNO PMTs that were repurposed for the use in OSIRIS are based on the 20-inch MCP tubes by NNVT. These tubes feature a shorter and slimmer neck (see figure 3.8) which led to the necessity of adjusting the PMT holders of OSIRIS. On the one hand, the clamps at the equator of the holder needed to be shortened and repositioned (see figures 4.16a and 4.16b), one the other hand the base plate of the holder was modified to accommodate the differences in the design of the PMT base of the NNVT PMTs (see figure 4.17). Each PMT is connected to a general control unit (GCU) which houses a HV power supply, two ADCs featuring two different gains, a SOC combining a FPGA and an ARM CPU as well as I/O electronics. Three PMTs can be connected to a GCU. Each GCU is connected to the back-end card BEC, which is then connected to the analysis computers via Ethernet.
A scheme of the GCUs can be found in figure 4.18 as well as a scheme of the data flow in figure 4.19.

(a) The original version of the PMT equatorial holding clamp. As can be seen, the space between the clamp and the PMT surface is much to large to support the PMT.

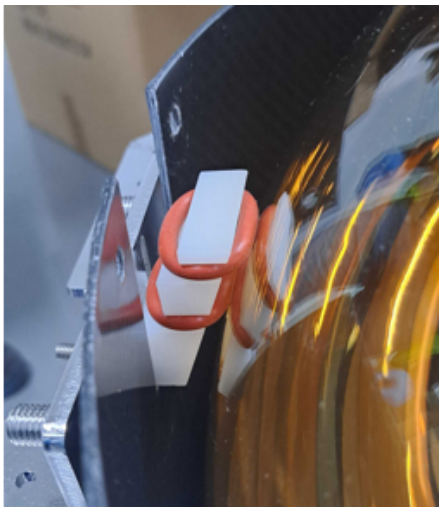

(b) The adapted version of the PMT holding clamp. After shortening and repositioning of the mounting holes of the clamp, a support of the PMT is possible.

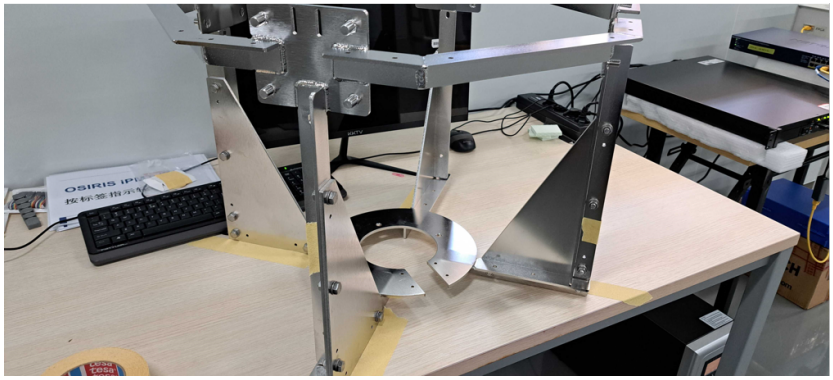

Figure 4.17: The already adapted PMT holder of OSIRIS. The slit in the bottom holding ring was introduced to take care of the LPMT cable which is fed into the PMT base from the side. Additionally, mounting holes for the PMT neck supporting clamps have been introduced.

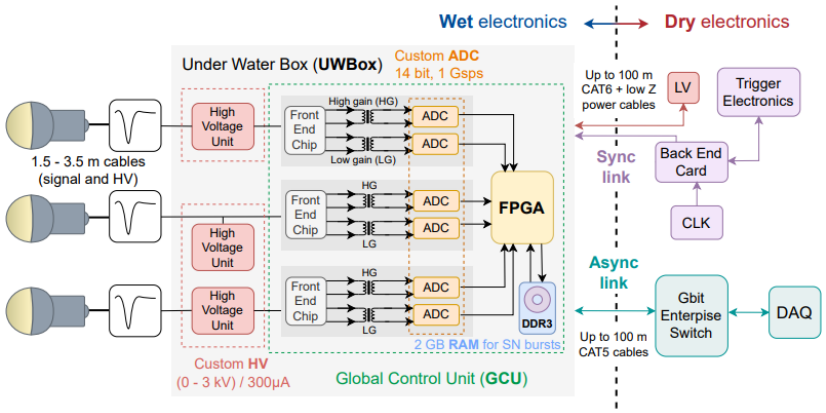

Figure 4.18: Scheme of the Global Control Unit (GCU) as used by both, JUNO and OSIRIS. In addition, back-end and support electronics are shown. Picture taken from [119].

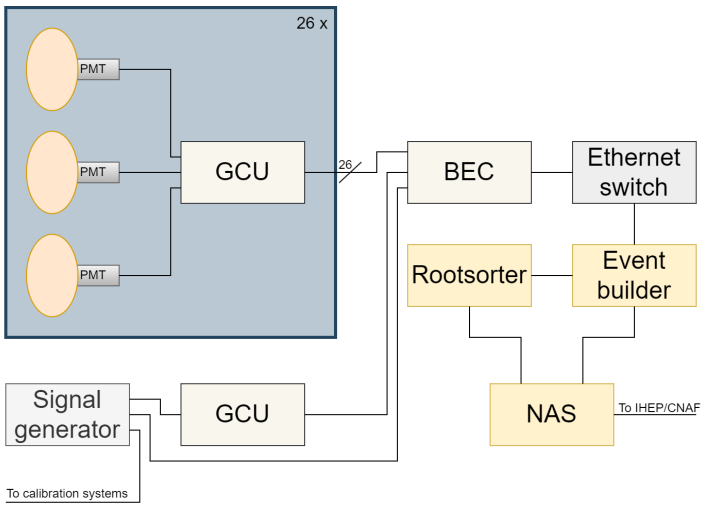

Figure 4.19: Data connections of OSIRIS from PMT to the JUNO computation centers. All PMTs are connected to the GCUs in groups of two or three. The GCUs are connected to the back-end card (BEC), which also includes the trigger GCU which is used to digitize the trigger signal of the optical calibration systems. In the next step, the data is sent from the BEC to the eventbuilder and, as a last step, to the rootsorter. Both computers saved their results (events and analysis) on the NAS which is then synced to the international JUNO computation centers. Not included in this scheme are the power-over-Ethernet connections for the PMTs as well as the time-syncing with the JUNO main system.

4.5 Calibration Systems

This section will describe the two independent calibration systems of OSIRIS: The automated calibration unit (ACU) and the laser calibration system (LCS).

4.5.1 Automated Calibration Unit (ACU)

The automated calibration unit (ACU) of OSIRIS is located in the top clean room. It was adapted from Daya Bay and will use the same type of sources: A LED light source, a potassium source and a multi-gamma source [102] [7].
Some parts of the ACU have been adapted or renewed: Firstly, the base of the bell jar of the ACU has been adapted to fit onto the corresponding flange in the top clean room of OSIRIS. Secondly, the LabVIEW control software used in Daya Bay has been adapted to fit the needs of OSIRIS (e.g., control via EPICS, etc.). Thirdly, some parts of the electronics of the ACU have been replaced (e.g., malfunctioning transformers, etc.). However, most of the system is used "as is" and features the same operational parameters as the ACUs of Daya Bay [7].
The three sources of the ACU are placed on acrylic winches that are mounted to a turntable. Each winch and the turn table is controlled by a stepper motor, that are connected to gear boxes and load cells to optimize positioning accuracy. To move a source into the detector, a winch is placed over the 1-inch calibration pipe located at the bottom plate of the ACU. The calibration pipe itself is located 1.2 m off-axis from the center of the AV, which provides the opportunity to maximize the detector response at different heights. A view of the opened bell jar can be found in figure 4.20 [102].
Since the OSIRIS PMTs feature a sensitivity maximum around $410 - 440\,\mathrm{nm}$, a LED with a wavelength of 435 nm was chosen for the use in the LED capsule. It will be adjusted to create light pulses in the single p.e. regime and allows repetition rates of up to 3 kHz. Additionally, a pulse width of 7 ns (FWHM) can be achieved. The exact light intensity of the LED will be determined during the commissioning phase of OSIRIS.
The primary source for energy and vertex reconstruction will be the multi-gamma source. It contains three different isotopes (^{137}Cs, ^{65}Zn and ^{60}Co) and is covered by PTFE. With a combined activity of approximately 9 kBq and an energy range between 0.66 MeV and 2.5 MeV, the crucial energy range for the detection of Bi-Po signals is covered.
As a long term monitoring source, a capsule with natural potassium is used. The contained ^{40}K gamma emission with an activity of $\leq 1\,\mathrm{Bq}$ allows the source to remain inside the vessel during normal operation. Thereby a continuous monitoring of the LS can be achieved by monitoring the position of the ^{40}K peak.
A complete, simulated spectrum of the two gamma sources can be found in figure 4.21.

Figure 4.20: ACU with opened bell jar. Visible are two of the three winches as well as the turn table. In red, control and supply cables can be seen. Picture taken from [102].

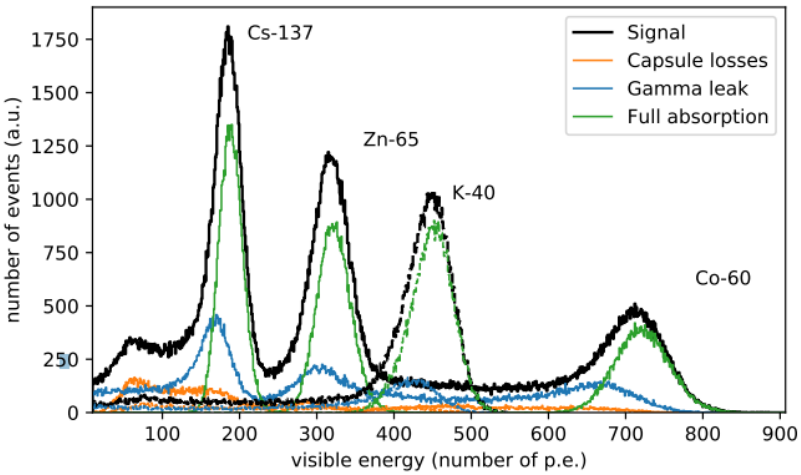

Figure 4.21: Simulated visible energy spectrum of the ACU. The simulation includes all geometrical properties of the calibration system (e.g., off-axis calibration pipe, etc.). Picture taken from [102].

4.5.2 Laser Calibration System (LCS)

The LCS of OSIRIS will feature 24 diffused light injection points distributed in the water tank. These diffusers are supplied by a pulsed laser which features a pulse width of 80ps ($1\,\sigma$). The development of this system was done in the scope of this work, further information can be found in chapter 5.

4.6 Run and Slow Control

In the case of OSIRIS, run (RC) and slow control (SC) are not easy to distinguish. Some hardware as well as software information is needed by both systems, leading to shared resource usage. The same is true when it comes to user interaction. Both systems need to be observable by a shifter but should only be manageable by an expert. To differentiate the two systems, it was decided to pass everything connected to the monitoring and control of the hardware to the SC, whereas the RC is responsible for everything that is connected to DAQ and data taking. More details can be found in chapter 7. A scheme of the systems, EPICS PVs, and access levels can be found in figure 4.22.

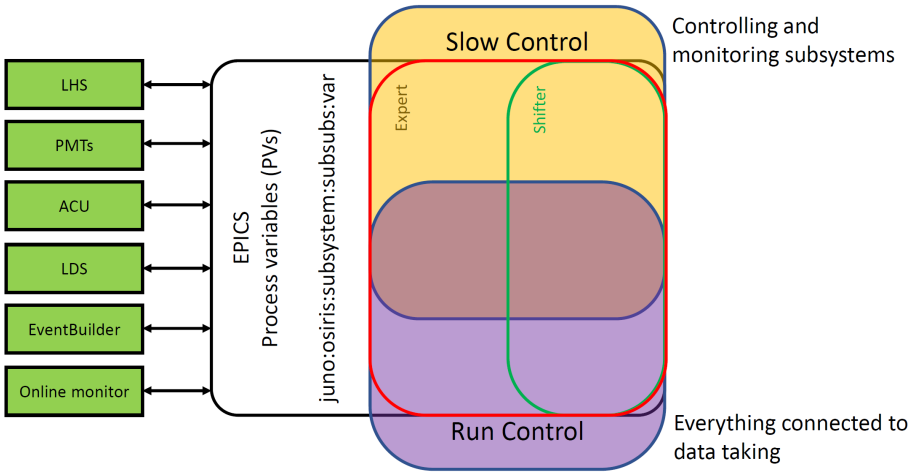

Figure 4.22: The differentiation of the JUNO OSIRIS SC and RC systems. In addition, all hardware systems as well as the different levels of access are displayed. Picture from [120].

The SC of OSIRIS is written in two different ways: On the one hand, standard stand-alone EPICS IOC is used (LPMT, computer health, NAS health and hardware calibration values). On the other hand, systems that use control software written in LabVIEW use the shared variables engine of LabVIEW to generate these IOCs either via VI or LabVIEW-GUI. Some parts of this software have been written in the scope of this work, see chapter 7.4 for details.
In addition to the underlying SC software, several GUIs have been written. They were created using the Control System Studio Phoebus (CSS) and feature not only display but also some logic capabilities. Most of these interfaces have been written in the scope of this work, details can be found in chapter 7.4, too.

4.7 Data acquisition

Even though OSIRIS had to change the PMT type (see chapter 4.4), the scheme of the OSIRIS DAQ stayed the same. It consists of two main parts: the event-builder and the analysis framework. Everything that is related to event building and triggering is part of the functionality of the event-builder, whereas the search for coincident Bi-Po events is part of the online analysis [102].
The standard physics trigger logic of the LPMTs used in OSIRIS is a coincidence trigger of twenty PMT time stamps within a window of 70 ns. All events within a pre-trigger window of 200 ns before the event and a post-trigger window of 800 ns are stored to generate a raw event. These events are saved on the NAS and forwarded to the online analysis framework. In addition to this standard physics trigger mode, OSIRIS features additional trigger modes (e.g., for debugging purposes) as well as a calibration mode. In this mode the system is externally triggered by an Agilent 33512b signal generator [121]. In this mode, the generated trigger is digitized simultaneously to be later used to reduce potential jitters that might occur due to clock uncertainties. In total, the event builder consists of four different layers, all monitored by a logger: Input handling, event sorting, trigger creation and output handling (see figure 4.23).
All online analysis tools of OSIRIS are based on the RootSorter online/offline analysis toolkit developed at COSY. It provides all required functionalities needed, including communication, interfaces to parameter objects as well as online monitoring possibilities. In addition, it can be used to run different analysis modules on the data provided to the software. The results of the online analysis framework are pushed to the NAS, displayed in the SC and further processed to create decisions (e.g., in the event of increasing rates of Bi-Po events). A more detailed description of the software logic of OSIRIS can be found in [102].

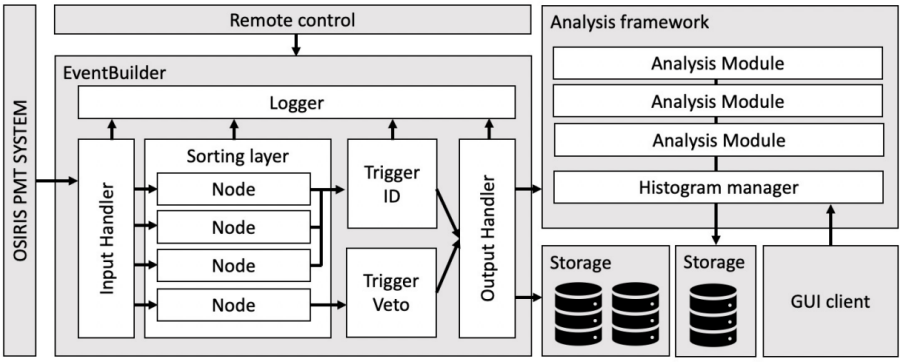

Figure 4.23: Software scheme of the OSIRIS DAQ. Picture taken from [102].

Chapter 5

The Laser Calibration System of OSIRIS

"In a dark place we find ourselves and a little more knowledge lights our way"
-Yoda

from "Star wars Episode III: Revenge Of The Sith", 2005

This chapter describes the laser calibration system of OSIRIS, which was developed as part of this work. The system needs to be able to calibrate the PMTs to a level in which both the possibility to separate BiPo coincidences as well as a precise counting of the number of photo electrons per event are possible. Based on a fast, pulsed laser, whose light is distributed to 24 diffused light injection points located in the detector, the system will be used for the weekly calibration of the OSIRIS detector.

5.1 Hardware of the laser calibration system

The Laser calibration system of OSIRIS was developed to create the opportunity to calibrate the PMTs in both timing (what is the uncertainty in the transit times of photo electrons in a PMT?) and charge (how precisely can the position of the single photoelectron peak maximum be determined?). Several design aspects were considered: The system needs to illuminate all PMTs roughly within the same level, since a change in the laser light intensity of most laser sources would also change the timing profile of the beam [122]. Furthermore, a homogeneous illumination of the PMTs is of importance, since it was shown that the PMTs feature an inhomogeneous timing over the whole cathode [92]. Furthermore, the system must be cost-effective, easy to be controlled remotely, and needs to fulfill the needs of the radio purity of the detector.
Taking these points into account, the resulting calibration system consists of three different parts: Light distribution system (LDS), diffuser capsules and (control) software.

5.1.1 Light Distribution System (LDS)

The LDS of the laser calibration system of OSIRIS is composed of three parts, which will be discussed in this subsection. These three parts are: The laser diode, the laser driver as well as the opto-mechanical cascade to distribute the laser light into the 36 channels.
The EIGDX2000 **Laser driver** (figure 5.1) by NKT Photonics (former A.L.S. GmbH), is a standard laser driver unit for pico-second laser diodes that feature a maximum internal trigger rate of 10 MHz, a maximum external trigger rate of 16 MHz and a broad range of external trigger capabilities (NIM, TTL and arbitrary). In OSIRIS, the device will be triggered by a frequency generator and is connected by a DVI cable to the LDS (see connecting scheme 5.7).
As source for very short light pulses a PiLas PiL042 **laser diode** by NKT Photonics is used. It features a pulse width of approximately 50 ps at an ideal tuning of 50 % [122]. It is connected to the first stage of the opto-mechanic cascade using a FC/APC fiber coupling (see figure 5.2). Selecting this laser system was based on the one hand on a series of tests of available light sources (e.g., also fast LEDs and chopped continuous wave laser have been taken into account) and on the other hand on the experience with this system after its use in the JUNO PMT testing containers [20]. Using a laser diode with a wavelength of 420 nm is caused by the sensitivity curve of the used PMTs.

Figure 5.1: Laser driver as currently available by NKT Photonics. Model used in this work is technically identical but branded differently. Image take from [123].

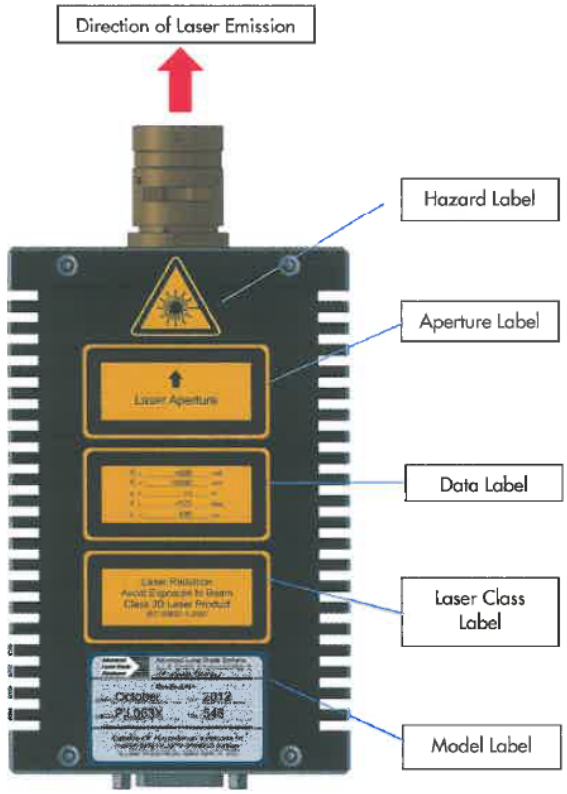

Figure 5.2: Laser head of the laser calibration system of OSIRIS. The fiber coupling is not included in this picture. Picture taken from [122].

One of the main challenges in the development of the LCS of OSIRIS was the distribution of the light to different injection points. At the start of the development of the system, the PMTs that would have been used in OSIRIS were the R12860 tubes by Hamamatsu, featuring a very short TTS of approximately 2 ns. The small size of the TTS of these PMTs leads to some implications for the light sources that can be used to measure this values. Using multiple light sources provide the challenge of syncing and characterizing these sources to a level that is comparable to the expected TTS of the PMTs. To avoid this necessity, it was chosen to use only one light source, even though such a use leads to the problem of how to distribute one light source to multiple outputs. This problem was solved by introducing an opto-mechanical cascade, starting at the fiber-coupling of the laser diode and ending at the ports of the fibers of the diffusers capsules.
An additional optimization idea that was taken into account during the development was the necessary time to actually perform the timing calibration of OSIRIS. It seemed inefficient to just use one diffuser at a time, since the inner and the outer volume of the detector are optically separated (see chapter 4). Therefore, a way to reduce the time needed to perform a complete calibration run is the simultaneous use of a diffuser in the inner and in the outer volume of the detector.
These considerations lead to the set-up shown in figure 5.3: The laser pulse emitted by the laser diode is fed into a 2ch fiber switch, which is used to switch between the two legs of the cascade. The first leg, leading to the single channel outputs, is used to feed the diffuser bellow and above the acrylic vessel. Leading to the double channel outputs, the second leg is used to provide light for the diffusers located on the PMT ring as well as in the veto volume. To provide the possibility to adapt to light intensity differences in the two legs, each leg features an individually controllable attenuator right after the output of the 2ch fiber switch[1]. The double channel leg then directly leads into a 12-ch switch, which has a 50 %:50 % beam splitter connected to each switch output. The two outputs of these splitters are then connected to two fibers leading to one diffuser located in the veto and to one diffuser mounted on the PMT ring, respectively. To ensure a comparable light intensity at the outputs of the LDS, a 50 %:50 % beam splitter has been introduced right after the attenuator of the single channel leg of the cascade. Using only one of the outputs of this splitter (and dumping the other one), another 12ch fiber switch is used to distribute the laser pulse to the PMTs below and above the acrylic vessel of OSIRIS. A list of parts used for this setup can be found in table 5.1, a sketch of the mounting positions of the diffusers can be found in figure 5.4. Additionally, figure 5.5 shows the interior of the LDS as installed in OSIRIS.

[1]The actual light intensities of the two legs differ due to differences in the production of the opto-mechanical parts used in the system. A calibration of these light intensities has been performed and can be found in chapter 5.6

Table 5.1: List of all parts used in the opto-mechanical cascade of the light distribution system. Technical drawings of the case can be found in appendix D.

Part	Vendor	Model	Amount
2 ch fiber switch	LEONI fiber Optics	mol 1 x 2 S50 VIS	1
12 ch fiber switch	LEONI fiber Optics	mol 1 x 12 S50 VIS	2
Attenuator	Thorlabs	VOAMMF	2
Beam dump	Thorlabs	FTFC1	1
50 % : 50 % Beam splitter	Thorlabs	TM50R5F1A	1
50 % : 50 % Beam splitter	Thorlabs	TM200R5F1A	12
FC/PC fiber ports	Thorlabs	ADAFC1	36
Case	Fischerelektronik	CE 3 360	1

Considering the amount of available ports of the 12 ch switches, several spare ports are available: four single, and eight double channels. This includes four ports for each of the subgroups: top/bottom PMTs, ring PMTs and veto PMTs. By the time of writing of this thesis, one of the double-channel ports has been found to be broken as well as two ports of the single-channel switch. The latter can possibly be restored, since the damage does not affect the optics but the threading of the fiber port (see chapter 6.1).
The opto-mechanic cascade is mounted in a standard 19-inch rack mount and installed in the calibration rack of the OSIRIS electronics platform. On the front panel of this mount, all relevant ports of the system are accessible (see figure 5.6). Prior to the shipment to China in winter 2021/2022, the system was characterized in a testing setup in Tübingen (see section 5.6).

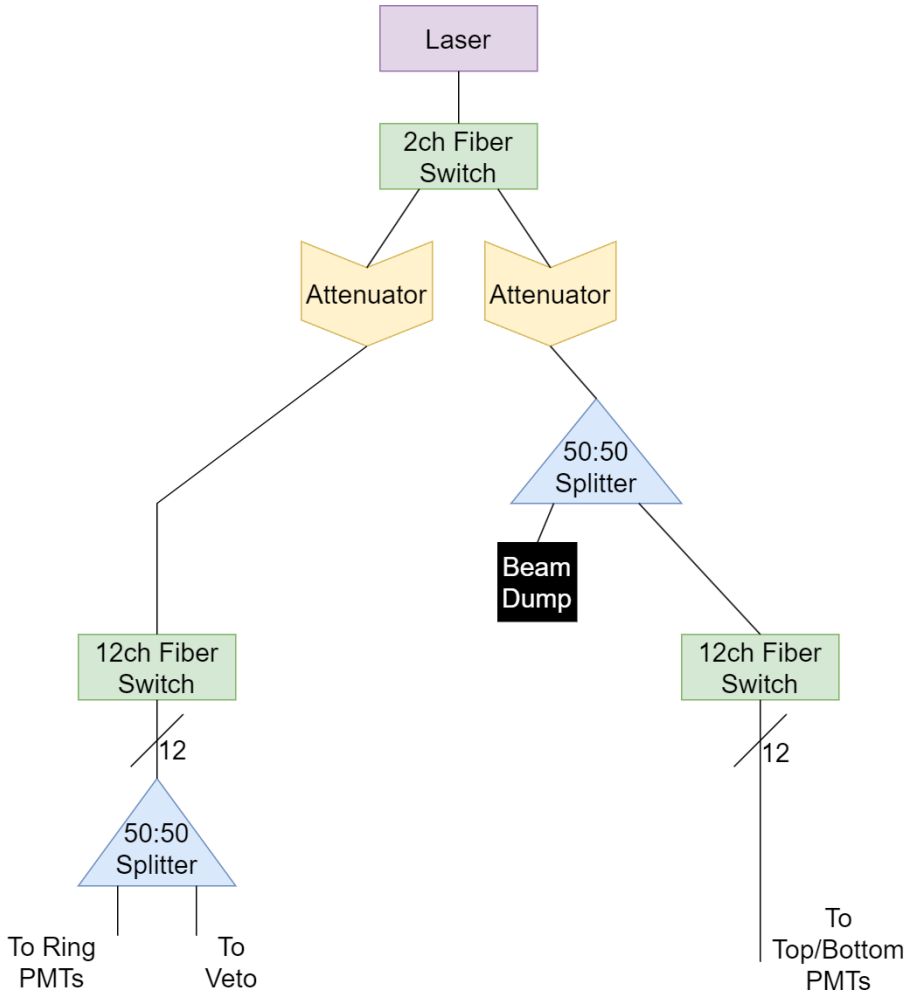

Figure 5.3: Optical cascade as implemented into the LDS of the laser calibration system of OSIRIS. The laser is coupled into a 2ch fiber switch via the fiber coupling mounted to the laser head. Both outgoing channels are then connected to attenuators, which can be adjusted individually. One of the two outputs is then directly connected to an 12ch fiber switch, the other to a 50:50 beam splitter. Each output of this optical switch of the first branch features a 50:50 beam splitter, whose outputs are then connected to the front plate connectors. The two outputs of the splitter of the second branch is on the one hand fed two a beam dump and to the other hand to a 12ch fiber switch. Subsequently, these outputs are then connected to the front plate outputs. 24 of the channels created in this way are connected to the several diffusers of the LDS: eight of them to the diffusers above and bellow the AV (right branch, single channels), 16 of them to the veto and the PMT ring (left branch, double channels).

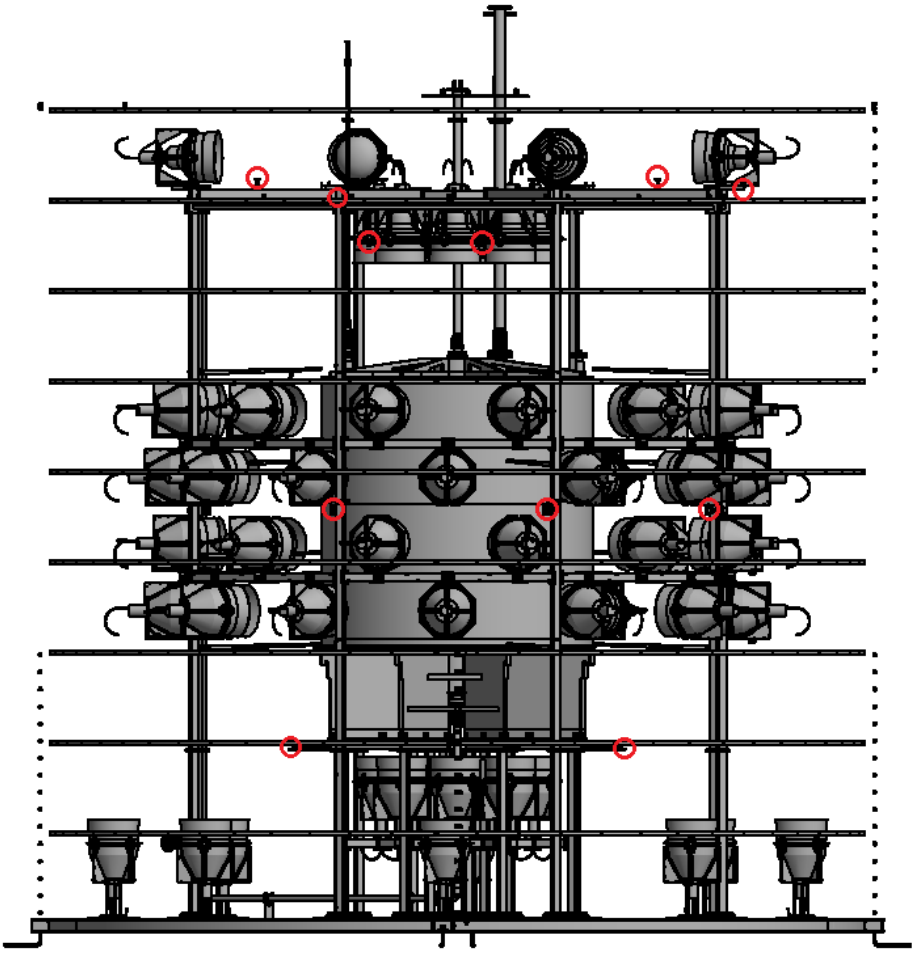

Figure 5.4: CAD sketch of the OSIRIS detector, which is simplified for better readability. Marked in red circles are some of the mounting positions of the diffusers. In each group these diffusers mounting points are distributed evenly in 90° (top veto, bottom veto, above vessel and bellow vessel) or 45° (PMT ring).

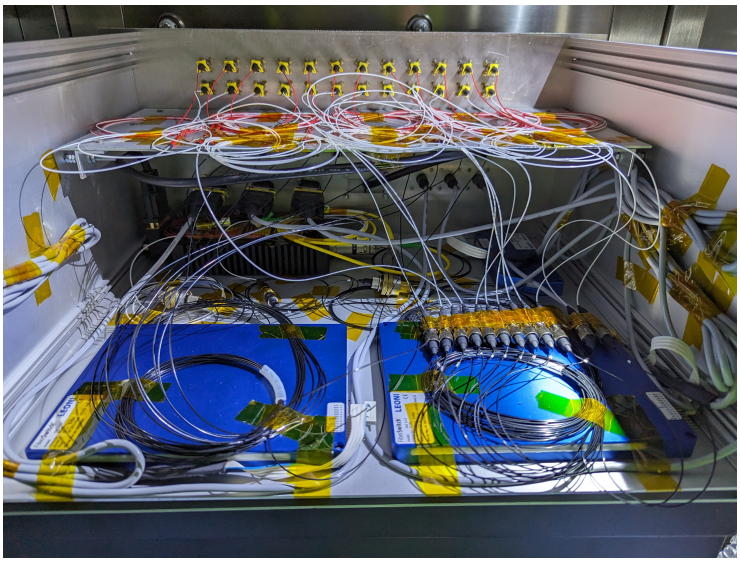

Figure 5.5: Interior of the LDS as installed in the electronics cabinet of OSIRIS. The optical switches (blue boxes on the bottom plate) and the laser head (black box in the bottom back) can be seen as well as the several beam splitter (red tubes) and the attenuators (large brass rings). At the back of the front plate the I/O ports of the LDS are placed.

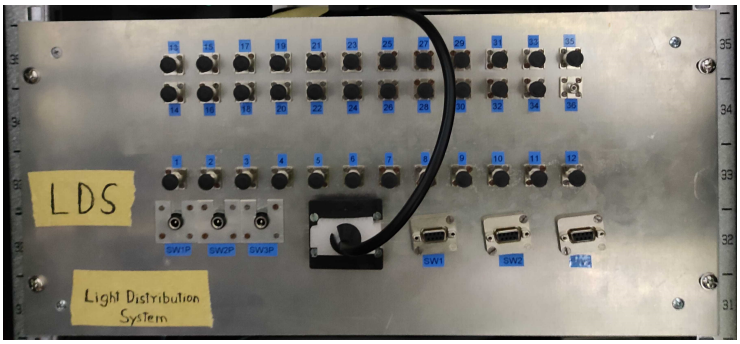

Figure 5.6: Front view of the LDS installed into the calibration rack at the electronics platform of OSIRIS. The FC/PC connectors are black capped, power connectors and control connectors of the optical switches can be found in the bottom row. In the center of the bottom row, the connection cable to the laser head can be found. To improve visibility of the ports, nothing is connected to the device in this picture.

5.1.2 Diffuser Capsules

The design of the diffuser capsules was chosen based on the requirements for the (long term) use inside a water filled detector. This includes limits for radio purity and general water contamination, as well as robustness. In addition, it must comply with the list of accepted materials of OSIRIS. A last design criterion was to keep the amount of air inside the diffuser capsule to a minimum to avoid possible radon contamination. From an optical point of view, the light field emitted by the capsule should be as homogeneous and broad as possible, to allow one diffuser to illuminate as much PMTs as possible with the same light intensity.
All of these considerations led to the final design of the capsule, consisting of a robust 316L stainless steel body and a PTFE diffuser bulb (see figures 5.8 and 4.13a). Into each capsule, an optical fiber[2] is fed from the back and glued into the capsule using Masterbond epoxy EP30-4. Results of the compliance tests to ultra-pure water of the epoxy can be found in figure 5.10 and table 5.2. To provide the highest possible level of flexibility in the mounting position, several adapter pieces have been developed (see appendix C). In total, 24 capsules have been placed inside the water volume of OSIRIS, for details about placements, see section 5.3. Technical drawings of all parts of the diffuser can be found in appendix B.

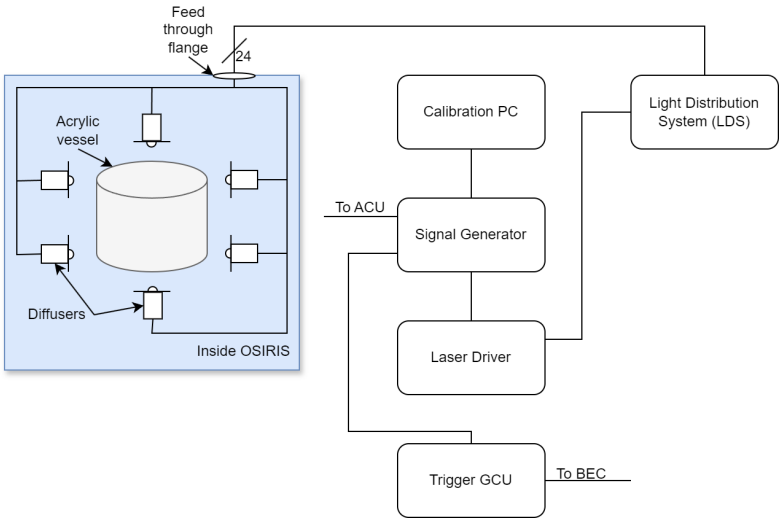

Figure 5.7: Scheme of the integration of the LCS into the OSIRIS electronics. To increase readability, the inside of OSIRIS has been simplified. All fibers are fed through a flange featuring a special single cable sealing by Pflitsch (See figure 5.11). The trigger GCU is a standard GCU (as mentioned in chapter 4), which is refitted to digitize the trigger pulse itself (see chapter 6.4.2).

[2]Custom made fibers based on the FG200LEA fiber by Thorlabs.

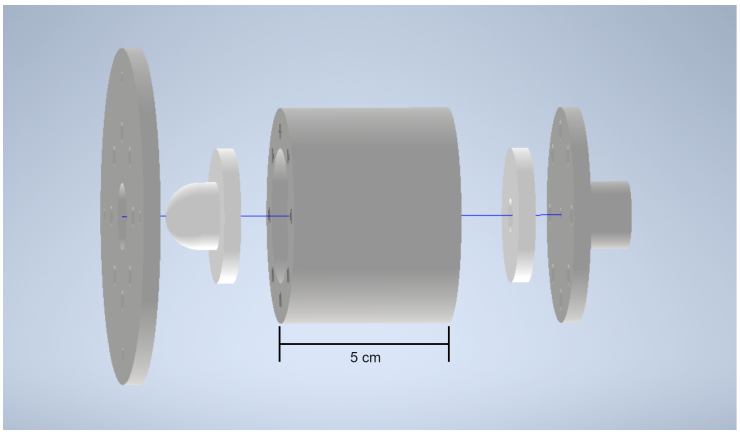

Figure 5.8: Explosion drawing of the diffusor capsules of OSIRIS. White parts are made of PTFE, grey is 316L stainless steel. In blue, the insertion direction of the optical fiber (diameter of 3.8 mm) is displayed. Detailed technical drawings can be found in appendix B. A detailed view of the PTFE tip can be seen in figure 5.9.

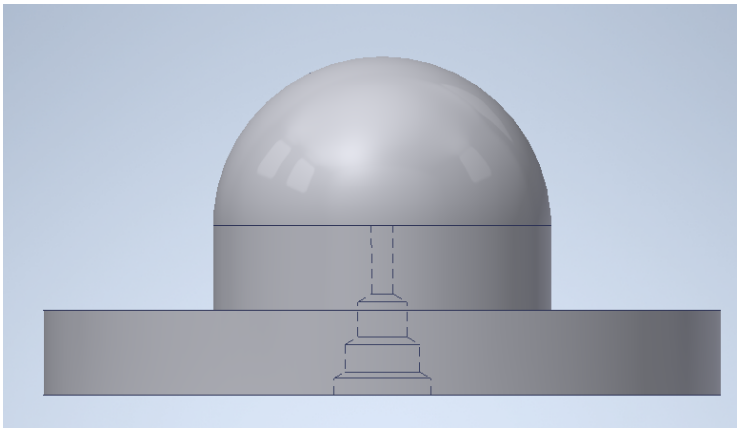

Figure 5.9: The PTFE diffuser tip, as installed in the capsule shown in figure 5.8. Into the dotted shape, the tip of the used fiber will be placed.

Table 5.2: Result of the gamma screen carried out at TUM. It only was possible for one isotope to be measured directly, while all other isotopes of relevance were only resulting in an upper limit. As a conclusion of this measurement, it can be stated that no breach of the radio purity limits of OSIRIS is expected with the use of the tested MASTERBOND EP30-4 epoxy.

Isotope	Activity [Bq]	Activity Error [Bq]	Upper Limit [Bq]
^{228}Ac	0	0	0.005331
^{212}Bi	0	0	0.028889
^{60}Co	0	0	0.0023478
^{137}Cs	0.0035135	0.0015797	-
^{40}K	0	0	0.015707
^{212}Pb	0	0	0.0049619
^{208}Tl	0	0	0.0020468

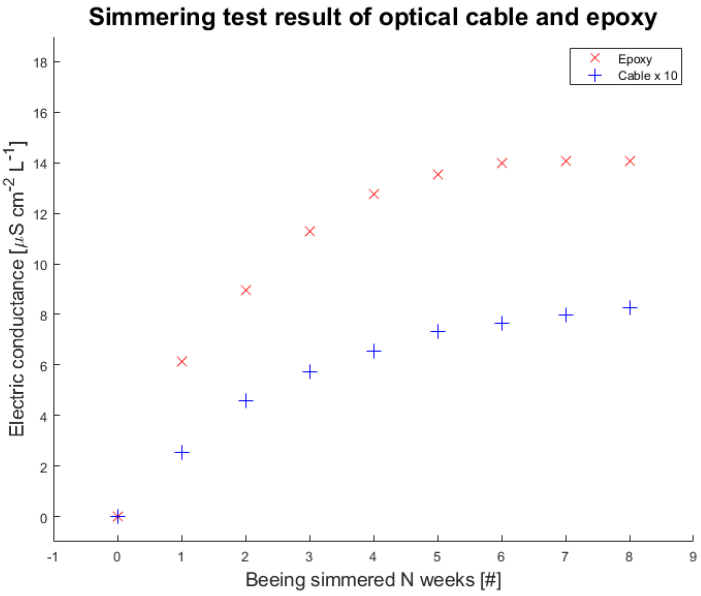

Figure 5.10: Results of the simmering test of the MASTERBOND EP30-4 and the stainless steel cladded optical fibers. Both parts were simmered in 80°C ultra pure water for eight weeks. Since the conductivity of the water can be used as a indicator for pollution of the ultra pure water, the conductivity was measured each week. This test showed that that the used material don't deteriorate in ultra pure water. Test was performed by Wilfried Depnering at the Johannes Gutenberg University, Mainz.

Another issue to consider during the design of the system was the feeding of the optical fibers into the individual capsules mounted on the PMT frame. On the one hand, the fibers need to be fixed to the frame to prevent any floating during the filling of OSIRIS. On the other hand, a feedthrough method needed to be used, that prevents any gas exchange between the detector and the hall. Since the same issue arose with PMT cabling, a shared solution was implemented.: A flange (diameter: 540 mm) is used, in which six M50 threadings are drilled. Into these threadings, special feedthroughs with an inner diameter of 35 mm (standard ISO 5211 F04) are installed (see figure 5.11). These feed-throughs provide easy use, air tightness and high connector density and are therefore used for all cable connections in and out of OSIRIS. To provide space for all fibers, sensor and GCU cables, two of these large flanges are used.

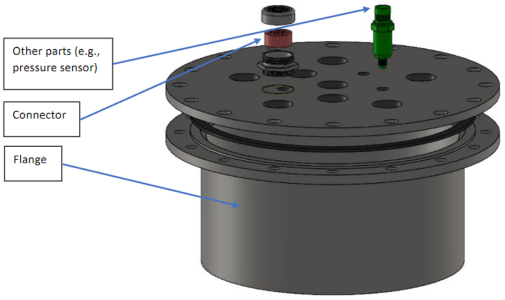

(a) The connecting flange (diameter: 540 mm) for the fibers of the LDS. All fibers are inserted with a special tool into the red sealing. Afterwards, the top cap is screwed onto the connector, which leads compresses the sealing and tightens it. In the case of the LCS only the large (M50) threadings are used, with the smaller ports being reserved for the inner sensor array of OSIRIS.

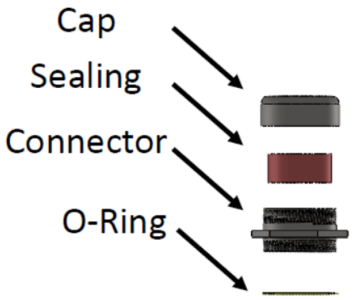

(b) Explosion view of the whole connector assembly. Each feedthrough has an outer M50 threading and an F04 feedthrough (35 mm) on the inside. Bottom O ring is used to guarantee tightness between steel flange and connector. Each connector allows up to fifteen fibers per connector.

Figure 5.11

5.2 Light shape characteristics of the Laser diffusers

In this section, the geometry of the emitted light field of the laser diffusers is discussed. Since these characteristics are important for determining the required number of diffusers as well as their positioning, the studies and optimizations outlined in this section were conducted.

5.2.1 Measurement setup and procedure

There are different possibilities to feed the ferrule of the optical fiber into the PTFE diffuser bulb, which led to a series of measurements of the resulting light field of the different configurations. To minimize the number of diffusers, the focus of the development was to create a light field that was both as wide and as homogeneous as possible. The measurement itself was performed by fixing the diffuser with the attached fiber on a stand with an attached camera that can be rotated 180° around the diffuser on one axis (see figure 5.12). Analyzing the resulting pictures, which were taken taken in steps of 10 degrees, led to the final verdict of the quality of the light field.

Hard and Software used for this measurement:

- Diffuser stand with rotational arm on top
- Prototype fiber (shorter version of the final fiber)
- Laser of the LDS (PiLas420, see section 5.1)
- Blackfly S USB3 camera
  - Sensor type: CMOS
  - Resolution: 720 x 540 pixels
  - Exposure time: 4 μs to 30 s
  - Absolute sensitivity threshold (y): 7.55
  - Gain range: 0 dB to 47 dB
  - Quantum Efficiency Blue: 49.86 @ 460 nm
- Spinnaker software development kit
- Matlab 2019

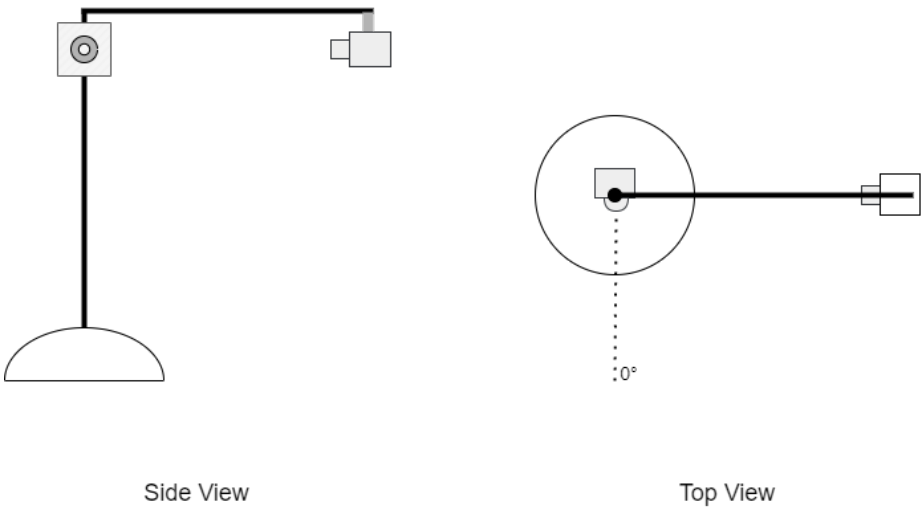

Figure 5.12: Schematic of the light field measuring setup. The camera arm can be rotated 180° around the stand, center of the camera lens is on the same height as the center of the diffuser bulb.

5.2.2 Optimization and results

The possibilities of guiding the light into the diffuser were limited by two parameters. On the one hand, the light field needs to be as homogeneous as possible, which leads to the necessity of a very symmetric scheme, whereas on the other hand, every possible light shaping from the light coupling out of the fiber needs to be diffused as much as possible. Considering these parameters, two designs have been produced with the tip of the ferrule located in the middle of the sealant brim and in the center of the diffuser hemisphere, respectively (see figure 5.13).
During the survey, it soon turned out that the first design is very unfavorable, since even by eye a very clear, bright "ring" around the center of the diffuser was visible, which was caused by the much shorter light paths to the edges of the diffuser bulb. But even though the PTFE parts of the diffuser would be encapsulated in the final design, the reflecting surface of the metal might increase the effect, which led to the choice of the second design option.
The black and white picture of the camera was converted into a bitmap in which each pixel is defined by its difference from black and therefore its brightness. To improve the sensitivity of the measurements, each run was background subtracted using a picture with the laser turned off[3]. As a last step, a cut was set in the light intensity to minimize blur and therefore only include pixels in the analysis from the actual diffuser in further analysis. An example of these

[3]Even though this measurement was performed in a darkroom, residual light from some of the DAQ electronics was unavoidable.

pictures used for the analysis can be found in figure 5.14.
By adding up all visible pixels that survived the cut, a total light intensity was created, which then has been standardized to the light intensity in 0° position. After taking measurements with additional rotations of the diffuser, an angular emission profile of the diffuser could be created (see figure 5.15). In the end, a slight asymmetrical behavior could be observed, the maximum total reduction of the light intensity in the relevant angular distribution of $\pm 70°$ is 8 %. The deviations from symmetry are presumably caused by expected tolerances during the manufacturing of the parts.

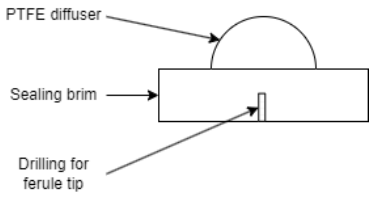

Scheme of the diffuser with the ferrule tip in the center of the sealing brim.

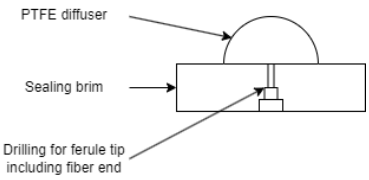

Scheme of the final diffuser with the ferrule tip in the center of the diffuser hemisphere.

Figure 5.13: The two different designs of the diffuser discussed in this section. The stepped shape of the right version is due to the shape of the end of the optical fiber, which in this case not only includes the ferrule itself, but also its fixation to fiber and cladding. The right-hand design was finally chosen.

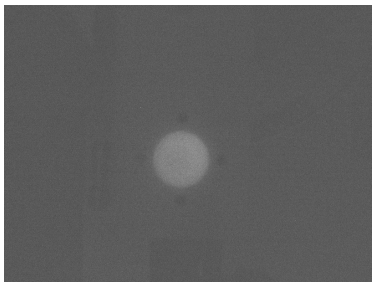

Example picture of a front view (0°). Picture is not background corrected, which is the reason for the slight shadows around the central diffuser that are caused by reflections by the ambiance on the stainless steel.

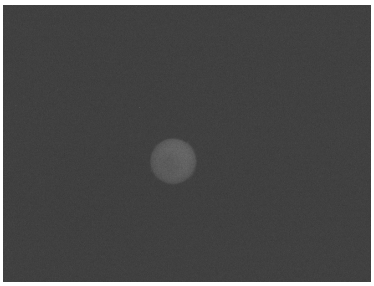

Picture of the front (0°) view with applied background reduction. No further background is visible.

Figure 5.14

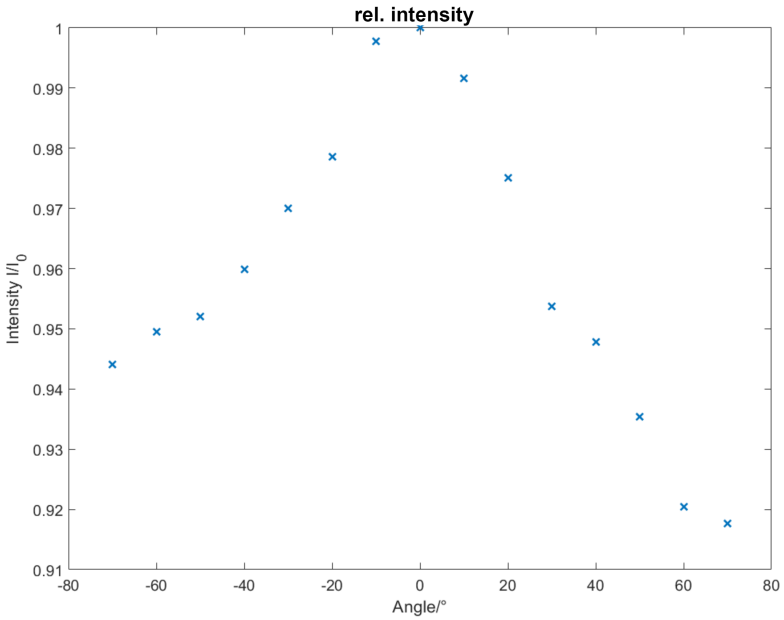

Figure 5.15: Measured relative angular light intensity distribution of the final diffuser design. For further simulation and reference, the angles between -70° and +70° were measured. Unsymmetrical behavior between left and right half is presumably due to tolerances in the production of the diffuser itself.

5.3 Diffuser positioning simulation

This section describes the steps to determine the number of diffusers necessary to perform a time and charge calibration of OSIRIS, as well as the optimization of the positioning of these diffusers within the detector.

5.3.1 OSIRIS simulation framework

During the development and planning phase of the OSIRIS detector, a complete simulation framework based on Geant4[124] was developed. It includes the geometry of the detector, electronics simulation modules, the relevant physics lists, as well as dedicated modes for the different use cases. Within this framework, a special mode for the calibration simulations was created which allows the distribution of point-like photon sources in the detector using a simple configuration file. To create a more realistic photon source, the angular distribution obtained in the measurements described in section 5.2 was used for the photon emission. In this mode, each diffuser is defined by two vectors: one giving the position and the other the direction of the normal vector, respectively. More information on the functionalities and capabilities of this framework can be found in [102].

5.3.2 Positioning simulations

As described above, the OSIRIS framework was used to optimize both the number and the positions of the diffusers. Four different groups of diffusers were identified (see also figures 5.16 and 5.17):

- **Top veto diffusers**:
  These diffusers are located on top of the PMT frame of OSIRIS, facing the PMTs of the top veto.
- **Bottom veto diffusers**:
  Diffusers point downwards to the bottom veto PMTs. They are located at the top edge of the PMT frame.
- **Diffusers above and below the AV**:
  These diffusers are mounted on the PMT holders of the PMTs above and bellow the AV pointing downward and upward, respectively, diagonally through the center of the AV.
- **PMT ring diffusers**:
  Mounted on the PMT ring, the light cones of these diffusers would point through the central axis of the AV to the PMTs on the other side of the ring.

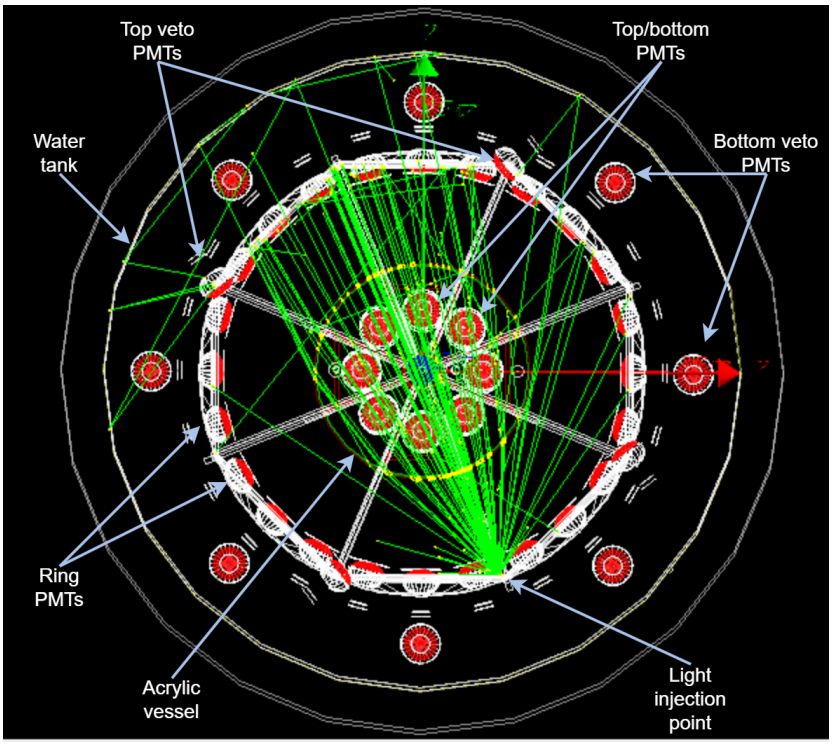

Figure 5.16: Simulated light cone (100 photons) of a diffuser mounted on the PMT ring. The lensing effect of the LS in the vessel is clearly visible. Photons leaking into the outer detector are caused by gaps between the sheets of the optical separation.

As a result, eight diffusers are placed outside of the optical separation on the PMT frame. Four of them facing a top veto PMT each and four located at the very edge of the frame pointing downwards to illuminate two bottom veto PMTs per diffuser (see figure 5.17).
As described in section 5.1.1, the laser slightly changes its timing profile when the light intensity is adjusted. Thus, it is favorable to operate the system with only one light intensity. To take this into account, the diffusers on top and below the AV are pointing through the center of the vessel to increase the area illuminated by these diffusers. Again, due to geometry, four diffusers per subgroup are used.
The last group of diffusers are the diffusers responsible for calibrating the ring PMTs. Even though the diffusers feature a quite large opening angle (see section 5.2), a lensing effect is expected due to the round shape of the vessel and the differences in the refractive index of water ($n = 1.34$ @ 20 °C)[125], acrylics ($n = 1.49$)[126] and LAB ($n = 1.466$)[127] (see figure 5.16).

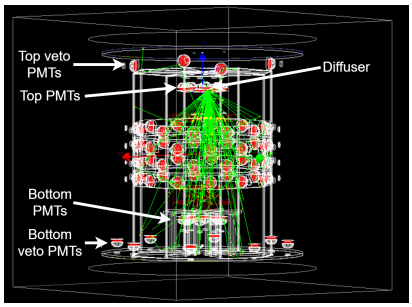

Light cone of a diffuser above the acrylic vessel, pointing from above the vessel to the PMTs below.

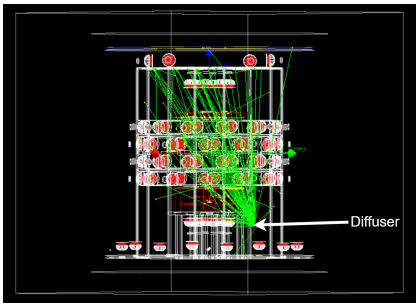

Light cone of a diffuser below the acrylic vessel, pointing from the bottom of the vessel to the PMTs above.

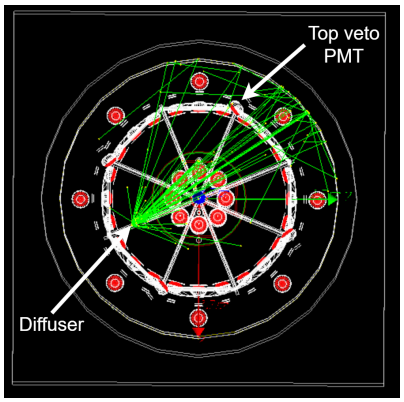

Light cone of a diffuser located in the top veto, pointing to the other side of the detector. To avoid excessive illumination, this diffuser is off-axis to the corresponding PMT.

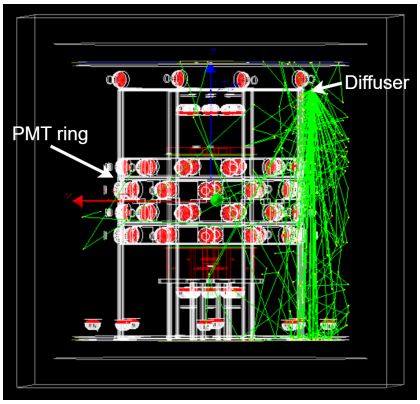

Light cone of a diffuser illuminating the bottom veto PMTs. The diffuser itself is mounted at the rim of the top PMT frame, pointing downward.

Figure 5.17: Simulated light cones (100 photons) of the different diffuser groups.

Given these positioning combinations of diffuser and PMT, the simulation was used to simulate one million photons per diffuser. The amount of photons seen by each PMT (see figure 5.20) was acquired in each run. To avoid contributions of reflected photons, a time cut depending on the time of flight of each PMT to the corresponding diffuser has been implemented.
The results of the simulation were evaluated by the condition, that each PMT should be illuminated within roughly a factor of two (which translates to 800-1800 detected photons in figure 5.18). In this way, the illumination of the detector for a given set of diffuser positions could be displayed and referenced against each other. The final result of this survey was the configuration, that uses the least amount of diffusers whilst having the least differences in illumination (see figure 5.18). An example of a failed simulation can be found in figure 5.19. In this case, the directions of the diffusers above and below the acrylic vessel were not correct.

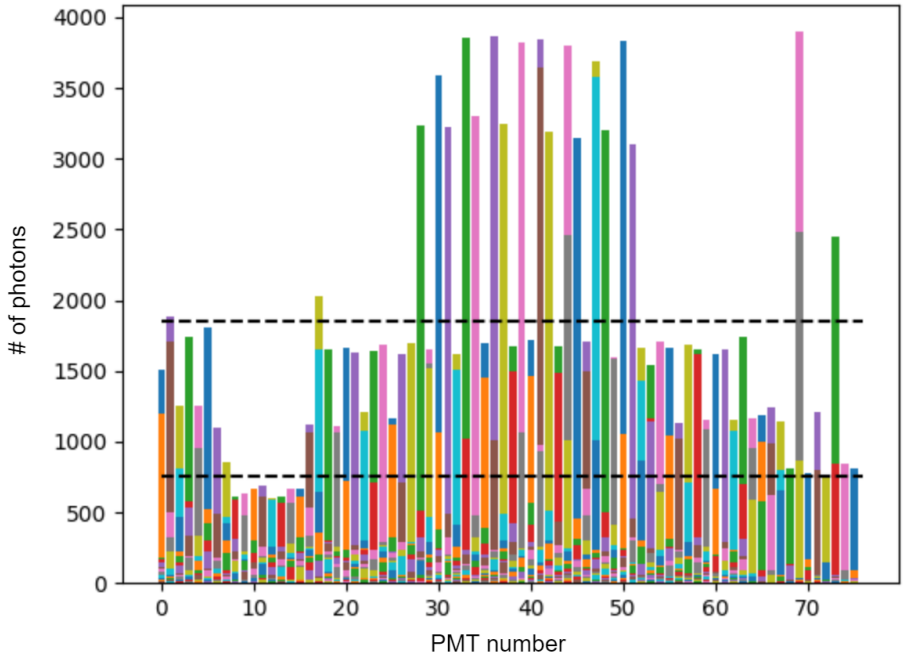

Figure 5.18: Result of the simulation. For each PMT number (x-axis) a superposition of all diffusers seen by that PMT is displayed. Each PMT should have at least one diffuser within the given illumination limit of a factor of two (dashed lines). Y-axis is the number of photons seen by a given PMT.

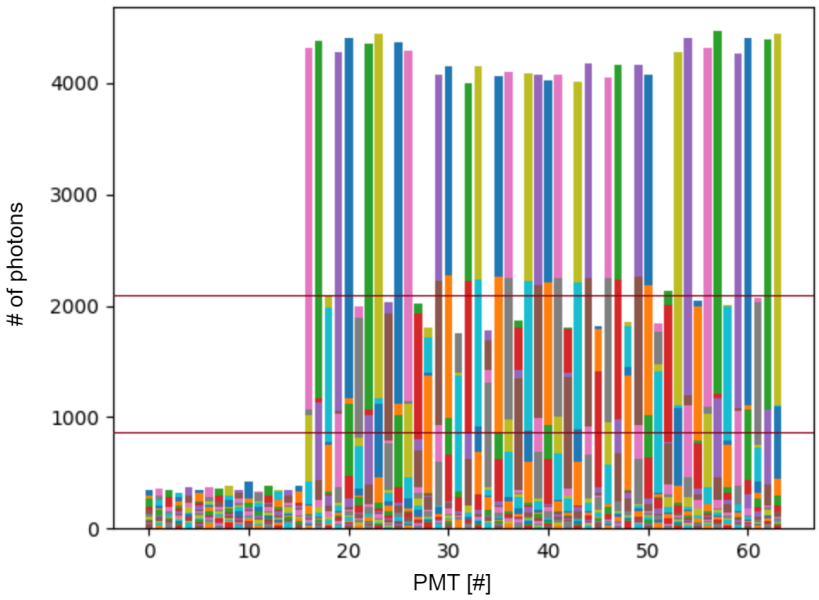

Figure 5.19: Result of a failed simulation. In this case, the directions of the diffusers above and below the acrylic vessel have been chosen wrongly.

Even though some of the PMTs see more light than the upper limit would allow, another diffuser is available that delivers an illumination in the desired level. Therefore, a specific mapping between a specific PMT and the diffuser that is bound to calibrate that PMT is necessary (see chapter 6.4).
During the installation of the system in spring 2023, it turned out, that the exact positions used in the simulation could not be used, since some changes in the basic architecture were necessary that have been introduced after this analysis. This led to the use of two different light intensities (see chapter 6.3), which also provides the opportunity to compensate for the slight under-illumination of PMTs 8-15.

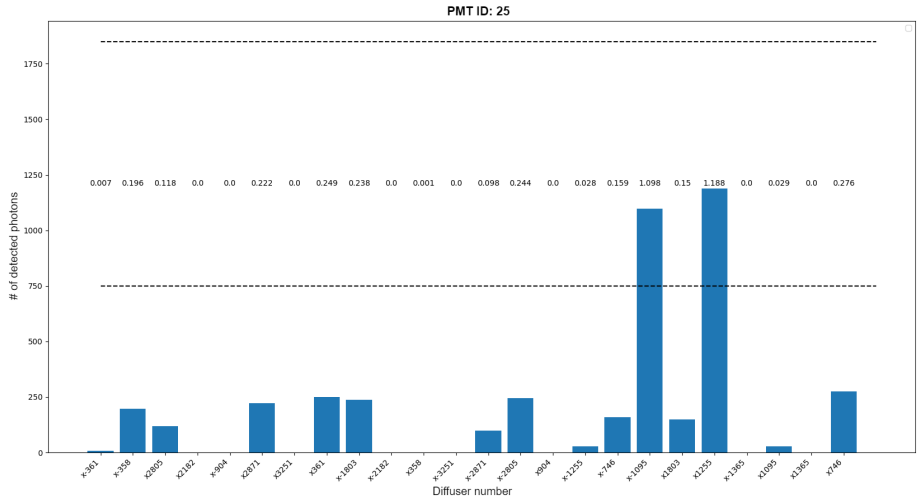

Example output of the diffusers seen by a single PMT of the inner detector. Numbers in the middle of the plot are the amount of photons detected of each diffuser, divided by 1000.

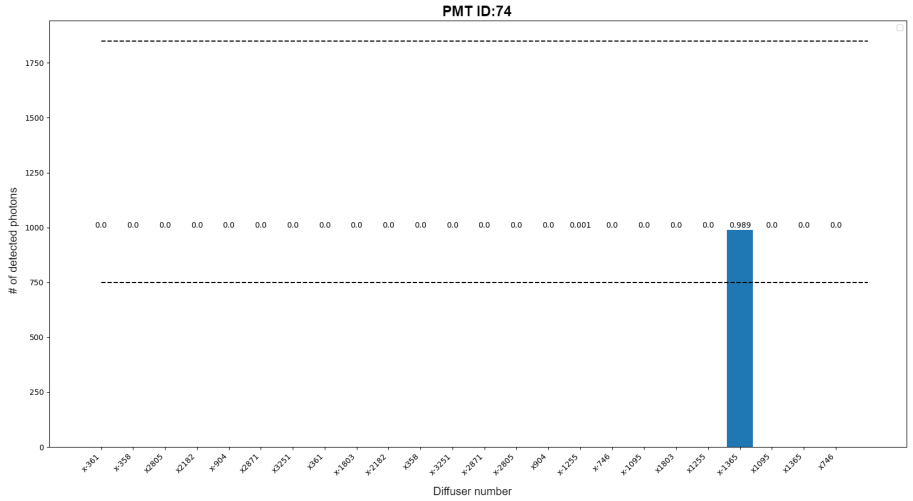

Example output of the diffusers seen by a single PMT of the veto. Numbers in the middle of the plot are the amount of photons detected of each diffuser, divided by 1000.

Figure 5.20: Outputs of two exemplary PMT channels of the simulation of the diffuser position. In the left plot, the several diffusers that can be seen by a PMT of the inner array are display. Given the geometrical challenges, a few of the inner PMTs see more than one diffuser. The right plot shows the result of a PMT in the veto, that can only be seen by a single diffuser.
The dashed lines show the desired illumination limits, x-axis shows the coded names of the diffusers, y-axis the number of hits detected. One million photons have been simulated per diffuser.

5.4 Control software of the laser calibration system

In this section, the control software of the laser calibration system will be discussed which is written in LabVIEW and EPICS. LabVIEW is a visual programming language designed for the use in scientific control and data acquisition systems [128]. It is developed by National Instruments Corporation. The version used in this work is LabVIEW2015 service pack 1.
EPICS, the Experimental Physics and Industrial Control System [129], is a set of software tools used to create distributed control systems. It was initially developed by the Los Alamos National Laboratory in 1989, but is now maintained by the community. As an open source tool, EPICS features a lot of additional tools that are not necessarily available in the basic installation. For this work EPICS was used in the versions 3.16 and 7, additional EPICS tools used were Control Systems Studio Phoebus (CSS), the EPICS State Notation Language (SNL, see 5.4.2) and the EPICS Archiver Appliance (see section 7.3). The reason why EPICS was chosen as a Slow Control (SC) and communications tool is its ability to broadcast a value into an EPICS “cloud" hosted on a network. The process variables (PVs) of an EPICS network, which contain the actual variables are normally controlled by an input-output controller (IOC)[4] which is also able to perform calculations, flagging and other minor software tasks. Operating systems are Windows 10 and Debian 11.8 (bullseye).

5.4.1 Hardware Control

The basic hardware control of the laser calibration system is written in LabVIEW using a plain RS232 interface and the NI-VISA libraries. Higher layers that include integration into run- and slow control are written in EPICS/EPICS SNL. A list of available serial commands can be found in [122]. All relevant I/O variables of the system are broadcast into EPICS using the LabVIEW shared variables engine, which provides direct PV broadcast without the necessity to use a dedicated EPICS installation. The control software of the laser calibration system is hosted on the common calibration computer, running on Windows 10. In figure 5.21 a sequence diagram of the control software can be found, table 5.3 shows the EPICS process variables of the respective I/O variables of the system.

[4]Some third-party software tools, like LabVIEW, come with an integrated EPICS solution, which makes the actual IOC inaccessible to the user.

Table 5.3: List of PVs broadcast to EPICS by the LabVIEW software of the laser calibration system. Each variable is preceded by the EPICS LDS preamble: "JUNO:OSIRIS:LDS:". All listed PVs comply with the official JUNO PV naming scheme.

PV	Data type	Description	Access Type
do_channel_to_set	string	Number of the channel to be set	write
do_laser_off	Boolean	Turn laser off	write
do_laser_on	Boolean	Turn laser on	write
do_set_channel	Boolean	Set the channel in do_channel_to_set	write
do_tuning_to_set	string	Tuning value to be set	write
do_set_tuning	Boolean	Set the tuning value in do_tuning_to_set	write
set_channel_num	int	Number of the channel that was actually set	read
emergency_stop	Boolean	Stop operation as fast as possible	write
error_message	string	Error message reported by LabVIEW	read
error_occurred	Boolean	Error flag	read
laser_on	Boolean	Laser status flag	read
set_channel	string	Channel currently set	read
tuning	double	Current tuning	read

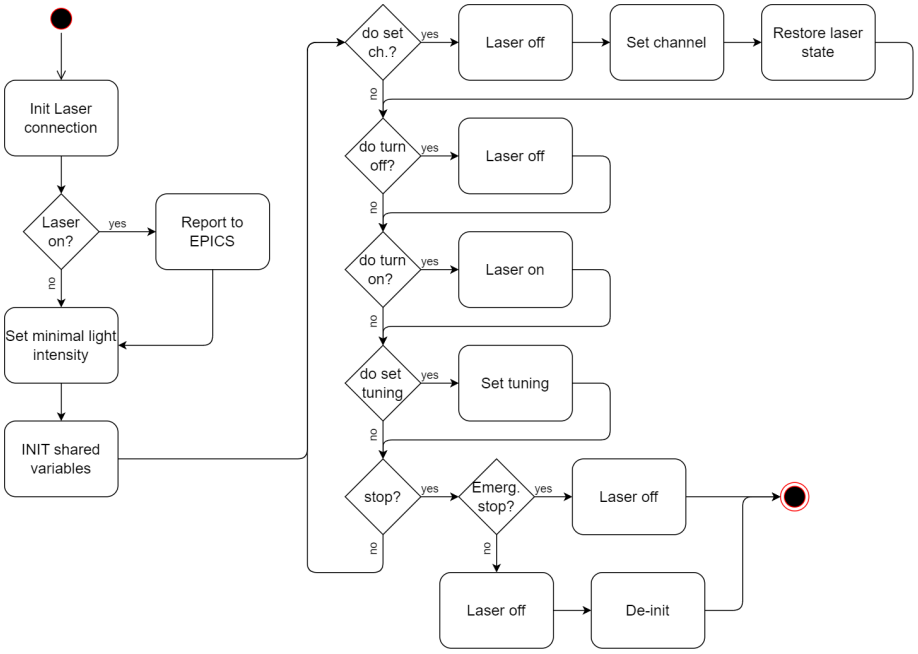

Figure 5.21: Sequence diagram of the basic hardware control software. The lower control levels, as well as the variable binding into the LabVIEW shared variables engine, are not included. Additionally, several fail-safes have been integrated, including emergency shutdown sequences, variable loopbacks and hardware connection tests.

5.4.2 State machine of the laser calibration system

The state notation language (SNL) of EPICS provides a simple but efficient way to create sequenced operation within an EPICS network. It can be used to create state machines without the necessity of controlling scheduling, hardware or i/o streams. Using state transitions that can be triggered by a variety of EPICS inputs (flags, PVs, time, etc.), complex operating sequences of an EPICS system can be implemented. In this work, the SNL is used to create a state machine that is responsible for the actual calibration sequence.
Above the basic hardware control layer described in section 5.4.1, the state machine that controls the actual calibration scheme has been introduced. It is written in the (SNL) of EPICS and defines the individual states of the hardware during the whole calibration operation. This includes an adaptable sequence of the diffusers, the switching logic between the different channels[5] as well as an error handler for both, hardware and EPICS based errors. A sequence diagram of a standard calibration run of the laser calibration system can be seen in figure 5.22. The actual logging of the states of the LCS is performed by the EPICS archiver appliance, see chapter 7.3.
The third part of the software is the integration of the state machine into the slow control. This slow control (SC) is implemented using the EPICS Control System Studio (CSS) Phoebus (see figure 7.10 and section 7.4.2). It is designed as an "intelligent" GUI which means, that it doesn't only create a graphic control of the I/O variables, but also contains logic which triggers different behavior under certain circumstances automatically (e.g., during error state, some functionalities are disabled, etc.). There are two different levels of access: standard (read only) and expert mode which is password protected. The password protected expert mode is to be used under supervision by the system expert only. A more detailed look at most of the GUIs written in the scope of this work and are used in OSIRIS can be found in chapter 7.4.

[5]The condition to switch to the next channel is the amount of desired triggers per channel in the standard mode of the state machine. An additional option to switch the channel by hand is available.

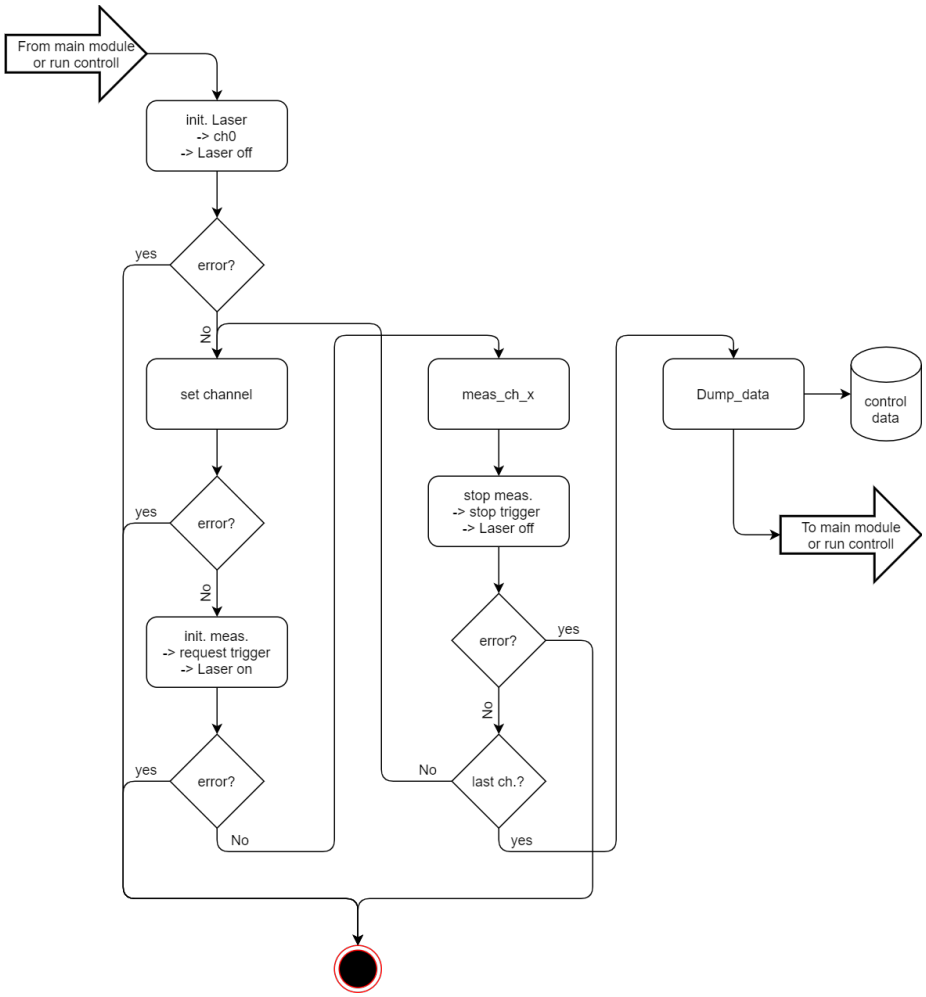

Figure 5.22: Sequence diagram of the core of the state machine of a standard calibration run. The complete sequence is triggered by the general run control. After an initialization of the whole hardware, a loop is entered which contains the setting of a new channel, the starting and stopping of a measurement and several error handlers. It ends after the last channel has been finished by dumping information about the run to EPICS. The very last step is returning to the main run control state machine

5.5 Calibration mode of the OSIRIS DAQ

There are several differences in the DAQ of OSIRIS between "standard" and calibration runs [102]. This includes for example hardware control (e.g., external trigger for the light sources), run control (e.g., state machine for operation of the LCS, see also chapter 5.4) and root sorter analysis[6]. There are different approaches/modes of the DAQ that can be used:

- **External trigger calibration mode**:
  In this mode, the system is configured to be triggered by external triggers only. A signal generator is used to create three synced trigger signals: one is used to trigger the actual DAQ system, one is used to trigger the optical systems (either LCS or ACU) and one is digitized to be used as a reference during analysis of the data (see chapter 6.4.2). In this mode, the run control uses special settings which use the individual state machines necessary to control the two optical systems. However, due to the significant hardware differences between the two optical systems, their state machines also differ considerably. Due to switching frequency limitations of the LED driver, the LED uses a maximum external trigger frequency of 2.5 kHz, whereas the LCS can be triggered with up to 10 kHz. In this mode, the root sorter will calculate the desired calibration values semi-online, since additional hardware bound information is necessary. In the case of the ACU LED this includes a Monte-Carlo based correction for the fact that the calibration axis of the sources of the ACU is not central in the detector but off-axis. The corrections applied here create the possibility to use the data as if the LED was lowered in the central axis of the acrylic vessel. In the case of the LCS, this includes the differences in light intensity of each channel of the LDS as described in section 5.6.2.

- **Majority trigger mode**:
  In this mode, the system only listens to the trigger created by the currently set majority level. Depending on the trigger window and majority level [7] a trigger is created and the event is read out. Different majority levels for inner and outer detector are available. Since no external information is required, the root sorter is doing a basic online analysis to create feedback to the user. In this mode, two different readout possibilities are available. On the one hand, the complete waveforms can be recorded and stored for further analysis. On the other hand, the reduced JUNO scheme of charge and time values (T-Q pairs) can be used. In this case, the amount of created data is significantly reduced since a pre-calculation is made in the FPGA of the GCUs. In this case, only pairs of charge and first-hit time stamp per event are sent to the DAQ system.

[6] Not all values that need to be calculated during a calibration run are also required in a standard run (e.g., gains, see also chapter 6

[7] As of the time of creation of this work, the trigger window used is 64 ns and the majority level is 20.

- **Hybrid mode**:
  This is the preferred operating mode of OSIRIS, as it avoids the need to change the event builder's operation mode and restart the entire system.[8]. In this mode, both kinds of triggers can be used, only limited by bandwidth of the OSIRIS computational system. Due to the comparably low trigger rates of the optical systems, the normal majority trigger still can be used. However, due to activity of the radioactive sources of the ACU, it is not recommended to use this mode in the case of this source.

[8]The situation described here is the situation at the time of writing of this thesis. Especially the hybrid mode is subject to changes.

5.6 Calibration of the light distribution system

In this subsection, the calibration of the LDS performed in 2020 in Tübingen will be discussed. After the calibration, the system was packed and sent to the JUNO laboratory in Kaiping, Jiangmen City, P.R. China.

5.6.1 Calibration setup of Tübingen

Since differences are expected in the two different legs of the optical cascade (see figure 5.3), a characterization and hence a calibration of the light distribution system needs to be performed. Examples of these behavioral differences can be seen in figure 5.28. To ensure comparability to the final setup of the LDS in OSIRIS, the calibration setup follows the final setup as close as possible. For example, the same trigger distribution and signal generator was used. However, due to the hardware development status of the GCUs that will be used as a digitization device in the final setup, a commercial oscilloscope (R&S RTO2064) was used instead of a FADC. A scheme of the complete calibration setup as installed in Tübingen can be found in figure 5.23.
The parameters of interest are on the one hand the timing differences between the relative LDS channels and on the other hand the light intensities of all channels. These parameters might differ due to tolerances in the production of the parts of the opto-mechanic chain of the LDS.
For each channel, at least one million triggers have been taken [9]. Furthermore, to reduce the required time for data acquisition, the light intensity used for this calibration was increased from 0.01 p.e. to a level of 0.1 p.e..
To reduce introduced backgrounds and cross-talk, several additional precautions have been made. Firstly, all (signal) carrying cables have been measured in length very precisely and the acquired run times corrected, accordingly. Secondly, the standard OSIRIS PMT has been exchanged by a fast HZC 9112B PMT, which features a TTS ($1\,\sigma$) of only 100 ps. In addition, the enclosure of the PMT is completely light tight, including all feedthroughs for high voltage, etc.

[9] To investigate possible large scale statistic effects, 3kk triggers were taken for channels 1-3. However, none have been found.

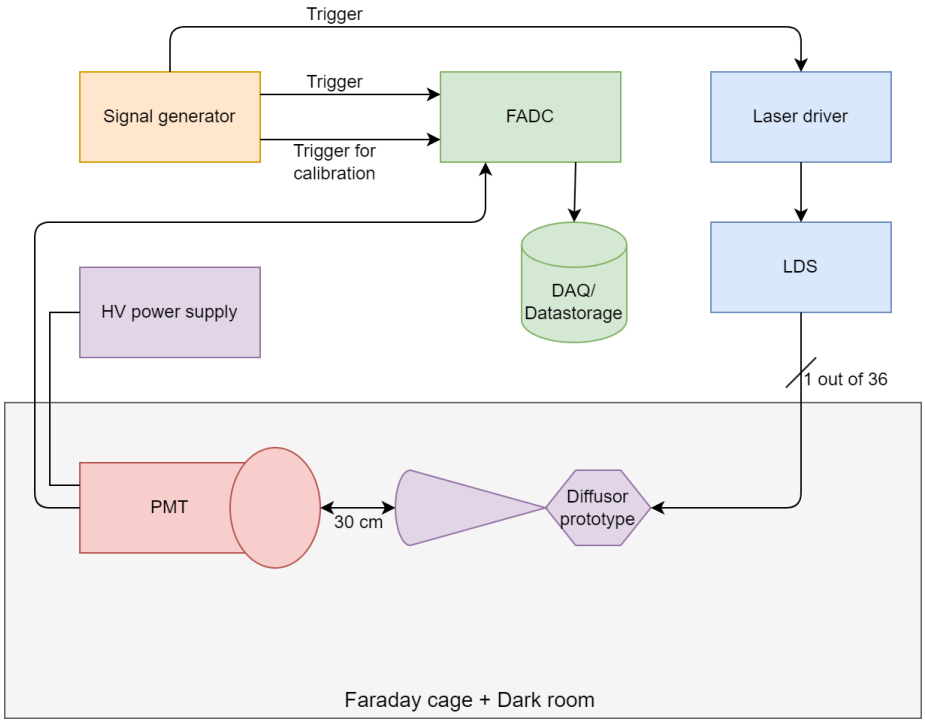

Figure 5.23: Scheme of the calibration setup installed in Tübingen. A signal generator (Agilent 33512B) is used to create three synced trigger signals, following the OSIRIS trigger scheme. The first trigger signal is used to trigger the oscilloscope (R&S RTO2064), the second to trigger the laser (that is later used in OSIRIS) and the third to be acquired by the oscilloscope to perform the actual timing calibration. Each LDS channel is measured sequentially using a fast (TTS ($1\,\sigma$) of 100 ps) HZC 9112B PMT. Light injection into the light tight enclosure is done by a prototype of the final diffuser capsules.

5.6.2 Calibration results

Timing calibration

To investigate possible timing jitter of each LDS channel, the constant fraction (50%) time of both, PMT pulse and trigger signal was evaluated for every event which contains a PMT pulse. The difference between these two was then plotted into a histogram and fitted using a Gaussian function (see figure 5.28), using approximately the first two thirds of the peak (which is due to the slightly asymmetry of peak). The histograms of the resulting means and σ-widths of this fit are then used for further analysis. The distribution of the means of the time differences of all measured channels shows two very sharp peaks (see figure 5.29), average transit times and hence cable/fiber lengths are comparable. The same is true for the comparison of the sigma of the fits (see figure 5.30). However, these sigma are of higher relevance since they describe the transit time spread of each channel. A large sigma would hint to high TTS contribution and hence reduce the usability of the LDS.
Investigating the results of the fit per channel, provides additional information about errors and spread (see figures 5.31 and 5.32). Even though the two groupings are clearly visible, the second group of double channels feature larger errors and spread. Larger deviations of the second group (double channels) are expected, since in this case, a larger number of optical parts is used, featuring an individual tolerance each.
The results are very promising: Taking the largest result of approximately 150 ps of the measurements of the widths[10] and the TTS of the PMT of 100 ps [122] into account, a total, additional jitter of the LDS of 50 ps can be calculated. Considering the expected TTS of the PMTs of OSIRIS (see chapter 3.6.2) the system is qualified to perform a timing calibration of the PMTs of OSIRIS.

Calibration of the light intensity

The reason to investigate the possible differences of the light intensity of each channel, is also given by the tolerances of the hand-made 50:50 fiber splitters. Due to the testing sheets of the splitters which are provided by the vendor, a deviation in the light intensities of up to 5 % is expected[11]. To measure this differences, the light intensity of the laser is set to 0.1 p.e., using one of the channels of the LDS as a reference. With the use of a standard, external triggered measurement of each channel, the number of waveforms containing a pulse (defined as signal larger then 2.5 mV) is divided by the total number of triggers. Yet again, a grouping of the two different kinds of channels is expected, since the single channel branch is only influenced by a single splitter, whilst the other branch features a splitter at each of the output ports of the fiber switch. The results of this measurement can be found in figures 5.33 and 5.34.

[10] The TTS is defined as the $1\,\sigma$ width of the transit time distribution
[11] same is true for the outputs of the 12-channel optical switches.

There are several possibilities to transfer these results into calibration constants that can be used by the root sorter analysis. On the one hand, the results can be referenced to the mean of the distribution, on the other hand, one channel can be used as a reference. In this work, channel 23 is used as a reference, since this channel was randomly chosen for the setting of the light intensity which is why it is closest to the initially introduced value of 0.1p.e. A benefit of choosing a channel as a reference is that the reference channel can easily be remeasured, if necessary, which provides possibility to check the LDS performance.
In figures 5.35 and 5.36 the results of this measurement can be seen in both, absolute and percentage values. These values will be provided to the analysis chain of OSIRIS via an EPICS IOC, a list of the final transmitted values can be found in the appendix, section E.
To conclude, it can be state that by using channel 23 to set the light intensity in the OSIRIS detector and by using the correction values calculated in this section, a charge calibration of the OSIRIS detector is possible without relevant light intensity deviations caused by the light distribution system.

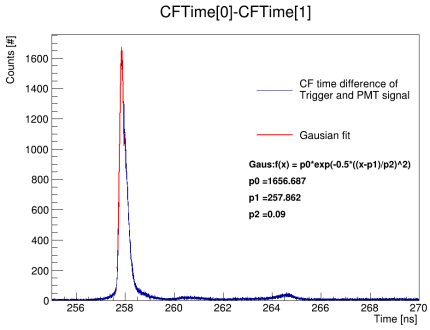

Timing histogram of single ch 2.

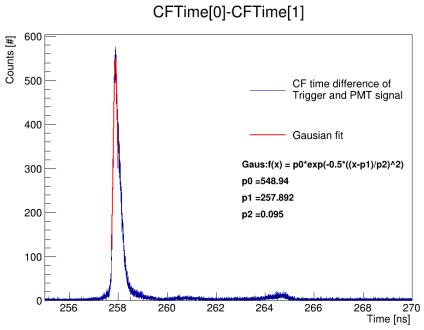

Timing histogram of single ch 11.

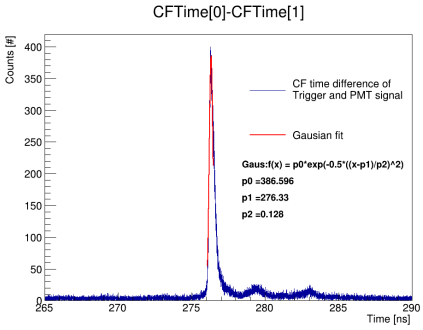

Timing histogram of double ch 23.

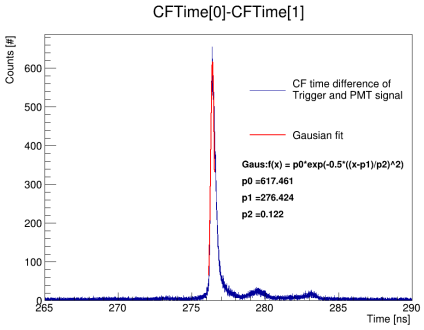

Timing histogram of double ch 32.

Figure 5.28: Examples of the timing calibration measurements. Differences in the time offset between the two different legs of the opto-mechanical cascade of the LDS are observed as expected. The channels of the single channel group are closer to the beginning of the acquisition frame and show fewer reflections. These reflections are expected due to a larger numbers of fiber connectors in the case of the double channel group. The time differences of the peaks are also expected due to differences in the length of the fibers of the individual branches of the cascade. Results of the Gaussian fits of all channels of one group are comparable.

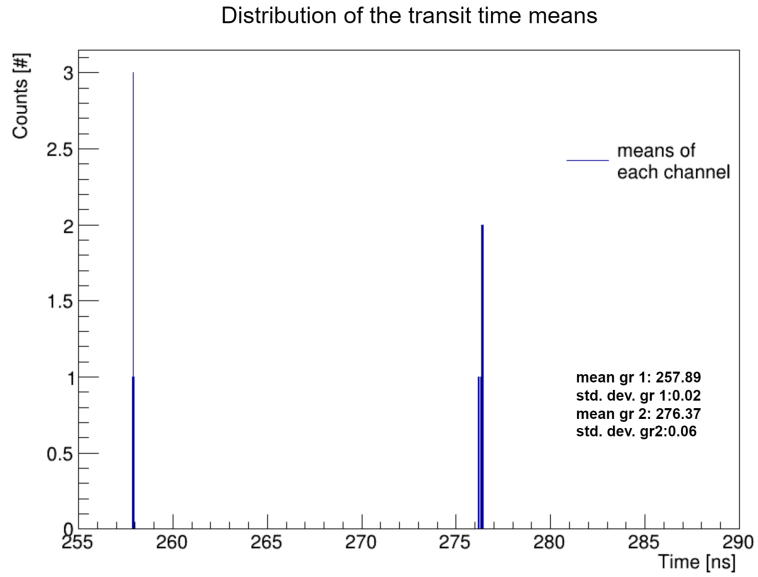

Figure 5.29: The distribution of the means of the transit times of all measured channels of the LDS. The distinct time difference of the two groups is clearly visible.

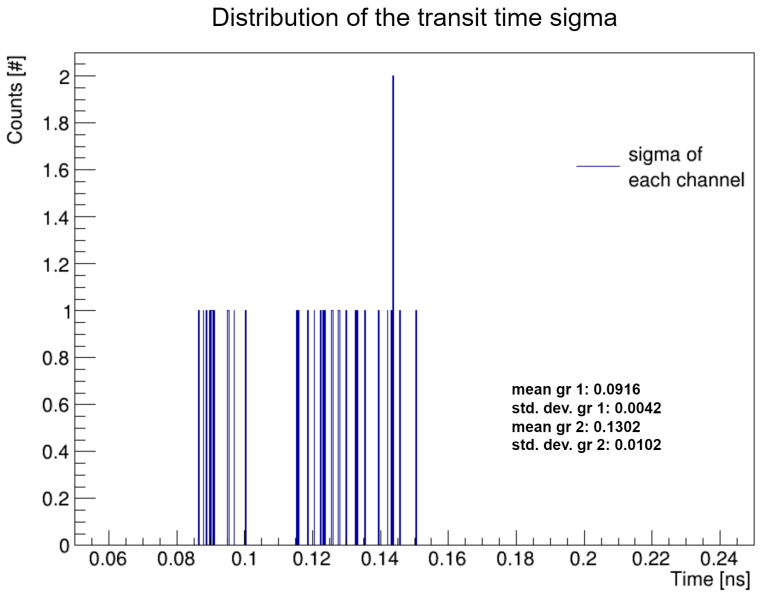

Figure 5.30: The distribution of the sigma of the transit times of all measured channels of the LDS. Again, the two groups of the LDS are clearly visible.

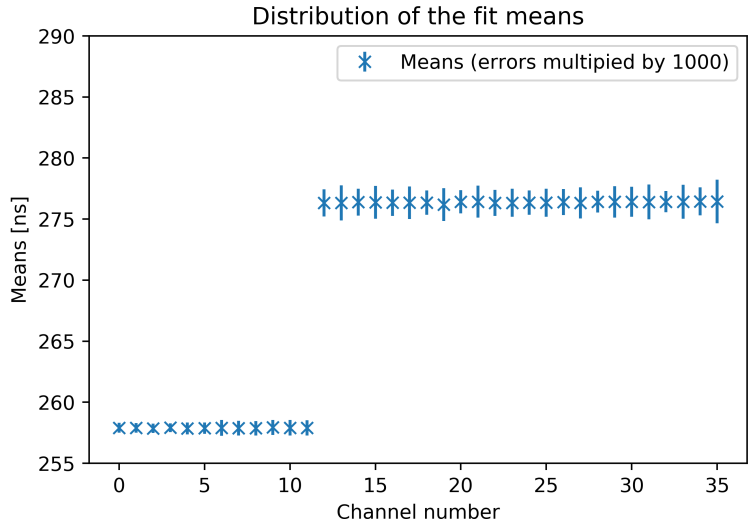

Figure 5.31: Time differences between trigger and PMT signal of the measured channels. The two different channel types can seen, larger errors can be observed for the double channels.

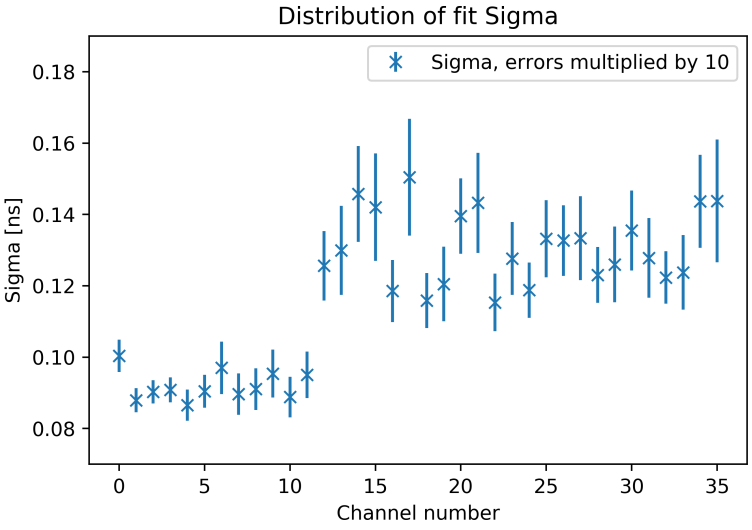

Figure 5.32: Sigma of the differences between trigger and PMT signal per channel. Again, the two types of channels and increased fit errors in the double channels can be seen.

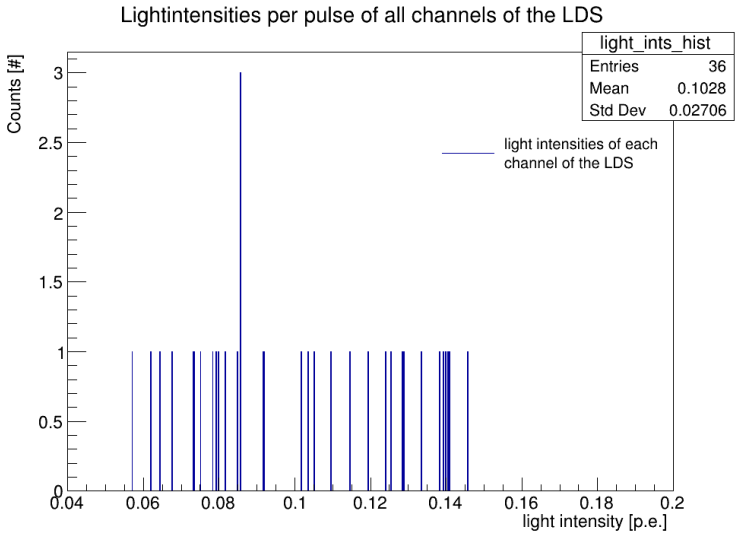

Figure 5.33: Distributions of the measured light intensities per channel with an initial light intensity of 0.1 p.e.. The resulting mean of 0.1028 p.e. is very close to the initially set light intensity.

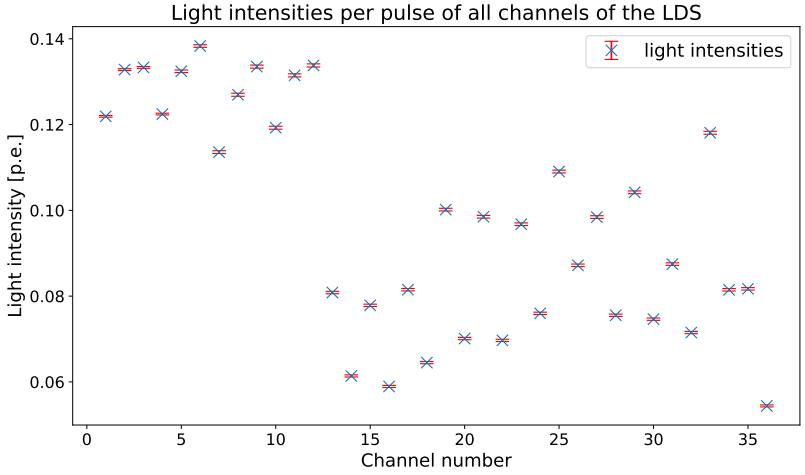

Figure 5.34: Measured light intensities of the LDS channels in respect to the channel number. Again, a distinct grouping can be seen, which is due to the differences of the two branches of the opto-mechanic cascade (see figure 5.3).

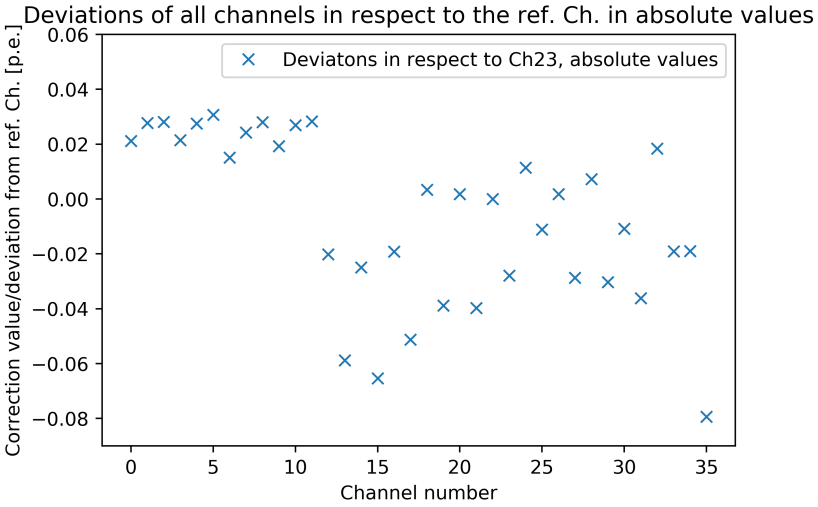

Figure 5.35: Correction values of the light intensity of all channels of the LDS providing the difference of the light output of each channel in respect to reference channel 23. All values are given in p.e., a complete table of the values can be found in appendix section E.

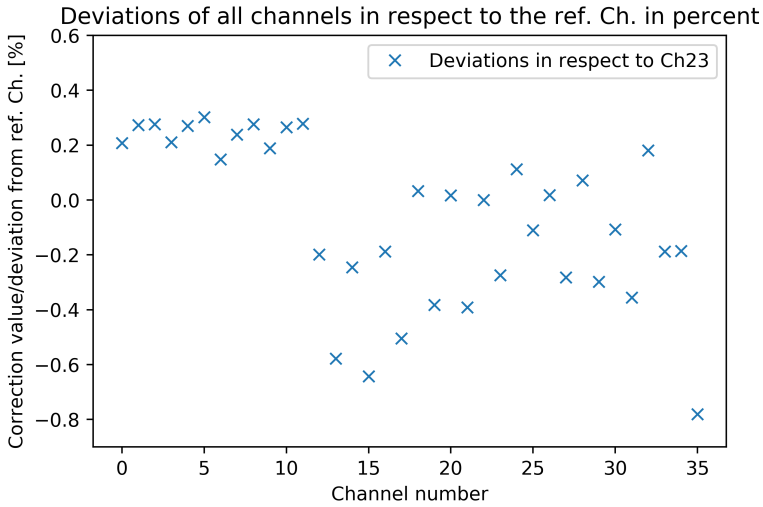

Figure 5.36: Correction values of the light intensity of all channels of the LDS providing the difference of the light output of each channel in respect to reference channel 23. All values are given in the decimal representation of per cent.

Chapter 6

The Commissioning of the LCS

"Testing is simply an artistic indulgence now."
-GLaDOS

from "Portal 2", 2011

This chapter will describe the steps taken during the commissioning of OSIRIS and present some results of the commissioning measurements, which have been carried out between Autumn 2022 and Spring 2024, onsite at the JUNO laboratory in Kaiping, Jiangmen. In total, for the installation and the commissioning of the systems discussed here, a total visit of approximately seven months was necessary. During this time, all parts of the LCS have been installed, several preparation tasks for the OSIRIS detector have been performed (support in adaption of the PMT holders from iPMT to LPMT, setup of the local Ethernet/subnet, setup of all computers, creation of control software for the environmental control of the electronics cabinet and uninterruptible power supplies, cleaning and purity surveys of the acrylic vessel, testing and adaption of the radon counter of OSIRIS, grounding survey and analysis, maintenance and testing of the systems) as well as first commissioning measurements have been performed.
This chapter will describe the different measurement runs that have been performed in air (August and November, 2023), water (March 2024) and LS (March 2024 and May 2024) and show data taken during these runs. In the last part of this chapter, PMT performance parameters calculated using the March 2024 data are compared with the values acquired during the PMT testing phase of

JUNO [92] and with the predictions from simulations used in the development of the LCS.

6.1 Air run of OSIRIS

As a first step of the commissioning, LCS system tests and transit time measurements have been performed. During these tests, the AV was filled with nitrogen while the steel tank was filled with air. These tests have proven very valuable for the first performance estimations of the system. Deviations are expected due to optical differences (e.g., in refractive indices of the materials of the system, reduced transparency of the PMMA parts due to the surface treatment of the acrylics, see figure 6.1), differences in hardware performance (e.g., temperatures of the in-detector electronics which are developed to operate in liquid which could force the CPUs of the GCUs to throttle), different shielding effects of electrical noise as well as the absence of potential hydrodynamic effects of the liquids in both the vessel and the veto tank.

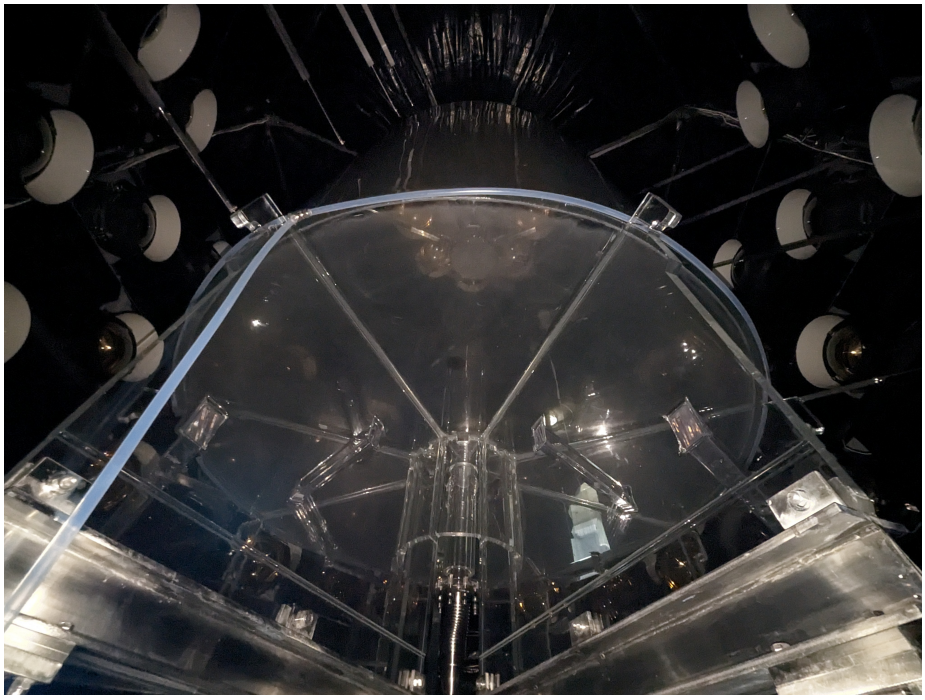

Figure 6.1: View up from below the acrylic vessel during the in-detector installations in August 2023 just before the closing of the detector. Visible is the opaque bottom of the acrylic vessel.

6.1.1 Operational test of the LCS

The first air run was taken to confirm the correct operation of the various parts of the LCS[1]. For this test, one million triggers per diffuser have been acquired, and the light intensity was set to an intensity in the range of 1 p.e.. During this test, a focus was placed on the electronic chain of the LCS as well as the functionality of the opto-mechanic cascade of the LDS. By sequentially testing each LDS channel for light output using a laser power meter (see exemplary plot 6.3), it was found that one channel was damaged, only showing approximately 10 % of the expected light output. A possible cause for this damage is vibrations that occur during the shipment by ship from Germany to China. All other channels of the LDS have been found to be working as expected.
After a subsequent test of the control software, the system was declared to be operable as intended and the optical fibers of the diffusers inside the water volume of OSIRIS were connected to the LDS. Due to the complex installation routine of the instrumentation inside the water tank, it was not possible to precisely identify the position and the direction of the diffusers. However, each diffuser (cable) was categorized into several diffuser groups (PMT ring, above the vessel, below the vessel, top and bottom veto) and connected to the LDS accordingly. For a detailed explanation of the different diffuser types see section 5, a picture of the LDS with all used ports equipped with an optical fiber can be found in figure 6.2.

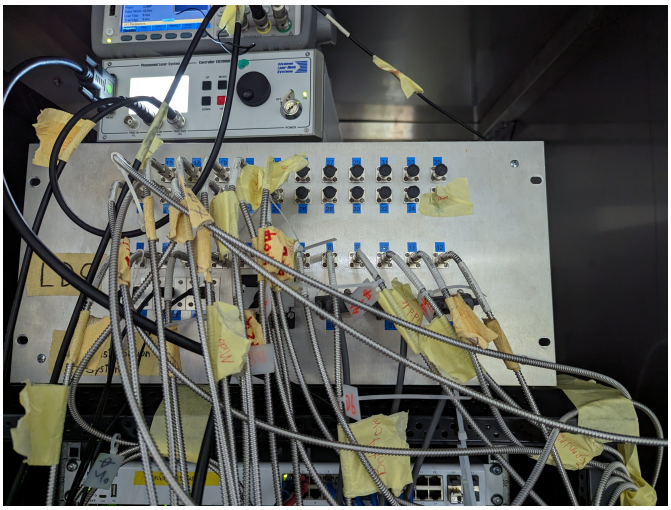

Figure 6.2: The LDS of OSIRIS fully equipped with all 24 optical fibers. This picture represents the situation in August 2023. In March 2024, two fibers were switched to other channels due to damage to the threading of the fiber ports.

[1]Since the optical switches of the LDS were found to be broken due to high humidity in December 2022 and consequently sent to the manufacturer for repair, this test, performed after re-installation of the switches, was of high priority.

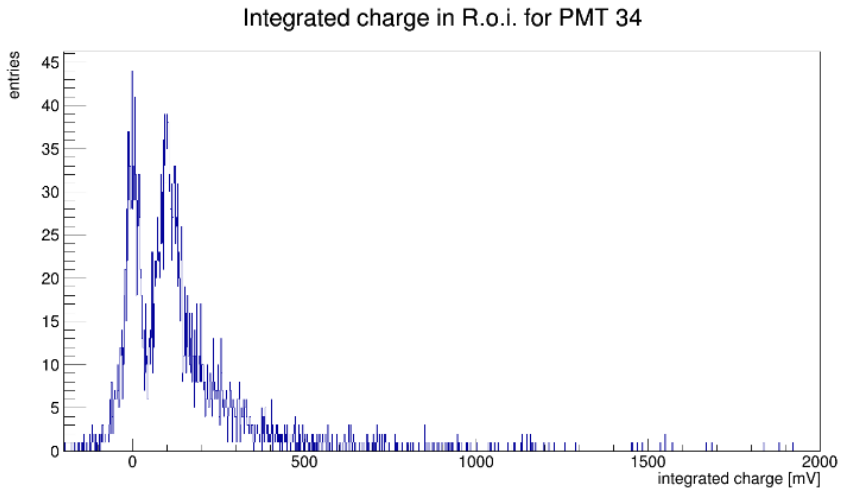

Figure 6.3: Exemplary charge histogram as taken during the air run tests. The histograms were obtained as-is from the rootsorter and used for the estimation of the light intensity of each channel. No further analysis has been performed with this data.

6.1.2 Transit time measurements of the PMTs

The air run provided a good opportunity to test the timing characteristics of the OSIRIS detector. In the measurement, the LCS was set to a light intensity higher than 1 p.e. to reduce the influence of the substructure of the transit time spread, which was observed during the testing and characterizing of the PMTs for JUNO. This substructure shows distinct, additional peaks on top of a broad Gaussian, which is very hard to model (see figure 6.4). The increased light intensity of the system will mask the substructure, since the distribution will include multi p.e. events, which will lead to a Gaussian distribution (see figures 6.5 and 6.6).

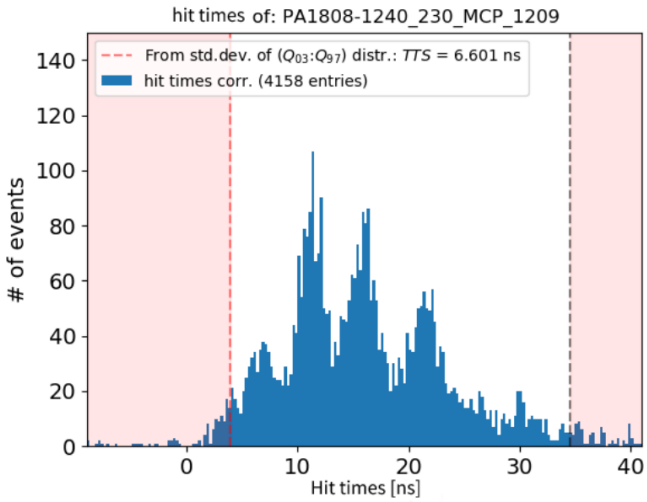

Figure 6.4: The substructure of the TTS as observed in the PMT testing containers of JUNO. This substructure was measured with the use of a light intensity in the range of 0.1 p.e.. Even though almost all measured PMTs show such a structure, the structure itself differs from PMT to PMT. Plot taken from [92].

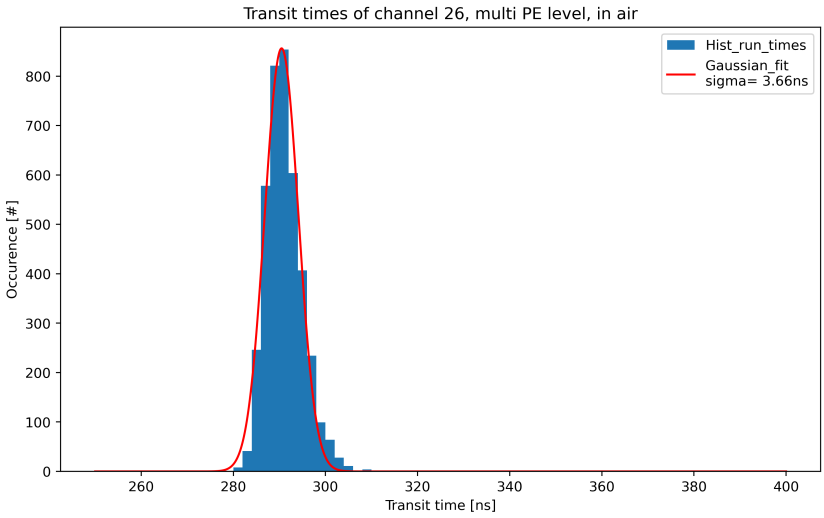

Figure 6.5: Exemplary result of ch 26 during a measurement of the OSIRIS detector in August 2023 using an illumination in the 1 p.e. regime. The Gaussian fit of the distribution results in a TTS of approximately 3.66 ns (σ). Due to the larger light intensity, the underlying substructure (see figure 6.4) is not visible in this case.

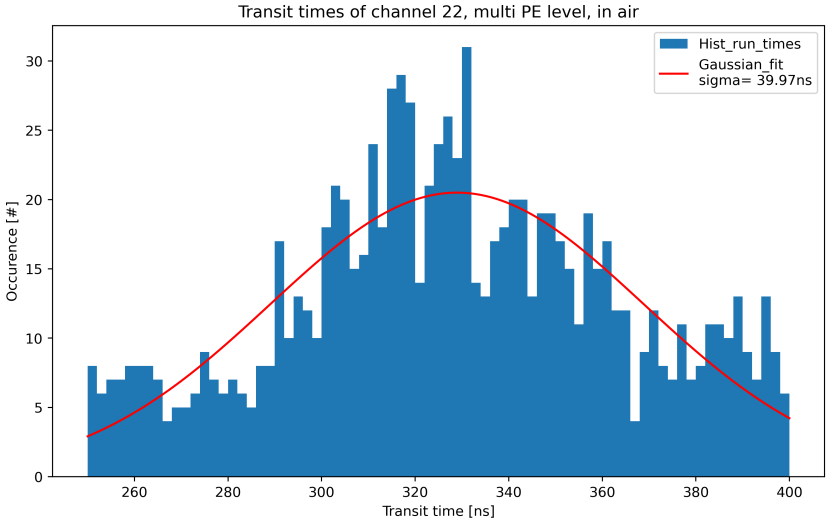

Figure 6.6: Ch22 during a low light intensity measurement taken in August 2023. In this channel, which has seen much less light in comparison to channel 26 (see figure 6.5) the substructure observed during the PMT testing is visible again. (see figure 6.4). As demonstrated, a simple Gaussian fitting is not possible anymore.

All 24 channels of the system have been tested this way, all results show values in the expected range between 3.5 ns and 6 ns[2] including the slight broadening of the TTS introduced by the LDS (see chapter 5.6).
Another short cross-check test performed with the water tank also filled with nitrogen in November 2023 showed no deviations in the performance of the system[3]. As a result, the LCS performance was considered stable over time and no further measurements using the LCS have been performed during the gas phase of OSIRIS.

[2]The expected values for the TTS are obtained from [92].

[3]Due to the short availability of the detector in the nitrogen phase, only a small data sample has been taken, which has only been used for an on-the-fly cross-check. No further analysis has been performed with this data.

6.2 The filling of OSIRIS

After the successful air run phase (see section 6.1), the detector was prepped for filling, which was performed in three stages:

- Nitrogen flushing of the water tank:
  The water tank was flushed with nitrogen to remove any residual air, to prevent to polluting the veto volume with radon[4]. This step was the transition between air and liquid phase.

- Water filling:
  The whole detector was filled with water, starting from the bottom of the veto water tank and reaching to the level of the bottom of the acrylic vessel. Consecutively, water was also filled into the acrylic vessel. After reaching the chimney of the vessel[5] the filling speed was reduced. After finishing this crucial level, the filling speed was increased again. As soon as the vessel has been filled, first water measurement tests with the LCS have been performed.

- LS filling:
  After completing the previous water filling step and after some time to perform system and leakage checks, the water of the AV was exchanged, again beginning at the top of the vessel. In this way, water could be removed from the bottom of the vessel, potential water-LS mixtures were divided using a special filter system. Several LCS measurements were foreseen in this step: at the beginning of the exchange, after the LS level reached the middle of the vessel and just before the end of this step.

The entire filling procedure of OSIRIS was executed from late January, to March 2024 and was paused during the Chinese New Year holiday[6] with the detector completely filled with water. The filling of OSIRIS took a total of four weeks and was carried out under close 24h, on-detector surveillance[7].

6.2.1 Water run

Performing a water run provides several benefits for the system test. On the one hand, the opacities mentioned in the previous chapters are no longer visible in the acrylics, on the other hand, most of the complex optical effects like changes in the optical paths due to differences in the refractive indices are much smaller if even present. In the case of the present work, several measurement runs have been performed during the liquid filling phase of OSIRIS in March 2024. These testing measurements include both calibration systems and include positioning

[4]The AV was always flushed with nitrogen during the whole installation phase.

[5]The inlet pipes of the AV (level measurement, filling and ACU) are referred to as the chimney.

[6]In combination with the spring collaboration meeting of JUNO, the filling was paused from February, 10th to February 27th.

[7]During this procedure, at least two people were supervising the detector around the clock.

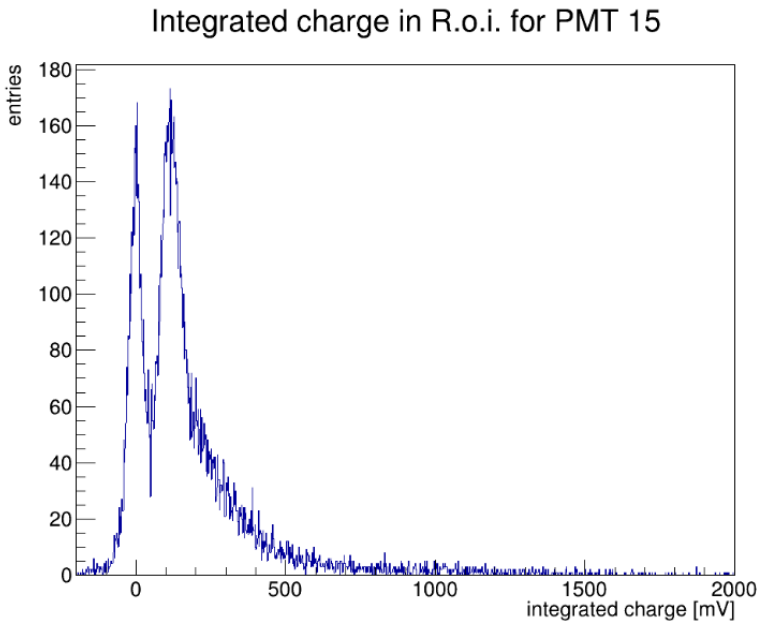

Figure 6.7: Charge histogram as taken during the water run of OSIRIS. Plot is as obtained from the rootsorter, no further analysis has been performed. In comparison to the histogram taken during the air runs (see figure 6.3), the second peak (the single p.e. peak) is more prominent. Additionally, on the right side of this peak a slight broading can be seen which is the double p.e. contribution. The increased illumination is expected and caused by the reduced opacity of the acrylic vessel.

reconstruction tests (LED position in the ACU axis and diffuser positions) as well as the first test for light intensity of the optical sources. However, due to the changes in both DAQ software and firmware of the GCU and BEC, a thorough analysis was not possible. Therefore, the data acquired during these runs has only been used for debugging, no analysis effort has been made. However, these water runs showed, that all diffusers work as intended, no channel was lost in the process of the liquid filling.
An exemplary charge histogram, again as obtained via the rootsorter, can be found in figure 6.7. The histogram is very similar to the plot obtained in air, even though all channels show a higher light intensity, which is expected due to the reduced opacity of the acrylics.

6.3 Liquid scintillator run

After the completion of the LS filling of the OSIRIS detector in spring 2024, a final set of system tests of the LCS was performed. In three measurement campaigns, different data sets have been obtained. However, due to changes in the LHS system of the whole LS hall, different batches of JUNO LS have been used. These batches do not only include different levels of radiopurity, but also different compositions of the LS itself which differ particularly in PPO[8] concentration. The measurements discussed in this chapter have been taken in March, May and August 2024.

6.3.1 Operational test of the LCS in liquid scintillator

In the first step, carried out in March 2024, the general performance of the system was tested. During this first tests, two more broken LDS channels have been found and replaced with spare channels. The expected cause of the damage was torque applied to the fiber couplers during installation/change of the fibers during the installation.
Since the general functionality of the system has already been tested in previous runs (see chapter 6.1), the focus of this measurement was the maximum achievable trigger rate for both hard and software. Especially, the reaction to frequencies greater than 2.5 kHz by the GCU and event builder was not known. Using the EPICS monitoring tools of OSIRIS (see chapter 7), a simple frequency test of the system was performed, whilst monitoring the reported trigger frequencies of the system. If the system is unable to accept the set trigger rate, the EPICS tools would have reported a discrepancy between the reported values and the set external trigger frequency at the signal generator. After intensive testing, a final external trigger rate for the LCS of 6 kHz has been defined[9].

6.3.2 Laser intensity measurement and optimization

The optical calibration of the PMTs of OSIRIS requires an average optical occupancy between 0.01 and 0.1 photo electrons per calibration trigger in a PMT. These limits are necessary to minimize the contribution of double p.e. events to the charge histogram to avoid fitting errors of the single p.e. peak and hence increased errors in the calculation of the charge resolution of the PMTs. As discussed in chapter 5.1, two options are available to adjust the light intensity of the system: Either by using the two attenuators in the optical cascade, or by changing the tuning of the laser after each channel. Since it is desirable to

[8] PPO (2,5-Diphenyloxazole) is one of the primary flours used in liquid scintillators. In the case of JUNO, the nominal concentration of this substance is 2.5g per liter.

[9] In fact, using 6kHz, the DAQ maxes out the bandwidth of the OSIRIS network, which is a hard limit for the system. In principle, the hardware components of the system are capable of higher frequencies.

change the tuning as rarely as possible (see chapter 5.3 for details), the basic tuning of the LCS must to be chosen carefully using the final setup and configuration. For this purpose, a set of measurements using different light intensities has been taken in March and May 2024 (see figure 6.8). The analysis of that data showed that the use of a single light intensity for all channels is not possible[10]. Due to possible future changes in the analysis modules of the rootsorter (e.g., background reduction and hence event rejection, cut definitions, etc.) and additional light intensity assessment of the LCS needs to be performed after the freezing of the analysis modules of the rootsorter. Due to an error in the slow control, the brightness of the laser during the data taking in May was too high (see figure 6.8. Therefore, the May dataset could not be used for the commissioning. The preliminary settings for light intensity of the system at the writing of this work are:

- global attenuators: 0 %
- LDS single channels: 78.0 %
- LDS double channels: 86.0 %

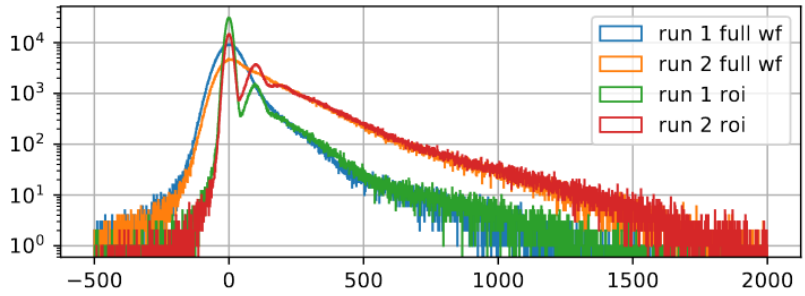

Figure 6.8: Charge histograms of one channel with region of interests (roi) and full waveform displayed. Measurements one and two (taken in March and May, respectively) are using the same set intensity but due to an error in the slow control, the results differ from each other. This brightness difference can be most prominently observed via the clear double p.e. peak of the red curve. The green curve shows an almost ideal light intensity, since the double event peak is almost invisible. Because of the deviation between red and green curve, a final light intensity measurement campaign is necessary. At the time of writing of this work, possible errors in the software have been fixed. Plot taken from [130].

[10]Since the geometry of the detector changed between the creation of the simulation shown in chapter 5.3 and the final data taking of the system, this result was expected. The changes were necessary due to unforeseen difficulties in the installation of other subsystems of the detector.

6.3.3 PMT - diffusor mapping

The mapping, assigning each PMT to a diffuser which will be used to calibrate this specific PMT, of the diffusers of the LCS is also a crucial part of the LS runs. Although a theoretical mapping and corresponding PMT response is available from simulations (see figure 5.18), the mapping resulting from actual data needs to be cross checked with this simulations. Especially, assigning each PMT to a diffuser,is important for reducing unnecessary data saved on disk[11]. As a first step to create this map, a run-time cut has been applied to exclude all PMTs on the same side of the detector or PMTs hit be photons which have been reflected multiple times, the cut is based on the expected distances from simulation and construction drawings[12]. Secondly, the charge histograms for each PMT diffuser combination was analyzed. To create the final map (see table 6.1) for each PMT, the one diffuser was selected, which provided an illumination as close to the desired 0.1 p.e. as possible. The resulting map is not symmetric which is also expected due to tolerances during the manufacturing of the diffusers, as well as asymmetries in the detector itself (piping, thermometer rod, etc.). In conclusion, table 6.1 shows that each PMT can be calibrated with one of the diffusers installed in OSIRIS.

Table 6.1: The final mapping of the diffuser channels to the corresponding PMTs. Due to the mentioned asymmetries and some changes in the detector geometry, some of channels are currently not used to calibrate any PMT. PMT channels 0-15 are located above and bellow the acrylic vessel, numbers 16-63 are located at the ring and numbers 64-75 are the veto PMTs.

Diffuser channel no.	Diffuser location	PMT no.
2	top/bellow AV	7
3	top/bellow AV	-
5	top/bellow AV	0,1,11,12,13,14
6	top/bellow AV	2,3,8
7	top/bellow AV	4,9,10,15
8	top/bellow AV	-
9	top/bellow AV	-
10	top/bellow AV	5,6
1314	ring/veto	29,30,32,35,45,65
1516	ring/veto	18,21,23,36,40,42,58,66

[11] All data acquired by PMTs that are not to be calibrated with the currently activated diffuser can be discarded.

[12] Same is true for the PMTs in the veto especially on the bottom. Even though timing cuts are a little bit more delicate since reflections at the walls of the veto only lead to small changes in the run-time. However, this cut could be applied successfully.

Diffuser channel no.	Diffuser location	PMT no.
1718	ring/veto	16,26,34,48,49,50,56,57,59,60,64
1920	ring/veto	24,25,27,31,39,43,51,63,67
2122	ring/veto	17,41,52,53,68,69
2324	ring/veto	33,47,54,61,70,71
2526	ring/veto	19,20,22,28,38,44,46,55,72,73
2728	ring/veto	37,62,74,75

6.4 Comprehensive Calibration

In this section, a more extensive test of the data taken with the light distribution system is described. For this purpose several PMT performance parameters will be calculated using data, that has been taken with the LDS in March 2024. In this measurement, using the reference channel 23 mentioned in chapter 5.6, an approximate light intensity of 0.1 p.e. was chosen. For each diffuser between 200k and 250k triggers have been acquired.
A few minor systematical differences are expected. On the one hand, the PMT bases used in the PanAsia testing system are not identical to those used in OSIRIS[13] On the other hand, the measurements of the testing facility have been carried out in air and ambient temperature, which will lead to differences in the performance of the PMTs caused by environmental deviations between the two measurements.

6.4.1 Charge calibration derived from the charge histograms

Due to the comparably large TTS of the PMTs used in OSIRIS, it was decided to use a charge based vertex reconstruction approach. Therefore, the charge calibration of the PMTs is of high relevance, as already slight changes in the charge calibration will have a large impact on the performance of the PMTs. Additionally, this calibration is relevant for the calculation of the energy scale. To calculate the charge resolution of a PMT, each pulse will be integrated and the result will be plotted into a histogram (see figure 6.9 for reference). Different methods can be used to process these histograms. On the one hand, a complete fit of the histogram can be performed which is the method that will be used in JUNO. To fit the charge histogram of a MCP PMT the use of a complex mixture of a Gamma function and a Tweedie function is foreseen:

$$f(Q) = p_0 \cdot f_\Gamma(Q, \alpha_p, \beta_p) + (1 - p_0) f_{Tw}(Q, \mu, \phi, p) \tag{6.1}$$

with the Gamma distribution

$$f_\Gamma(Q, \alpha, \beta) = \frac{\beta^\alpha}{\Gamma(\alpha)} \cdot Q^{\alpha-1} e^{-\beta \cdot Q} \tag{6.2}$$

and the (general) Tweedie distribution

$$f_{Tw}(Q, \mu, \phi, p) = exp\left(\frac{1}{\phi}\left(Q\frac{\mu^{1-p}}{1-p} - \frac{\mu^{2-p}}{2-p}\right) - A(\Theta)\right) \tag{6.3}$$

With Q being the charge, β being the inverse rate parameter and α the shape parameter of the Gamma distribution. In the case of the Tweedie distribution, Q is the charge, μ the mean, ϕ the dispersion parameter, Θ the canonical parameter

[13]The bases follow the same scheme but feature different components with different tolerances.

and p the power parameter. The additional term $A(\Theta)$ is included in the general form of the Tweedie distribution and responsible for the normalization of the distribution[14].
On the other hand, only a selection of the histogram can be fitted, by cutting the large tail of the histogram (see figure 6.9). After this cut, a simple sum of two Gaussians can be used:

$$f_{dG}(Q, a_1, \mu_1, \sigma_1, a_2, \mu_2, \sigma_2) = f_G(Q, a_1, \mu_1, \sigma_1) + f_G(Q, a_2, \mu_2, \sigma_2) \tag{6.4}$$

with the Gaussian distribution:

$$f_G(Q, a, \mu, \sigma) = \frac{1}{\sigma\sqrt{2\pi}} \cdot exp\left(-\frac{(Q-\mu)^2}{2\sigma^2}\right) \tag{6.5}$$

Since this work will compare values taken during the PMT characterization campaign with the measurements taken by OSIRIS in a later section (6.4.3), it will use the approach used during the characterization of the PMTs, which is the double Gaussian approach. Even though the combination of Tweedie and Gamma distribution provides a more complete fitting of the charge histograms and is therefore used in the final OSIRIS analysis, a fair comparison to the database values will not be possible. The analysis of the OSIRIS PMTs using the combined Tweedie Gamma fit function will be published by the JUNO collaboration in the coming years.

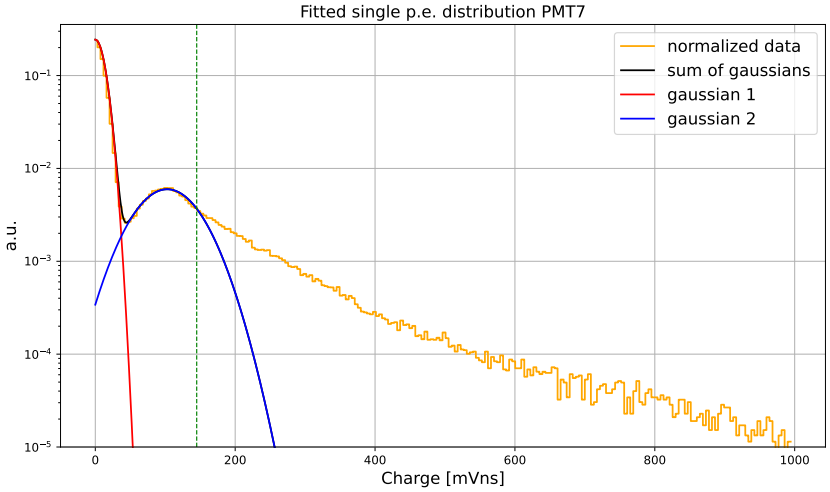

Figure 6.9: Exemplary charge histogram of PMT number 7 using data taken in March 2024. The fitting function used is a sum of two Gaussian functions, which covers both the pedestal and the single p.e. peak. In green, the limit of the data used for the fit is given. Data is normalized.

[14]The mean μ and the term $A(\Theta)$ are related via: $\mu = \frac{\partial A(\theta)}{\partial \Theta}$

The parameters calculated in this work using the fitting results of the charge histograms are the signal-to-noise ratio, the peak-to-valley ratio, the charge resolution and the gain of each PMT. Using the maximum ($Q_{ped/sig}$) and the sigma ($\sigma_{ped/sig}$) of the two Gaussians fitted to the histogram, divided by $50\,\Omega$, which is the impedance of the PMT[15][131], the PMT parameters can be derived. The definitions are:

- **Gain**:
  One can define the gain of a PMT at a set voltage as:

$$G = \frac{Q_{sig} - Q_{ped}}{e} \tag{6.6}$$

  with e being the elementary charge. The target gain of the 20-inch PMTs used in the JUNO experiment is 1x10^7.

- **Signal-to-noise ratio**:
  The signal-to-noise ratio (S/N) is a data quality control parameter providing an estimate of the amount of noise included in a measurement of a signal. During the PMT testing of JUNO it was mainly used to estimate the validity of the charge resolution measurement. It is defined as:

$$S/N = \frac{Q_{sig} - Q_{ped}}{\sigma_{ped}} \tag{6.7}$$

  This value is highly dependent on base and DAQ electronics and differs from PMT to PMT. A shift of this value hints to a hardware problem of this PMT, an investigation of the corresponding PMT should be considered.

- **Peak-to-valley ratio**:
  Using the height of the signal peak and the minimum between signal and pedestal, the peak-to-valley ratio (P/V) can be defined.

$$P/V = \frac{N_p}{N_v} \tag{6.8}$$

  It provides a measure on the distinctiveness of pedestal and signal. The

[15] This factor re-scales the unit of the charge of the histogram from [mV x ns] to Coulomb and, respectively, the elementary charge.

height of the signal peak (N_p) can directly be obtained via the Gaussian fitting, while the valley needs to be calculated separately. In this work, it is calculated by fitting a parabolic function into the valley between pedestal and signal. The minimum of the resulting fitting function (N_V) is used as an input for this parameter. Decreasing values of P/V hint to a problem with the fits used for the calculation of the charge resolution. A manual check of such results is necessary.

- **Charge resolution**:
  To monitor the charge resolution of the PMTs of OSIRIS is one of the primary goals of the LCS (see chapter 5.1).

$$Charge\ Res.\ in\ \% = \frac{\sigma_{sig}}{Q_{sig} - Q_{ped}} \,\mathrm{x}\, 100 \tag{6.9}$$

  Due to the fact that almost all analysis topics of OSIRIS are based on the charge rather than on the timing, even slight changes in the charge resolution of the PMTs need to be taken into account. This value is the only parameter derived from the charge histogram, which results in a calibration factor that is provided to the rootsorter analysis framework of the detector.

Using the mentioned data taken in March 2024, each of these parameter has been calculated for all PMTs of OSIRIS. The results of this analysis are:

- **Gain:** In figure 6.10, the result of the gain determination can be found. The errors provided in this measurement are the statistical uncertainties of the fit. As can be seen, almost all PMTs show a gain that is larger than the anticipated $1\,\mathrm{x}\,10^7$. Even though this was not expected, a possible explanation for this behavior is the source of the voltages applied to the PMTs. These voltages have been created using the JUNO PMT testing system [20], which slightly differs in hardware. On the one hand, the back-end electronics between the two systems is different (GCUs in the case of OSIRIS and a commercial FADC in the case of the testing system). On the other hand, even though the base of the PMTs follows the same scheme, the base produced for JUNO differ from the bases used in the testing facility. To re-calibrate the gains to the desired level, a high voltage - gain scan can be performed[16]. As a result, the spread can be reduced and all channels set to the desired value of $1\,\mathrm{x}\,10^7$.

[16]Such a scan includes the calculation of the gain from the charge histogram with data taken with different high voltages. A consecutive linear fit results in a HV - gain function providing the option to set the gain precisely to the desired level of $1\,\mathrm{x}\,10^7$.

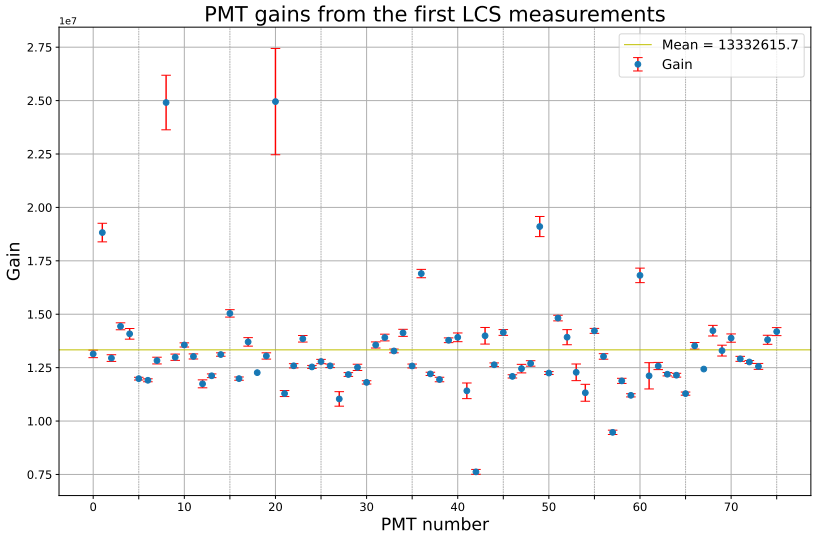

Figure 6.10: Result of the gain measurements. Additionally, the mean is given. The values are higher than the anticipated 1×10^7, which is due to the fact that the PMTs are using the voltages calculated during the PMT testing of JUNO. This setup slightly differs in hardware, which is a probable explanation of the differences. To tackle these deviations, a HV-gain scan will be performed in Autumn 2024 that will re-calculate a HV for each PMT corresponding to a gain of 1×10^7.

- **S/N:** Figure 6.11 shows the results of the signal-to-noise ratio calculation. Most channels show values in the expected range between seven and twelve. Errors given in the calculation are the statistical errors of the fitting, enlarged error of some channels is caused by bad statistics and resulting difficulties in the fitting. Given this result, almost all PMT electronics and their corresponding DAQ chain work in order. Only the outlying PMT 42 should be monitored closely in the future.

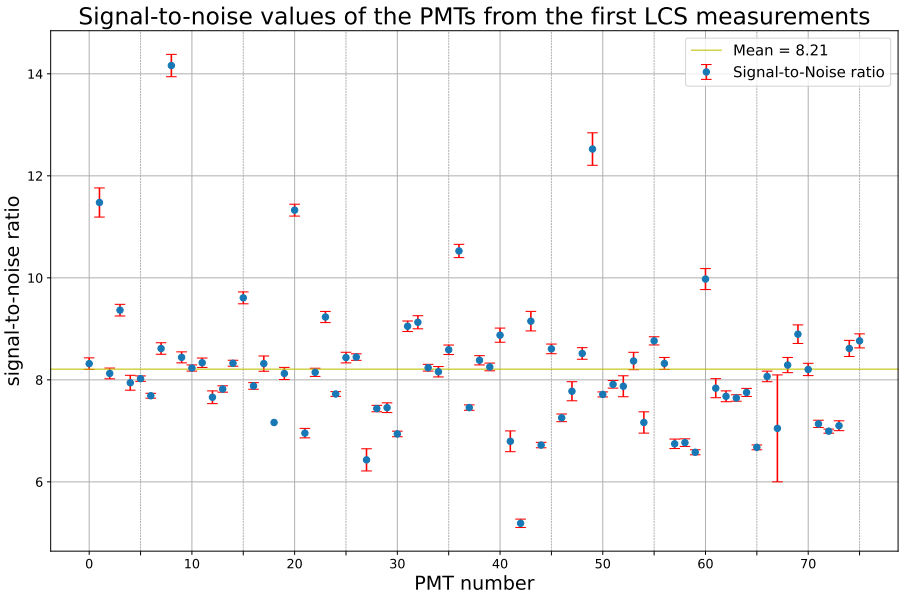

Figure 6.11: Signal-to-noise (blue dots with red error bars) and its mean (yellow). The larger errors are due to small statistics of the March 2024 data set in some channels. Almost all PMTs feature a signal to noise value of more than six, which is expect for the class of PMTs used in OSIRIS. Channels missing this criterion need to be closely monitored and reevaluated during the final commissioning phase.

- **P/V:** The peak-to-valley ratio, which is the histogram quality parameter considered by this work, also shows good results (see figure 6.12). The expected range is 2 - 4. Only very few channels show a considerably small P/V ratio, which is again caused by bad statistics of the corresponding channel. In the case of the P/V a larger error robustness than the signal-to-noise ratio can be observed, which is reasoned on the one hand by the definition of the parameter and on the other hand by the additional fitting of the parabolic function. Even though some PMTs show values smaller than two, no PMT shows values that might hint to issue identifying the single p.e. peak. However, PMTs featuring higher values will provide an increased fit performance.

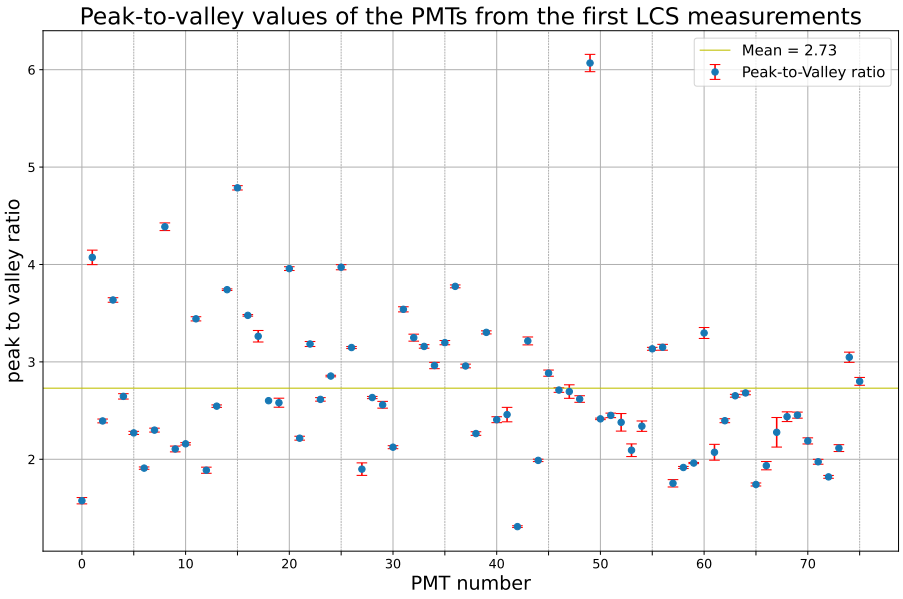

Figure 6.12: Peak-to-valley ratio (blue dots with red error bars) and its mean (yellow). Larger errors are again due to bad statistics, with the same channel sticking out as in the case of the signal-to-noise ratio in addition to the first channel. During the final commissioning of OSIRIS this channel needs to be investigated.

- **Charge resolution:** As a last step, the distribution of the charge resolution needs to be discussed. The charge resolution result (see figure 6.13) features a little larger errors, due to its definition (as always, the errors are calculated using the results of the fitting and the Gaussian error propagation). However, absolute value and error are within the expected margin. A possible solution to reduce the size of the errors would be a measurement featuring even larger statistics ($\geq 5\,\mathrm{kk}$) or by fitting the whole distribution using the Tweedie Gamma combination discussed prior in this chapter. A measurement using much higher statistics is planned to be done in the last calibration prior to the nominal operation of the detector. The charge resolution as discussed here will be used to provide calibration values to the rotsorter framework of OSIRIS.

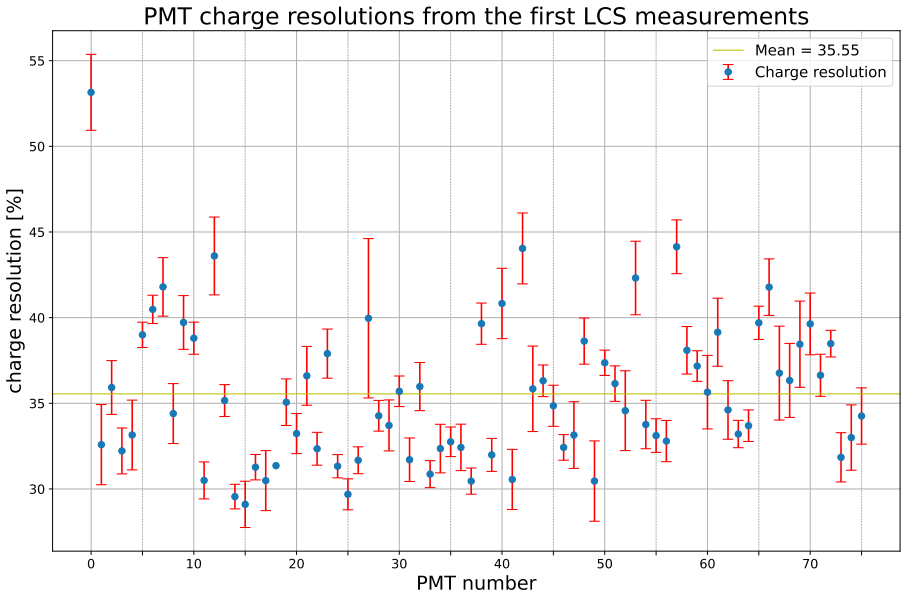

Figure 6.13: Charge resolution for all PMTs (blue dots with red error bars). Differences in the errors are due to different fitting performances because of statistics. Statistical errors are dominant in comparison to systematical effects. These results of the charge resolution will be used in the final DAQ chain of OSIRIS. The charge resolution is given in per-cent.

To exclude systematics introduced by the LCS that might not be visible in the sole analysis of the discussed values, correlation plots have been created. To test a possible correlation between gain, P/V and S/N two plots have been created. Since a higher gain will also increase the height of the signal, a positive correlation is expected for this combination. In the case of the peak-to-valley ratio, a slighter yet visible dependence is expected since a higher gain will slightly move the single p.e. peak and hence, depending on the PMT, slightly deepen the valley which leads to an increasing P/V. Both expected correlations can be seen in figures 6.14 and 6.15.

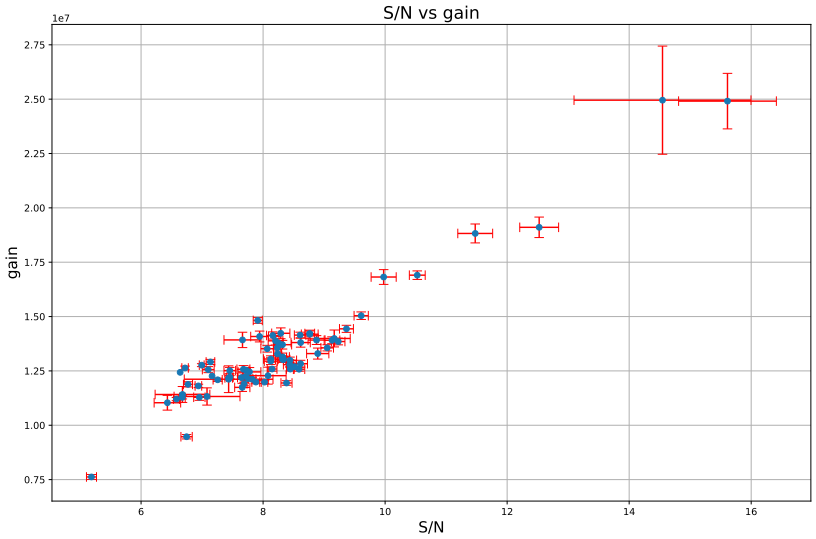

Figure 6.14: Correlation plot of gain and signal-to-noise ratio. The visible positive correlation is expected since a larger gain will also create larger signals and hence a larger signal-to-noise ratio.

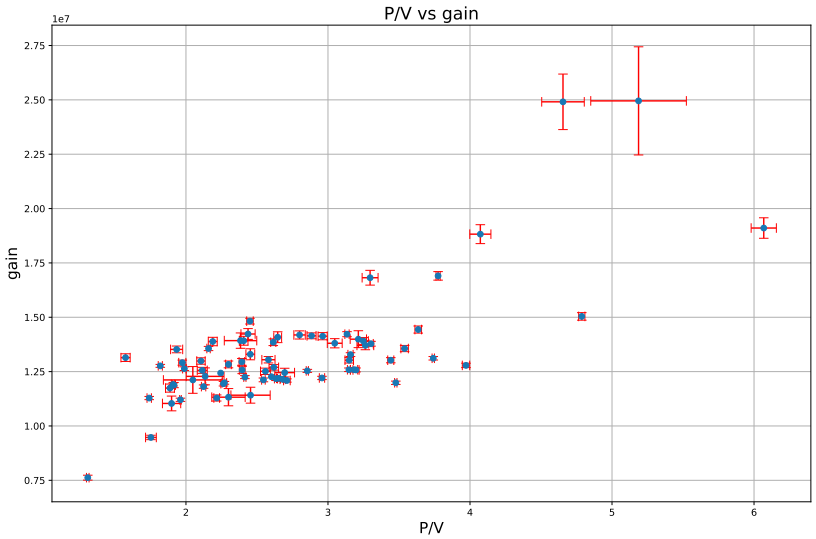

Figure 6.15: Correlation plot of gain and peak-to-valley ratio. A small correlation can be seen, which is also expected due to a possible deepening of the valley with an increasing gain.

To conclude, it can be stated that the system is able to measure and cal-

culate data quality values as well as gain and charge resolution of the PMTs of OSIRIS. S/N and P/V ratios are in the expected margins for most PMTs. Even though the calculated gains show a slight excess over the expected values, this is anticipated to be a result of hardware differences between OSIRIS and the JUNO PMT testing system. Some channels of the charge resolution results show values larger than the limit of 40 % of JUNO [92]. However, since the main argument for the limits of JUNO is the required energy resolution, which is not of a high priority for OSIRIS, these PMTs can still be used.

The expected systematical errors of the LCS are driven by the laser and the signal generator used for triggering of the system. In the case of the laser, a frequency stability of < 50 ppm is given by the manufacturer [122], which translates to an error of 0.01 Hz using the applied trigger frequency of 200 Hz, a full pulse width at half maximum of 72 ps as well as a spectral width of 2.6 nm centering around the peak maximum at 420 nm. Furthermore, the systematical error of the signal generator is given with 50 ps jitter (RMS) per channel and 200 ps skew between the synced channels [121]. Quadrature addition of the frequency errors lead to an expected error of 218.4 ps.
It was planned to perform the same analysis with the dataset acquired in May. This data set was taken remotely and due to a bug in the remote control of the LCS, the laser was operated using an intensity, which was to large[17]. Therefore, no analysis has been performed using the May dataset. A further, final calibration measurement will be done by end of 2024.

6.4.2 Timing calibration

Due to the large TTS of the MCP type PMTs, the importance of the time calibration is reduced in the case of OSIRIS. However, comparing the results of the timing measurements with the values stored in the database of the PMT testing facility provides a way to test the performance of the calibration system. Deviations between the two measurements are expected not only because of the systematic differences of the two setups (see the beginning of this section and [20]) but also because of the use of another light source, which is a laser in the case of OSIRIS and a fast LED in the case of the PMT mass testing system[18]. During the data taking of the system, the trigger is also digitized. Using this trigger and the first hit time at the different PMTs, it is possible to create a transit time histogram. In the special case of the GCUs of JUNO, the pre-analysis chain of the system always uses both gain modes at the same time to take timing data. The result is a histogram with two separated distributions instead of one, which both describe the same PMTs only differing in the ADC used to process the data and in the shift of 130 ns.
The traditional way to calculate the transit time spread using these distributions would be the fitting of a Poisson function or a Gaussian to the distribution and

[17] Analysis have resulted in a light intensity of a few p.e..

[18] Even though the container system featured the same laser as the one used in this setup, it was not used for almost all of the PMTs now used in OSIRIS.

calculating their $1\,\sigma$ width. However, as demonstrated in figure 6.4, the MCP PMTs of OSIRIS, show a very distinct substructure, prohibiting the use of a Gaussian fitting function. Instead, the [Q3,Q97] quantile was used and the standard deviations calculated[19] (see figure 6.16). As can be seen, the sub-structure visible in the container system is not visible in the data taken with OSIRIS. As of writing of this work, the cause has not yet been completely identified, though several factors need to be considered: First of all, it could be possible, that the light intensity was just too high, the substructure would be reduced due to the smearing of multi-p.e. events. However, this does not seem likely, since the charge histograms do not show any distinct double p.e. peak which would be expected in such a case. Secondly, the precise timing of the laser could be smeared by some parts inside the detector. For example, reflections inside the walls of the acrylic vessel could add up to such a smearing. Furthermore, the manufacturing of the capsules could not have been ideal. A small gap between the tip of the fiber and the PTFE diffuser could create a resonator that also adds to the smearing. The actual TTS analysis for the commissioning of OSIRIS includes both of the two gains (see figure 6.17). Errors provided in this plot is the statistical error, calculated using the error propagation method. To check for possible, in this case unexpected correlations between gain and TTS another correlation plot has been produced. It can be found in figure 6.18. As expected, no correlations can be seen.

In this chapter, the transit time spread (TTS) of all PMTs of OSIRIS has been calculated. Using the standard deviation of the percentile of the transit time distribution, values for both, high and low gain outputs have been presented. The results for the TTS are better than the values measured during the JUNO PMT testing campaign, reducing the mean by $0.4(1.0)\,\mathrm{ns}$ (high/low gain). However, this reduction is caused by differences in the used light source, which is a fast LED with a TTS of $1\,\mathrm{ns}$ ($1\,\sigma$) in the case of the testing system and the laser with a TTS in the order of $100\,\mathrm{ps}$ ($1\,\sigma$).

[19] It has been shown that this approach is indeed valid to be used in the case of this PMTs [22].

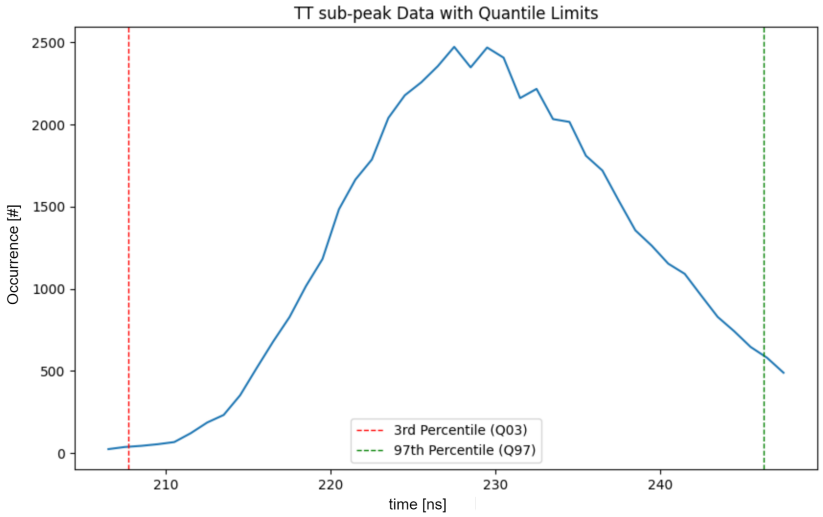

High gain output of the transit time measurement.

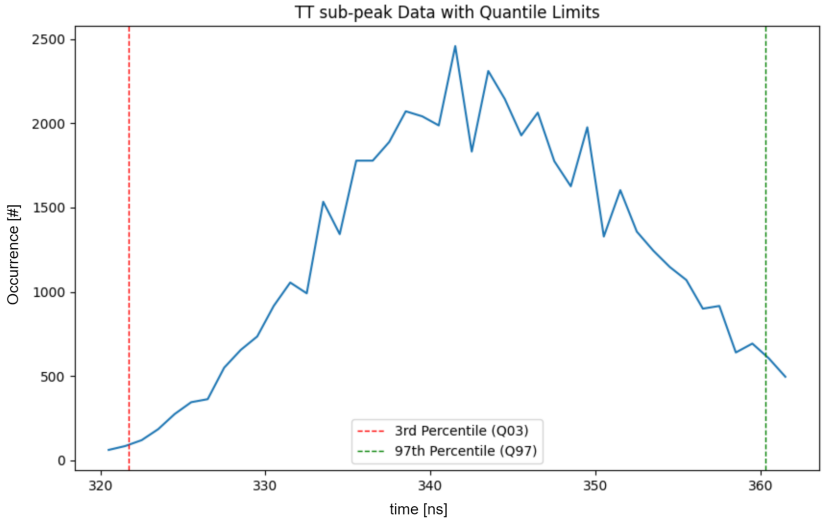

Low gain output of the transit time measurement.

Figure 6.16: The two sub peaks of the transit time measurement of PMT 7, including the quantile limits as used during the PMT testing phase of JUNO. Differences in the shapes of the two peaks are caused by the different ADC gains with which they were recorded.

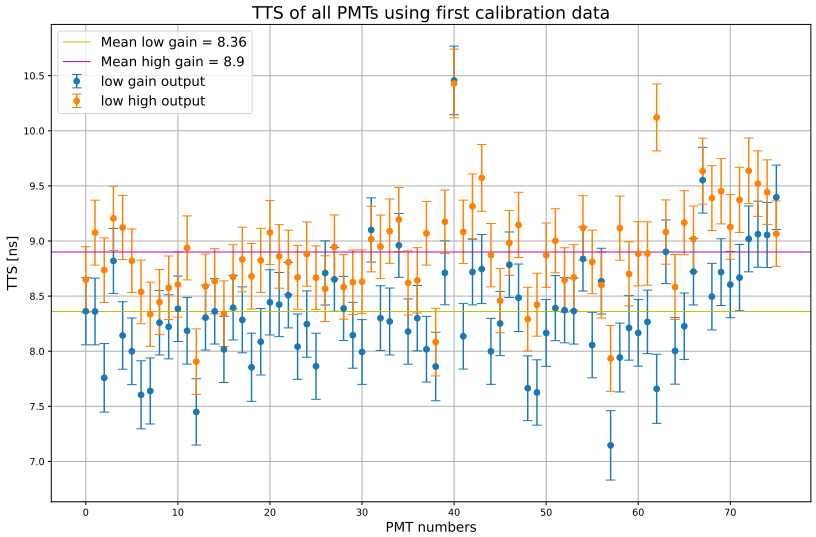

Figure 6.17: Result of the transit time spread analysis of all PMTs using the March 2024 dataset. Both gain ranges of the GCUs can be seen (blue dots with blue error bars for the low gain output, orange dots with orange error bars for the high gain output). In green, the values from the PMT testing database are given. Slightly decreased values are due to the intrinsic TTS of the light sources used, which is a LED in the case of the PMT testing and a laser in case of OSIRIS.

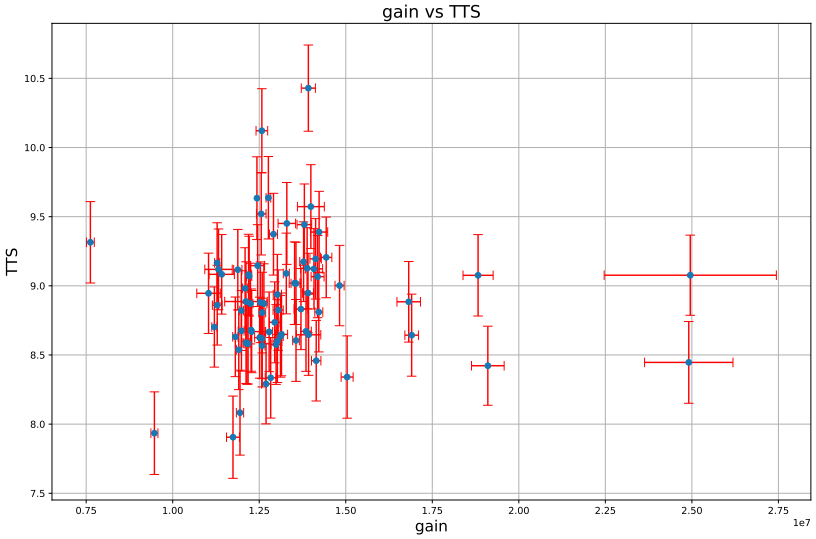

Figure 6.18: Correlation plot of TTS and gain. As expected, no correlation can be observed.

6.4.3 Comparison of measured PMT parameter to the characterization data-base

In this subsection, a comparison between the PMT performance parameters calculated in the previous section and the parameters acquired during the PMT characterization campaign of JUNO will be performed.
The testing campaign has been carried out between 2017 and 2022 at the PMT testing facility at PanASIA in Zhongshan, China. All PMTs bound to be installed in the JUNO main detector have been tested using this setup [92]. However, since OSIRIS is also using PMTs that failed one or more of these performance goals, not all PMTs have been tested this way.
The setup used during the characterization tests of JUNO was housed in a standard shipping container and featured 36 PMT testing channels. The light sources used for the testing of the PMTs of OSIRIS was a LED, featuring an intrinsic TTS of 1 ns. However, the light intensity and stability over time could be controlled very precisely using several reference PMTs that stayed in the detector during each measurement [20].
All values, that have been acquired in the campaign have been stored in a database which will now be used to check the performance of the PMTs and hence provide a test of the performance of the laser calibration system.
In a first comparison, the measured gain of both systems is compared (see figure 6.19. Even though the bases of the PMTs of both systems follow the same scheme, the parts used to build the bases as well as the back-end electronics differ. Therefore, a shift of the gains can be observed.

Secondly, the charge resolution of the two measurements is compared (see figure 6.20). The distribution of these two histograms is comparable, which is expected since the same fitting methods and light intensities have been used. Small observable differences are due to statistical errors due to the small statistics of some channels (see previous chapter for details).

As a last comparison, the different TTS results are compared (see figure 6.21). Due to the DAQ of OSIRIS, two values are given for each channel, resulting in two different histograms (high and low gain). As discussed in section 6.4.2 these two don't fully agree with each other due to differences in the ADC gains. In this analysis, the high gain output has been used, since it is foreseen as the OSIRIS standard ADC. Furthermore, as mentioned the measurements taken with the JUNO testing system have used a LED that is slower than the laser of the LCS.

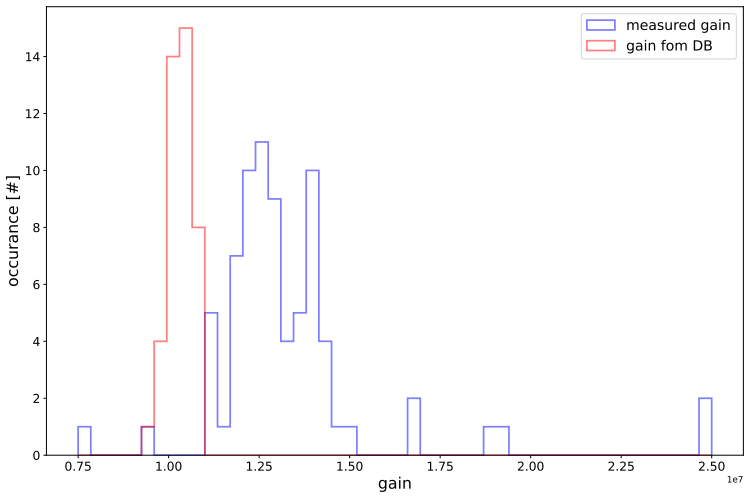

Figure 6.19: Histogram of the gains of the PMTs of OSIRIS calculated in the scope of this work (blue) and during the PMT characterization campaign of JUNO (red). The values acquired in OSIRIS are slightly shifted to right which is due to differences in the electronics. Also, an increased spread can be observed, which will be removed by an additional HV-gain scan performed in autumn 2024.

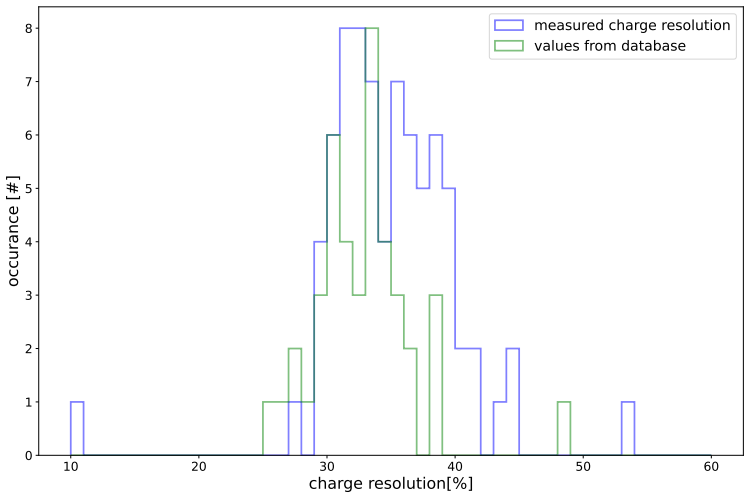

Figure 6.20: Histogram of the charge resolution of the PMTs used in OSIRIS as measured in the detector (blue) and in the JUNO PMT testing station (green). The histograms are mostly in agreement, slight deviations are due to statistical errors as discussed in chapter 6.4.

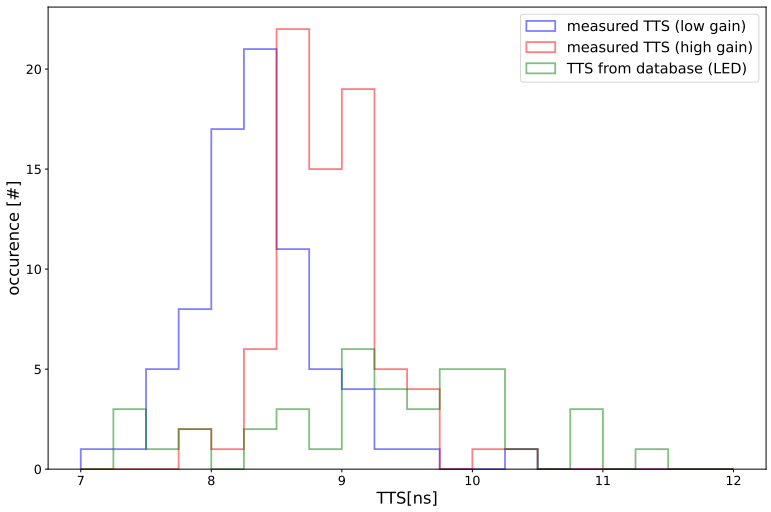

Figure 6.21: Histograms of the two TTS results of the measurement in OSIRIS (blue and red) as well as the result taken from the testing database (green). The shift and, respectively, the spread of the two measurements ofOSIRIS are due to the different gains of the ADCs used to digitize the data. The much larger spread of the result of the JUNO testing facility is due to the use of a LED which features an intrinsic TTS of 1 ns.

The histograms examined in this chapter did not provide any unexplained deviations. All observed differences between the values are either explained by differences of the systems. As an outlook, a per-channel investigation could be carried out which would could be used to cross-check the PMT identification in the detector.

6.4.4 Illumination level comparison

As a last survey, the illumination level of each PMT is investigated. As described in section 5.3, one design goal of the system was an illumination of all PMTs within a rough factor of two. Using the charge histograms created in the previous sections, an illumination of each PMT has been calculated (see figure 6.22). By selecting the dataset of the ideal diffuser of each PMT (see table 6.1, the corresponding charge histogram was split into two parts, cutting in the minimum of the valley[20]. Adding up the number of entries of each side and dividing them

[20]For the definition of the valley see the discussion of the peak-to-valley ratio and equation 6.8

consecutively, led to an estimation of the illumination:

$$\text{Illumination} = \frac{\Sigma \text{ sum of entries right of the cutting point}}{\Sigma \text{ sum of all entries}} \tag{6.10}$$

Almost all PMTs are illuminated within the given interval, which is the same as used in the simulation. As mentioned, some parts of the geometry of OSIRIS have changed in comparison to the situation described in the simulation, which is why outliers are expected. However, since these outliers are still within a reasonable margin, the use of these channels is still possible. The illumination design goal of the system has been reached.

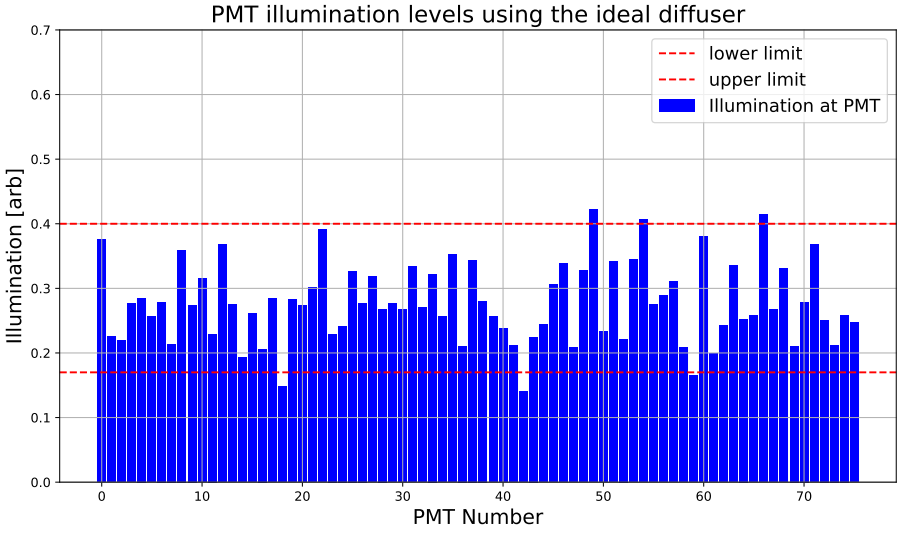

Figure 6.22: Resulting illumination levels calculated using the March 2024 dataset. Upper and lower level are in the same proportion as used in the simulation, that was used as a basis for the illumination design goal of the LCS. Almost all channels are found to be within these limits. Outliers are expected to be due to changes in the geometry not covered by the simulation.

In total, all measurements shown above are in agreement with their respective expectations. Even though some deviations can be seen, these can be explained by known systematical differences between OSIRIS and the PMT testing facility of JUNO or the simulation, respectively. Since no unexplained deviations can be found and hence the measurements of the PMT testing system as well as the simulation successfully be repeated, the laser calibration system can be declared working fully as expected. The LCS can be used to perform the optical calibration of the PMTs of the OSIRIS detector.

Chapter 7

The Slow Control System of OSIRIS

"He created me. Quis custodiet ipsos custodes? Who watches the watchmen? Me. I watch him. Always" -The Entity

from "Thud!" by Terry Pratchett, 2005

7.1 The Experimental Physics and Industrial Control System - EPICS

At OSIRIS, EPICS is used as a general slow control and archiving tool as well as a base for the run control[1]. EPICS is the "Experimental Physics and Industrial Control System", which is used today by more than 50 large-scale scientific setups (see also section 5.4).
Using a server-client architecture and a publish/subscribe model to communicate between computers, EPICS is a very powerful tool, able to handle a very large number of process variables[2]. The core of the system are the Input-Output controllers (IOCs), which can be configured to be both a client and a server. These IOCs are connected by a broadband channel access (CA) system broadcasting data in real-time to the system. All IOCs contain records

[1]The run control of OSIRIS is beyond the scope of this work. Further information about the structure can be found in [102]

[2]In fact, there are no intrinsic limits of PVs that can be controlled. The performance of an EPICS system is mainly limited by the performance of the computing hardware used

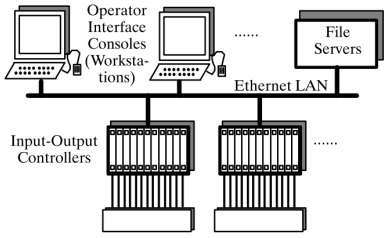

Figure 7.1: Layout of a standard EPICS network. Image taken from [132].

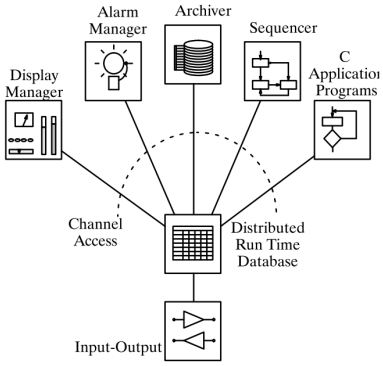

Figure 7.2: Scheme of the several EPICS subsystems. Image taken from [132].

which can function as databases, used to perform low-level calculations or to create different levels of warnings and flags. All process variables (PVs) of an IOC can be accessed via a unique address[3] from the whole network (see figure 7.1). In addition to the basic communication software, several software packages are available (see figure 7.2). The packages used in the case of OSIRIS are the archiver appliance (see chapter 7.3), a software suite for the creation of graphical user interfaces (GUIs, see chapter 7.2) and the closed-source LabVIEW-EPICS interface (LabVIEW shared variables engine).
In total, the EPICS implementation of OSIRIS will control approximately 850 integer, floating point, and string PVs.

[3]In the case of OSIRIS, the address pre-fix is $JUNO : OSIRIS : \_SUB\_SYSTEM : XXX$

7.2 EPICS Control System Studio Phoebus (CSS)

CSS is the GUI development suite of EPICS. Of the two available versions (standalone and Eclipse-based[4]) the standalone version, called CSS phoebus, is used [133]. It is available under an open source license.
The suite can be used to generate GUIs in a drag-and-drop manner, using pre-defined widgets and design elements. According to the different kinds of widgets (getters, setters, interactive elements, see figure 7.3), different connections to EPICS resources (PVs or network resources like the archiver) can be established. In addition to the pure interaction with the plain EPICS resources, operations can be performed using external scripts (python or JavaScript) or via different rules or macros directly created within the widget. Each GUI will be saved in a separate, XML[5] style file, which makes it possible to modify the GUIs even without a running version of CSS. A running version of CSS is required to display the created GUIs. However, access to development features can be restricted to prevent accidental modifications.

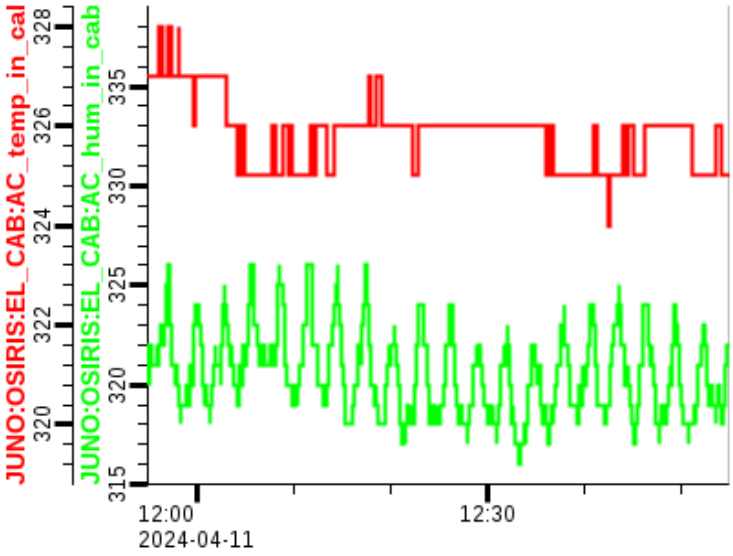

Figure 7.3: Example of a CSS design element, which is an interactive data browser. In this case the browser is exemplary showing the temperature (red) and humidity (green) inside the electronics cabinet of OSIRIS. It can be connected to the archiver appliance (see chapter 7.3) or a PV directly.

[4]Eclipse is an integrated development environment (IDE) which was initially developed for the Java programming language.

[5]XML (Extensible Markup Language) is a markup language used to display complex, hierarchic data in the form of a simple text file.

Several GUIs were created for OSIRIS, although not all of them are within the scope of this work. In chapter 7.4, the focus will be set on the GUIs that have been created in the scope of this work.

7.3 EPICS Archiver Appliance

The EPICS archiver appliance is the second important EPICS extension used in OSIRIS. It was developed by Murali Shankar at SLAC as a general slow control logging system for the experiment [134]. OSIRIS uses the archiver appliance as a logging system, too. However, in the case of OSIRIS only a selection of the existing PVs is logged by the archiver, which is caused by the fact that some of the subsystems (e.g., the LHS) feature a lot of flag and internal status PVs that are not needed to understand the performance of the detector at a later stage. Since the appliance is running on Apache Tomcat[6] and MySQL[7], the archiver offers flexible installation, maintenance and control options (see figure 7.4). Over the foreseen operation time of OSIRIS it is expected to generate a database of approximately 1 TB in size given the archiving sampling rate of 1 s-5 s[8]. It is stored on the network-attached storage (NAS) of the detector.
For direct user interaction with the appliance, two different interfaces are available: A direct PV query input (see figure 7.5), and a more sophisticated GUI that also allows users to display debugging and status information of the archiver appliance (figure 7.6). Both interfaces are available via web browser. In the case of OSIRIS, only the query interface can be used outside of the OSIRIS sub-net due to software security reasons.
The implementation of the archiver appliance into the slow control of OSIRIS that has been done in the scope of this work, played a crucial role in the testing and observation of the OSIRIS detector in both the filling and commissioning phase. It was used to monitor and log the filling of the detector (see figure 7.7), to debug responses of subsystems to slow control requests, and to monitor the tests of PMTs and their control software (see figure 7.8). In the final setup of the archiver appliance, the system monitors 494 PVs, produces 120 Mb of data per day, and writes approximately 69 events per second to disk.

[6] Apache Tomcat is an open source web server with servlet capabilities. It can be used to generate a variety of web appliances and in this case the basic interaction GUI of the archiver.
[7] MySQL is a standard, open source database server language
[8] The actual sampling frequency depends on the PV due to hardware limitations of some of the devices.

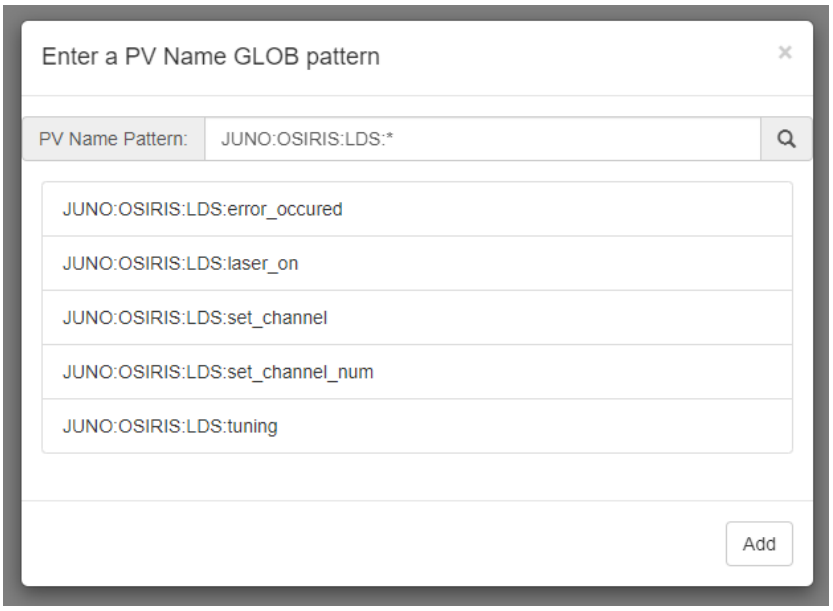

Figure 7.5: GUI of the general inquiry interface of the EPICS archiver appliance as used in OSIRIS. Each PV that is known by the appliance can be searched and viewed in this GUI. In the displayed case, all archived PVs of the light distribution system were selected.

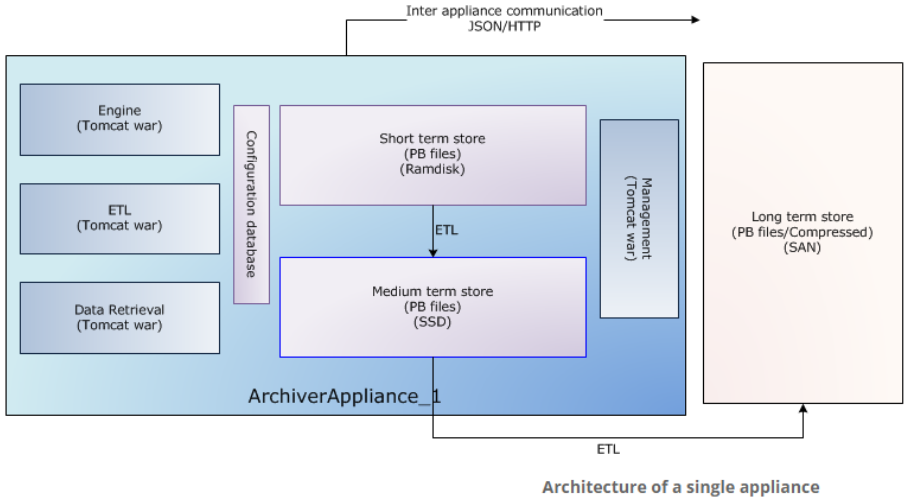

Figure 7.4: Software architecture of the EPICS archiver. Image taken from [135].

Home Reports Metrics Storage Appliances Integration

25 Page 1 of 1

Instance Name	Status	PV Count	Connected	Event Rate	Data Rate (GB/day)	Engine write thread(s)	Max ETL(%)
appliance0	Working	494	484	67.95	0.11	0.01	0

Here are the some detailed metrics of the appliance **appliance0**

Attribute	Detail
Appliance Identity	appliance0
Total PV count	494
Disconnected PV count	10
Connected PV count	484
Paused PV count	0
Total channels	3154
Approx pending jobs in engine queue	1
Event Rate (in events/sec)	67.95
Data Rate (in bytes/sec)	1,400.22
Data Rate in (GB/day)	0.11
Data Rate in (GB/year)	41.12
Time consumed for writing samplebuffers to STS (in secs)	0.01
Benchmark - writing at (events/sec)	61,877.86
Benchmark - writing at (MB/sec)	1.22
PVs pending computation of meta info	0
Total number of reference counted channels	3081
Total number of CAJ channels	3081
Channels with pending search requests	140 of 3081
Total number of ETL(0»1) runs so far	611
Average time spent in ETL(0»1) (s/run)	0.11
Average percentage of time spent in ETL(0»1)	0
Approximate time taken by last job in ETL(0»1) (s)	0
Estimated weekly usage in ETL(0»1) (%)	0
Avg time spent by getETLStreams() in ETL(0»1) (s/run)	0.03
Avg time spent by free space checks in ETL(0»1) (s/run)	0
Avg time spent by prepareForNewPartition() in ETL(0»1) (s/run)	0
Avg time spent by appendToETLAppendData() in ETL(0»1) (s/run)	0.07

Figure 7.6: Part of the general information view of the status page of the archiver appliance. Other views are available for individual PVs, which display general information including the amount of requesting channels, polling frequency, flagging information and connection status.

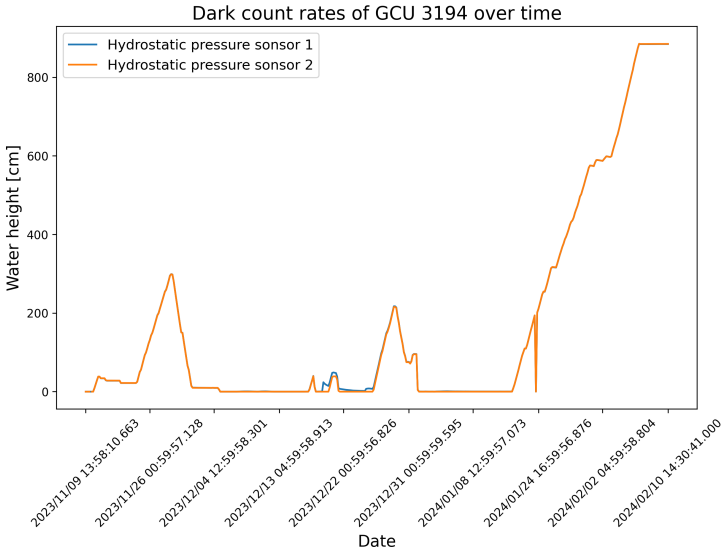

Figure 7.7: Plot of the two hydro-static pressure sensors of the water tank during the filling phase of OSIRIS. The three different fillings and the two emptying phases during the system tests can be clearly seen. A slight deviation between the sensors, which was identified (and fixed), during the LHS sensor test can be seen.

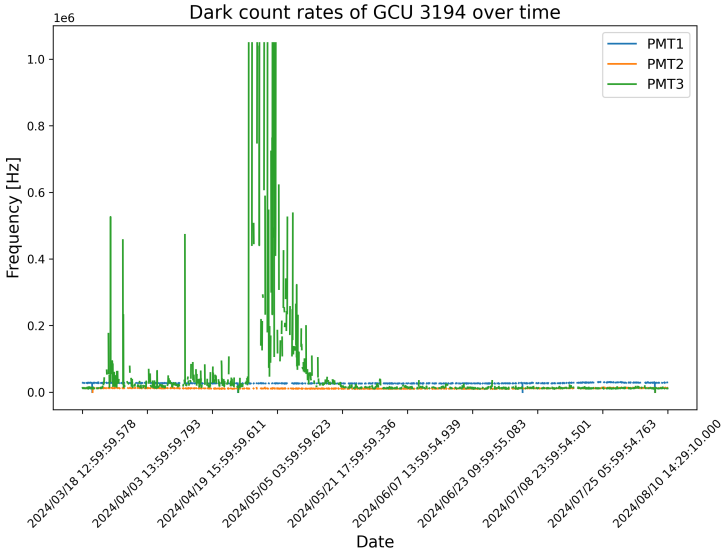

Figure 7.8: Plot of the DCR of GCU 3194. Using the appliance, a DCR issue of one of the PMTs of this GCU could be identified. The issue has been resolved over time.

7.4 Graphics user interface of the slow control of OSIRIS

In this section, a short description of the GUIs of OSIRIS that have been developed for the slow control (SC) in the scope of this work is outlined. The following GUIs are created using CSS phoebus (see chapter 7.2). The GUIs will be used daily in the standard operation of OSIRIS during the filling phase of JUNO.

7.4.1 Overview GUI

In the scope of this work, GUIs for four different subsystems of OSIRIS have been developed. These systems are the LCS (see section 7.4.2), the ACU (see section 7.4.3), the environmental control (see section 7.4.4) and the PC monitoring (see section 7.4.5). Several other GUIs have also been created, although these will not be operated by OSIRIS on a regular basis. The complete scheme of the GUIs, featuring all GUIs of OSIRIS can be found in figure 7.9. At the time of writing of this thesis, some GUIs have been written in LabVIEW2015 (LHS), some are not yet finished (general) or even still in the planning phase (UPS status).

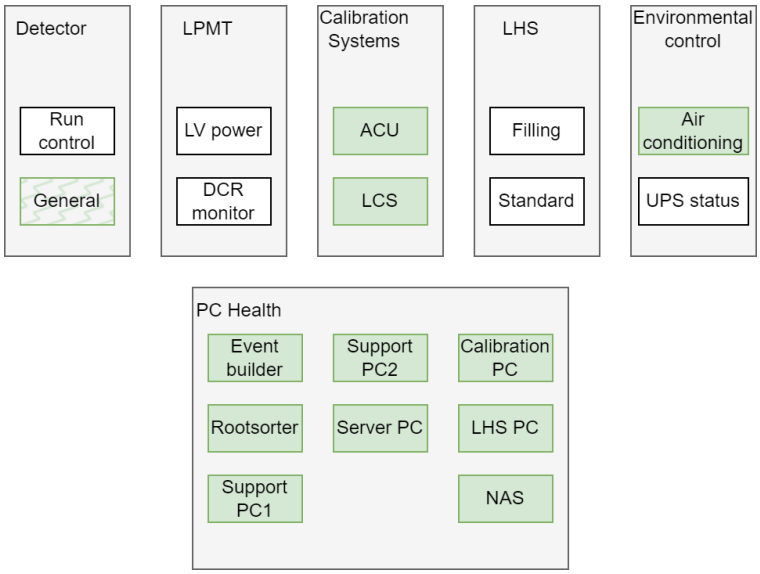

Figure 7.9: The different GUIs developed for OSIRIS. Marked in green are the GUIs developed in the scope of this work (including the general GUI which has not yet been finalized at the time of the creation of this thesis). Most CSS based GUIs are available in two access levels: shifter (general view for every day use) and expert (for debugging and trouble shooting).

All GUIs listed in figure 7.9 are planned to be used in the general control room of JUNO during the regular operation of OSIRIS. During the pre-filling detector testing phase as well as in the different filling stages and the commissioning of OSIRIS (see chapter 6), most of the GUIs were already used, too, even though some of them are slightly modified to provide additional functionalities only necessary during commissioning.

7.4.2 Laser calibration system GUI

Even though the LCS will be primarily controlled by the run control of OSIRIS, a stand-alone control is necessary for testing, commissioning and debugging purposes. As already mentioned in section 7.4.1, the GUI is available in both read-only (shifter mode) and full control (expert) mode.
The main purpose of the (expert) laser GUI is to control and display all relevant features of the laser which includes the current channel(s), the tuning and the laser status (for details see chapter 5). Additionally, an emergency stop script can be triggered, which cuts of the laser power immediately. Since this kind of shutdown is not a "safe" way to power down the system [9], the system needs to be manually rebooted afterwards. Additionally, the system error output is displayed, providing additional feedback during debugging. A picture of the finished GUI with the LDS set to channel 3 can be seen in figure 7.10.
During the standard operation of OSIRIS, the filling of JUNO, the read-only standard view will also be operable which provides the opportunity for a cross-check during operation.

[9] Due to some of the fast shutdown commands the system will be in a locked state after the emergency stop trigger.

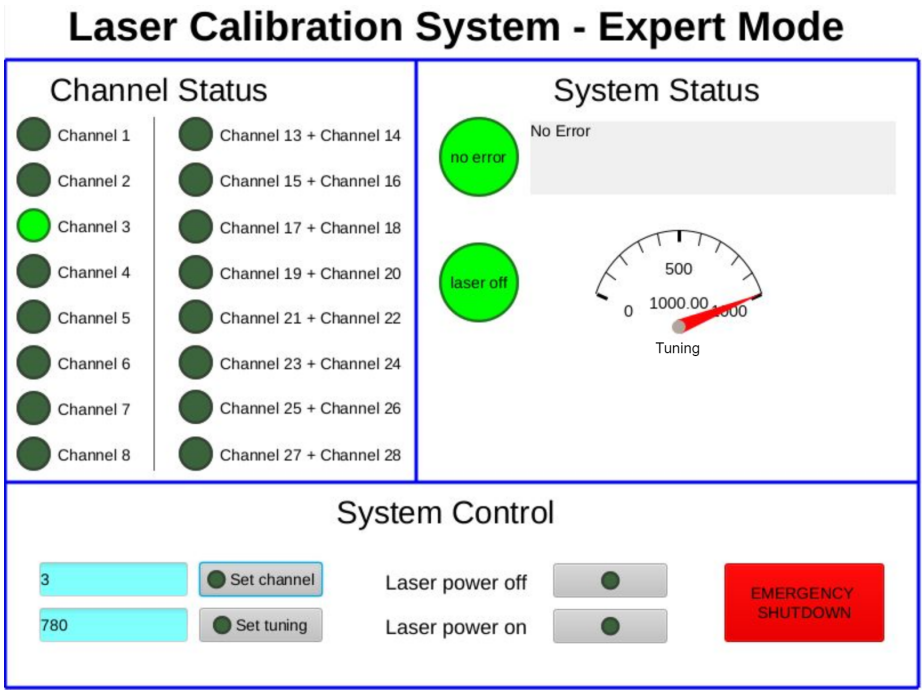

Figure 7.10: The expert mode of the GUI written for the LDS. On the left, the currently activated channel is marked in green. On the right, the laser parameters are displayed: error state, laser status (on or off), and the laser tuning (provided in per mill). In the bottom compartment of the GUI, the laser controls are located. The displayed state is the laser turned off, the tuning at 100,0 % with the change to 78,0 % already prepared and channel 3 selected as active.

7.4.3 Automated Calibration Unit GUI

Since there should be the possibility to monitor all subsystems of OSIRIS during operation in the general control room above ground, an EPICS GUI was developed for the ACU[10]. Due to the greater complexity of the mechanical hardware of the ACU, the GUI developed for this system also features an increased range of widgets. The system will be operated by hand by an expert using pre-defined scripts[11], a GUI feedback is available in addition. This feedback includes readouts of most of the sensors (e.g., load cells of the sources and limit switches of the stepper motors) and rudimentary control of some non-critical hardware parts, e.g., the power of the light source of the ACU. Further information about

[10]Even though the LabVIEW software of the ACU features a GUI, too, this GUI can't be mirrored to the control room due to network limitations.

[11]Due to the increased complexity of the mechanics of the ACU the system can't be operated without supervision of an expert, since hardware defects can occur without proper operation

the hardware of this system can be found in [116]. The general connection of the ACU control software to EPICS is done via LabVIEW in the same way as in the case of the LCS. A picture of the GUI of the ACU can be found in figure 7.11.

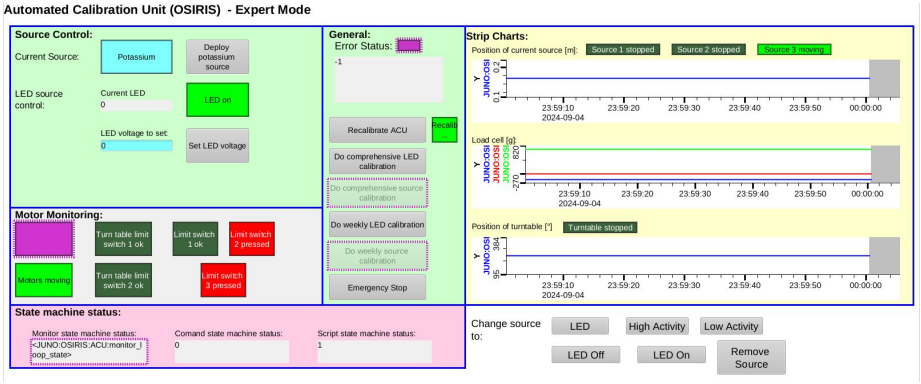

Figure 7.11: The GUI as used for the ACU. Several direct feedback displays of the hardware are available. On the right side, stripping charts showing positioning information of the sources and the deployment turntable as well as the current load on each deployment wheel can be found. Left, several general information and command options are provided. This GUI is primarily used for debugging and crosschecking from remote during the use of the device. The standard LabVIEW GUI will only be available directly on the electronics platform of OSIRIS.

7.4.4 Environmental Monitoring and Control GUI

To control the environmental situation of the electronics cabinet of OSIRIS, especially monitoring temperature, humidity and power is crucial. On the one hand, an increased temperature will lead to reduced cooling efficiency of computers and DAQ electronics (and ultimately reduce their operation speed), on the other hand, an increased humidity would potentially harm the LDS as well as some of the other control devices like the analog-digital converter cards used to digitize the temperature sensor of the inner tank (e.g. due to possible condensation while opening the cabinet for maintencance, etc.). The air conditioning (AC) used to control the electronics cabinet of OSIRIS is located on top of the cabinet and is equipped with sensors to report the situation inside the cabinet by monitoring the incoming and outgoing air streams. A LabVIEW software that serves as a low-level command and control was created and connected to a consecutive EPICS GUI which can be used from within the whole JUNO on-site network. In addition, all relevant values of the system are reported to the archiver appliance. Since the environmental situation in the cabinet is very

crucial, an additional sensor system has been placed in the cabinet that reports directly to the JUNO general detector control system to provide values in the case of a system failure of the OSIRIS control computer.
The expert mode of the GUI is capable of controlling all settings of the AC, with the limits of temperature and humidity being the most important. The situation in the cabinet is displayed both as a current value and as an archiver readout. A picture of the GUI can be found in figure 7.12.

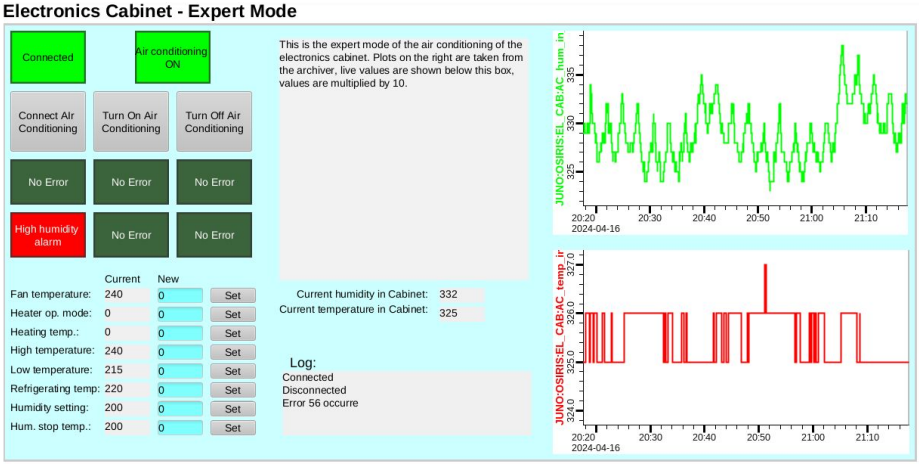

Figure 7.12: Expert mode of the AC controlling GUI. On the top left the different flags of the system can be seen. Bottom left, the several control values of the system can be set. Mid features the current values of temperature and humidity, as well as the activity log. On the right, the time development of these two values can be found as read out of the archiver appliance.

7.4.5 PC monitoring

The final relevant GUI of OSIRIS that has been created within the scope of this work is the PC monitoring GUI. Consisting of a sub-GUI for each computer of OSIRIS, it shows all relevant hardware performance parameters of these machines. This includes: Root sorter PC, event builder PC, the support PCs 1 and 2, the server PC, the LHS PC and the calibration computer. Although not all PCs share the same operating system, all report the same values to EPICS which are then read by the archiver appliance and the GUI. Since these sensors are read-only, the GUI is always in monitoring mode. The values reported by the GUI are: CPU load and temperature, the load of the network interface card, the used space of the hard disks and the amount of memory currently

used. Additional values (e.g., additional temperatures) are available for debugging purposes but not reported to either the archiver or the GUI. A picture of the PC monitoring GUI can be found in figure 7.13.

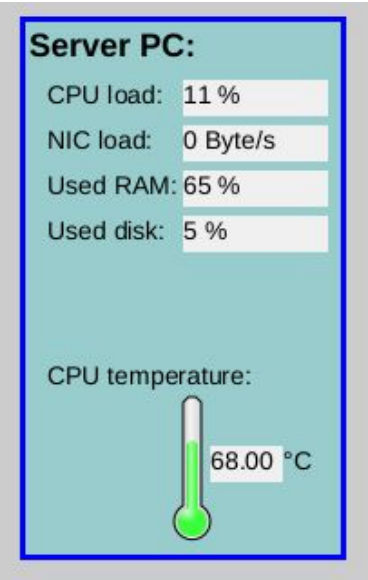

Figure 7.13: Snipped of the PC-health GUI, displaying the reported values of the Server PC. By combining eight of these GUIs, one for each of the computers used in OSIRIS, the final PC health GUI is created. Each individual field of the GUI contains value limits and will trigger an alarm when these limits are reached.

Chapter 8

Conclusion and Outlook

"I will not say: Do not weep; for not all tears are an evil"
-Gandalf the White

from "The Lord of the Rings - The Return of the King" by J.R.R.

Tolkien, 1955

The Jiangmen Underground Neutrino Observatory (JUNO), located in southwest China, aims to determine the neutrino mass ordering with a significance of $3\,\sigma$ within the next 6.5 years. It will use two nearby nuclear power stations as neutrino sources and feature an unprecedented energy resolution of $3\,\%/\sqrt{E[MeV]}$. Several requirements on detector design and background arise that require careful choosing and testing of the materials used. These requirements not only include the precise testing and characterizing of all PMTs used in JUNO, but also the keeping of limits of radioactive backgrounds in the liquid scintillator. Especially reducing backgrounds that might mimic the signals of the inverse beta decay (IBD), which is used to detect neutrino interactions in JUNO, is of high importance. To maintain these limits of $10^{-15}\,g/g$ (IBD) and $10^{-16}\,g/g$ (solar) of uranium and thorium in the LS, the Online Scintillator Internal Radioactivity Investigation System (OSIRIS) was created. Using the same PMTs and electronics as JUNO and a vessel with a capacity of 18 t of LS, OSIRIS will be monitoring the radioactivity levels of the LS during the six-months-long filling phase of JUNO. OSIRIS features 76 PMTs, 12 of them located within a water Cerenkov muon veto and 64 in the inner detector, which

will be calibrated by two independent calibration systems (the Automated Calibration Unit (ACU) and the Laser Calibration System (LCS)) on a weekly basis. In the scope of this work one of the calibration systems, the LCS, was developed, built, tested and installed on-site in OSIRIS. This laser calibration system consists of two parts: The light distribution system (LDS) and an array of 24 diffuser capsules, which are distributed in the detector volume. The system is driven by a pico-second laser, featuring a pulse width of $\approx 80\,\text{ps}$. It is connected to an opto-mechanical cascade, which distributes the signal to 36 output channels. Twelve of these output channels can be controlled individually with the remaining 24 channels being controllable in pairs.

It was shown that the developed LDS does not change the timing profile of the laser and that a timing calibration of the OSIRIS detector is possible using this system. Additionally, a thorough calibration of the LDS has been performed, resulting in correction values for the light output of each optical channel of the system, reaching from $0\,\%$ to up to $45\,\%$. The simulation used to determine the positions of the diffusers was explained as well as the result and the final placement of all 24 diffusers. A final comparison of the illumination levels between the simulation and the actual measurement found that the design goal of an illumination within a rough factor of two has been met.

Furthermore, an analysis of the first set of data taken with the system in March 2024 was presented. As a result, it could be shown that the system works as expected and that a mapping of the detector with the system was possible. Additionally, a measurement of several PMT parameters has been performed and successfully compared with the values taken with the same PMTs during the PMT characterization campaign of JUNO. The parameters determined include the gain of the PMTs (with a resulting mean of $1.33 \cdot 10^7$), signal-to-noise ratio (mean 8.21), peak-to-valley ratio (mean 2.73), charge resolution (mean $35.55\,\%$) and transit time spread (high gain mean $8.9\,\text{ns}$). As an additional cross-check, correlation plots have been created demonstrating the expected correlations between gain, peak-to-valley ratio, signal-to-noise ratio and time transit spread. Hence, the laser calibration system could be declared operational, working within its design parameters and fit for the optical calibration of the OSIRIS detector.

As the second part of this thesis, the slow control (SC) software developed within the scope of this work is presented. Besides the underlying LabVIEW software that controls the system on a hardware level, a focus was set on the Experimental Physics and Industrial Control System (EPICS), which is used as communication system for all parts of OSIRIS. Consecutively, the remaining parts of the slow control, (e.g., GUIs) built using the several EPICS extensions, have been presented.

Finally, the implemented EPICS archiver system has been presented, which is crucial for the control and logging of OSIRIS. This system archives all ≈ 500 process variables in OSIRIS, creating $\approx, 120\text{MB}$ of data per day. Additionally, this system provides a self-archiving database, as well as GUIs showing the temporal development of each process variable or provide additional information of the variables via database query.

OSIRIS will start the regular operation in the beginning of 2025. More advanced analysis methods of the calibration data are already in development and will be in place by then, providing a general time and charge calibration of the detector. The resulting values will be used by passing the values into a database which can be read by the online analysis framework of OSIRIS. Additionally, more statistics will be available, providing the opportunity of analyzing the time development of the detector. Some possible improvements and tests should be considered. These include a per-channel comparison of the resulting PMT parameters with the database, a HV-gain scan for performance optimization and a comparison of the laser calibration data with the data acquired by the ACU. Furthermore, the final commissioning of OSIRIS and the whole LS production chain will provide a good test of both, the slow control of OSIRIS and the archiver appliance. In the end, OSIRIS will have a future beyond its primary purpose of ensuring the purity of LS for JUNO. An additional (physics) program is planned, either as a test bed for the $0\nu\beta\beta$ future of JUNO, or in the form of the SERRAPIS extension of OSIRIS, which could be probing the neutrino production cycles of the sun.

Appendix A

List of EPICS process variables of OSIRIS

Table A.1: List of PVs used in the LabVIEW based SC of the LDS of OSIRIS.

PV	Type	Comment
JUNO:OSIRIS:LDS:set_channel_num	int	current channel
JUNO:OSIRIS:LDS:error_occured	bool	error flag
JUNO:OSIRIS:LDS:error_message	string	error message thrown
JUNO:OSIRIS:LDS:laser_on	bool	status of the laser LED
JUNO:OSIRIS:LDS:tuning	float	breightness of the laser
JUNO:OSIRIS:LDS:client_do_channel_to_set	int	channel setter input
JUNO:OSIRIS:LDS:client_do_set_channel	bool	channel setter flag
JUNO:OSIRIS:LDS:client_do_tuning_to_set	float	tuning setter input
JUNO:OSIRIS:LDS:client_do_set_tuning	bool	tuning setter flag
JUNO:OSIRIS:LDS:client_do_laser_off	bool	turn laser emission off
JUNO:OSIRIS:LDS:client_do_laser_on	bool	turn laser emission on
JUNO:OSIRIS:LDS:emergency_stop	bool	turn of laser and lock system in safe mode

Appendix B

Technical drawings of the diffuser capsule

In this chapter, all relevant technical drawings of the diffuser capsule and their holders are given. Chosen materials are stainless steel 316L/1.4404 (all metal parts), as well as PTFE (diffuser bulb and seal of the capsules). All technical drawings were created using Autodesk Inventor 2020. Parts them selves were developed in collaboration with Norbert Stockmaier, Rainer Othegraven and Yatian Pei.

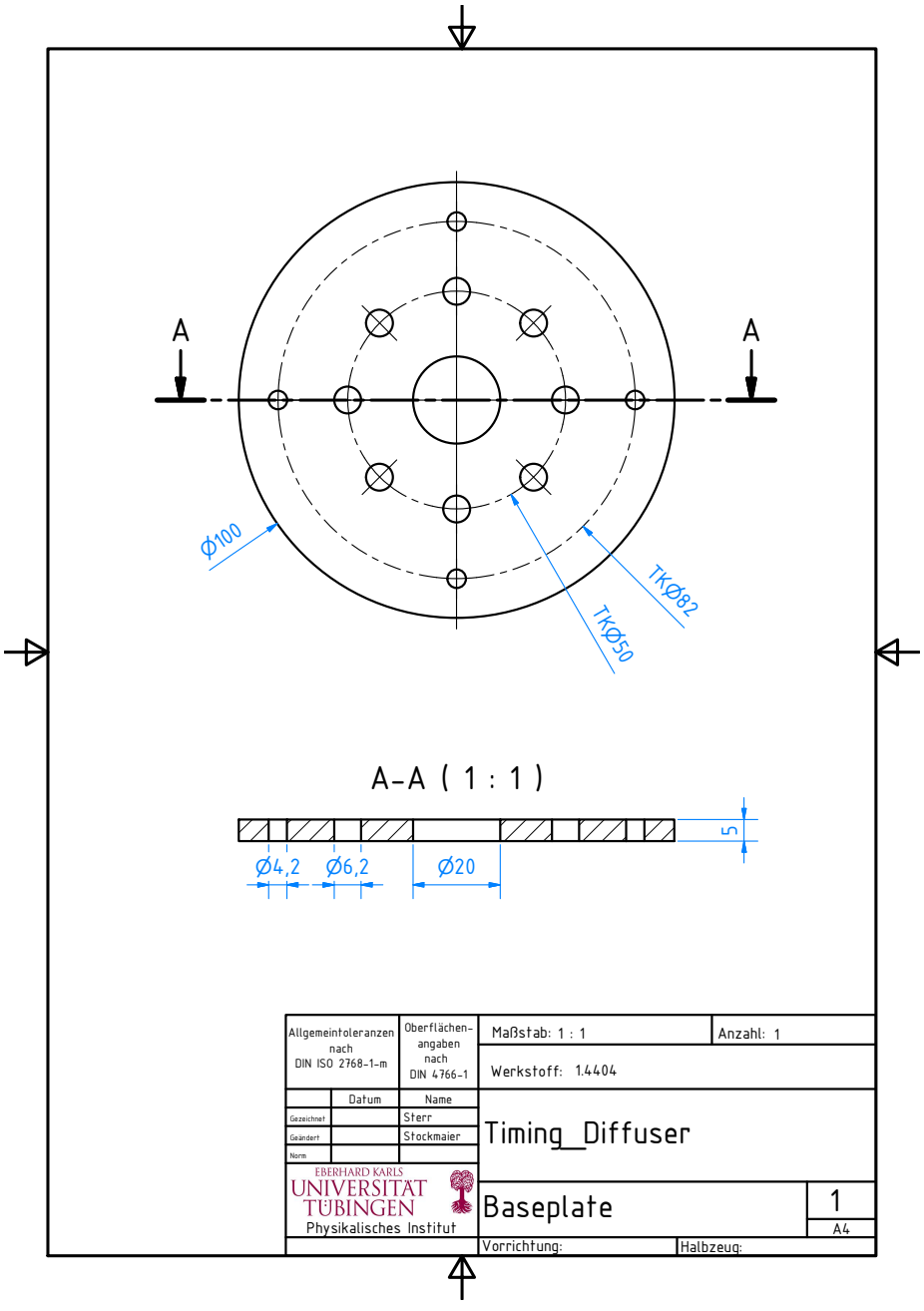

Figure B.1: Base plate of the diffuser capsule

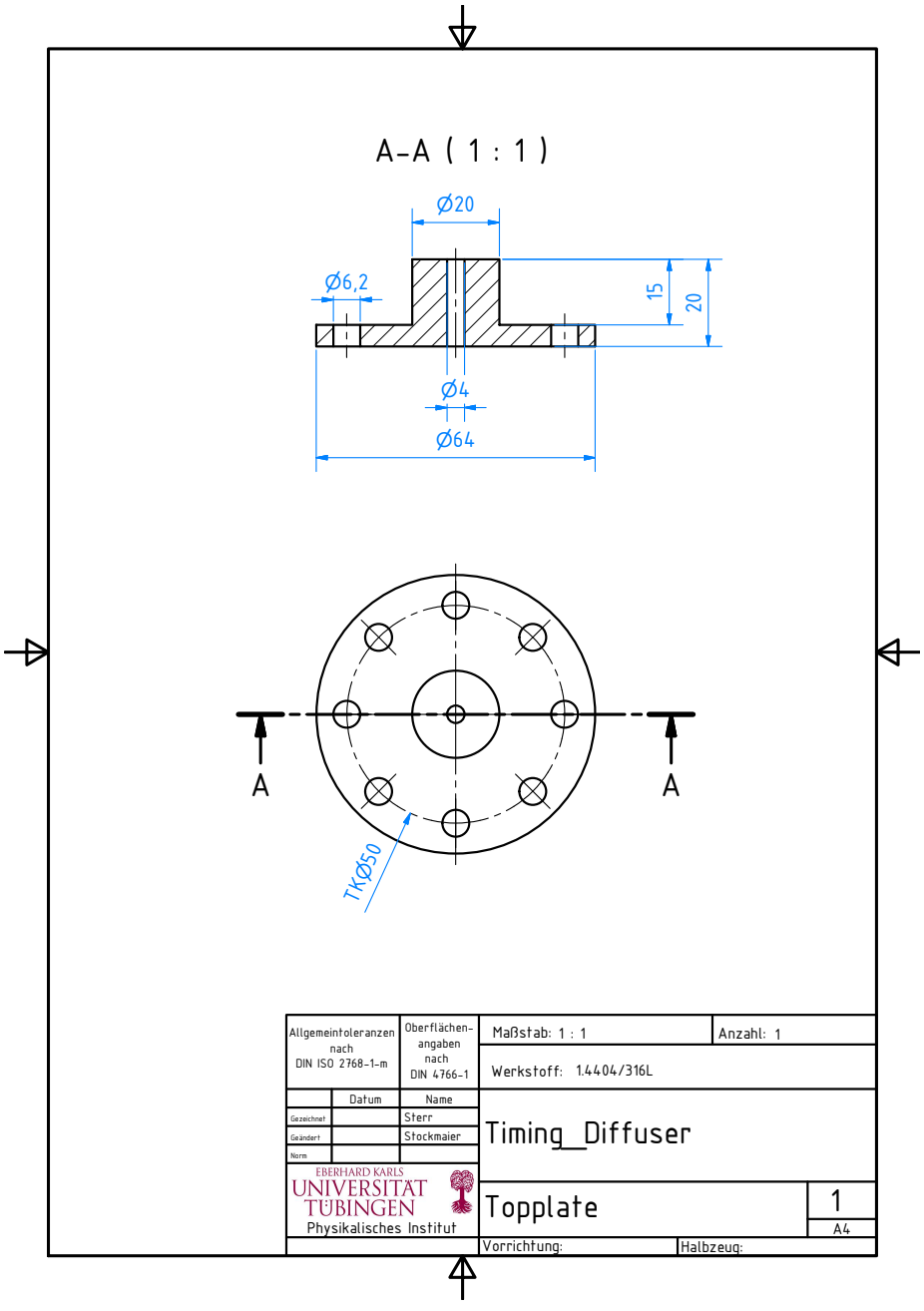

Figure B.2: Top plate of the diffuser capsule.

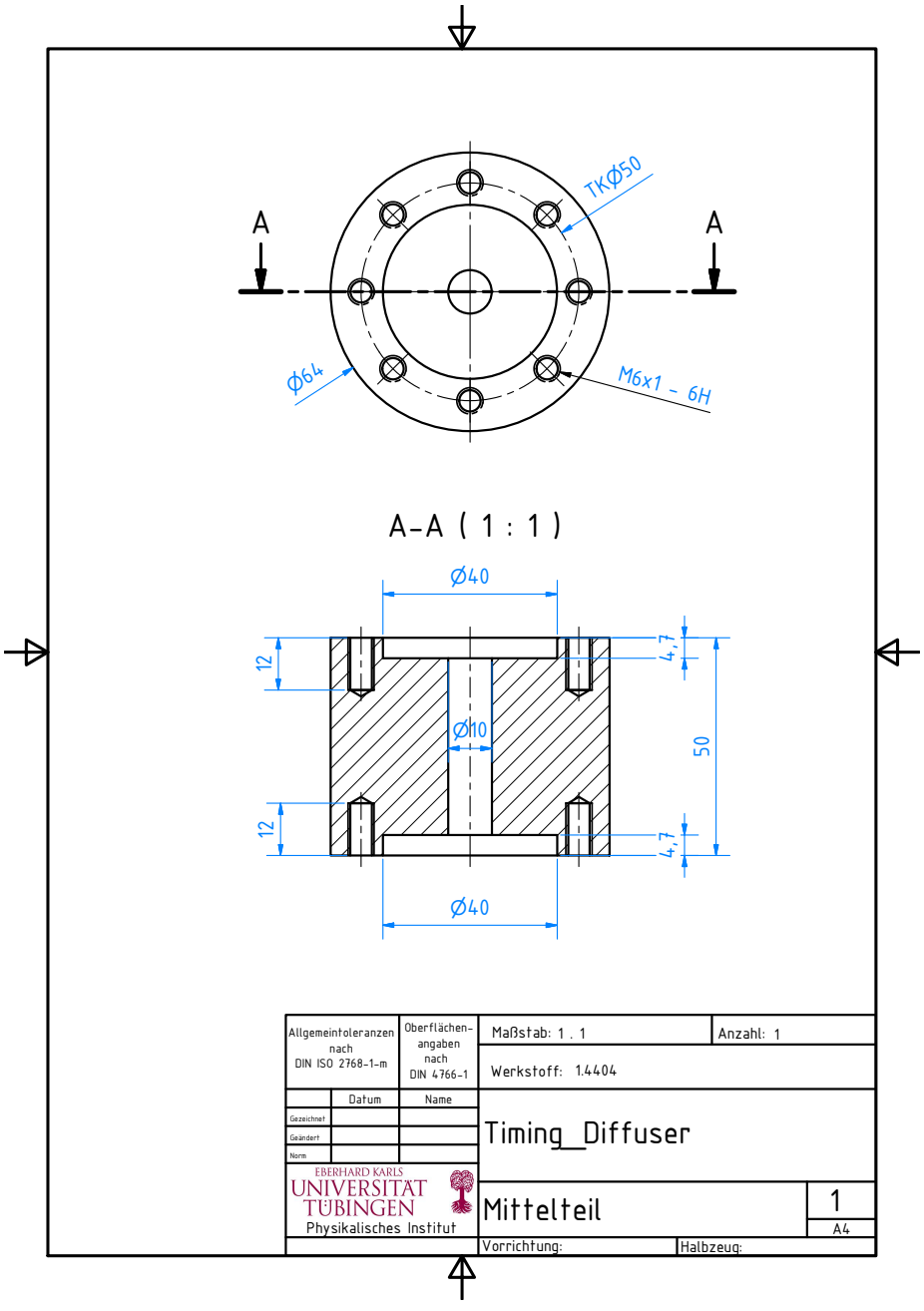

Figure B.3: Body of the diffuser capsule.

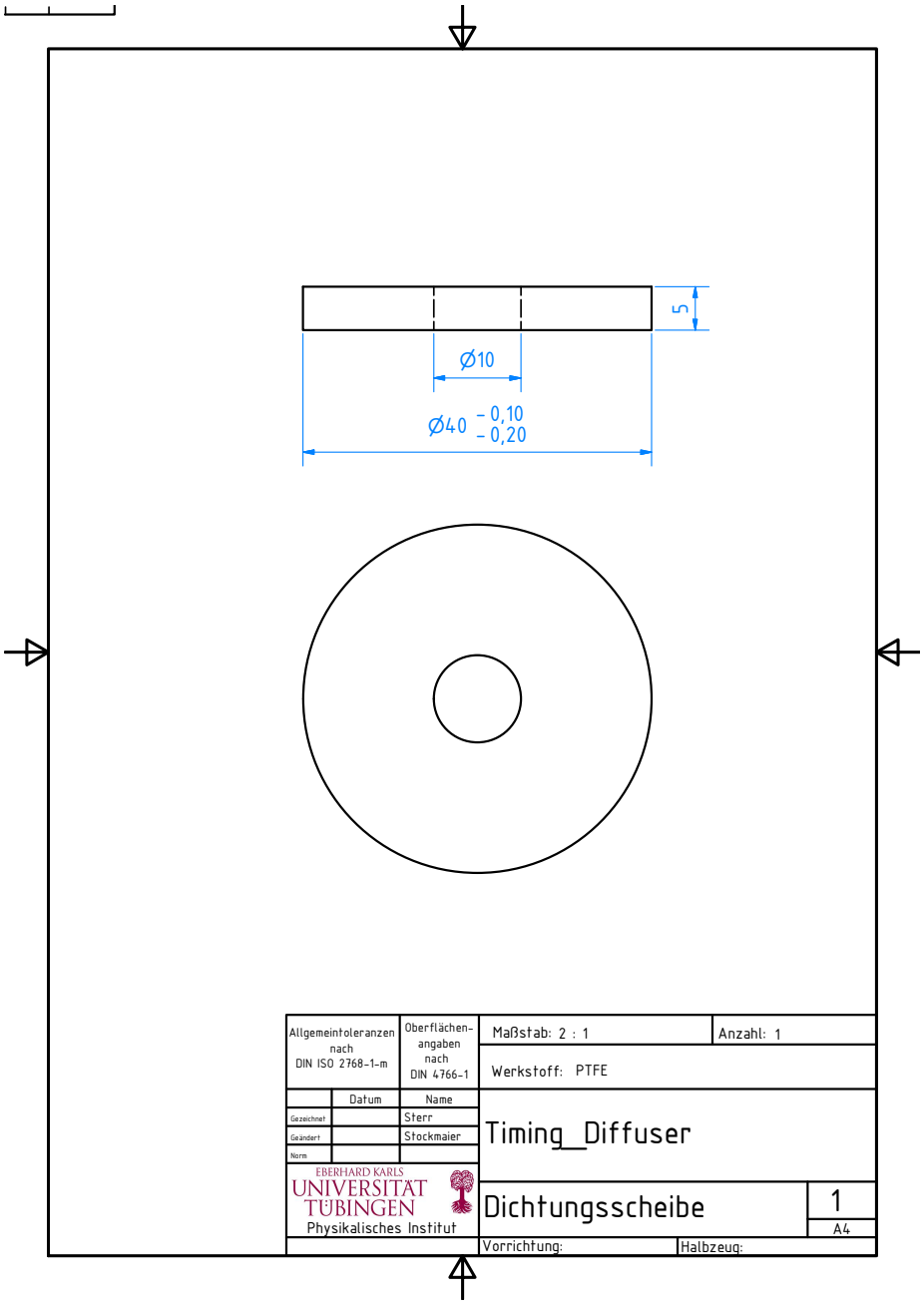

Figure B.4: PTFE sealing plate of the diffuser capsule.

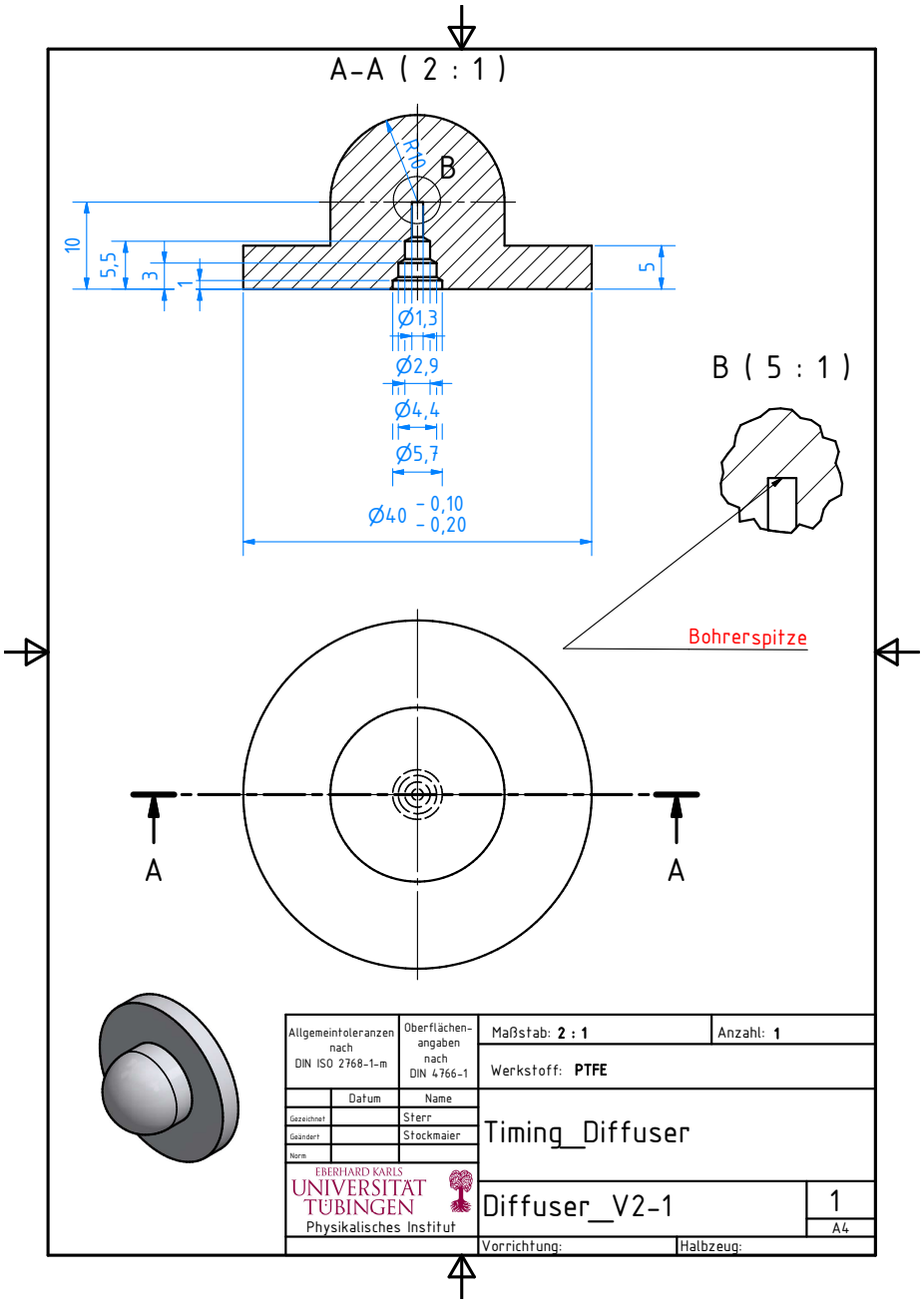

Figure B.5: Diffuser bulb of the diffuser capsule.

Appendix C

Technical drawings of the diffuser holders

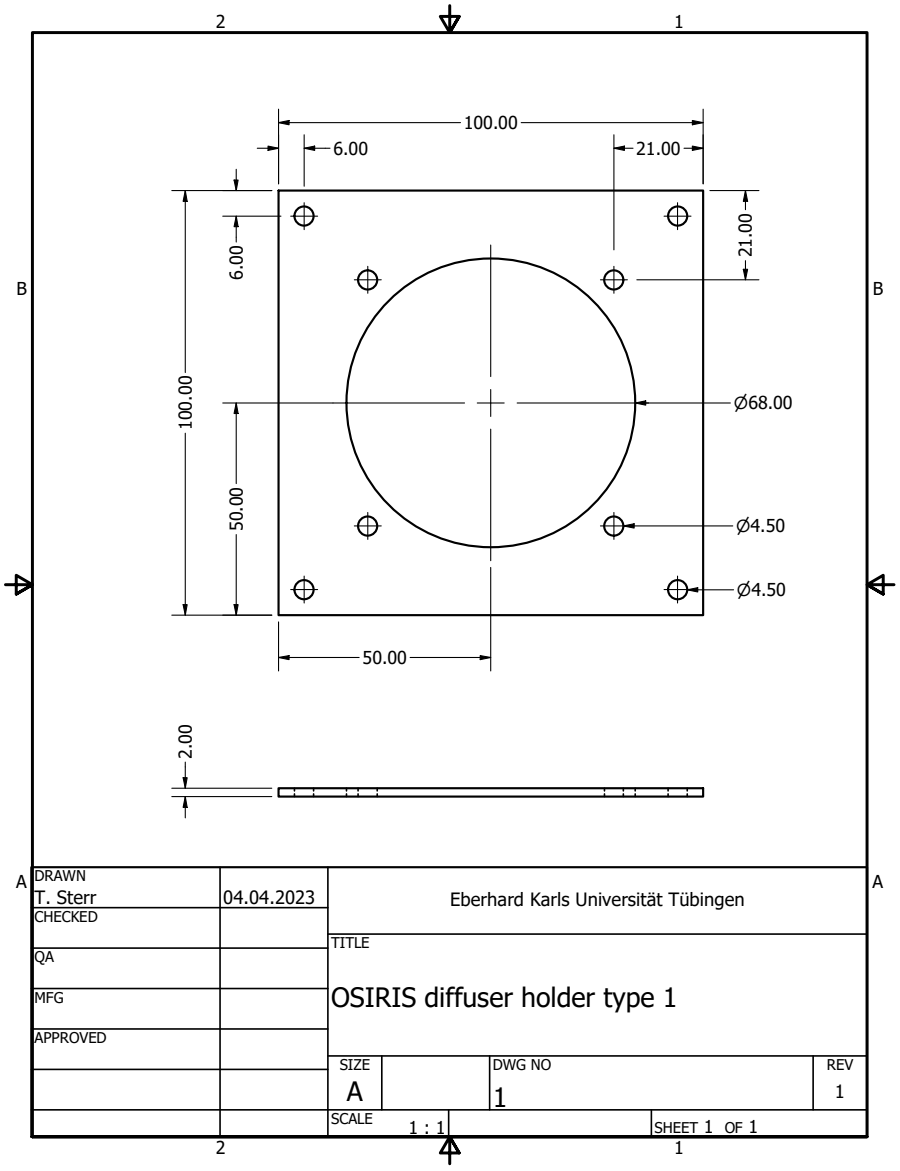

Figure C.1: First type of the holder plate of the diffusers of the LDS.

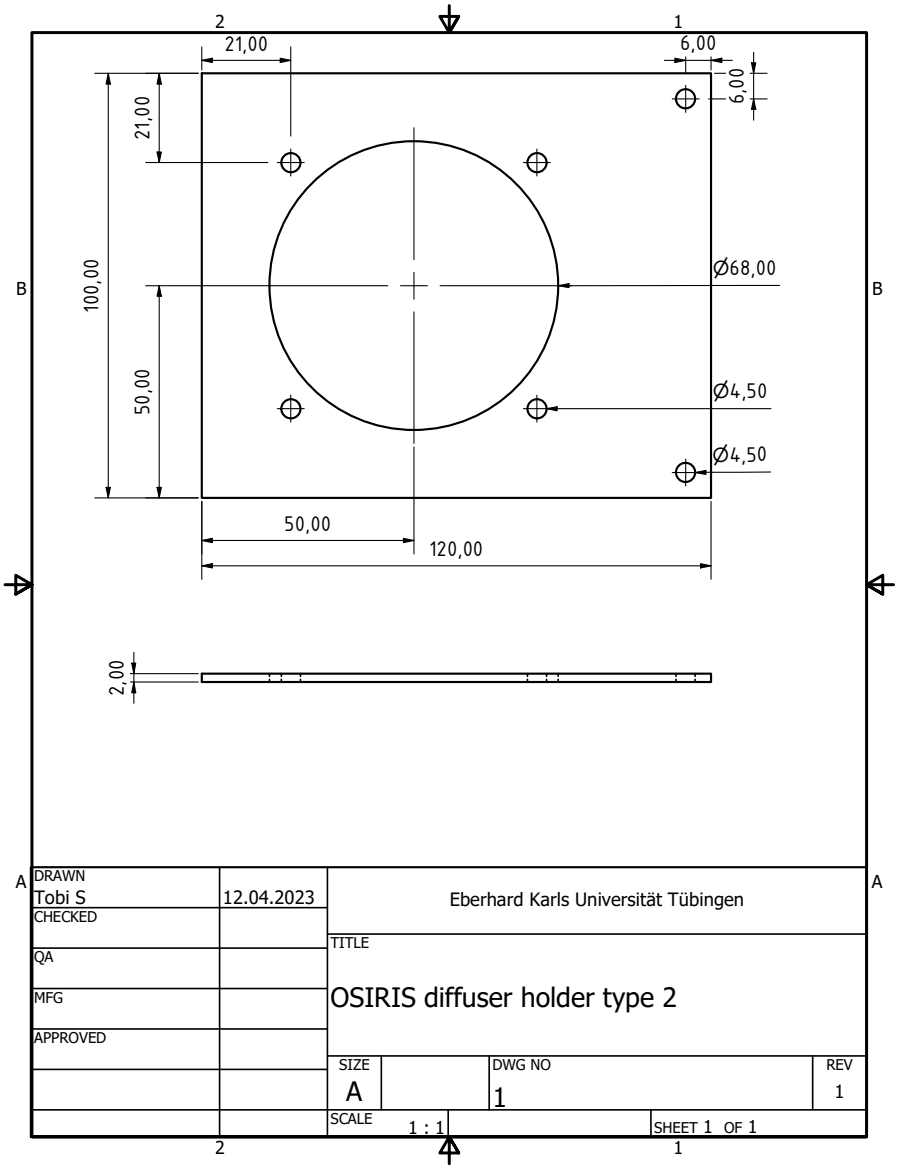

Figure C.2: Second type of the holder plate of the diffusers of the LDS.

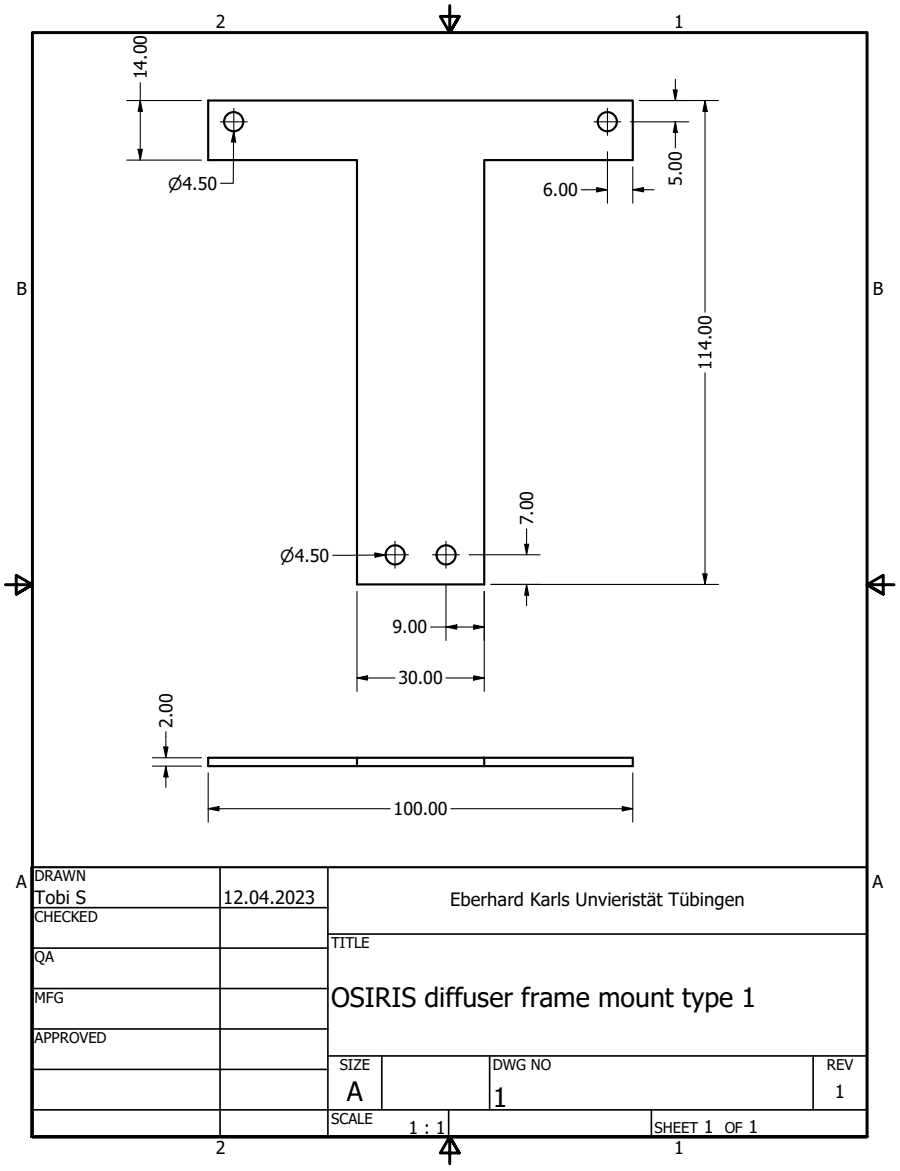

Figure C.3: PMT frame mount of the diffusers to be used on top of the frame.

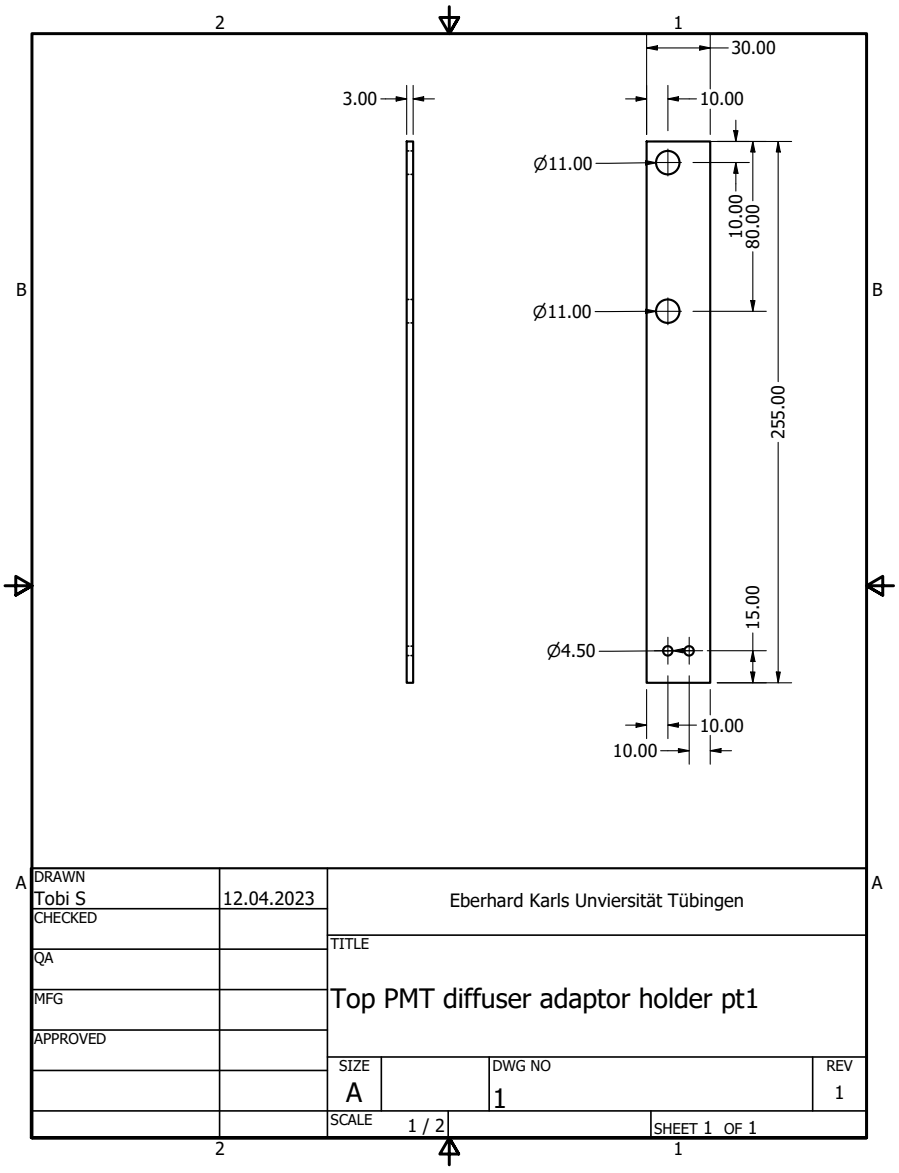

Figure C.4: First part of the diffuser holder adaptor of the diffusers mounted to the PMTs above the AV.

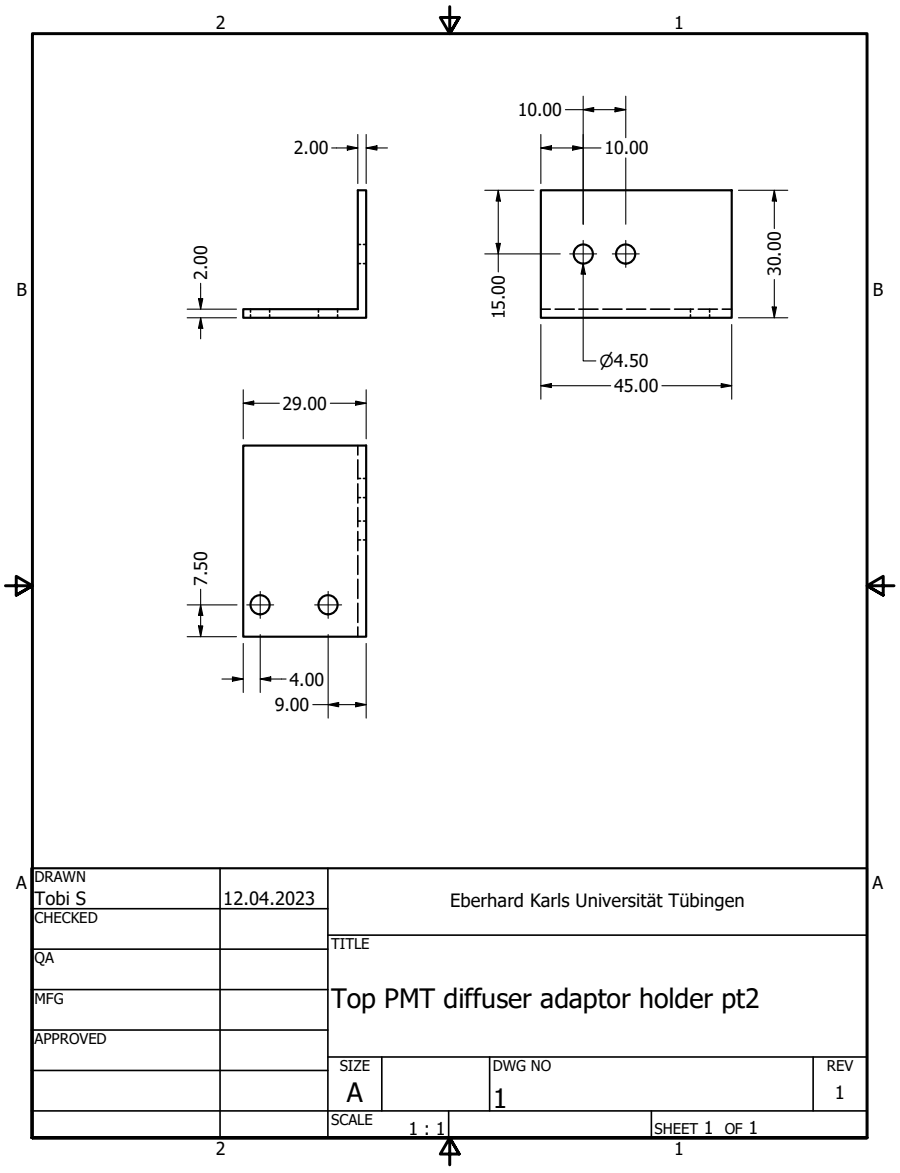

Figure C.5: Second part of the diffuser holder adaptor of the diffusers mounted to the PMTs above the AV.

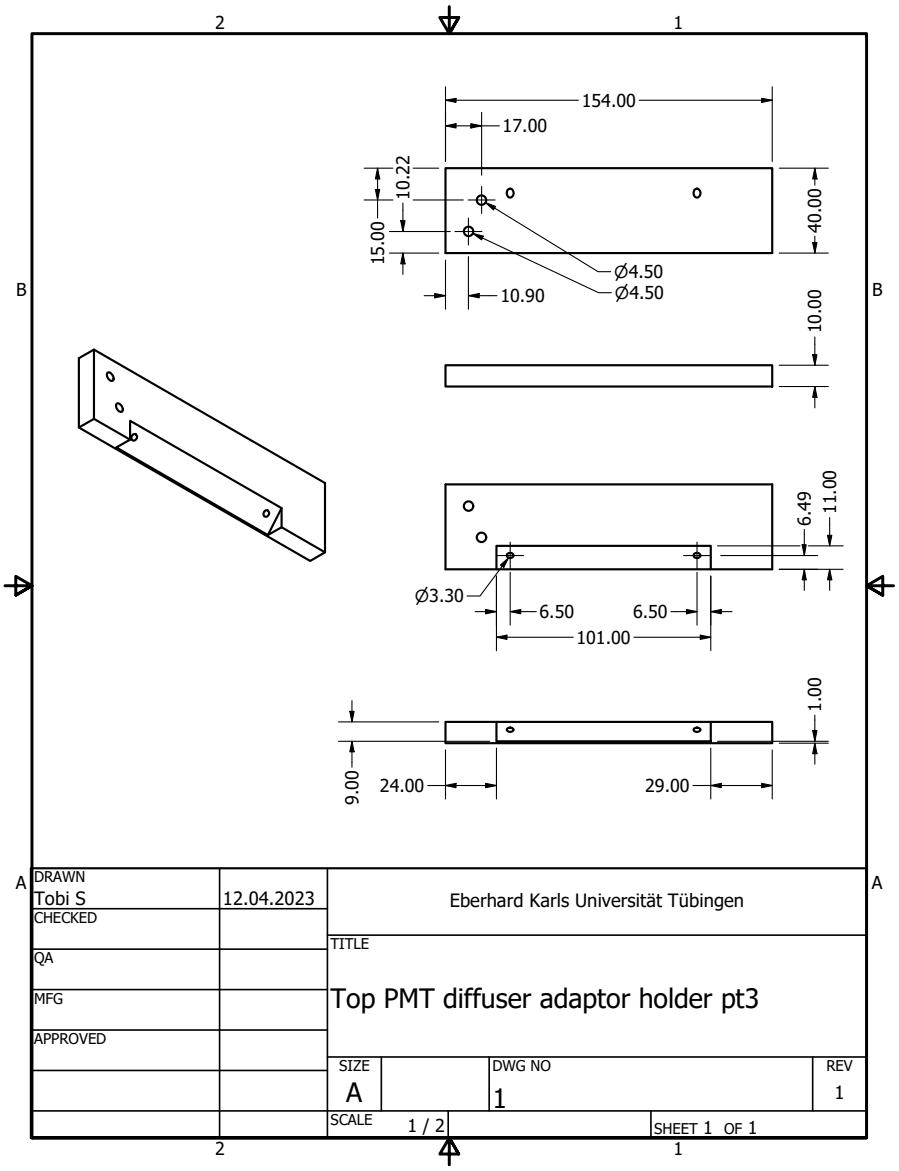

Figure C.6: Second part of the diffuser holder adaptor of the diffusers mounted to the PMTs above the AV.

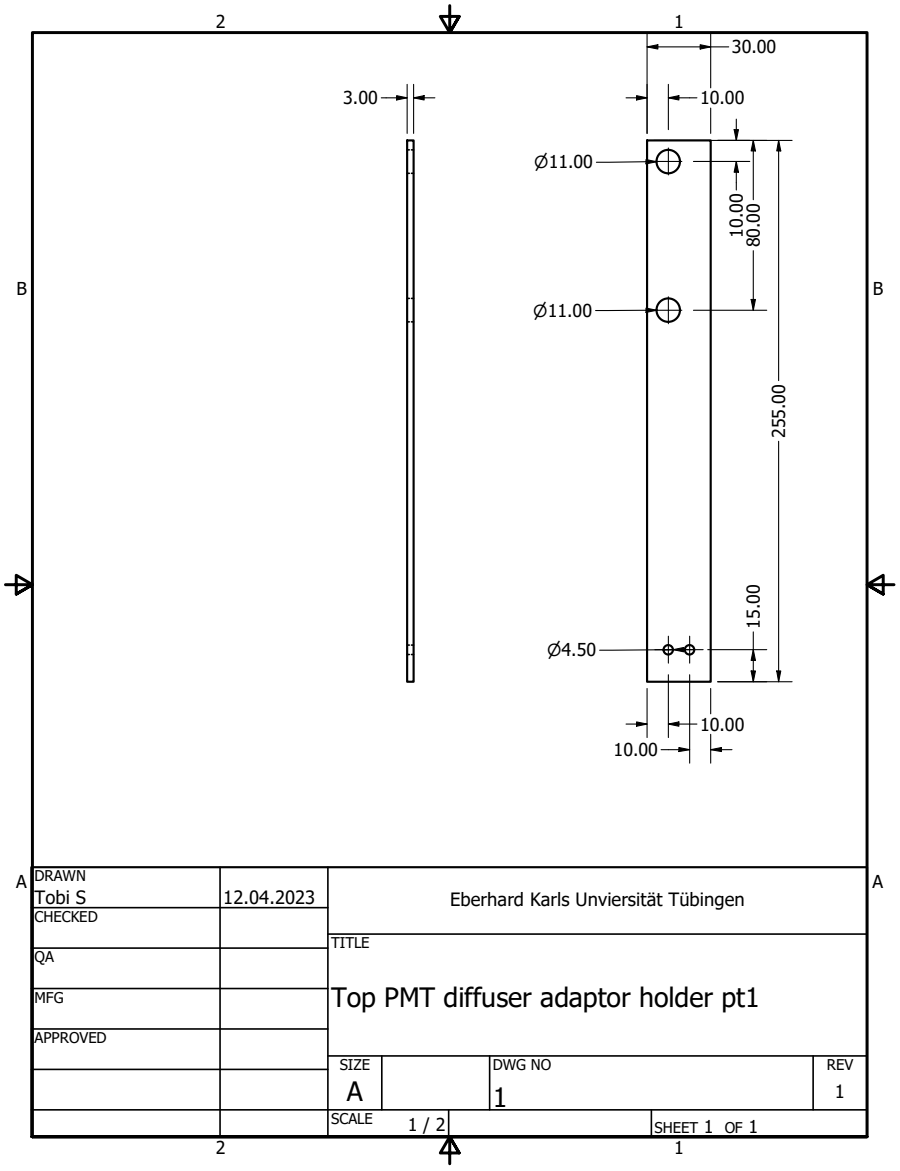

Figure C.7: First part of the diffuser holders located bellow the AV.

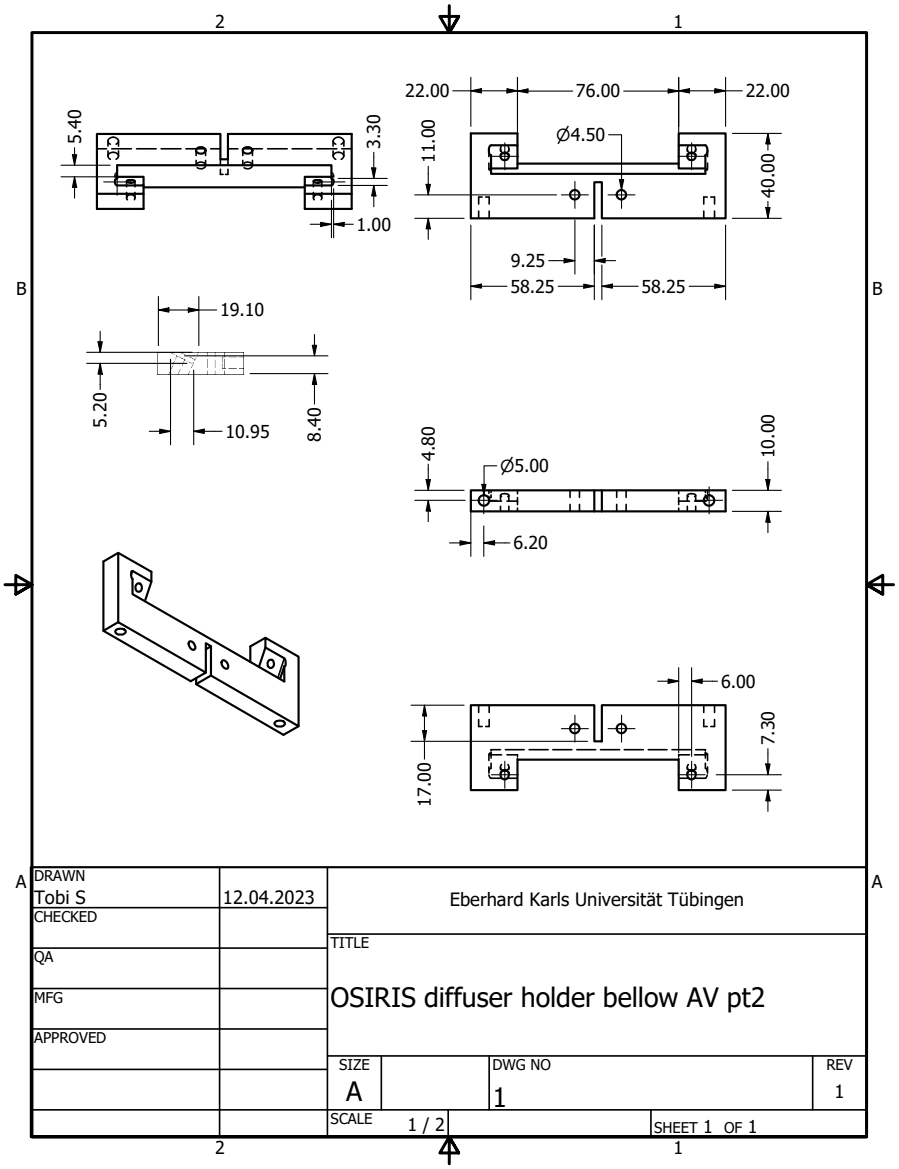

Figure C.8: Second part of the diffuser holders located bellow the AV.

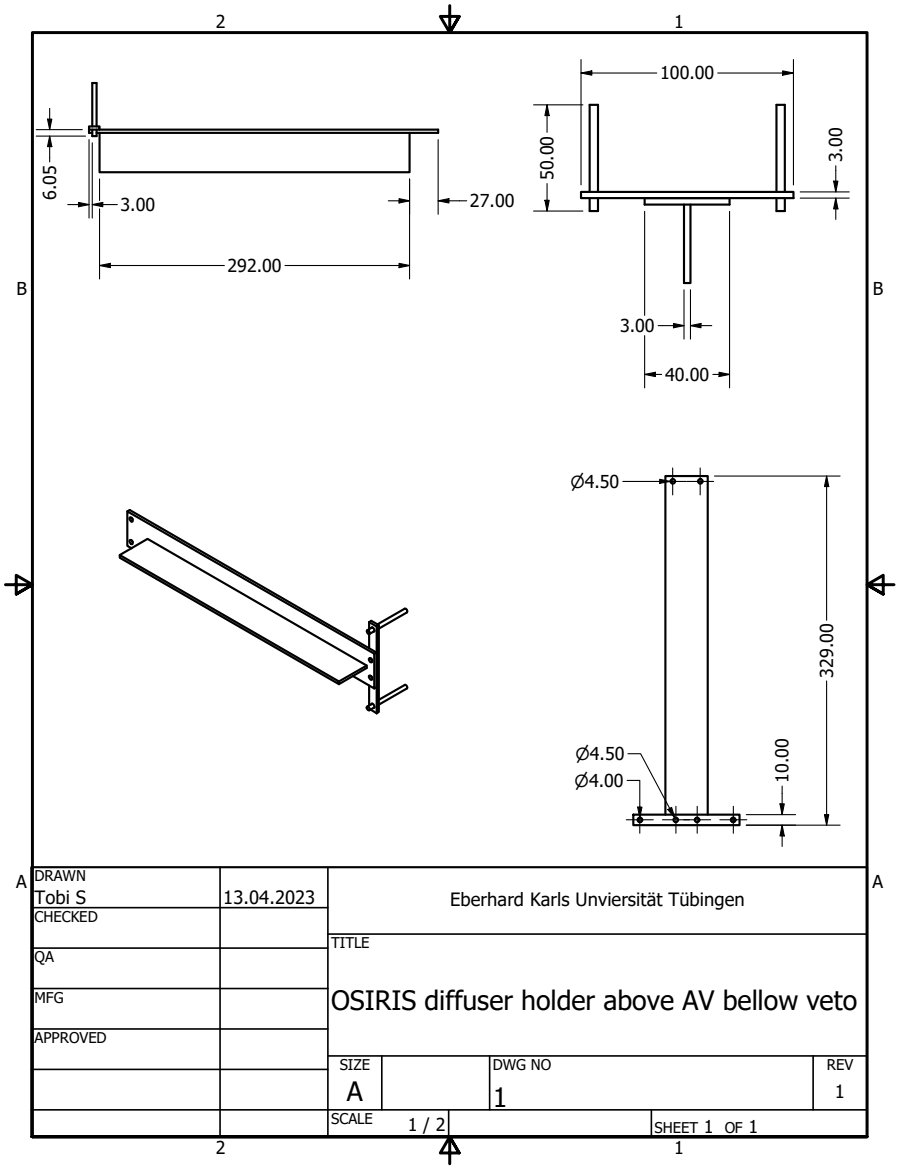

Figure C.9: Caption

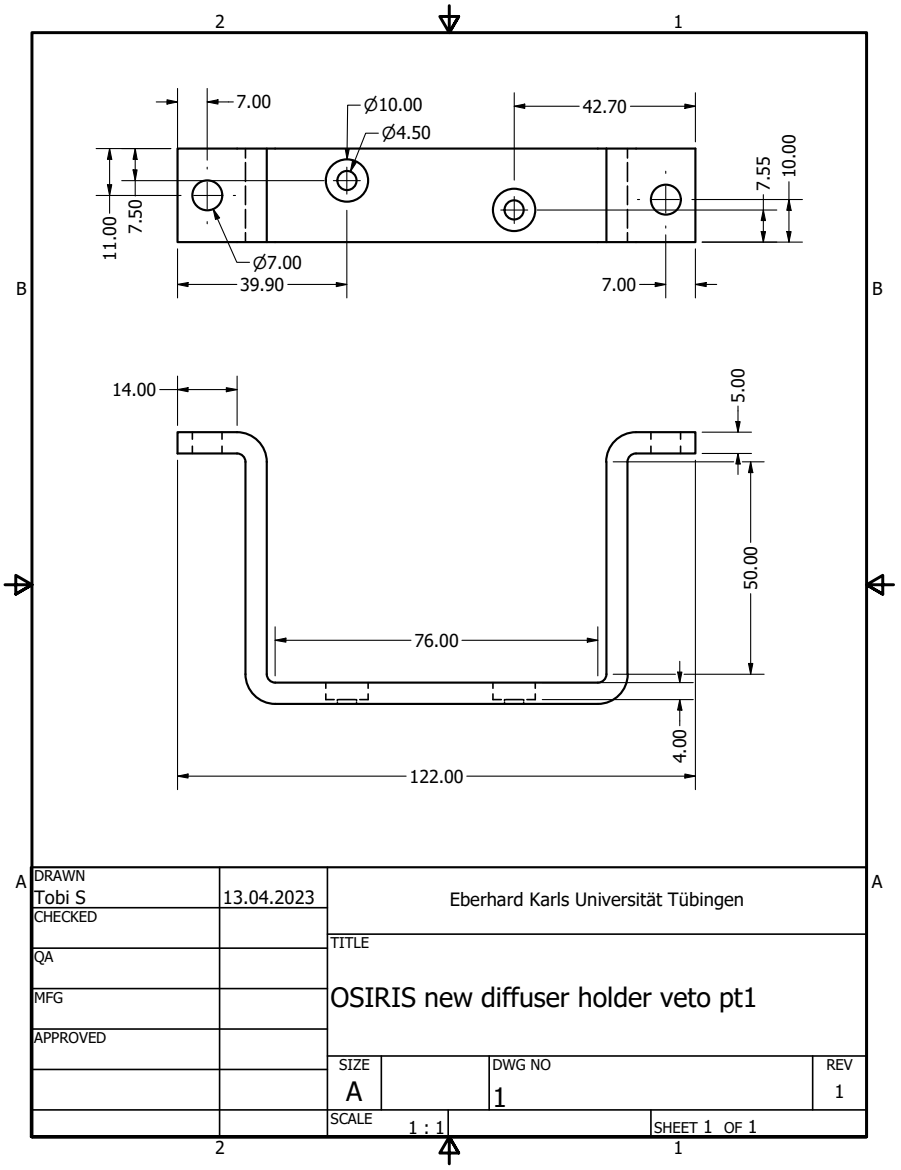

Figure C.10: First part of the new version of the diffuser holders to be used in the veto of OSIRIS.

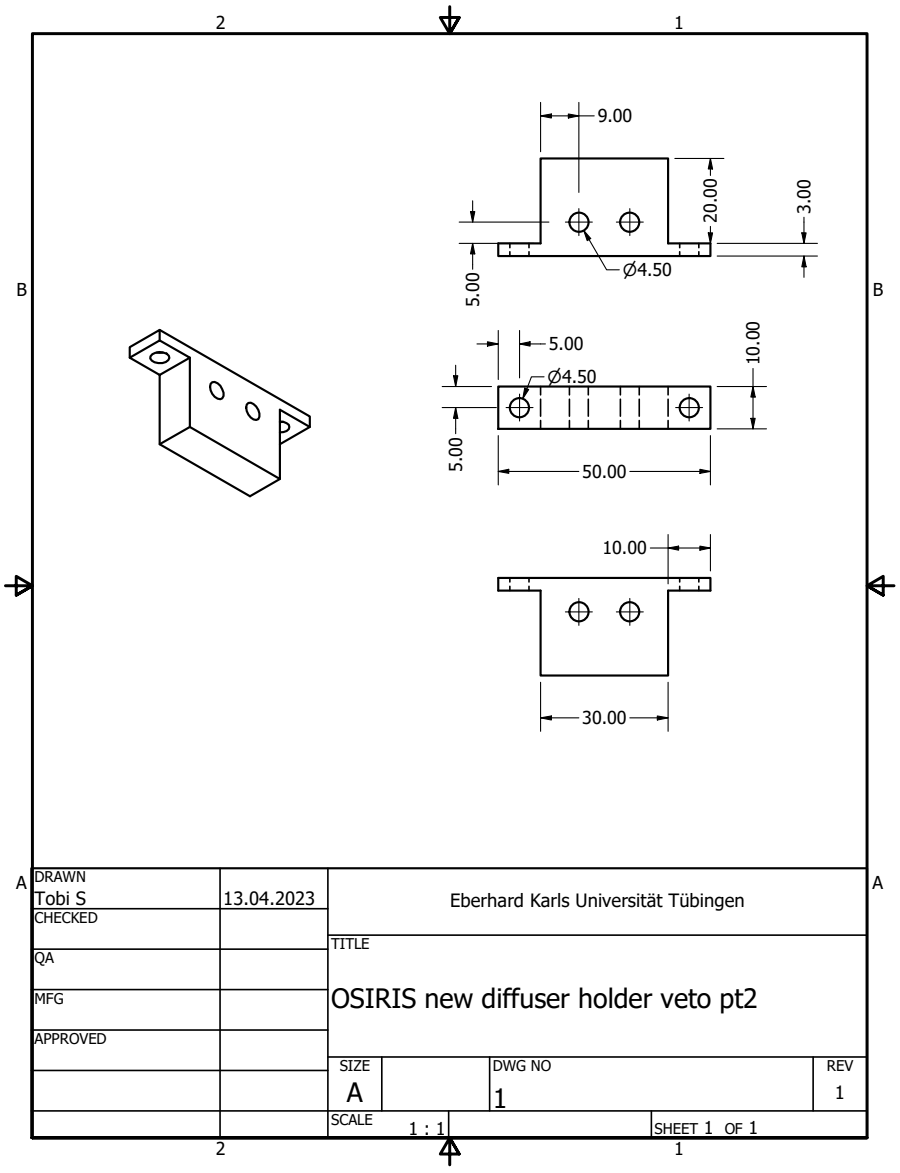

Figure C.11: Second part of the new version of the diffuser holders to be used in the veto of OSIRIS.

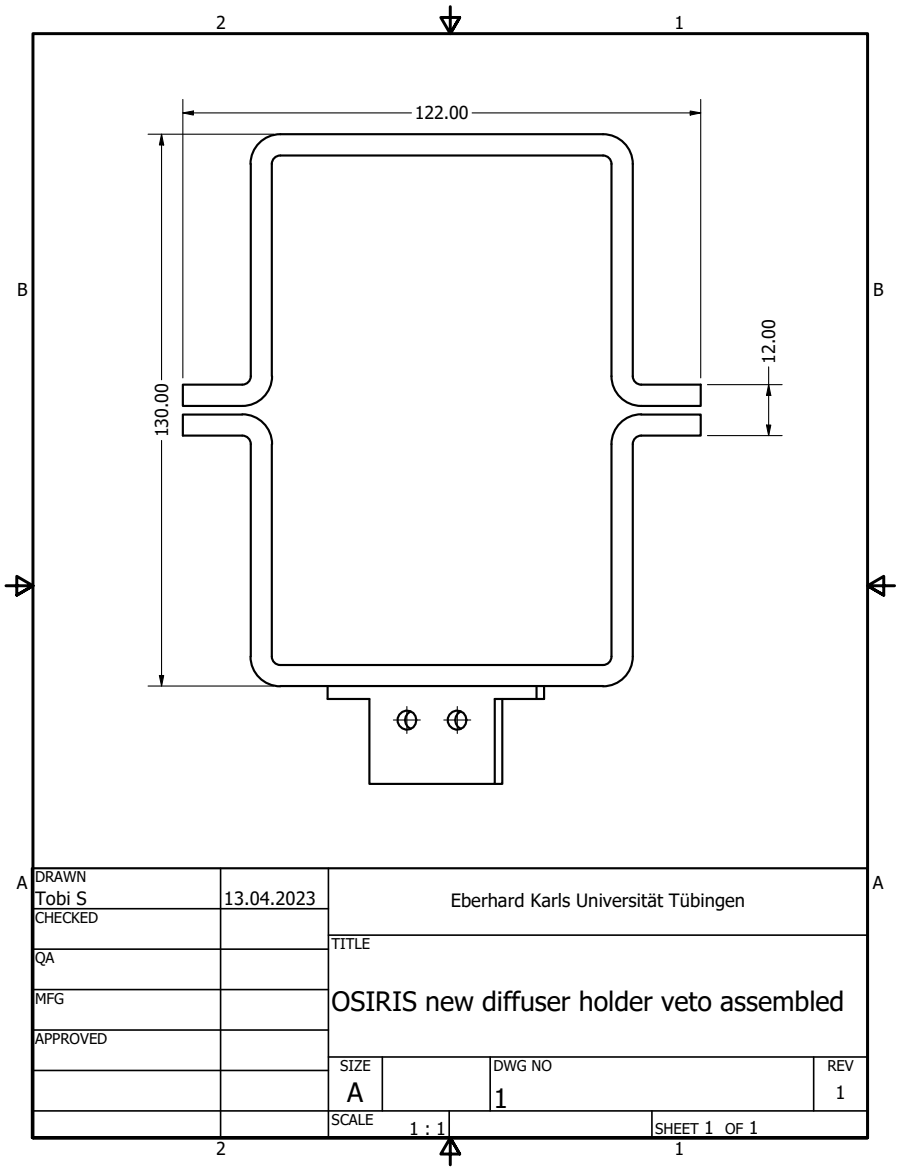

Figure C.12: Assembly of the complete new diffuser holder that is used in the muon veto of OSIRIS.

Appendix D

Technical drawings of the case of the LDS

Technical drawings of the different parts of the light distribution system. In addition to the parts displayed here, a 19" standard rack-mount was used.

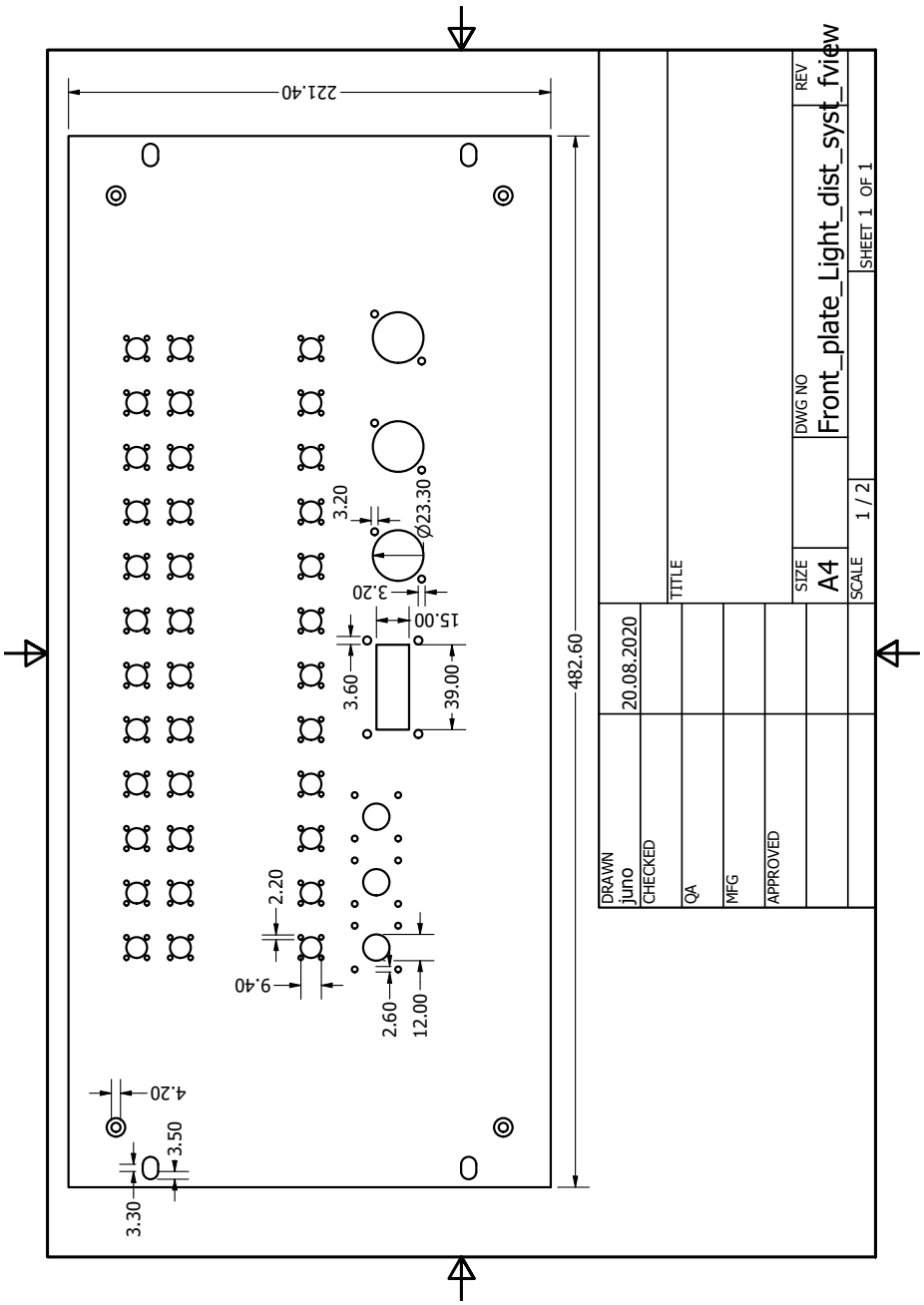

Figure D.1: Front plate of the LDS as used in this work. Large rectangular port is the connector for the laser head, small round ports for power of the optical switches and large round ports for controlling the switches. Ports in three rows are the FC/PC connectors of the fibers.

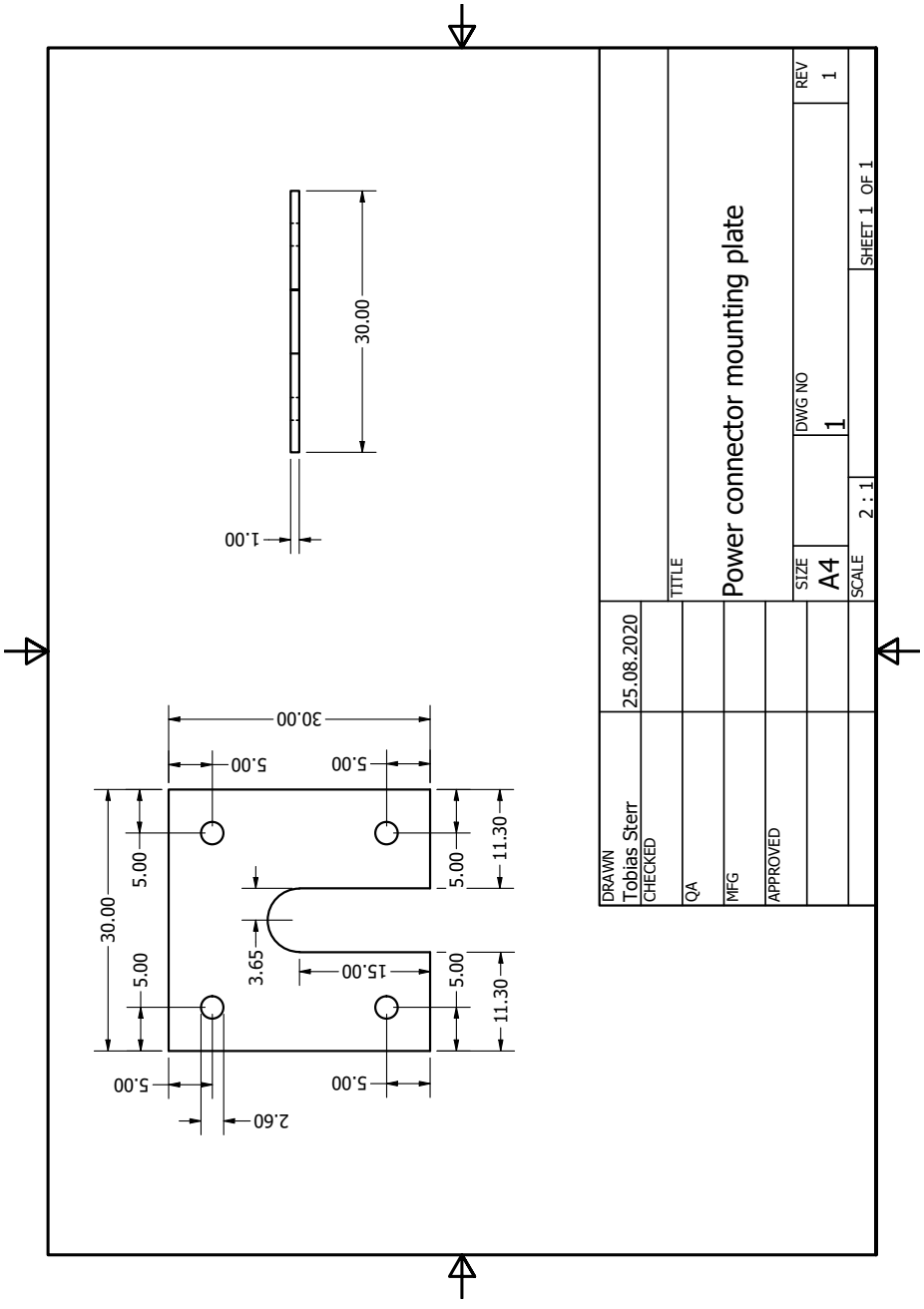

Figure D.2: Holding adapter plate of the power connectors of the optical switches of the LDS.

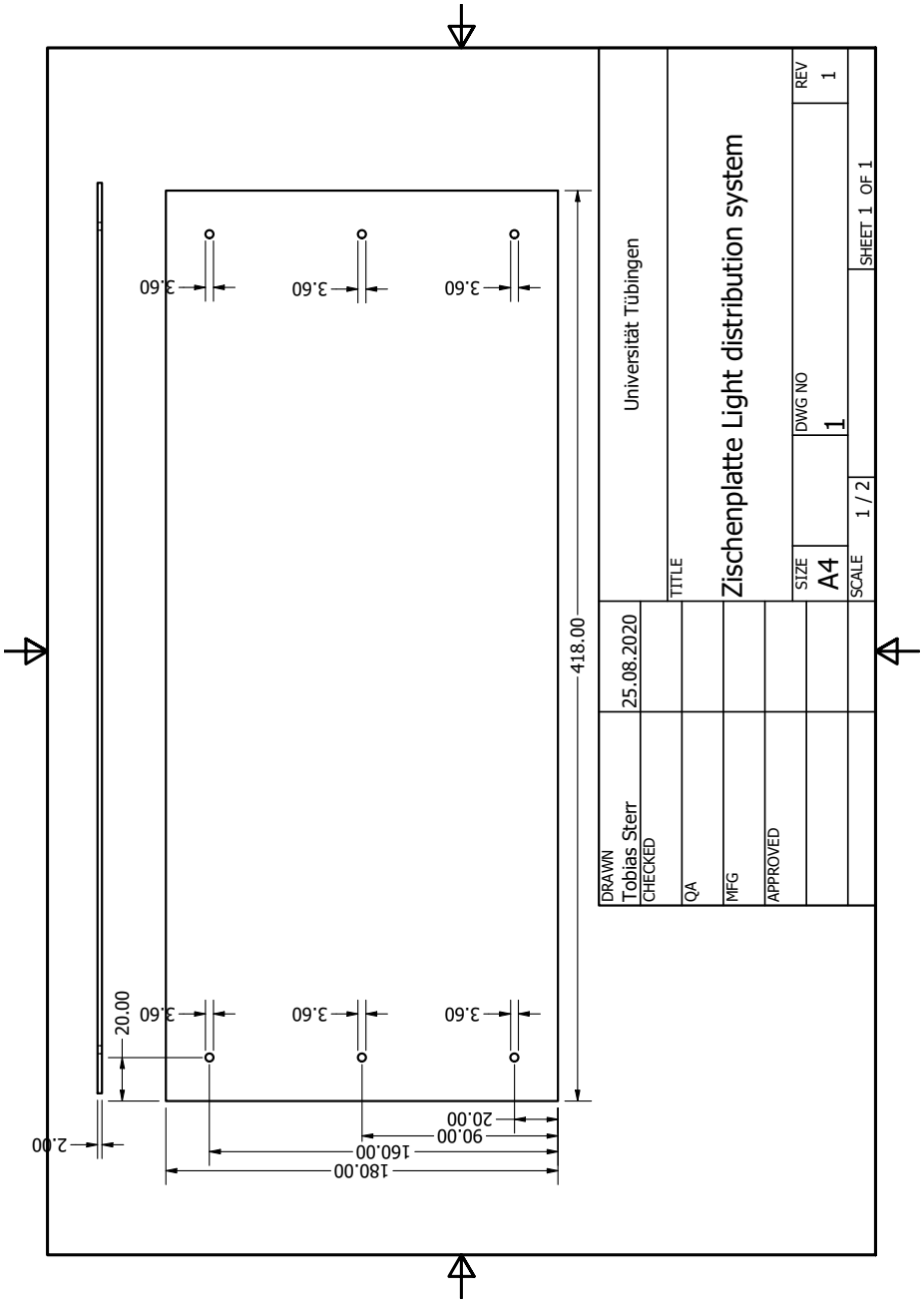

Figure D.3: Holding plate of the 50 %:50 % beam splitters of the LDS. The plate is installed in side the LDS box and can't be accessed from the outside.

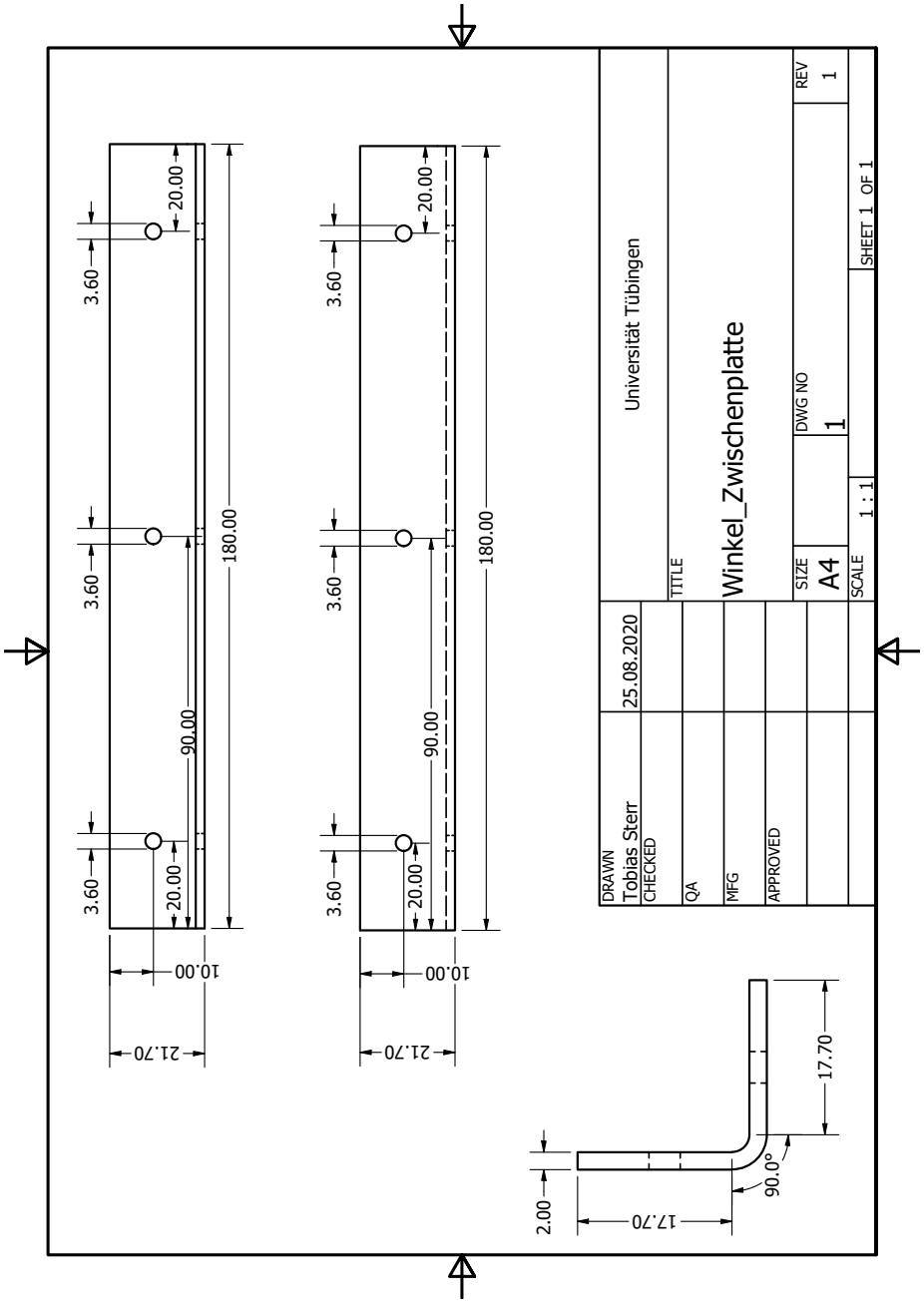

Figure D.4: Holding brackets of the mounting plate of the beam splitters. Brackets are mounted to the side of the LDS box.

Appendix E

Light intensity calibration values

Table E.1: Calibration values of the light intensity of each channel of the LDS. Values are in units of photo electrons (p.e.) and in respect to channel 23. Further details can be found in section 5.6.2.

Channel	Value [p.e.]	Channel	Value [p.e.]
1	0.2081	19	-0.0328
2	0.2728	20	-0.3821
3	0.276	21	0.0172
4	0.2107	22	-0.391
5	0.2701	23	0
6	0.3016	24	-0.2745
7	0.1483	25	0.1127
8	0.2383	26	-0.1098
9	0.2758	27	0.0176
10	0.189	28	-0.2818
11	0.2651	29	0.0713
12	0.2782	30	-0.2978
13	-0.1984	31	-0.1069
14	-0.5781	32	-0.3553
15	-0.2451	33	0.1808
16	-0.6426	34	-0.1875
17	-0.1882	35	-0.1861
18	-0.5042	36	-0.7807

List of Figures

List of Tables

Glossary

$0\nu\beta\beta$ Neutrinoless double beta decay. 13, 15, 183

AC Air Conditioning. 146, 147, 196

ACU Automated Calibration Unit. 37, 46, 47, 50, 53, 54, 61, 62, 94, 95, 112, 143, 145, 146, 150, 151, 185, 187, 188, 196

ADC Analog-to-Digital Converter. 57, 58, 127, 129, 131, 133, 194, 195

ARM ARM Ltd, Cambrdige, UK. 57, 58

ASIC Application-Specific Integrated Circuit. 54, 57

AV Acrylic Vessel. 41, 43, 46, 47, 51, 61, 83, 84, 107, 112, 165–169, 186, 197

BEC Back-End Card. 58, 60, 113, 188

Bi Bismuth. 41, 42

CAD Computer-aided Design. 47–49, 51–53, 186, 187

CAS Chinese Academy of Science. 19

CE Collection Efficiency. 33

CLS Cable Loop System. 37, 185

CMB Cosmic microwave background. 6

CMOS Complementary metal-oxide-semiconductor. 79

Co Cobalt. 61

COSY Cooler synchrotron. 65

CPU Central Processing Unit. 58, 107, 147

Cs Cesium. 61

CSS Control Systems Studio. 64, 89, 92, 137, 143, 195

DAQ Data Aquisition. 31, 46, 56, 64, 65, 80, 94, 120, 122, 125, 131, 146, 188, 194

DC Direct Current. 58

DCR Dark Count Rate. 33, 142, 196

DSNB Diffuse Supernova Background. 20

DUNE Deep underground neutrino experiment. 7, 14

DVI Digital Visual Interface. 68

ELT Extremely Large Telescope. 20

EM Electro-magnetic. 20

EPICS Experimental Physics and Industrial Control System. 61, 64, 89, 90, 92, 93, 99, 114, 135–137, 139, 140, 145–147, 150, 191, 195, 200

FADC Flash Analog Digital Converter. 96, 121

FC/APC Fiber-optic connector standard. 68

FC/PC Fiber-optic connector standard. 71, 74, 176, 189, 197

FOC Filling-Overflow-Circulation. 35, 185

FPGA Field-programmable Gate Array. 57, 58, 94

FV Fiducial Volume (cut). 41, 45, 185

FWHM Full width at half maximum. 61

GALLEX Gallium-Experiment. 8

GCU Global Control Unit. 48, 58, 60, 75, 94, 96, 107, 113, 114, 121, 127, 142, 187–189, 196

Geant4 Geometry and Tracking 4. 83

GNO Gallium Neutrino Observatorium. 8

GUI Graphic User Interface. 5, 64, 92, 136, 137, 139, 143–148, 150, 196

GUT Grand Unified Theory. 22

HDPE High-density polyethylene. 50

HV High voltage. 55, 57, 58, 121, 122, 187, 194

HyperK hyper Kamiokande. 7, 14

HZC Hainan Zhanchuang Photonics Technology Co., Ltd. 33, 34

IBD Inverse Beta Decay. 20, 23–27, 29, 30, 37, 41, 42, 149, 184, 199

IceCube IceCube neutrino observatory. 7

IDE Integrated Development Environment. 137

IHEP Institute of High Energy Physics, Beijing. 19

IO Inverted ordering. 13, 14, 16, 184

IOC Input Output Controller. 64, 99, 135, 136

iPMT Intelligent Photomultipliertube. 4, 33, 54, 55, 57, 58, 105, 187, 199

JUNO Jiangmen Underground Neutrino Observatory. i, iii, 2, 7, 14, 17–21, 23–37, 39, 41, 42, 45, 55, 58, 60, 64, 68, 90, 94, 96, 105, 106, 109, 110, 114, 118–122, 127, 128, 131–134, 143, 144, 146, 147, 149–151, 184, 185, 187, 188, 193–195, 199, 200

K Potassium. 61

KATRIN Karlsruhe Tritium Neutrino Experiment. 6

LAB Linear Alkylbenzene. 23, 30, 31, 35, 48, 50, 53, 84, 185–187

LCS Laser Calibration System. 53, 54, 61, 63, 70, 75, 92, 94, 105–109, 111, 112, 114–116, 121, 125, 127, 131, 134, 143, 144, 146, 150, 187, 189, 195

LDS Light Distribution System. 4, 46, 68, 70, 72, 74, 78, 90, 94, 96–101, 103, 104, 108, 111, 114, 115, 118, 144–146, 150, 153, 162, 163, 176–179, 181, 188–192, 196, 197, 200

LED Light emitting diode. 61, 94, 127, 128, 130, 131, 133, 153, 194, 195

LHS Liquid Handling System. 39, 46, 50, 51, 114, 139, 142, 147, 186, 196

LIGO Laser Interferometer Gravitational-Wave Observatory. 20

LPMT Large Photomultipliertube. 33, 55, 64, 65, 105, 187

LS Liquid Scintillator. 2, 21, 24–27, 29, 30, 35–37, 40–43, 51, 52, 61, 105, 112, 114, 116, 149, 151, 185, 187

MCP Micro Channel Plate. 33, 34, 36, 55, 58, 118, 127, 128, 184

MiniBooNE Mini Booster Neutrino Experiment. 7

MINOS Main Injector Neutrino Oscillation Search. 8

MSW Michejew-Smirnow-Wolfenstein-Effekt. 13, 14

NAS Network attached storage. 60, 64, 65, 139, 188

nEXO next Enriched Xenon observatory. 7

NMH Neutrino mass hierarchy. 13

NNVT North Night Vission Technologies, Co. Inc.. 28, 33, 34, 56, 58, 184

NO Normal ordering. 13, 14, 16, 184

NOνA NuMI Off-Axis ν_e Appearance. 7, 8, 13, 14

NPP Nuclear Power Plant. 6, 18–20, 199

OPERA Oscillation Project with Emulsion-tRacking Apparatus. 8, 31, 36

OSIRIS Online Scintillator Internal Radioactivity Investigation System. i, iii, 2, 3, 33, 35, 39–43, 45, 46, 48–61, 63–65, 67–72, 75–78, 83, 92, 94–99, 105, 108–114, 116, 118, 119, 121, 124, 125, 127, 128, 130–140, 143–147, 149–151, 153, 171–173, 185–189, 191–197, 200

p.e. photon electron. 96, 109, 110, 116, 118, 123, 125, 193

PCB Printed Circuit Board. 57

PDE Photo Detection Efficiency. 33

PET Polyethylene terephthalate. 48

PMMA Polymethylmethacrylat. 107

PMNS Pontecorvo-Maki-Nakagawa-Sakata. 8, 9

PMT Photomulitpliertube. 2, 4, 27, 28, 30, 31, 33, 34, 36, 39, 47–50, 53–61, 65, 67, 68, 70, 71, 78, 83, 84, 86, 88, 96–98, 102, 105, 108–111, 114, 116, 118–123, 125, 127–134, 139, 142, 149–151, 164–167, 184, 186–188, 190–197, 199, 200

Po Polonium. 41, 42

PoE Power over Ethernet. 58

PPO 2,5-Diphenyloxazole. 114

PTFE Polytetrafluoroethylene. 53, 55, 61, 76, 79, 80, 128, 155, 159, 187, 189, 197

PV Process variable. 64, 89, 90, 135–137, 139, 140, 153, 195, 200

QE Quantum Efficiency. 33

RC Run control. 64, 188

RWTH Rheinisch-Westfälische Technische Hochschule. 55, 187

SAGE Soviet–American Gallium Experiment. 8

SC Slow Control. 46, 64, 65, 89, 92, 143, 150, 153, 188, 200

SCCU Slow Control and Configuration Unit. 55, 187

SiPM Silicon Photo-Multiplier. 37

SLAC Stanford Linear Accelerator Center. 139

SM Standard model (of particle physics). 6, 8

SN Supernova. 20

SNL State Notation Language. 89, 92

SNO Sudburry Neutrino Observatory. 8, 21

SOC System on Chip. 54, 57, 58

SSM Solar standard model. 8

SSS Stainless-steel Support Structure. 32, 184

STEREO Search for Sterile Reactor Neutrino Oscillations. 7

Super-K Super Kamiokande. 8, 13, 15, 183

T2K Tokai to Kamioka. 7, 13

TAO Taishan Antineutrino Observatory. 36, 37, 185

Th Thorium. 42, 43, 185

TTS Time Transit Spread. 33, 70, 96, 98, 110, 111, 118, 127, 128, 130, 131, 133, 193–195

TUM Technische Universität München. 77, 200

U Uranium. 42, 43, 185

VI Virtual instrument. 64

Zn Zink. 61

ZYNQ System on chip by Xilinx/Advanced Micro Devices. 54

Bibliography

[1] F. Reines and C. L. Cowan, "Detection of the Free Neutrino," *Phys. Rev.*, vol. 92, pp. 830–831, Nov 1953. [Online]. Available: https://link.aps.org/doi/10.1103/PhysRev.92.830

[2] Y. Ashie *et al.*, "Evidence for an Oscillatory Signature in Atmospheric Neutrino Oscillations," *Phys. Rev. Lett.*, vol. 93, p. 101801, Sep 2004. [Online]. Available: https://link.aps.org/doi/10.1103/PhysRevLett.93.101801

[3] K. Abe *et al.*, "Search for CP Violation in Neutrino and Antineutrino Oscillations by the T2K Experiment with 2.2×10^{21} Protons on Target," *Phys. Rev. Lett.*, vol. 121, p. 171802, Oct 2018. [Online]. Available: https://link.aps.org/doi/10.1103/PhysRevLett.121.171802

[4] N. Agafonova *et al.*, "Discovery of τ Neutrino Appearance in the CNGS Neutrino Beam with the OPERA Experiment," *Phys. Rev. Lett.*, vol. 115, p. 121802, Sep 2015. [Online]. Available: https://link.aps.org/doi/10.1103/PhysRevLett.115.121802

[5] M. A. Acero *et al.*, "First measurement of neutrino oscillation parameters using neutrinos and antineutrinos by NOvA," *Phys. Rev. Lett.*, vol. 123, p. 151803, Oct 2019. [Online]. Available: https://link.aps.org/doi/10.1103/PhysRevLett.123.151803

[6] H. de Kerret *et al.*, "The Double Chooz antineutrino detectors," *The European Physical Journal C*, vol. 82, 2022.

[7] F. An *et al.*, "The detector system of the Daya Bay reactor neutrino experiment," *Nuclear Instruments and Methods in Physics Research Section A: Accelerators, Spectrometers, Detectors and Associated Equipment*, vol. 811, pp. 133–161, 2016. [Online]. Available: https://www.sciencedirect.com/science/article/pii/S0168900215015636

[8] M. Aartsen *et al.*, "The IceCube Neutrino Observatory: instrumentation and online systems," *Journal of Instrumentation*, vol. 12, no. 03, p. P03012, mar 2017. [Online]. Available: https://dx.doi.org/10.1088/1748-0221/12/03/P03012

[9] Q. R. Ahmad *et al.*, "Direct Evidence for Neutrino Flavor Transformation from Neutral-Current Interactions in the Sudbury Neutrino Observatory," *Phys. Rev. Lett.*, vol. 89, p. 011301, Jun 2002. [Online]. Available: https://link.aps.org/doi/10.1103/PhysRevLett.89.011301

[10] B. T. Cleveland, T. Daily, J. Raymond Davis, J. R. Distel, K. Lande, C. K. Lee, P. S. Wildenhain, and J. Ullman, "Measurement of the Solar Electron Neutrino Flux with the Homestake Chlorine Detector," *The Astrophysical Journal*, vol. 496, no. 1, p. 505, mar 1998. [Online]. Available: https://dx.doi.org/10.1086/305343

[11] P. Anselmann *et al.*, "Solar neutrinos observed by GALLEX at Gran Sasso," *Physics Letters B*, vol. 285, no. 4, pp. 376–389, 1992. [Online]. Available: https://www.sciencedirect.com/science/article/pii/037026939291521A

[12] J. N. Abdurashitov *et al.*, "Measurement of the Solar Neutrino Capture Rate by SAGE and Implications for Neutrino Oscillations in Vacuum," *Phys. Rev. Lett.*, vol. 83, pp. 4686–4689, Dec 1999. [Online]. Available: https://link.aps.org/doi/10.1103/PhysRevLett.83.4686

[13] G. Bellini *et al.*, "Final results of Borexino Phase-I on low-energy solar neutrino spectroscopy," *Phys. Rev. D*, vol. 89, p. 112007, Jun 2014. [Online]. Available: https://link.aps.org/doi/10.1103/PhysRevD.89.112007

[14] M. S. Athar, S. W. Barwick, T. Brunner, J. Cao, M. Danilov, K. Inoue, T. Kajita, M. Kowalski, M. Lindner, K. R. Long, N. Palanque-Delabrouille, W. Rodejohann, H. Schellman, K. Scholberg, S.-H. Seo, N. J. Smith, W. Winter, G. P. Zeller, and R. Z. Funchal, "Status and perspectives of neutrino physics," *Progress in Particle and Nuclear Physics*, vol. 124, p. 103947, 2022. [Online]. Available: https://www.sciencedirect.com/science/article/pii/S0146641022000084

[15] T. Adam and others (JUNO Collaboration), "JUNO Conceptual Design Report," 2015. [Online]. Available: https://arxiv.org/abs/1508.07166

[16] Hyper-Kamiokande Proto-Collaboration, "Hyper-Kamiokande Design Report," 2018.

[17] DUNE Collaboration, "Long-Baseline Neutrino Facility (LBNF) and Deep Underground Neutrino Experiment (DUNE) Conceptual Design Report Volume 2: The Physics Program for DUNE at LBNF," 2016.

[18] A. Ishihara, "The IceCube Upgrade – Design and Science Goals," Available: https://arxiv.org/abs/1908.09441, 2019.

[19] F. An *et al.*, "Neutrino physics with JUNO," *Journal of Physics G*, vol. 43, no. 3, feb 2016. [Online]. Available: https://dx.doi.org/10.1088/0954-3899/43/3/030401

[20] B. Wonsak *et al.*, "A container-based facility for testing 20'000 20-inch PMTs for JUNO," *Journal of Instrumentation*, vol. 16 T08001, 2021.

[21] C. Liu *et al.*, "Check on the features of potted 20-inch PMTs with 1F3 electronics prototype at Pan-Asia," *Journal of Instrumentation*, vol. 18, P02003, 2023.

[22] A. Tietzsch, "Development, Installation and Operation of a Container-based Mass Testing System for 20-inch Photomultiplier Tubes for JUNO," Ph.D. dissertation, Eberhard Karls Universität Tübingen, 2020.

[23] Particle Data Group and Workman, "Review of Particle Physics," *Progress of Theoretical and Experimental Physics*, vol. 2022, no. 8, 08 2022, 083C01. [Online]. Available: https://doi.org/10.1093/ptep/ptac097

[24] M. K. Gaillard, P. D. Grannis, and F. J. Sciulli, "The standard model of particle physics," *Rev. Mod. Phys.*, vol. 71, pp. S96–S111, Mar 1999. [Online]. Available: https://link.aps.org/doi/10.1103/RevModPhys.71.S96

[25] M. Goldhaber, L. Grodzins, and A. W. Sunyar, "Helicity of Neutrinos," *Phys. Rev.*, vol. 109, pp. 1015–1017, Feb 1958. [Online]. Available: https://link.aps.org/doi/10.1103/PhysRev.109.1015

[26] T. Yanagida, "Horizontal Symmetry and Masses of Neutrinos," *Progress of Theoretical Physics*, vol. 64, no. 3, pp. 1103–1105, 09 1980. [Online]. Available: https://doi.org/10.1143/PTP.64.1103

[27] R. N. Mohapatra and G. Senjanović, "Neutrino Mass and Spontaneous Parity Nonconservation," *Phys. Rev. Lett.*, vol. 44, pp. 912–915, Apr 1980. [Online]. Available: https://link.aps.org/doi/10.1103/PhysRevLett.44.912

[28] J. Schechter and J. W. F. Valle, "Neutrino masses in SU(2) $\bigotimes$ U(1) theories," *Phys. Rev. D*, vol. 22, pp. 2227–2235, Nov 1980. [Online]. Available: https://link.aps.org/doi/10.1103/PhysRevD.22.2227

[29] T. Yanagida, "Horizontal Symmetry and Masses of Neutrinos," *Progress of Theoretical Physics*, vol. 64, no. 3, pp. 1103–1105, 09 1980. [Online]. Available: https://doi.org/10.1143/PTP.64.1103

[30] M. Aker, D. Batzler *et al.*, "Direct neutrino-mass measurement based on 259 days of katrin data," 2024. [Online]. Available: https://arxiv.org/abs/2406.13516

[31] K. Assamagan, C. Brönnimann, M. Daum, H. Forrer, R. Frosch, P. Gheno, R. Horisberger, M. Janousch, P. R. Kettle, T. Spirig, and C. Wigger, "Upper limit of the muon-neutrino mass and charged-pion mass from momentum analysis of a surface muon beam," *Phys. Rev. D*, vol. 53, pp. 6065–6077, Jun 1996. [Online]. Available: https://link.aps.org/doi/10.1103/PhysRevD.53.6065

[32] ALEPH Collaboration, "An upper limit on the τ-neutrino mass from the three- and five-prong tau decays," *The European Physical Journal C*, vol. 2, pp. 395–406, 1998. [Online]. Available: https://doi.org/10.1007/s100529800850

[33] The Planck Collaboration, "Planck 2018 results," *Astronomy & Astrophysics*, vol. 641, 2020. [Online]. Available: https://doi.org/10.1051/0004-6361/201833910

[34] The LEGEND Collaboration, "LEGEND-1000 Preconceptual Design Report," 2021. [Online]. Available: https://doi.org/10.48550/arXiv.2107.11462

[35] G. Adhikari *et al.*, "nEXO: neutrinoless double beta decay search beyond 1028 year half-life sensitivity," *Journal of Physics G: Nuclear and Particle Physics*, vol. 49, no. 1, p. 015104, dec 2021. [Online]. Available: https://dx.doi.org/10.1088/1361-6471/ac3631

[36] A. A. Aguilar-Arevalo *et al.*, "Search for Electron Neutrino Appearance at the $\Delta m^2 \sim 1$ ev^2 scale," *Phys. Rev. Lett.*, vol. 98, p. 231801, Jun 2007. [Online]. Available: https://link.aps.org/doi/10.1103/PhysRevLett.98.231801

[37] H. Almazán *et al.*, "Sterile Neutrino Constraints from the STEREO Experiment with 66 Days of Reactor-On Data," *Phys. Rev. Lett.*, vol. 121, p. 161801, Oct 2018. [Online]. Available: https://link.aps.org/doi/10.1103/PhysRevLett.121.161801

[38] K. Abe *et al.*, "Measurement of neutrino and antineutrino oscillations by the T2K experiment including a new additional sample of ν_e interactions at the far detector," *Phys. Rev. D*, vol. 96, p. 092006, Nov 2017. [Online]. Available: https://link.aps.org/doi/10.1103/PhysRevD.96.092006

[39] R. Davis, D. S. Harmer, and K. C. Hoffman, "Search for Neutrinos from the Sun," *Phys. Rev. Lett.*, vol. 20, pp. 1205–1209, May 1968. [Online]. Available: https://link.aps.org/doi/10.1103/PhysRevLett.20.1205

[40] J. N. Bahcall, N. A. Bahcall, and G. Shaviv, "Present Status of the Theoretical Predictions for the ^{37}Cl Solar-Neutrino Experiment," *Phys. Rev. Lett.*, vol. 20, pp. 1209–1212, May 1968. [Online]. Available: https://link.aps.org/doi/10.1103/PhysRevLett.20.1209

[41] B. T. Cleveland, T. Daily, J. Raymond Davis, J. R. Distel, K. Lande, C. K. Lee, P. S. Wildenhain, and J. Ullman, "Measurement of the Solar Electron Neutrino Flux with the Homestake Chlorine Detector," *The Astrophysical Journal*, vol. 496, no. 1, p. 505, mar 1998. [Online]. Available: https://dx.doi.org/10.1086/305343

[42] J. N. Bahcall and R. D. Jr., "Solar Neutrinos: A scientific puzzle," *Science*, vol. 191, pp. 264–267, 1976.

[43] P. Adamson *et al.*, "Improved Search for Muon-Neutrino to Electron-Neutrino Oscillations in MINOS," *Phys. Rev. Lett.*, vol. 107, p. 181802, Oct 2011. [Online]. Available: https://link.aps.org/doi/10.1103/PhysRevLett.107.181802

[44] The NOvA Collaboration, "First Measurement of Electron Neutrino Appearance in NOvA," *Phys. Rev. Lett.*, vol. 116, p. 151806, Apr 2016. [Online]. Available: https://link.aps.org/doi/10.1103/PhysRevLett.116.151806

[45] R. N. Mohapatra and G. Senjanović, "Neutrino Mass and Spontaneous Parity Nonconservation," *Phys. Rev. Lett.*, vol. 44, pp. 912–915, Apr 1980. [Online]. Available: https://link.aps.org/doi/10.1103/PhysRevLett.44.912

[46] J. Schechter and J. W. F. Valle, "Neutrino masses in SU(2) $\bigotimes$ U(1) theories," *Phys. Rev. D*, vol. 22, pp. 2227–2235, Nov 1980. [Online]. Available: https://link.aps.org/doi/10.1103/PhysRevD.22.2227

[47] I. Esteban *et al.*, "The fate of hints: updated global analysis of three-flavor neutrino oscillations," *J. High Energ. Phys.*, vol. 178, 2020.

[48] I. Esteban, C. G. Garcia *et al.*, "NuFIT 5.2," 2023, Online available, last accessed: 31.10.2023. [Online]. Available: http://www.nu-fit.org

[49] S. Bilenky, "On atmospheric neutrino mass-squared difference in the precision era," 2015. [Online]. Available: https://arxiv.org/abs/1512.04172

[50] L. Wolfenstein, "Neutrino oscillations in matter," *Phys. Rev. D*, vol. 17, pp. 2369–2374, May 1978. [Online]. Available: https://link.aps.org/doi/10.1103/PhysRevD.17.2369

[51] S. P. Mikheyev and A. Smirnov, "Resonant Amplification of ν Oscillations in Matter and Solar Neutrino Spectroscopy," *Il Nuovo Cimento C*, 1986.

[52] S. S. Chatterjee and A. Palazzo, "Nonstandard Neutrino Interactions as a Solution to the NOνA and T2K Discrepancy," *Phys. Rev. Lett.*, vol. 126, p. 051802, Feb 2021. [Online]. Available: https://link.aps.org/doi/10.1103/PhysRevLett.126.051802

[53] C. Adams *et al.*, "Neutrinoless Double Beta Decay," 2022.

[54] D. Moore, "Double Beta Decay review (theory & experiment)," 2023, Online available, last accessed: 27.12.2023. [Online]. Available: https://indico.cern.ch/event/1199289/contributions/5262783/attachments/2704274/4695972/20230829_TAUP_Moore_0vbb.pdf

[55] R. Patterson, "Prospects for Measurement of the Neutrino Mass Hierarchy," *Annual Review of Nuclear and Particle Science*, vol. 65, no. 1, pp. 177–192, 2015. [Online]. Available: https://doi.org/10.1146/annurev-nucl-102014-021916

[56] S. Choubey, "Prospects to determine the neutrino mass hierarchy," in *50th Rencontres de Moriond on EW Interactions and Unified Theories*, 2015, pp. 255–260.

[57] L. Zhan, Y. Wang, J. Cao, and L. Wen, "Determination of the Neutrino Mass Hierarchy at an Intermediate Baseline," *Phys. Rev. D*, vol. 78, p. 111103, 2008.

[58] P. F. de Salas, S. Gariazzo, O. Mena, C. A. Ternes, and M. Tórtola, "Neutrino Mass Ordering from Oscillations and Beyond: 2018 Status and Future Prospects," *Frontiers in Astronomy and Space Sciences*, vol. 5, 2018. [Online]. Available: https://www.frontiersin.org/articles/10.3389/fspas.2018.00036

[59] B. Jamieson, "Future Neutrino Experiments," in *20th Conference on Flavor Physics and CP Violation* , 7 2022.

[60] P. Lipari, "Matter effects in long-baseline experiments, the flavor content of the heaviest (or lightest) neutrino, and the sign of Δm^2," *Phys. Rev. D*, vol. 61, p. 113004, May 2000. [Online]. Available: https://link.aps.org/doi/10.1103/PhysRevD.61.113004

[61] M. C. Banuls, G. Barenboim, and J. Bernabeu, "Medium effects for terrestrial and atmospheric neutrino oscillations," *Phys. Lett. B*, vol. 513, pp. 391–400, 2001.

[62] S. Palomares-Ruiz and J. Bernabeu, "Atmospheric neutrinos and nu mass hierarchy," *Nucl. Phys. B Proc. Suppl.*, vol. 138, pp. 398–401, 2005.

[63] X. Qian and P. Vogel, "Neutrino mass hierarchy," *Progress in Particle and Nuclear Physics*, vol. 83, pp. 1–30, 2015. [Online]. Available: https://www.sciencedirect.com/science/article/pii/S0146641015000307

[64] The JUNO Collaboration, "JUNO International Collaboration established," 2015, Web source, last accessed 27.09.2024. [Online]. Available: http://juno.ihep.cas.cn/PPjuno/201408/t20140801_665585.html

[65] B. P. Abbott *et al.*, "LIGO: the Laser Interferometer Gravitational-Wave Observatory," *Reports on Progress in Physics*, vol. 72, no. 7, p. 076901, jun 2009. [Online]. Available: https://dx.doi.org/10.1088/0034-4885/72/7/076901

[66] I. M. Hook, "Supernovae and cosmology with future European facilities," *R. Soc. A*, vol. 371, 2013.

[67] K. Abe *et al.*, "Diffuse supernova neutrino background search at Super-Kamiokande," *Phys. Rev. D*, vol. 104, p. 122002, Dec 2021. [Online]. Available: https://link.aps.org/doi/10.1103/PhysRevD.104.122002

[68] D. Basilico *et al.*, "Final results of Borexino on CNO solar neutrinos," *Phys. Rev. D*, vol. 108, p. 102005, Nov 2023. [Online]. Available: https://link.aps.org/doi/10.1103/PhysRevD.108.102005

[69] A. Bellerive, J. Klein, A. McDonald, A. Noble, and A. Poon, "The Sudbury Neutrino Observatory," *Nuclear Physics B*, vol. 908, pp. 30–51, 2016, neutrino Oscillations: Celebrating the Nobel Prize in Physics 2015. [Online]. Available: https://www.sciencedirect.com/science/article/pii/S0550321316300736

[70] M. Agostini *et al.*, "Improved measurement of ^{8}B solar neutrinos with 1.5 $\mathrm{kt \cdot y}$ of Borexino exposure," *Phys. Rev. D*, vol. 101, p. 062001, Mar 2020. [Online]. Available: https://link.aps.org/doi/10.1103/PhysRevD.101.062001

[71] A. Gando *et al.*, "^{7}Be solar neutrino measurement with KamLAND," *Phys. Rev. C*, vol. 92, p. 055808, Nov 2015. [Online]. Available: https://link.aps.org/doi/10.1103/PhysRevC.92.055808

[72] F. Capozzi, G. L. Fogli, E. Lisi, A. Marrone, D. Montanino, and A. Palazzo, "Status of three-neutrino oscillation parameters, circa 2013," *Phys. Rev. D*, vol. 89, p. 093018, May 2014. [Online]. Available: https://link.aps.org/doi/10.1103/PhysRevD.89.093018

[73] C. Jaupart, S. Labrosse, and J.-C. Mareschal, "7.06 - Temperatures, Heat and Energy in the Mantle of the Earth," in *Treatise on Geophysics*, G. Schubert, Ed. Amsterdam: Elsevier, 2007, pp. 253–303. [Online]. Available: https://www.sciencedirect.com/science/article/pii/B9780444527486001140

[74] R. Han *et al.*, "Potential of geo-neutrino measurements at JUNO*," *Chinese Physics C*, vol. 40, no. 3, p. 033003, mar 2016. [Online]. Available: https://dx.doi.org/10.1088/1674-1137/40/3/033003

[75] R. N. Mohapatra and G. Senjanović, "Neutrino Mass and Spontaneous Parity Nonconservation," *Phys. Rev. Lett.*, vol. 44, pp. 912–915, Apr 1980. [Online]. Available: https://link.aps.org/doi/10.1103/PhysRevLett.44.912

[76] M. Gell-Mann, P. Ramond, and R. Slansky, "Complex Spinors and Unified Theories," *Conf. Proc. C*, vol. 790927, pp. 315–321, 1979.

[77] S. Davidson, E. Nardi, and Y. Nir, "Leptogenesis," *Physics Reports*, vol. 466, no. 4, pp. 105–177, 2008. [Online]. Available: https://www.sciencedirect.com/science/article/pii/S0370157308001889

[78] P. Huber, "Determination of antineutrino spectra from nuclear reactors," *Phys. Rev. C*, vol. 84, p. 024617, Aug 2011. [Online]. Available: https://link.aps.org/doi/10.1103/PhysRevC.84.024617

[79] C. Giunti and M. Laveder, "Statistical significance of the gallium anomaly," *Phys. Rev. C*, vol. 83, p. 065504, Jun 2011. [Online]. Available: https://link.aps.org/doi/10.1103/PhysRevC.83.065504

[80] J. A. Formaggio and G. P. Zeller, "From eV to EeV: Neutrino cross sections across energy scales," *Rev. Mod. Phys.*, vol. 84, pp. 1307–1341, Sep 2012. [Online]. Available: https://link.aps.org/doi/10.1103/RevModPhys.84.1307

[81] F. von Feilitzsch, A. Hahn, and K. Schreckenbach, "Experimental beta-spectra from 239Pu and 235U thermal neutron fission products and their correlated antineutrino spectra," *Physics Letters B*, vol. 118, no. 1, pp. 162–166, 1982. [Online]. Available: https://www.sciencedirect.com/science/article/pii/0370269382906220

[82] A. Hahn, K. Schreckenbach, W. Gelletly, F. von Feilitzsch, G. Colvin, and B. Krusche, "Antineutrino spectra from 241Pu and 239Pu thermal neutron fission products," *Physics Letters B*, vol. 218, no. 3, pp. 365–368, 1989. [Online]. Available: https://www.sciencedirect.com/science/article/pii/0370269389915980

[83] P. Vogel, G. K. Schenter, F. M. Mann, and R. E. Schenter, "Reactor antineutrino spectra and their application to antineutrino-induced reactions. II," *Phys. Rev. C*, vol. 24, pp. 1543–1553, Oct 1981. [Online]. Available: https://link.aps.org/doi/10.1103/PhysRevC.24.1543

[84] P. Huber, "Determination of antineutrino spectra from nuclear reactors," *Phys. Rev. C*, vol. 84, p. 024617, Aug 2011. [Online]. Available: https://link.aps.org/doi/10.1103/PhysRevC.84.024617

[85] T. A. Mueller, D. Lhuillier, M. Fallot, A. Letourneau, S. Cormon, M. Fechner, L. Giot, T. Lasserre, J. Martino, G. Mention, A. Porta, and F. Yermia, "Improved predictions of reactor antineutrino spectra," *Phys. Rev. C*, vol. 83, p. 054615, May 2011. [Online]. Available: https://link.aps.org/doi/10.1103/PhysRevC.83.054615

[86] M. Wurm, F. von Feilitzsch, and J.-C. Lanfranchi, *Neutrino Detectors*. Cham: Springer International Publishing, 2021, pp. 371–412. [Online]. Available: https://doi.org/10.1007/978-3-319-93785-4_14

[87] C. Genster, "Software and hardware development for the nextgeneration liquid scintillator detectors JUNO and OSIRIS," Ph.D. dissertation, RWTH Aachen, 2019.

[88] B. Wonsak, C. Hagner, D. Hellgartner, K. Loo, S. Lorenz, D. Meyhöfer, L. Oberauer, H. Rebber, W. Trzaska, and M. Wurm, "Topological track reconstruction in unsegmented, large-volume liquid scintillator detectors," *Journal of Instrumentation*, vol. 13, no. 07, p. P07005, jul 2018. [Online]. Available: https://dx.doi.org/10.1088/1748-0221/13/07/P07005

[89] L. Zhan, "JUNO: A Next Generation Reactor Antineutrino Experiment," *Nuclear and Particle Physics Proceedings*, vol. 273-275, pp. 1825–1829, 2016, 37th International Conference on High Energy Physics (ICHEP). [Online]. Available: https://www.sciencedirect.com/science/article/pii/S240560141500783X

[90] H. Nunokawa, S. Parke, and R. Z. Funchal, "Another possible way to determine the neutrino mass hierarchy," *Phys. Rev. D*, vol. 72, p. 013009, Jul 2005. [Online]. Available: https://link.aps.org/doi/10.1103/PhysRevD.72.013009

[91] A. Cabrera, M. Grassi, and Y. Han., "JUNO Energy Spectrum," 2018, Internal JUNO collaboration dokument, DocDB#3497-v4.

[92] S. A. A. Abusleme, T. Adam *et al.*, "Mass testing and characterization of 20-inch PMTs for JUNO," *The European Physical Journal C*, vol. 82, 1168, 2022.

[93] A. Abusleme, T. Adam, S. Ahmad *et al.*, "Radioactivity control strategy for the JUNO detector," *Journal of High Energy Physics*, vol. 102, 2021.

[94] F.-J. Luo, Y.-K. Heng, Z.-M. Wang, P.-L. Wang, Z.-H. Qin, M.-H. Xu, D.-H. Liao, H.-Q. Zhang, Y.-B. Huang, X.-C. Lei, S. Qian, S.-L. Liu, Y.-B. Chen, and Y.-F. Wang, "PMT overshoot study for the JUNO prototype detector*," *Chinese Physics C*, vol. 40, no. 9, p. 096002, sep 2016. [Online]. Available: https://dx.doi.org/10.1088/1674-1137/40/9/096002

[95] X. Dong-Mei *et al.*, "Temperature dependence of the light yield of the LAB-based and mesitylene-based liquid scintillators," *Chinese Physics C*, vol. 38, no. 11, p. 116001, nov 2014. [Online]. Available: https://dx.doi.org/10.1088/1674-1137/38/11/116001

[96] A. Formozov *et al.*, "The measurement of liquid scintillator nonlinear response and intrinsic energy resolution," *Journal of Physics: Conference Series*, vol. 1390, no. 1, p. 012111, nov 2019. [Online]. Available: https://dx.doi.org/10.1088/1742-6596/1390/1/012111

[97] X. Zhou *et al.*, "Spectroscopic study of light scattering in linear alkylbenzene for liquid scintillator neutrino detectors," *EPJC*, 2015.

[98] H. tao Chen, B. xiang Yu, Q. Shan, Y. yun Ding, B. Du, S. tong Liu, X. Zhang, L. Zhou, W. bao Jia, J. Fang, X. chen Ye, W. Hu, S. li Niu, J. qing Yan, H. Zhao, and D. jin Zhao, "Aging research of the LAB-based liquid scintillator in stainless steel container," 2014.

[99] A. Abusleme *et al.*, "The JUNO experiment Top Tracker," *Nuclear Instruments and Methods in Physics Research Section A: Accelerators, Spectrometers, Detectors and Associated Equipment*, vol. 1057, p. 168680, 2023. [Online]. Available: https://www.sciencedirect.com/science/article/pii/S0168900223006708

[100] The JUNO Collaboration, "Drawing of JUNO Detector-A.png," 2023, Part of the official publication material of the JUNO collaboration.

[101] Q. Sen, "The Industrialization of MCP-PMT," 2016, Internal JUNO collaboration dokument, DocDB#1310-v1.

[102] A. Abusleme, T. Adam, S. Ahmad *et al.*, "The design and sensitivity of JUNO's scintillator radiopurity pre-detector OSIRIS," *The European Physical Journal C*, vol. 81:973, 2021.

[103] C. Cao *et al.*, "Mass production and characterization of 3-inch PMTs for the JUNO experiment," *Nuclear Instruments and Methods in Physics Research Section A: Accelerators, Spectrometers, Detectors and Associated Equipment*, vol. 1005, p. 165347, 2021. [Online]. Available: https://www.sciencedirect.com/science/article/pii/S0168900221003314

[104] A. Di Giovanni, A. Candela, N. Di Marco, M. D'Incecco, C. Gustavino, M. Lindozzi, D. Orlandi, and E. Tatananni, "The Veto system of the OPERA experiment," *Nuclear Physics B - Proceedings Supplements*, vol. 158, pp. 40–43, 2006, proceedings of the 8th International Workshop on Resistive Plate Chambers and Related Detectors. [Online]. Available: https://www.sciencedirect.com/science/article/pii/S0920563206004233

[105] C. Genster, M. Schever, L. Ludhova, M. Soiron, A. Stahl, and C. Wiebusch, "Muon reconstruction with a geometrical model in JUNO," *Journal of Instrumentation*, vol. 13, no. 03, p. T03003, mar 2018. [Online]. Available: https://dx.doi.org/10.1088/1748-0221/13/03/T03003

[106] B. Wonsak, C. Hagner, D. Hellgartner, K. Loo, S. Lorenz, D. Meyhöfer, L. Oberauer, H. Rebber, W. Trzaska, and M. Wurm, "Topological track reconstruction in unsegmented, large-volume liquid scintillator detectors," *Journal of Instrumentation*, vol. 13, no. 07, p. P07005, jul 2018. [Online]. Available: https://dx.doi.org/10.1088/1748-0221/13/07/P07005

[107] The JUNO Collaboration, "Global TT 05.png," 2023, Part of the official publication material of the JUNO collaboration.

[108] C.-F. Yang, Y.-B. Huang, J.-L. Xu, D.-R. Wu, H.-Q. Lu, Y.-P. Zhang, W.-M. Luo, M. He, G.-M. Chen, and S.-Y. Zhang, "Reconstruction of Muon Bundle in the JUNO Central Detector," 2022. [Online]. Available: https://arxiv.org/abs/2201.11321

[109] C. Lombardo, "Overview of the JUNO-TAO detector," *Nuclear Instruments and Methods in Physics Research Section A: Accelerators, Spectrometers, Detectors and Associated Equipment*, vol. 1048, p. 168030, 2023. [Online]. Available: https://www.sciencedirect.com/science/article/pii/S0168900223000207

[110] D. V. Forero, R. Hawkins, and P. Huber, "The benefits of a near detector for JUNO," 2017. [Online]. Available: https://arxiv.org/abs/1710.07378

[111] T. Heinz, "JUNO's sensitivity to the Neutrino Mass Ordering in Presence of a Fine Structure in the Reactor Antineutrino Spectrum," Ph.D. dissertation, Eberhard Karls Univeristät Tübingen, 2024.

[112] JUNO Collaboration, "TAO Conceptual Design Report: A Precision Measurement of the Reactor Antineutrino Spectrum with Sub-percent Energy Resolution," 2020. [Online]. Available: https://arxiv.org/abs/2005.08745

[113] H. e. a. Xu, "Calibration strategy of the JUNO-TAO experiment," *The European Physical Journal C*, vol. 82, 2022.

[114] M. A. Hoffmann, "Liquid scintillators and liquefied rare gases for particle detectors. Background-determination in Double Chooz and scintillation properties of liquid argon," Ph.D. dissertation, TU Munich, 2012.

[115] A. Müller, "Simulation based software and hardware development for the active reduction of muon induced background in the liquid scintillator detectors JUNO and OSIRIS / vorgelegt von Axel Müller," Ph.D. dissertation, Eberhard Karls Universität Tübingen, 2022.

[116] A. Göttel, "Solar neutrino detection: CNO discovery with borexino and preparations for success in JUNO and OSIRIS," Ph.D. dissertation, RWTH Aachen, 2023.

[117] J. Liu, B. Cai, R. Carr, D. Dwyer, W. Gu, G. Li, X. Qian, R. McKeown, R. Tsang, W. Wang, F. Wu, and C. Zhang, "Automated calibration system for a high-precision measurement of neutrino mixing angle θ_{13} with the Daya Bay antineutrino detectors," *Nuclear Instruments and Methods in Physics Research Section A: Accelerators, Spectrometers, Detectors and Associated Equipment*, vol. 750, pp. 19–37, 2014. [Online]. Available: https://www.sciencedirect.com/science/article/pii/S0168900214002332

[118] C. Vollbrecht, "Software and hardware development for the liquid scintillator detector OSIRIS of the JUNO experiment," Ph.D. dissertation, RWTH Aachen, 2024.

[119] R. Triozzi *et al.*, "Implementation and performances of the IPbus protocol for the JUNO Large-PMT readout electronics," 2023. [Online]. Available: https://arxiv.org/abs/2302.10133

[120] K. Loo, "Update on Osiris run control," 2022, Internal JUNO collaboration dokument, DocDB#8689-v1.

[121] Keysight Technologies, "33500B and 33600A Series Trueform Waveform Generators," Available: https://www.keysight.com/de/de/assets/7018-05928/data-sheets/5992-2572.pdf, 2023, Web resource, last accessed 27.09.2024.

[122] Advanced Laser Diode Systems A.L.S. GmbH, *Picosecond Diode Laser - PiLas*, 2015.

[123] NKT Photonics A/S, "NKT Photonics website," 2023. [Online]. Available: https://www.nktphotonics.com/

[124] The Geant4 Collaboration, "Introduction to Geant4," 2023, Online available, last accessed: 03.04.2024. [Online]. Available: https://geant4-userdoc.web.cern.ch/UsersGuides/IntroductionToGeant4/fo/IntroductionToGeant4.pdf

[125] Internetchemie ChemLin, "Brechungsindex Wasser," 1996 - 2024, Online available, last accessed: 04.04.2024. [Online]. Available: https://www.internetchemie.info/chemie-lexikon/daten/b/brechungsindex%20wasser.php

[126] Kern GmbH, "Brechungsindex | KERN," 2024, Online available, last accessed: 04.04.2024. [Online]. Available: https://www.kern.de/de/kunststofflexikon/brechungsindex

[127] H. W. C. Tseung and N. Tolich, "Ellipsometric measurements of the refractive indices of linear alkylbenzene and EJ-301 scintillators from 210 to 1000nm," *Physica Scripta*, vol. 84, no. 3, p. 035701, aug 2011. [Online]. Available: https://dx.doi.org/10.1088/0031-8949/84/03/035701

[128] National Instruments Corp., "What is NI LabVIEW?" Avialble: https://www.ni.com/en/shop/labview.html, 2024, Online source, last accessed 18.09.2024.

[129] EPICS Controls, "EPICS Documentation," 2023, Online available, last accessed: 03.04.2024. [Online]. Available: https://docs.epics-controls.org/en/latest/

[130] R. Wirth, "OSIRIS calibration update," 2024, Internal talk, given at the 2024 JUNO collaboration meeting.

[131] A. Coppi *et al.*, "Mass testing of the JUNO experiment 20-inch PMT readout electronics," *Nuclear Instruments and Methods in Physics Research Section A: Accelerators, Spectrometers, Detectors and Associated Equipment*, vol. 1052, p. 168255, 2023. [Online]. Available: https://www.sciencedirect.com/science/article/pii/S0168900223002450

[132] L. Delasio, M. Kraimer, and A. Kozubal, "EPICS Architecture*," Online available, last accessed 08.04.2024. [Online]. Available: https://epics.anl.gov/EpicsDocumentation/EpicsGeneral/EPICS_Architecture.pdf

[133] The CS Studio Collaboration, "Control System Studio," Available: https://www.controlsystemstudio.org/, 2024, Online source, last accessed 13.09.2024.

[134] S. Brewer and M. Shankar, "EPICS Archiver Appliance," Available: https://epicsarchiver.readthedocs.io, 2024, Online source, last accessed 13.09.2024.

[135] M. Shankar, "Architecture of a single appliance," Online available, last accessed 11.04.2024. [Online]. Available: https://slacmshankar.github.io/epicsarchiver_docs/details.html

Danksagung/Acknowledgements

Dieses Kapitel möchte ich nutzen, um all denen "Danke" zu sagen, die mir diese Arbeit überhaupt ermöglicht haben.

Zunächst natürlich Prof. Dr. Tobias Lachenmaier dafür, dass ich diese Arbeit überhaupt machen durfte. Ebenso für die hilfreichen Diskussionen und Ratschläge zu PMTs, OSIRIS und Auswertungsstatistik waren extrem hilfreich. Auch das Ermöglichen der vielen Reisen zu Meetings und nach China waren wirklich hilfreich. Meine Doktorarbeit bei OSIRIS machen zu dürfen war trotz der zum Teil harten Zeiten on-site eine Erfahrung die ich nicht missen wollen würde.

Des weiteren möchte Prof. Dr. Michael Wurm danken für all den Support während der Arbeit an, auf, in und um OSIRIS. Trotz der vielen "wir sollten mal dringend über ... reden" Mails und Calls wurde uns On-sitlern immer so gut wie Möglich geholfen. Und zu guter Letzt natürlich auch für das Vertrauen das in mich gesetzt wurde am Ende doch so große Teile von OSIRIS machen zu dürfen.

Der On-Site Crew Oliver Pilarczyk, Cornelius Vollbrecht, Arshak Jafar, Rosmarie Wirth und Meishu Liu für die Zeit on-site. Ohne euch wäre die zeit am Detektor viel unangenehmer gewesen, der nächste Karton Tsingtao geht auf mich ;-).
Addittionally, I would like to thank Zhimin Wang for his local support during our stays in both, work related stuff and removing language barriers.
Kai Loo, Konstantin Schweizer und Rosmarie Wirth für ihre Arbeit an der DAQ, ohne euch hätte ich es am Ende nicht doch noch zu einer Datenanalyse geschafft.

Außerdem möchte ich mich bei der Gruppe Jochum/Lachenmaier in Tübingen bedanken. Bei Axel Müller bei seiner großen Hilfe bei der Erzeugung der Simulationsergebnisse und bei Alexander Tietzsch bei dem ich bereits im Bachelor sehr viel über Hardware, wissenschaftliches Arbeiten und Planung lernen durfte.
Dann natürlich bei den "Gentlemen": An-Ka, Katha, Katja, Gina, Jessi, Marc, Tobi, Rauschi, Lukas und Collin, ohne euch hätte ich wahrscheinlich nicht durch gehalten. Danke für all die langen Stunden die wir im Büro damit verbracht haben einfach mal über was anderes zu reden, für die Grillabende und das Feiern gehen. Danke das ihr mich ausgehalten habt, auch wenn es manchmal zu einem "Diva"-Vorfall kam ;-). Aber natürlich auch danke dafür das man trotzdem immer zu euch kommen konnte, wenn man mal Hilfe gebracht hat, ihr hattet immer ein offenes Ohr. Für euch steht immer ein Bier oder Cider bereit.
Ich wäre wahrscheinlich schon in meinem ersten Jahr unter dem nötigen Papierkram untergegangen, wenn Gaby Behring nicht gewesen wäre. Vielen Dank

dafür, das du mir nicht nur einmal den Hintern gerettet hast beim Bewältigen dieses Bürokratiemonsters.

Wilhelm Mack für den gelegentlich nötigen, abendlichen Ausgleich, vor Allem in den letzten Jahren meiner Arbeit. Die vielen Gespräche (und das eine oder andere Bier) haben wirklich sehr geholfen nicht zu verzweifeln, wenns mal wieder nicht so voran ging, wie erhofft.
Danken möchte ich außerdem Dr. Hans Steiger für die Gespräche über die Wissenschaft im Allgemeinen, JUNO im besonderen und natürlich deren (politische) Hintergründe. Diese Gespräche haben mir sehr geholfen, vieles zu Verstehen und auch richtig einordnen zu können und mir über manche Kommentare und Reaktionen nicht zu sehr den Kopf zu zerbrechen.
Hanne, Jule, Flo und Morty für die Beste Zeit in einer WG die man nur haben kann. Ohne euch hätte vor Allem die Zeit und die Arbeit während Covid nicht mal halb so viel Spaß gemacht.

Außerdem meiner Familie, vor allem meinen Eltern, die immer an mich geglaubt haben und mich unterstützt haben, wo es nur ging. Sei es nach der Realschule, sei es nach dem Gymnasium oder in den verschiedenen Abschnitten meines Studiums. Ihr habt mich immer unterstützt und machen lassen und, wo's nötig war, auch mal geschubst ;-).
Dann noch meiner kleinen Oma. Ohne dich wäre ich nicht so wie ich jetzt bin. Ich weiß das du das hier nicht mehr lesen kannst, aber es hat mir unendlich viel bedeutet, das du dich bis zuletzt so mit mir über mein Studium gefreut hast.

Vanessa, natürlich will ich auch dir danken, für deine Zeit, das du mich trotz der Rückschläge immer wieder aufgebaut und mir Mut gegeben hast (auch wenn ich mir leider nicht immer hab anmerken lassen, dass es geklappt hat) und die ganze Sache überhaupt so mitgemacht hast. Ich glaube ohne dich wär ich nie soweit gekommen über eine Doktorarbeit überhaupt nachdenken zu können. Ich kann nur "danke" sagen und freue mich unglaublich auf unsere weitere Zeit.